Politecnico di Torino

ScuDo
Scuola di Dottorato ~ Doctoral School
WHAT YOU ARE, TAKES YOU FAR

Doctoral Dissertation
Doctoral Program in Electrical, Electronics, and Communications Engineering
(34^{th}cycle)

A Bio-Inspired Processing Unit for Surface Electromyography Applications

By

Fabio Rossi

******

Supervisor(s):
Prof. D. Demarchi, Politecnico di Torino, Supervisor
Ph.D. P. Motto Ros, Politecnico di Torino, Co-Supervisor

Doctoral Examination Committee:
Prof. S. Conoci., Referee, University of Messina
Prof. L. Seminara, Referee, University of Genoa
Prof. G. Pagana, Politecnico di Torino
Prof. F. Pareschi, Politecnico di Torino
Ph.D. F. Begarani, Omnidermal Biomedics S.r.l.

Politecnico di Torino
2022

Declaration

I hereby declare that, the contents and organization of this dissertation constitute my own original work and does not compromise in any way the rights of third parties, including those relating to the security of personal data.

Fabio Rossi
2022

* This dissertation is presented in partial fulfillment of the requirements for **Ph.D. degree** in the Graduate School of Politecnico di Torino (ScuDo).

Abstract

Device wearability and operating time are trending topics in recent state-of-art works on surface ElectroMyoGraphic (sEMG) muscle monitoring. No optimal trade-off, able to concurrently address the several problems of the acquisition system like robustness, miniaturization, versatility, and power efficiency, has yet been found. This thesis aims to present a feasible solution to overcome most of these issues, embedding in a single device both an sEMG bipolar acquisition channel, exploiting the custom event-driven hardware feature extraction technique (named Average Threshold Crossing - ATC), and a digital part, which includes a microcontroller unit, for (optionally) sEMG sampling and processing, and a Bluetooth communication, for wireless data transmission.

The combination of the design paradigms with an accurate selection of each single component results in a very efficient prototype, with a comfortable final size of 57.8 mm length $\times$ 25.2 mm height $\times$ 22.1 mm width and a weight of 27.4 g (rechargeable battery included), perfectly suitable to be used without impacting the freedom of movement. It features a consistent signal-to-noise ratio of the acquired sEMG (higher than 15 dB) tested on various sessions, from static isometric standardized exercises to dynamic contraction (e.g., human gait). Furthermore, a precise design of the firmware has been performed, handling both signals acquisition and Bluetooth transmission concurrently, thanks to a custom implementation of the FreeRTOS kernel. In particular, the system adapts to both sEMG and ATC transmission, with an application throughput up to 2 kB s^{-1} and an average operating time of 80 h (for high resolution sEMG sampling), relaxable to 8 B s^{-1} throughput and about 230 h operating time (considering a 110 mAh battery), in case of ATC acquisition only.

Its application in building biomedical systems led to very promising results. In the active control of the Functional Electrical Stimulation (FES), a good similarity (above 85 %) has been obtained in replicating voluntary and stimulated movements during simulated therapist-patient rehabilitative sessions, also achieving the ATC-FES pulses pattern definition within 6 ms, largely satisfying the typical 300 ms real-time constraint for bio-medical data processing. For Human-Machine Interface (HMI) applications, seven units have been arranged to create an armband, to be worn around the forearm, able to recognize 9 hand gestures by using an embedded Artificial Neural Network (ANN) classifier, which, combining an accuracy of 91.6 %, a minimal prediction latency of 1.49 ms, and limited power consumption of 10.8 mW, allows the device to run unaltered for up to 60 h.

As a consequence of the above achievements, the developed ATC sensing node performs pretty well both in the monitoring of the skeletal muscle activity, featuring strong robustness to environmental noise and enabling the possibility to operate unaltered for a week at least, and when it is employed for building up real-time processing bio-medical systems, they are either the application of rehabilitative procedure or the recognition of functional hand movements. In this perspective, considering the relaxation of the design and application requirements and looking at the improvements in the operating time of the devices, the benefits of the event-driven ATC technique are practically visible, thus opening novel studies towards bio-inspired research.

Contents

List of Figures

List of Tables

Chapter 1

Introduction

1.1 Motivation

In recent years, thanks to significant advancements in developing bio-electronic systems, monitoring the body's parameters (e.g., cardiac rhythm, glucose concentration) is revolutionizing the standard medicine based on a diagnosis approach. The possibility to easily and constantly look at what happens inside (and outside) our body allows the medical science to disclose the diseases before their onset.

Among the diagnostic tools enclosing the preventive medicine, the Surface ElectroMyoGraphy (sEMG) covers a central role in all the scenarios concerning the evaluation of human skeletal muscle activity. Indeed, by placing bio-potential electrodes directly on skin surface, sEMG provides an accessible and low-cost way to monitor the health of our muscle tissues [1, 2]. During the last 30 years, beyond the constant evolution of sEMG in clinical applications [3–5], its practice also branches, reaching different non-medical sectors [6], e.g., fitness monitoring [7], (therapeutic) gaming control [8], virtual reality interaction [9], human-machine interface [10, 11], speech [12] and gesture [13, 14] recognition.

Consequently to the sEMG applications spreading, related scientific publications [15, 16] describe the potentialities and diversities in developed sEMG systems: indeed, digging into the multitude of published documents, we can understand how the technology progress allowed the realization of functional and efficient solutions [17–20]. By analyzing the current sEMG works [21, 22], focusing on State-of-Art (SoA) wearable systems, the extraction of the common functional features

from all of them brings to the identification of the following ones as application-key aspects [14]:

- Accurate representation of muscular activity [23, 24]: good signal detection with respect to environmental noise sources (i.e., Signal-to-Noise Ratio (SNR) in 10 dB–30 dB range) and sufficiently representative digitization level (i.e., analog to digital conversion on 12 bit–24 bit);
- Fast system response to input variability: the overall application latency has to fulfill the real-time constraints (i.e., 100 ms to 300 ms) requested by the user application [25];
- Miniaturization of the final device dimensions: packaging all the system components in a small, light, and comfortable solution in order to monitor bio-signal activities without any bias due to the wearable device;
- Robust and accessible data streaming [7]: the wireless transfer of the data has to be stable over-time while providing a standard and versatile interface with smart devices (e.g., smartphone, smartwatch);
- Sufficiently long operating time: multi-days human activities monitoring could be investigated by using power-efficient devices able to work continuously without a frequent recharge of the battery.

However, although these milestones can be easily summarized in a five-points list, many literature works [26–31] still struggled to integrate all of them into a single optimized solution. Among the reasons, accurate signal digitization increases the amount of data to be processed and transmitted, thus impacting on power consumption of the device. Miniaturization (avoiding dedicated microchip) often brings to circuitry simplification, which relies on signal quality. Low-energy wireless transmission could be a bottleneck in terms of data payload, which could be overcome by wiring the connections, but sacrificing sensor wearability. Dedicated user applications [21, 17–19] can solve some of the above issues, but generally losing the possibility to be implemented in different configurations.

Therefore, looking at this open scenario, this Ph.D. project focuses on the design and development of an sEMG system able to face these challenges concurrently.

Taking inspiration from event-driven processing approaches and bio-inspired electronics [32], three design paradigms (i.e., bio-inspired, event-based, and information synthesis) will be combined to define the low-computational Average Threshold Crossing (ATC) feature extraction technique. Starting from this novel event-driven processing, the main goal of this thesis will be the realization of an sEMG sensing node prototype able to perform a good muscle activity detection, an on board feature extraction process (i.e., ATC), and a reliable data transmission into a compact and wearable solution, which operating time can reach up to 24 h at least. Additionally, dedicated attention will be given to the system versatility, making the device(s) able to be used in different configurations depending on the application requirements, also considering and discussing the limitations and benefits of the ATC approach.

1.2 Fundamentals of the musculo-skeletal system

The starting point for an adequate comprehension of the works involving the surface ElectroMyoGraphy (sEMG) technique lies in the description of the basic physiological unit responsible for the generation of this bio-electronic signal, the skeletal muscle tissue.

The skeletal muscle is one of the organs of the muscular system (together with cardiac and smooth muscles) which is under the volitional control of the somatic nervous system. It belongs to the striated tissue typology since its structure presents bands of cross-striations (referred as stripe) as the results of the thick and thin myofilaments overlapping inside the muscle cell [33], as shown in the top left image of Fig. 1.1. The highly ordered structure of the skeletal muscle is evolved in order to accomplish increasingly complex tasks related to the mechanical, homeostatic and biochemical functions [34]: indeed, if from a direct point of view, the contraction of the muscles maintains the upright posture and generates the movement, by converting chemical energy into mechanical one, it also carries out lots of concealed tasks, such as the maintenance of the proper blood flow through the synergistic activation of different muscles, the accumulation of important substrates (e.g., amino acids and carbohydrates), or the heat production to support body temperature.

Muscle weight composition is basically divided into a 75 % of water, 20 % of protein, and the residual 5 % comprises inorganic salts, minerals, fat, and carbohydrates. In the human body, the muscular system covers approximately the 40 % of the total body weight, containing from the 50 % to 75 % of all proteins and accounting for 30 %-50 % of the protein turnover [34].

Since the muscle contraction is a consequence of nervous stimuli, the nervous system together with the muscular one form the *neuromuscular system*, which links the idea of action with the physical action itself. Moreover, the stable connection between muscles and bones (through the tendons) allows the body to move as the result of the muscle contraction which moves close/far two or more bones; the interaction between the muscle and the skeletal systems is named *musculo-skeletal* system.

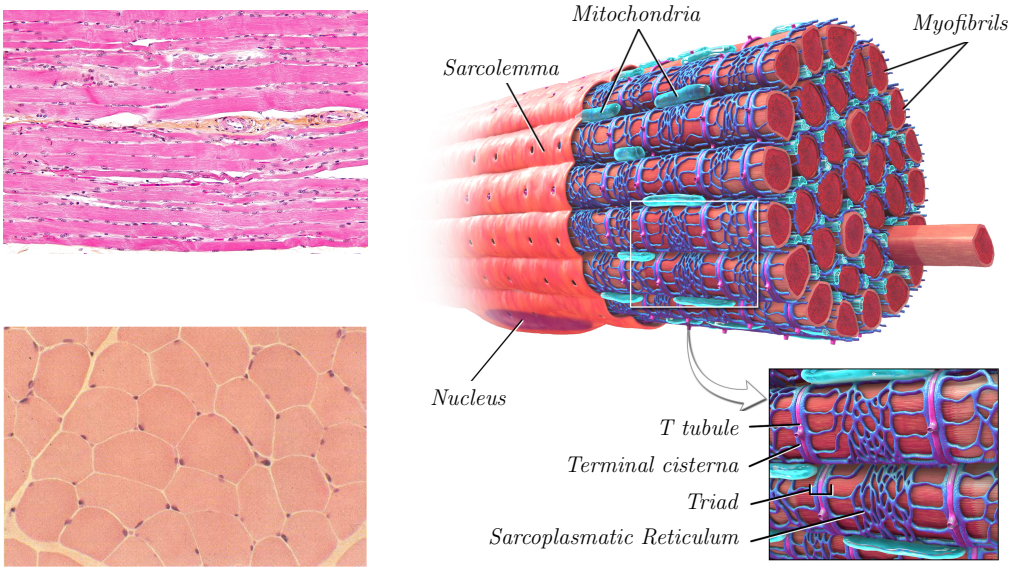

Fig. 1.1 The skeletal muscle. **(top left)** Longitudinal micrograph of (right *peroneus longus*) skeletal striated muscle [35]. **(bottom left)** Cross-section of human adult skeletal muscle: multiple peripheral nuclei of the muscle fibers, separated by the thin endomysium, are shown employing haematoxyline eosine staining process [36]. **(right)** Myocyte: representation of the structural organization for the principal components of muscle cell. (adjusted from [37]).

1.2.1 Skeletal muscle: cellular structure

The architecture of the skeletal muscle can be described as a highly organized arrangement of muscle fibers (also referred as muscle cell, myofibers or *myocytes*) and connective tissue. Typical fiber dimensions are approximately 1 cm in length and 100 µm in diameter, although differences depends on muscle type, fiber typology composition, age, gender, and other physiological factors.

Myocytes are multi-nucleated cells (see Fig. 1.1, right), where each nucleus, usually located superficially w.r.t. the cellular body, controls the synthesis of the proteins in specific regions of the cell (nuclear domains), leading to coordination and organization across the length of the fiber. Such proteins (e.g., contractile, regulatory, cytoskeletal) cover about the 80 % of fibers composition, excluding the water content and the subgroups featuring the contractile properties (i.e., actin and myosin) of the muscle, which are defined *myofilaments*. The orderly assembly of the myofilaments forms the *sarcomere*, which is the basic contractile unit of the skeletal muscle. Sarcomeres are longitudinally arranged into myofibrils, which are disposed

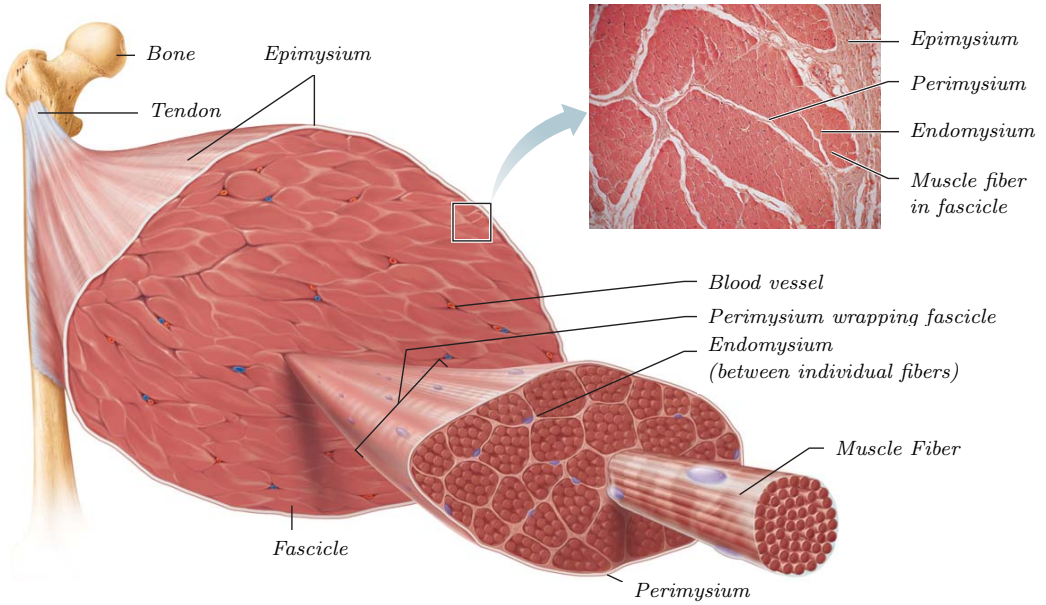

Fig. 1.2 Skeletal muscle structure: the muscular body is decomposed into fiber fascicles and, in turn, into single fibers composed by myofibrils; different layers of connective tissue provide structure and protection to the muscle by enveloping its body externally (*epimysium*), spacing the fascicles (*perimysium*) and interposing among fibers (*endomysium*) internally [38].

parallel one to the others, as represented in Fig. 1.2, giving the typical straight shape to the muscle fiber. Numerically, a single fiber is divided into thousands of myofibrils, each one containing billions of myofilaments. The muscle cell is surrounded by the *sarcolemma*, the specialized membrane of the striated muscular fiber, which, by means of membrane proteins, provides a contraction/force pathway linking the intra-cellular cytoskeleton with the external connective tissue forming the tendons. The other fundamental cellular elements contained in the sarcoplasm (myocyte cytoplasm) are (Fig. 1.1, left): the transverse tubular system (T tubule), which conducts nerve action potentials to the interior of the cell, as an invagination of the sarcolemma; the Sarcoplasmatic Reticulum (SR), which stores and releases calcium (in and from terminal regions of this reticulum, called cisternae) during the muscle contraction; the mytochondrial network, which, locating these organelles both closer to the sarcolemma (reducing the diffusion distance for oxygen) and in the inter-myofibrillar space, ensures the proper energy generation needed by the contraction.

From microscopic to macroscopic level, groups of fibers are bundled into fascicles (Fig. 1.2) which, as in the myofibrils case, are arranged longitudinally w.r.t. the

muscle orientation and isolated by connective tissue. The muscle body is composed by the totality of these fascicles wrapped together by a dense irregular connective tissue (*epimysium*), which forms the tendons at the muscle extremities and protects the muscle from friction against bones or other muscles. As introduced, this tissue penetrates inside the muscle both enveloping each fibers fascicle (*perimysium*) and covering myocytes (*endomysium*), where, with a close contact with their sarcolemma, provides an appropriate chemical environment. The resulting network performs the summation of the force of all the fibers, transmitting the sarcomeres contraction from the intra-cellular environment to bone-muscle interface.

1.2.2 Skeletal muscle: molecular structure

Covering approximately the 70 % to 80 % of the total protein content of a single fiber, *actin* and *myosin* are the most abundant proteins of the myofilaments.

As represented in Fig. 1.3, actin G (globular) monomers (molecules), each one presenting a bonding site for myosin, are connected at their extremities forming a filamentous structure denoted as actin F (fibrous). When two actin F are twisted together, they assume the double-stranded spiral shape typical of the actin filaments, which is stabilized by the regulatory proteins tropomyosin and troponin. Each myosin filament is composed by hundreds myosin molecules, each one characterized

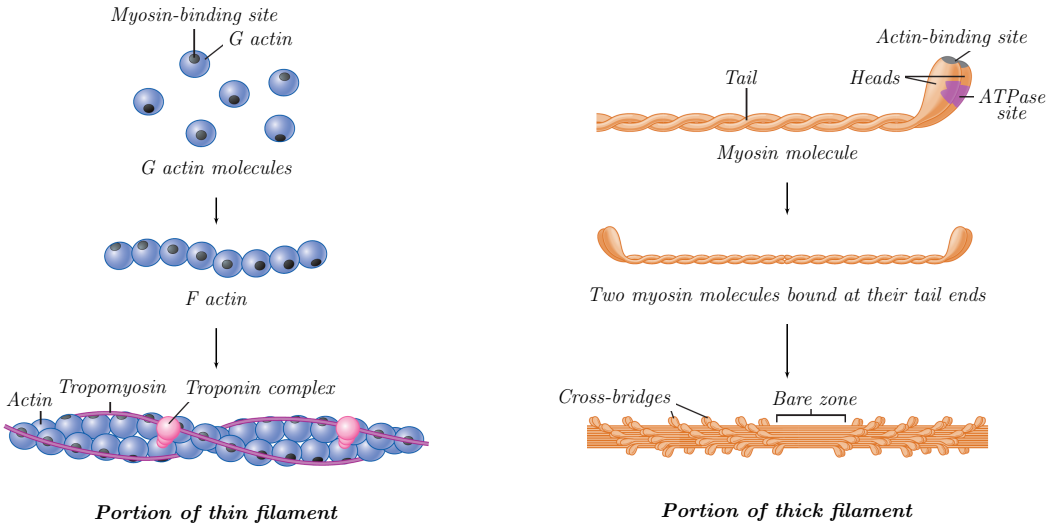

Fig. 1.3 Actin and myosin contractile proteins: from single molecules to myofilaments generation (images adapted from [39]).

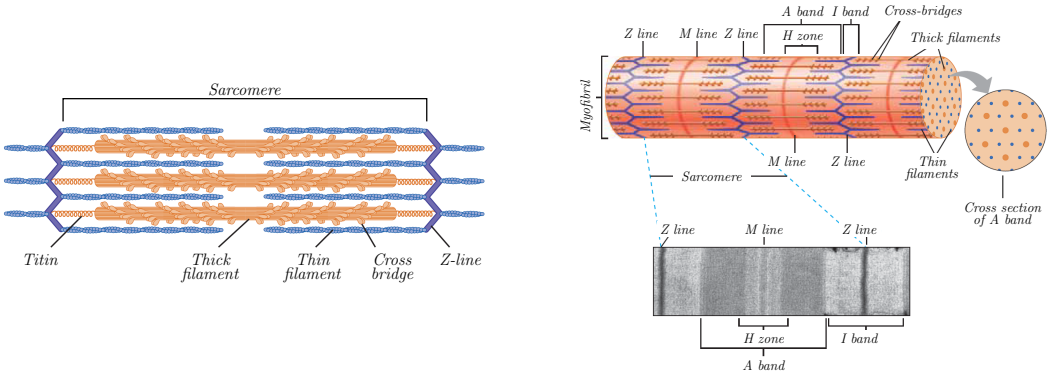

Fig. 1.4 The structure of a sarcomere and the visible myofibril microscopy bands (images adapted from [39]).

by two subunits wrapped together along the same orientation. The resulting structure presents a tail and two heads, where both the actin-binding site and the ATPase site (ATP is the energy molecule of eukaryotic cells) are located. In the myosin filaments, the molecules joint at the tail extremity positioning the heads along opposite directions. The heads arrangement forms an helicoidal pattern (*cross-bridges*) because of the shifting among adjacent myosin molecules, with the exception of the filament center (bare zone).

Actin and myosin myofilaments, which are respectively defined as thin and thick filaments due to related dimensions, are neatly disposed to form the sarcomere, which represents the basic contractile structure inside of a myofibril, as represented in Fig. 1.4. A radial and longitudinal composition of sarcomeres assemble into the myofibril.

A visible bands division of sarcomeres and their interaction has been developed by analyzing striated muscle with optic microscopy: A-band represents the region containing the totality of thick filaments, which can be partially overlapped with the thin ones (dark area inside A-band) or not (H-zone, inside which M-line connects thick filaments radially); light zone includes only actin filaments and takes the name of I-band, at whose center the Z-line links the thin filaments orthogonally w.r.t. the longitudinal myofibril direction. From a band point of view, the sarcomere is defined as the segment between two neighbouring Z-lines.

1.2.3 Cross-bridge cycle: force generation

The myofilaments organization and interaction inside the sarcomere are the key aspects of the skeletal muscle contraction mechanism, which takes the name of *cross-bridges cycle* and it is described by the sliding filaments theory. The central role of this process consists in an oscillatory dynamics between actin filaments and myosin heads, which induces thin filaments to move toward the center of the sarcomere as the consequence of cross-bridges motion. Fig. 1.5 shows the five phases of the cross-bridge cycle:

1. *Binding of myosin to actin*: myosin heads are in the high energy state, because both ADP (Adenosine diphosphate) and P_i (inorganic phosphate) are bond to the ATPase site, and present high affinity to actin monomers.

2. *Power stroke*: by releasing ADP and P_i molecules, myosin heads rotate toward the center of the sarcomere, also pulling actin filaments along the same direction.

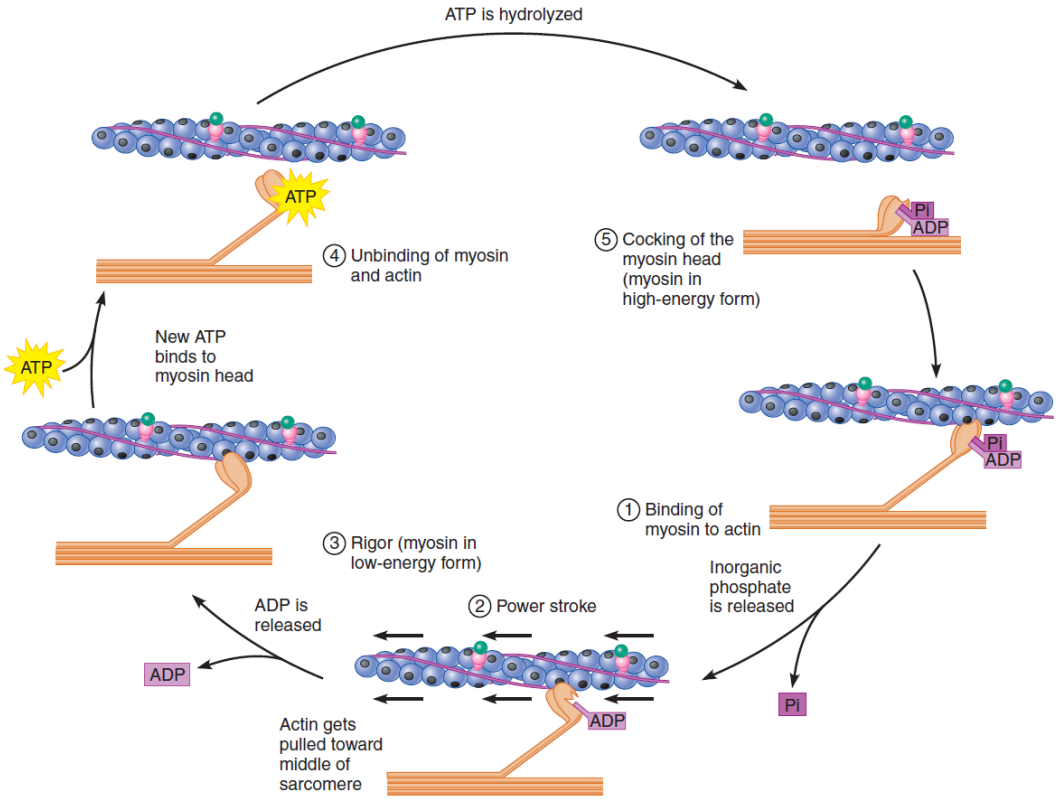

Fig. 1.5 Phases of the myofilaments cross-bridge mechanism. [39]

3. *Rigor state*: low energy state of myosin heads which strictly chains myofilaments together.

4. *Unbinding of myosin and actin*: the detachment occurs when a new ATP molecule bind the ATPase site, which cause a morphological modification of myosin heads with a resulting low affinity for actin.

5. *Coocking of the myosin head*: the hydrolysis of ATP (into ADP and P_i) releases the energy needed by myosin head to reach its high energy state, from which the cycle can start again.

Although single cross-bridge generates force only for a limited time (during the power stroke), myocyte continuously produces force since cross-bridges start the cycle slightly out of phases. Moreover, this asynchronous activation, in conjunction with titin protein (linking thick filaments to Z-line), provides an efficient control in maintaining the relative position of the myofilaments during the entire cycle.

Visually, during the contraction of the sarcomere, the length of the A-band remains unaltered while both I-band and Z-zone become shorter due to the overlap between thin and thick filaments.

1.2.4 Physiology of muscle activation

The physiologic activation of skeletal muscle is a complex multi-level mechanism that involves the cascade cooperation of different (bio-)signal pathways [34], from the generation of neural spikes in the Central Nervous System (CNS) to the biochemical factors governing the contraction features of the myofilaments.

According to [40], a *motor unit* is defined as the basic functional unit of the neuromuscular system comprising a motor neuron and the muscle fibers innervated by its axon (approximately 150 on average [41]). The motor neurons, whose the ones acting on extrafusal muscle fibers are α-motor neurons, are located in the ventral horn of the spinal cord (or in brain stem). There, they receive descending and sensory inputs from other parts of the nervous system, and transmit their action potentials along the peripheral nerves to the target muscles. The axon terminals of a motor neuron interface with the sarcolemma of the muscle fibers, forming chemical synapses called NeuroMuscular Junctions (NMJs). Similar to ordinary

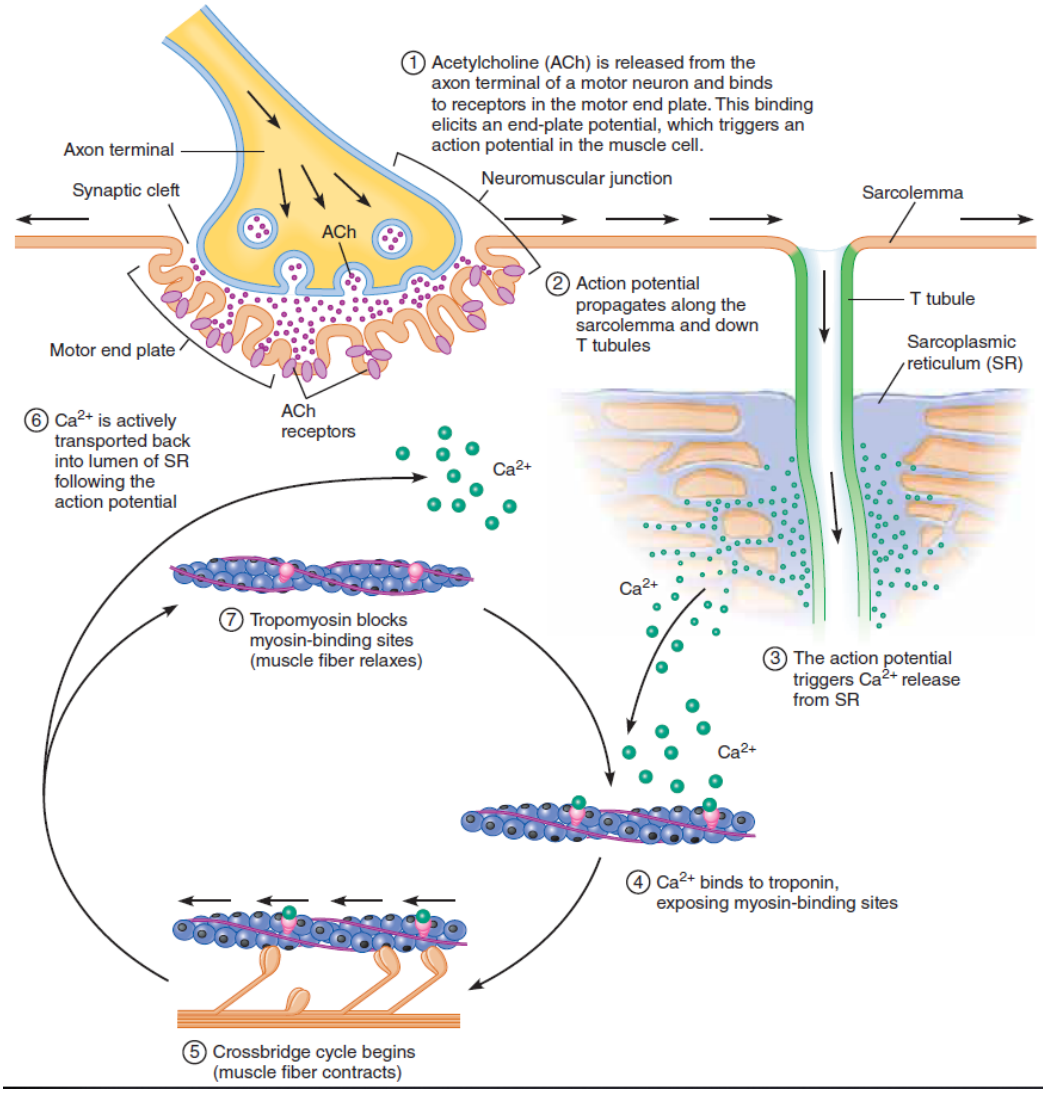

Fig. 1.6 From motorneuron action potential to muscle contraction (images adapted from [39]).

neural synaptic [42], the axon terminal (pre-synaptic region) induces the release of a neurotransmitter (i.e., Acetylcholine), which, diffusing in the synaptic cleft, reaches its receptors, whose higher number is concentrated in specific region denoted as motor end plate. The binding of the acetylcholine to its receptor triggers the opening of the ions channels in the sarcolemma causing the depolarization of the muscle fiber (post-synaptic region). In a healthy person, motor neuron action potential invariably results in the activation of the innervated muscle fibers. As represented in Fig. 1.6, the action potential propagates along the sarcolemma and canalizes into the T tubule network, reaching the triad (region where the T tubule is in close proximity with

SR calcium cisternae). As a consequence, the opening of the calcium ion channels in SR allows Ca^{2+} to chemically diffuse inside the sarcoplasm. There, the calcium binds the troponin complex exposing the myosin-binding sites of actin filaments, normally inaccessible at low Ca^{2+} concentration. In this way, the myosin heads, which are in the high energy state (as described in the previous Section 1.2.3), binds the actin monomeres and the cross-bridge cycle begins. When the cycle is concluded, a new one can start if further action potentials depolarize the fiber maintaining the sarcoplasmatic calcium concentration at the proper level to allow troponin to expose myosin-binding sites; otherwise, Ca^{2+} is stored again into SR and myofilaments return in their rest state.

The above process, here described for a single muscle cell, is known as Excitation-Contraction Coupling (ECC) since it represents the coordination between the propagation of a nervous stimulus, which releases the calcium from SR, and the interaction between actin and myosin filaments, forming the cross-bridges.

Considering a myocyte, if the sarcomeres belonging to same myofibrils contract, the result is the shortening of all the involved myofibrils and, consequently, of the muscle fiber. Moving to a macroscopic view, myofibers contraction brings to the reduction of the length of fascicles and, finally, to the shortening of the entire muscle. At this point, the force is produced transmitting the contraction tension to the bones by means of inelastic tendons tissue.

1.2.5 Mechanics of muscle contraction

Although the force generated by a muscle is the result of spatial and temporal summation of different motor units activation (recalling that at each motor unit corresponds to the simultaneous contraction of all the fibers innervated by the α-motor neuron), it can be analyzed by referring to the simple muscle *twitch*, which corresponds to the mechanical response of a single myocyte, motor unit or muscle to an action potential [39].

Fig. 1.7 (left) shows the three distinguished phases describing the muscle response. The *latent period* (usually corresponding to some ms) represents the delay between reception of the nervous stimulus and the beginning of fiber contraction, which is caused by physiological processes timings (e.g., action potential propagation and ECC initiation). Afterwards, the *contraction phase* begins and lasts until

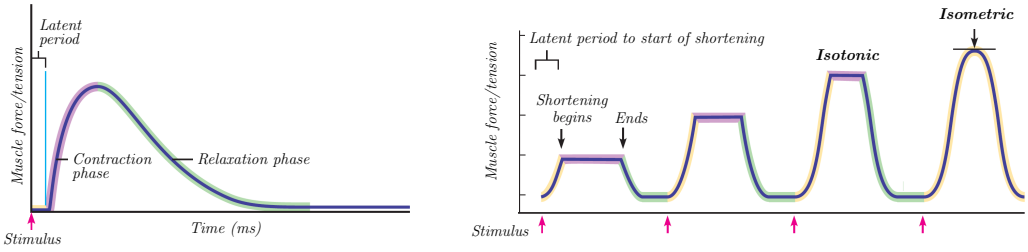

Fig. 1.7 **(left)** Phases of twitch. **(right)** Difference between isometric and isotonic muscle contraction (images adapted from [39]).

the tension reaches its maximum value (variable duration in the 10 ms to 100 ms range), which coincides with the high release of calcium ions inside the sarcoplasm triggering the cross-bridge cycles. Last, the longest phase is the *relaxation phase*, which starts after the force peak and ends when the tension comes back to zero value, covering the period during which Ca^{2+} has been reabsorbed by SR.

Muscle contractions can be classified as *isometric* and *isotonic* depending on the possibility of muscle shortening: basically, during isometric contraction the length of muscle fiber (or whole muscle) remains constant, while in isotonic contraction the generated tension is equal to the opposition forces. The difference between the two type of force-profiles is represented in Fig. 1.7 (right), where developed tension evolves from isotonic to isometric contraction by increasing an hypothetical weight to be lifted (see duration and height of *plateau*).

Moreover, the frequency of nervous stimulation plays a central role in the force modulation because, depending on the number of active cross-bridges, at increasing action potential burst corresponds a greater calcium release with a direct proportional effect on available myosin-binding sites of actin filaments. This process is shown in Fig. 1.8: if additional action potentials arrive before twitches completion, the twitches

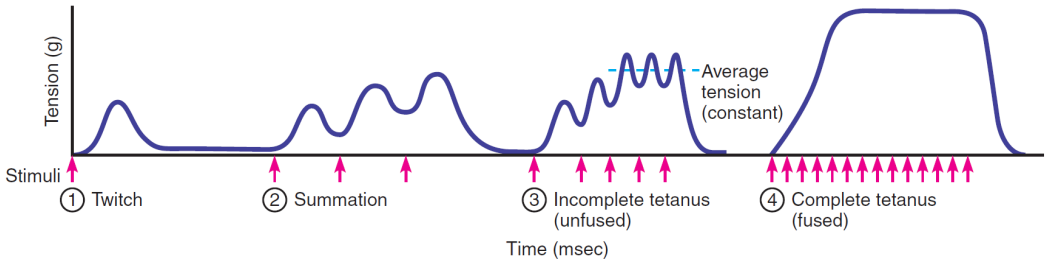

Fig. 1.8 From single twitch to complete tetanus by increasing the stimulation frequency [39].

superimpose on one another, yielding to higher force w.r.t. single twitch tension; this phenomenon has been called *summation* and the physiological cause is related to the amount of cytosolic calcium, which constantly increases after each stimulus (since Ca^{2+} release is faster than its removal). At higher stimulation frequency, the force reaches a peak called *tetanus*, which reflects the calcium saturation of troponin and myosin-binding sites. The tetanus can be *unfused*, therefore presenting some peaks oscillation, or *fuse* (complete), characterized by a force plateau.

Other factors influencing the muscle force are the diameter and the length of the fiber. Large fibers are able to produce greater force w.r.t. smaller myocytes since they present a higher number of sarcomeres arranged in parallel, so providing more cross-bridge interactions. In the same way, the proper fiber length (usually the 100 %-120 % of the length at the muscle at rest) maximizes actin and myosin coupling, providing the maximal exerted tension.

During a muscle contraction, the recruitment of the proper amount and typology of myofibers to exert a determined force follows a rule indicated as *the size principle*. According to it, since the dimension of a motor unit (i.e., size of α-motor neuron and the number of fibers it innervates) reflects the magnitude of produced force, small or big motor units are recruited to generate low or high tension, respectively. Moreover, the temporal combination of different sizes of motor units carries to generate high-level time control of the force allowing the body to perform complex movement patterns.

In conclusion, a last fundamental aspect of the muscle contraction mechanic involves its movement classification in *static* and *dynamic* [34]. The former basically represents an isometric muscle contraction which does not involve any movements of joint or limbs. On the opposite case, dynamic action provides force generation and consecutive limbs movement. It can be divided into *dynamic conentric*, when the action results in the shortening of the muscle (e.g., *biceps brachii* during elbow flexion), and *dynamic eccentric*, when the muscle increases its length (e.g., *biceps brachii* during elbow extension).

1.3 Surface Electromyography (sEMG)

Once the principles of the generation of the skeletal muscle contraction are known, we can now pass to explaining how these ionic flows can be converted into electrical signals, which can be accessed and processed in order to assess the muscle activity.

ElectroMyoGraphy (EMG) has been defined as an electrodiagnostic medicine technique for the evaluation and the recording of the electrical activity produced by skeletal muscle [43]. It is based on the capture of the electric potential field generated during the depolarization of the outer muscle fibers membrane (i.e., sarcolemma).

EMG signal is classified as *biosignal* since it is associated with ions and charged molecules distributions, and their biologic or biochemical time-dependent changes, resulting from the specific processes introduced in Section 1.2. As it, the trasduction of ionic charge movements into electric currents is fundamental in order to pick up this signal by using electronic instrumentation [44]. This trasducing function is achieved by employing bio-potential electrodes, which can be placed inside the muscle belly or on the skin surface above the muscle of interest, distinguishing between *intramuscular* EMG (iEMG) and *surface* EMG (sEMG) respectively. Whatever, they are located at a certain distance from the signal sources, defining a volume conductor, whose properties determine the features of the detected signals [45]. Indeed, the biological tissues separating the recording electrodes from signal sources (e.g., muscle tissue, skin and fat layer) act as spatial and temporal low-pass filters on the potential distribution, whose effect is predominant in sEMG w.r.t iEMG due to major dimension of the volume conductor.

Anyway, since the amplitude (peak-to-peak) of detected signals is very low, varying from tens of μV to a maximum value of 10 mV (sEMG) or 30 mV (iEMG) (typical values are around 100 μV) [23], signal amplification procedure is fundamental in order to adequately record the EMG signal and to further process it. This task is achieved by the biopotential amplifier, which, as the name suggest, is an electronic amplifier properly design to detect biomedical signal; it is one of the main blocks of a biosignal acquisition chain, along with some filters, which avoid corruption of the signal by the noise sources present in the acquisition environment. These essential stages define the conditioning circuit for the EMG signal and constitute one of the main part of an electronic biosignal acquisition system, whose final task is the signal

digitalization in order to further analyze it on a calculator.

As a consequence, the detection of EMG signal is a complex scenario which requires an in-depth knowledge of signal sources and biological tissues effect, and an accurate design of electronic circuitry able to amplify and isolate (from noise) it. Therefore, this section provides a brief review of the more efficient State-of-the-Art (SoA) considerations (solutions and current problems) about the muscle signal acquisition and features extraction process (carrying information on muscular state) fundamental to open the way to the bio-inspired signal processing approach.

Considering the two main EMG detection techniques, next sections will mainly focus on the surface one (sEMG) because of the advantages with respect to deep method, which include low-cost and easy-accessible electrodes placing location, enhanced comfort for the subjects and the possibility to perform dynamic acquisition.

1.3.1 Generation of the sEMG Signal

A holistic description is required to understand how the sEMG signal represents the activity state of a muscle, where the biological activations of each muscular sub-unit (myofiber or motor unit) merge together to form the electrical response of the whole muscle. Therefore, the following subsections report the fundamental concepts at the basis of the electrical generation of the muscle signal, starting from the variation of the membrane potential inside a single myocyte, passing through a brief description about the signal propagation along the muscle surface, to the complete generation of the visible sEMG signal.

Signal source

The EMG signal has been defined as a stochastic (random) process [23], which can be represented by a Gaussian distribution function, since surface electrodes detect a signal which is the superposition of the electrical activity of single fibers (or motor units) over space and time. Thus, understanding these waveforms and their overlapping (i.e., spacial summation and frequency modulation), it is possible to explain and manage the high variability of the global sEMG signal.

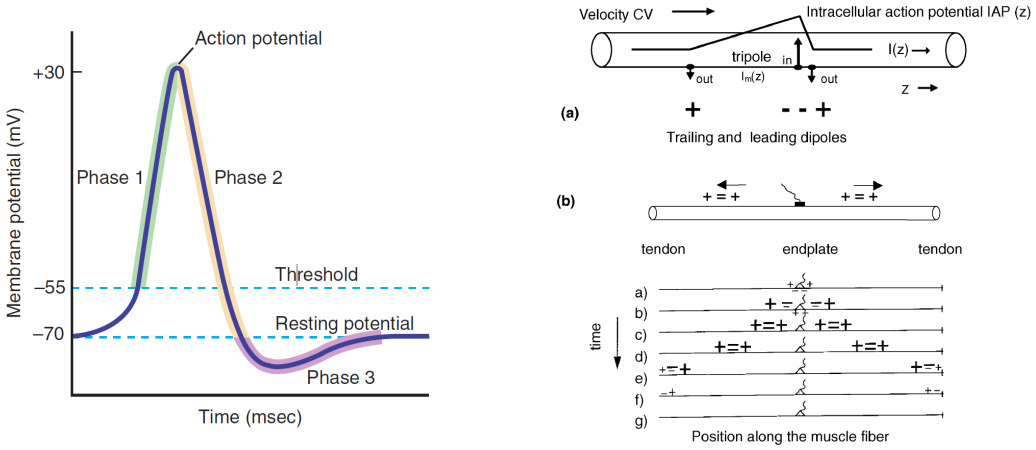

Fig. 1.9 **(left)**Main phases of a general intracellular action potential. [39]. **(right)** Tripole model describing how the IAP propagate from neuromuscular junction to fiber endings. [45]

Intracellular Action Potential (IAP)

When a neural action potential reaches the neuromuscular junction of a muscle fiber, it induces a cellular inward current which changes the myocyte potential with respect to the rest state (i.e., 70 mV to 90 mV, negative inside the cell), a phenomenon called Intracellular Action Potential (IAP) generation. A typical life-cycle of an excitatory IAP (i.e., provoked by neuron-to-neuron or (motor-neuron)-to-myofiber synapses) can be generally divided into the three phases represented in Figure 1.9: starting from the myocyte resting potential, the neurotransmitter released by pre-synaptic cell causes the depolarization of the muscle fiber (Phase 1), followed by a repolarization (Phase 2) and a long afterpotential hyperpolarization (Phase 3) of the cell membrane, which allows the potential to return at its equilibrium by time-varying the ions channels activity.

The *depolarization zone*, which consists of the IAP period including Phase 1 and Phase 2, propagates along the muscle fibers from the innervation zone (i.e., neuromuscular junction) to the tendons endings [45]. Figure 1.10 shows the Motor Unit Action Potential (MUAP), detected using surface electrodes, which reflects the spatial summation of the synchronous activation of all the fibers excited by the motor neuron. The length of the depolarization zone (usually in the mm order) and its propagation velocity (3 m/s to 5 m/s), defined as Conduction Velocity (CV), depend on the muscle condition and fiber diameter. The propagation of this waveform on each fiber membrane has fundamental effect of surface signal, and a simple

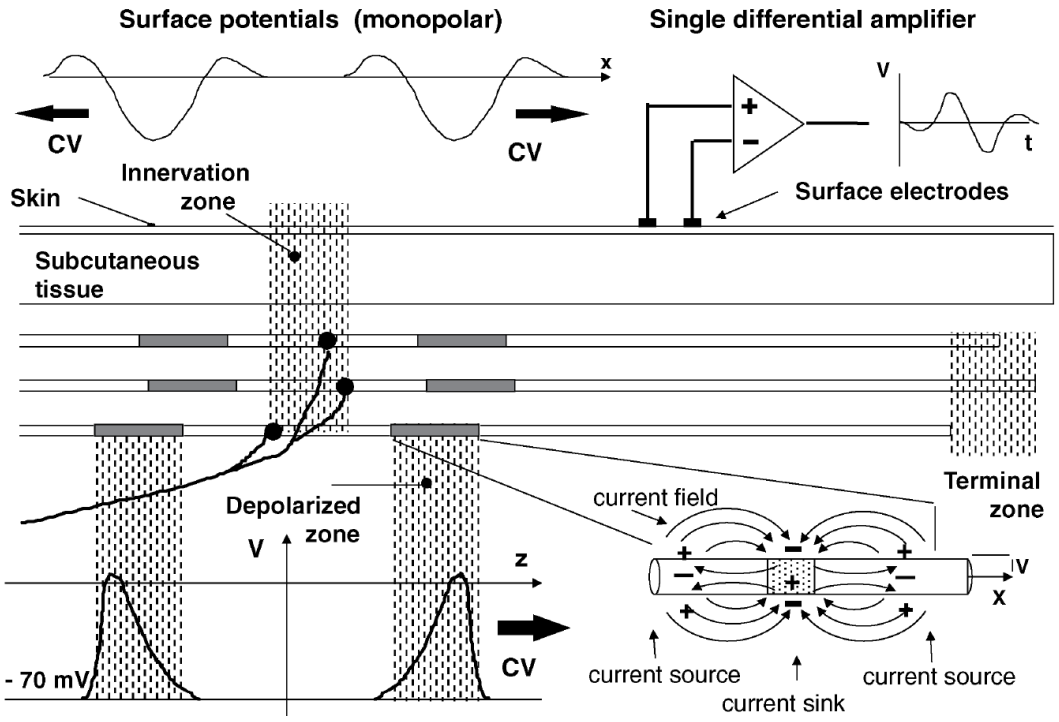

Fig. 1.10 Representation of a motor unit and its action potential detected by surface electrode in different configurations. [45]

mathematical model to describe it has been presented in [46]. As depicted on the right of Figure 1.9, the IAP can be approximated by a triangular wave or a tripole: the model represents the IAP as combination of a leading (-+) and trailing (+-) dipole pair, developed after motor-neuron AP excitation (a, b); this double balanced pair (+=+) propagates from the end-plate in opposite direction (c, d), until it reaches the tendon, where both the leading and trailing dipoles progressively decline their strength and disappear (e, f, g). As a consequence, although IAP morphology repeats while spreading along the muscle fibers, appearance and disappearance of leading and trailing dipoles generate a signal component which is not propagating and have an effect on the detected signal.

Motor Unit Action Potential Train (MUAPT)

As introduced in Section 1.2, each motor unit codifies its activation (able to substain muscle contraction) in terms of simulation frequency, better know as motor unit *firing rate*. The resulting sequence of action potentials, each one delayed by the Inter-Pulse

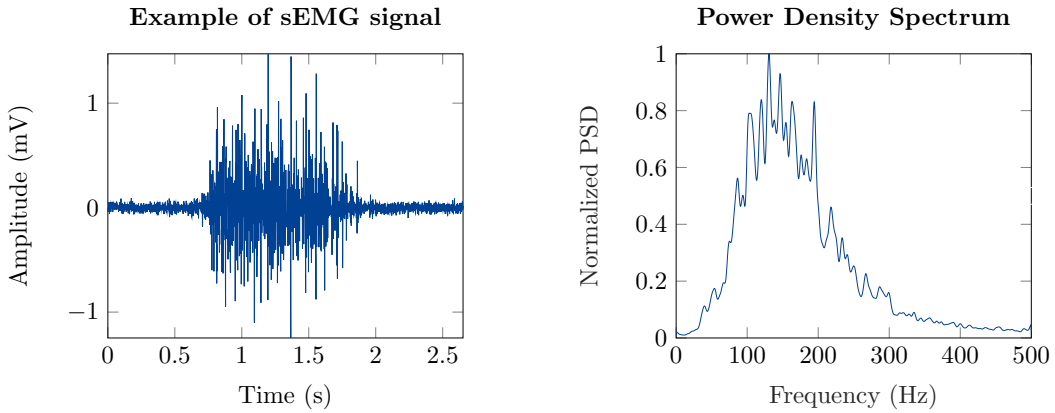

Fig. 1.11 **(left)** Example of muscle activation detected by surface electromyographic signal acquired from *extensor carpi ulnaris* muscle, using a differential electrodes configuration. **(right)** Power Density Spectrum (PSD) extracted from the signal on the left; as expected from a surface EMG signal, its frequencies varies from 10 Hz to 500 Hz with a predominant energy content in 70 Hz to 150 Hz.

Interval (IPI) [47], is called Mort Unit Action Potential Train (MUAPT), where each MUAP preserves its shape during activation (assuming no change in volume conductor, electrode properties and biochemical muscle behavior) [48]. Anyway, because of the random distribution of the myofibers inside the muscle body, and their intermingling, single MUAPT can be detected in very specific situation (i.e., very weak contraction) while, during general movement, the surface signal represents the train superposition of different motor units.

Therefore, the surface EMG signal is composed by the spatial (volume conductor properties and acquisition approach) and temporal (firing rate of motor-neuron) summation of the activated motor units, each one resulting from the IAP superimposition of associated myofibers. As a result, the detected superficial signal, as an instance the one represented on the left of Figure 1.11, presents high variability in terms of peak-valley oscillations.

Generally, sEMG signal has physiological amplitudes varying from 0 mV to 10 mV peak-to-peak or 0 mV to 1.5 mV Root Mean Square (RMS, amplitude estimator), and its energy content is limited from 0 Hz to 500 Hz range (which accounts for myofibers frequency summation), whose dominant power is distributed in 50 Hz to 150 Hz range [23].

Once the main factors characterizing the the source of the signal and its propagation on the detecting site have been clarified, next sections focus on the conditioning of sEMG signal, starting from the interface between electrode and skin.

1.3.2 Electrode properties and skin coupling

Bio-potential electrodes trasduce ionic currents, e.g., generated during muscle fibers contraction, into electric currents compatible with electronic measurement system.

Generally, since electrodes are primarily metal-based to be electrical conductors, redox (oxidation-reduction) reactions occur at the interface between electrode and ionic solution (skin in our case) [44]. At equilibrium (no current flowing through electrode-electrolyte interface), ions produce concentration changes at metal surface causing the electrolyte surrounding the metal to be at a different electrical potential with respect to the rest of the solution, which potential difference has known as *half-cell* potential (V_{hc}). However, if there is a current (e.g., MUAPT), the related alteration of the charge distribution results in potentials variation. Therefore, by referring these potential oscillations to V_{hc}, it is possible to monitor the physiological processes responsible of such perturbations.

A fundamental electrode classification divide them into *polarizable* and *nonpolarizable*, according to the current flowing mechanism, which is due by electrode-electrolyte surface concentration modification or free current passage respectively. Usually, nonpolarizable electrodes are preferred for biomedical signals acquisition since they limit motion artifacts. Indeed, the changes of the charges concentration, induced by the relative motion between electrode and electrolyte during dynamic measurements, greatly affect polarizable electrode detection by causing potential variations not associated with the physiological phenomenon of interest.

The electrode-skin interface is characterized by charge distribution (i.e., Helmholtz layer), which generates the half-cell potential . This contact, which can be *wet* (if is mediated by gel or conductive paste) or *dry* (direct contact between electrode and skin), is intrinsically noisy due to the continuous bidirectional oxidation and reduction reactions at the interface. Schematic electrical representation of gelled and dry electrode-skin couplings are represented in Figure 1.12, where each coupling layer (included the outermost layer of epidermis, i.e., the *stratum corneum*) can be described by parallel RC elements [49]. In particular, resistor and capacitor account

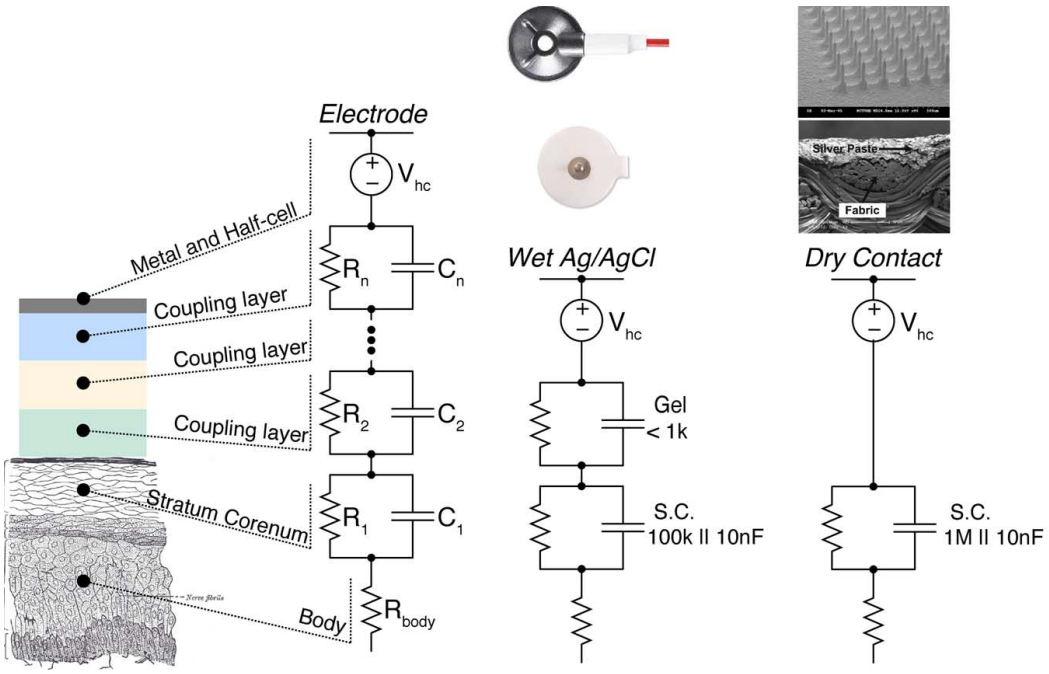

Fig. 1.12 Electrical model of *wet* and *dry* electrodes art skin interface. [49]

for the electrode inward current and the charge distribution at electrode-skin interface, respectively. As reported, dry and wet electrodes differ in the number of coupling layers (for gelled electrode, impedance is primarily contributed by gel-skin layer) and typical impedance values ($R_{wet} \simeq 100\,k\Omega$ vs. $R_{dry} \simeq 1\,M\Omega$, $C_{wet,\,dry} \simeq 10\,nF$).

1.3.3 Electrode placement

The placement of the electrodes above the muscle tissue follows a standardization in order to detect an sEMG signal which is the most describable of the contraction phenomenon.

As shown in Fig. 1.13, the location of the sensing sEMG sensors (i.e., exploring electrodes) considerably modifies the quality of the detected muscle signal. Best practices [23, 51, 50] advise to place the electrodes between a motor point and the tendon or between two motor points, also assuring to follow the longitudinal midline of the muscle body. The longitudinal axis of the two exploring electrodes (passing through the detection surfaces) should be aligned parallel to the direction of the muscle fibers.

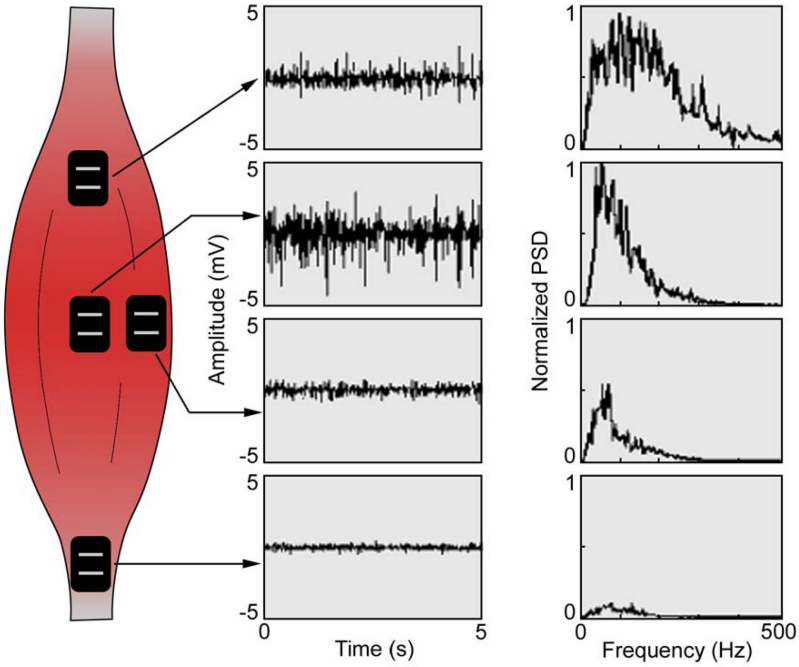

Fig. 1.13 sEMG electrodes placement over the muscle bellies. The preferred location is in the midline of the muscle belly, where the sEMG signal presents the greater amplitude (w.r.t. others distal/proximal or medial/lateral positions) [50].

Indeed, positioning the electrode near the tendon of the muscle can be improper because the myofibers become thinner and fewer in number at this region, making difficult to effectively monitor the target muscle (e.g., crosstalk phenomenon) or to detect an sEMG signal featuring an adequate amplitude.

Neither the motor point is an optimal location to sense the sEMG signal since, at this site, the action potentials travel caudally and rostrally along the muscle fibers, thus impacting the addition and subtraction operations of their positive and negative phases and resulting in an unstable and high frequency sEMG signal.

Lastly, also the outside edges of the muscle should be avoided because the electrode are susceptible to the crosstalk from adjacent muscles.

On the other hand, the reference electrode, which does not capture any signals but provides the body an external reference voltage, should be placed on a neutral electrical tissue (e.g., on a bony prominence) in order to achieve its effect, avoiding the superimposition of the sEMG signal. Anyway, this arrangement is often inconvenient because it requires separating the detection and reference electrodes, generally

making the setup more susceptible to noise sources and unwieldy to the freedom of movement. For these reasons, nowadays, the reference electrode is moved near the acquisition ones in order to promote the system wearability, although the slight decrease of the detection performance.

Sometimes, a skin preparation procedure can be follow to optimized the electrode-skin contact and enhance the quality of the detected signal (e.g., fewer and smaller artifacts, better balance between the electrodes, higher signal-to-noise ratio) [51]. Generally, the procedure consist of two steps: first, the skin surface is shaved if it is significantly covered with hairs; then, the skin is further cleaned with alcohol, guaranteeing the complete solvent vaporization before the application of the electrode. However, the skin preparation could be avoided if the acquisition device is equipped with active electrodes (i.e., featuring the conditioning circuitry pretty closed to the sensing electrodes) [23].

1.3.4 Acquisition methodologies

After the introduction to the sEMG generation and to the electrode properties, a summary of the sEMG acquisition configurations is fundamental.

The sEMG signal is acquired through the differential amplification technique, which generally employs an instrumentation amplifier [24, 52, 53], as the one reported in Fig. 1.14. Generally, this amplifier provides an output signal (V_{out}) which corresponds to the subtraction of its input voltages (V_1 and V_2) amplified by a differential gain (A_d), as reported in the formulas 1.1 and 1.2. In this way, the noise sources identified as common components to both the electrode inputs (e.g., powerline interference) are eliminated, while the differential signal is amplified. The characteristic of a differential amplifier to reject the common mode signal is known as Common Mode Rejection Ratio (CMRR), and its acceptable values range from 90 dB to 120 dB.

$$V_{out} = (V_2 - V_1) * A_d \tag{1.1}$$

$$A_d = (1 + \frac{2 * R_1}{R_{gain}}) * \frac{R3}{R2} \tag{1.2}$$

From this general setup, the following three literature standards have been defined for the acquisition of the sEMG signal:

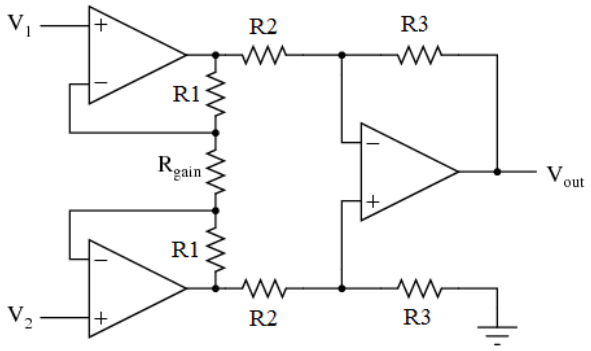

Fig. 1.14 Schematic of the instrumentation amplifier: the output signal (V_{out}) corresponds to the subtraction of the inputs ($V_2 - V_1$) multiplied by the differential gain of the amplifier [52].

- Monopolar sampling: this configuration involves the use of a single sensing electrode, placed on the skin above the muscle of interest, whose signal is referred to the reference electrode. Although the simplicity of this approach, which clearly speeds up the setup, it is not recommended since the sensing electrode detects all the electrical signals in the proximity of its surface, thus resulting more noisy w.r.t. the other approaches.

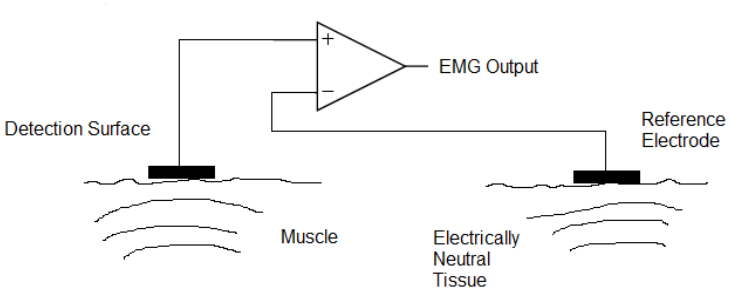

Fig. 1.15 Monopolar configuration [52].

- Bipolar sampling: it consists of applying two sensing electrodes plus one for reference, and it is the most employed configuration. Indeed, since the two electrodes are placed about 1 cm or 2 cm away from each other, they sense the same common noise signals at the source, thus eliminating them during the subtraction process and providing a more cleaned and robust sEMG signal (overcoming the limitation of the monopolar sampling). This mode is also referred as single differential.

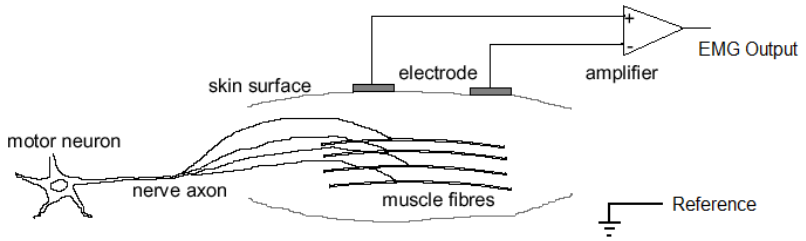

Fig. 1.16 Bipolar configuration [52].

- Multipolar sampling: this configuration, following the scheme of the bipolar acquisition, employs more than two detecting electrodes. The signals coming from the sensing surfaces, always distanced by 1 cm or 2 cm, are passed through two or more differential amplification stages. For example, considering the case with three acquisition electrodes, the configuration results in a double differential technique. The advantages of the multipolar sampling consist of further reducing the crosstalk and noise components, enabling more deeper muscular study concerning the assessment of the muscle fiber orientation, conduction velocity and motor point localization.

1.3.5 Noise sources

Considering the very low amplitude of the sEMG signal, special attention needs to be addressed in understanding how the electrical noise can corrupt the signal. In particular, the following four main points include all the possible sources from which the noise can emanates [23]:

- Ambient noise: this component originates from any electromagnetic device (e.g., radio and television, electrical-power wires, light bulbs) and its dominant frequency is 50 Hz in Europe, or 60 Hz in America, (along with its harmonics) because of the major contribution of the power sources. Since the surface of our body is constantly inundated with the electromagnetic radiation and it is impossible to avoid such exposure, this phenomenon has to be considered carefully, also because the noise amplitude can be one or three orders of magnitude greater then the one of the sEMG signal. Typical guidelines [53] suggest to twist the electrode cables, to reduce and match the electrodes impedance as

much as possible, and to chose a bio-amplifier with a large common mode input impedance. Alternative strategies to remove the power-line interference [54] apply analog notch filter (centered at 50/60 Hz) or digital signal post-processing, but they can cause signal distortion or loss of information (also considering the main sEMG power in the 50 Hz to 150 Hz range).

- Motion artifacts: these noises are caused by the unstable interfaces between the detection location of the sEMG signal (skin) and the bio-electronic device. A first component is related to the electrode-skin contact, which could be less or more noisy depending on the type of sensors (i.e., wet or dry) and on its adherence to the skin (e.g., sticky layer, elastic band). A second contribution is given by the relative movement of the connecting cable to the amplifier. The resulting electrical signal presents an energy content in the 0 Hz to 20 Hz low frequency band, and they can be reduced by properly designing the electronic input circuitry of the acquisition unit.

- Inherent noise of electronics instrumentation: all the electronics equipment generates electrical noises in the frequency band from 0 Hz to several thousand Hz. Due to the intrinsic nature of this noise, it can not be eliminated. The combination of intelligent circuit design, construction techniques, and the choice of high-quality electronic components are the best solution to reduce it.

- Inherent instability of the sEMG signal: the muscle signal presents a particularly unstable behavior in the 0 Hz to 20 Hz frequency band because of the quasi-random nature of the firing rate of the motor units. As a good practice, considering the unstable nature of these components of the signal, it is better to discard the information contained in this frequency region.

1.3.6 Conditioning circuitry

Using the background information described until here, we can now introduce the typical conditioning circuitry for the sEMG detection. Considering the discussion about the acquisition methodologies carried in the previous Section 1.3.4, here the description will be focused on the single differential method since it provides the best trade-off between speed setup and robust measurements.

Lots of literature works [23, 50, 2, 55, 21, 27] reports their design considerations for the detection of the sEMG signal, each one adapting its work to the target application. By comparing all of them together, and trying to generalize the main concepts, the following list of guidelines can be extracted:

- The first stage, just after the connectors for the electrodes cables, has to work as a decoupling circuit, aiming to isolate the remaining circuitry from the subject's body and to provide the proper protection in case overvoltages occur.
- The second stage corresponds to a high-pass filter, generally with a cut-off frequency in the 20 Hz to 30 Hz range, to remove the possible DC offset and to limit low-frequency noise contributions (e.g., movement artifacts, sEMG signal instability) below of the sEMG band of interest.
- Then, as introduced in Section 1.3.4, a first amplification stage, based on an instrumentation amplifier, takes place in order to provide the differential signal. The gain of this stage should not be too high because, despite an elevate CMRR of the amplifier, not the totality of the common mode can be rejected, thus propagating amplified along the conditioning chain.
- The fourth stage can corresponds to a second amplification stage, which can provide additional gains to adapt the sEMG dynamics to the one of the Analog to Digital Converter (ADC) module used for the signal sampling and digitization.
- Last stage is a low-pass filter, which confines the bandwidth of the sEMG signal to 500 Hz (its upper limit) in order to avoid the corruption of the signal from higher frequency noise sources (e.g., radio-frequency and electronic artifacts) and to provide its anti-aliasing functionality.
- Optionally, a circuit known as Driven Right Leg (DRL) can be added to the default conditioning chain to actively drive the body's potential. In this configuration, the reference potential, instead of being simply driven in output at a fixed value, is processed together with the sensed common-mode in order to limit the effect of the disturbances directly at the source.

At this point, the amplified and filtered sEMG signal can be digitized by the microcontroller, using its internal ADC module, for further processing.

1.3.7 sEMG sampling and digital recording

The analog conditioned sEMG signal needs to be converted into a digital numerical sequence, through the analog-to-digital conversion process, in order to be further processed by using microcontrollers or calculators. Generally, the analog values of the signal amplitude, which typically vary continuously in the its range, are captured at a specific point in time (i.e., sample) and represented by associated digital numbers (i.e., conversion levels). The sampling timing, better expressed in Hz by the sampling frequency, has to follow the Shannon-Nyquist theorem, which assesses that the minimum sampling frequency of a signal has to be no less than twice its highest frequency component [24]. Please note that not respecting this rule (e.g., sampling the signal at a minor frequency w.r.t. its spectrum) could bring to corruptions of the sampled signal, an effect known as aliasing, making its interpretation misleading. As anticipated in the previous section, this effect can be controlled by adopting low-pass anti-aliasing filters, which limits the maximal frequency of a signal before its analog-to-digital conversion.

Practically, the digitization process is performed by means of an ADC module, which, depending on the quality of the electronic component, can represents the signal on a certain number of bynary digits (bits, b), following the Eq. 1.3.

$$\text{Range of n-bits ADC} = 2^n \text{values} \tag{1.3}$$

Clearly, the proportioning of a range of values over a fixed number of levels has an impact on the minimal signal resolution, as outlined by Eq 1.4.

$$V_{resolution} = \frac{V_{range}}{2^n} \tag{1.4}$$

If past ADCs are limited to 8 b or 12 b, nowadays ADCs can sample at 24 b and over, thus reaching high resolutions suitable for the quasy-totality of the biological signal.

Focusing now on the sEMG signal, and its frequency content up to 500 Hz, the minimal acceptable sampling frequency should be 1 kHz, employing ADC able to convert onto 8 b, 12 b, 16 b, or 24 b depending on the application requirements and its technical specification. Further considerations on the suitable choice for the right

ADC are related to the gain of the conditioning circuits, the noise interference, the signal range, and the ADC range [24].

1.3.8 Time and frequency sEMG features

This section aims to introduce the parameters which can be extracted from the digitized sEMG signal, both analyzing its time and frequency domain. Table 1.1 summarizes the most prominent features, indicating their calculation formulas (considering a discrete sEMG signal of N samples, each one identified with x_n) [56, 57]. From the one belonging to the time-domain, some are generally used to monitor the muscle activity merely from an amplitude point of view, e.g., Integrated EMG (IEMG), Mean Absolute Value (MAV), Absolute Rectified Value (ARV), Root Mean Square (RMS), while others better describe the energy content of the signal, e.g., Simple Squared Integral (SSI), Variance (VAR). Willison Amplitude (WL), Slope Sign Change (SSC), and Zero Crossing (ZC) are based on the derivative of the signal (and its sign), thus describing the morphology of the sEMG and its variability. On the other side, the frequency-domain parameters, e.g., Median Frequency (MDF), Mean Frequency (MNF), Dimitrov Spectral Index (FI_{nsmk}), integrate the power of the signal in its frequency band (i.e., 0 Hz to 500 Hz) and are generally employed to provide an indication of the muscle fatigue.

Table 1.1 sEMG parameters extracted from the time and frequency domain.

Parameter	**Acronym**	**Formula**
Integrated EMG	IEMG	$\sum_{n=1}^{N} \lvert x_n \rvert$
Mean Absolute Value	MAV	$\frac{1}{N} \sum_{n=1}^{N} \lvert x_n \rvert$
Absolute Rectified Value	ARV	$\frac{1}{N} \sum_{n=1}^{N} \lvert x_n \rvert$
Simple Squared Integral	SSI	$\sum_{n=1}^{N} \lvert x_n \rvert^2$
Variance	VAR	$\frac{1}{N-1} \sum_{n=1}^{N} \lvert x_n \rvert^2$
Root Mean Square	RMS	$\sqrt{\frac{1}{N} \sum_{n=1}^{N} \lvert x_n \rvert}$
Willison Amplitude	WA	$\sum_{n=1}^{N} f(\lvert x_{n+1} - x_n \rvert) \quad f(x) = \begin{cases} 1, & \text{if } x < 0. \\ 0, & \text{otherwise.} \end{cases}$
Waveform Length	WL	$\sum_{n=1}^{N-1} \lvert x_{n+1} - x_n \rvert$
Slope Sign Change	SSC	$\sum_{n=2}^{N-1} f[(x_n - x_{n-1}) * (x_n - x_{n+1})] \quad f(x) = \begin{cases} 1, & \text{if } x \geq threshold. \\ 0, & \text{otherwise.} \end{cases}$
Zero Crossing	ZC	$f(x) = \begin{cases} 1, & \text{if } x_n \cdot x_{n+1} < 0 \text{ and } \lvert x_n - x_{n+1} \rvert \geq threshold. \\ 0, & \text{otherwise.} \end{cases}$
Median Frequency	MDF	$\sum_{f=f_{min}}^{MDF} PSD_f = \sum_{MDF}^{f=f_{max}} PSD_f = \frac{1}{2} \sum_{f=f_{min}}^{f=f_{max} PSD_f}$
Mean Frequency	MNF	$\frac{\sum_{f=f_{min}}^{f=f_{max} f * PSD_f}}{\sum_{f=f_{min}}^{f=f_{max} PSD_f}}$
Dimitrov Spectral Index	FI_{nsmk}	$\frac{\sum_{f=f_{min}}^{f=f_{max} f^{-1} * PSD_f}}{\sum_{f=f_{min}}^{f=f_{max} f^{k} * PSD_f}}$

1.4 Commercial sEMG acquisition devices

Now that the basis of sEMG signal, its detection circuitry, and digitization process have been described, the focus will be moved to analyzing the commercial sEMG systems, trying to figure out which are the current limitations of these devices and why a bio-inspired approach could be a promising solution.

Indeed, considering the high relevance of the sEMG technique in the assessment of the muscular health state, different acquisition systems have been developed to supply the clinical and costumers requests. The following paragraphs briefly review these devices, summarizing their main functional features, e.g., acquisition methodology, wireless data transmission, package size, weight, and battery life. The selected systems have been filtered searching from wearable, wireless, and sEMG acquisition node solutions.

FREEEMG

The FREEEMG system (Fig. 1.17), produced by the BTS Bioengineering Corp., is an electromyography device with wireless probes for the dynamic analysis of the muscle activity [58]. Thanks to a wearable custom case, constituted by the mother unit ($41.5\times24.8\times14$ mm) and its satellite electrode ($\varnothing16\times12$ mm), and very light weight of 13 g (battery included), each probe is a suitable solution for the monitoring of any type of movement, for each body part, without altering the natural movement itself. Each unit is equipped with two connectors for wet electrode (none acquisition methodology available) and samples the sEMG signal with a resolution of 16 b at 1 kHz frequency. Data are directly transmitted, using a customized version of the IEEE 802.15.4 wireless standard, to a central USB receiver, which is able to manage up to 10 probes concurrently. Moreover, the units are also equipped with an internal memory unit, able to save 2 h of data, to ensure an uninterrupted signal recording in case of temporary connection loss. All the above considered, each probes features a battery life of 6 h of continuous operation. The same company also developed the twin device FREEEMG 1000 H_2O [59], which water (and sweat) proof cover allows the device to be employed under water (up to 3 meter), further extending the applicability of the system to neuromotor and post-injury aquatic rehabilitation.

Fig. 1.17 FREEEMG acquisition unit produced by BTS Bioengineering Corp [58].

DataLITE wireless EMG sensor

A similar solution is provided by the Biometrics Ltd company, which has developed wireless and wired sEMG sensors [18]. Focusing on the wireless one (DataLITE), two models are available (see Fig 1.18) depending on the need to have a variable or fixed inter-electrode distance. With various user-selectable full scale, in order to better adapt to the signals produced by muscles of different anatomy, the units have a wireless range up to 30 m, also achieving a battery life of about 8 h. In particular, considering the LE230 model (no cables for electrodes), it provides integral dry reusable electrodes directly accessible on the bottom surface of its package which, in addition to an amplifier input impedance higher than 100 MΩ, do not require any procedures for skin preparation or any conducting gels. In conclusion, also this sensor presents an optimal comfort for the subjects since all the components are packaged in a wearable case with a size of $42\times24\times14$ mm and a weight of 17 g.

Fig. 1.18 DataLITE wireless sEMG sensors from Biometrics Ltd company: (left) unit featuring electrode on the bottom of its case to reduce interference at minimum; (right) cable-model, suitable when a variable inter-electrode distance is requested [18].

Cometa EMG system

The Cometa srl developed different sEMG sensors to adapt the device to the user needs and to different environmental conditions [17]. In particular, as shown in Fig. 1.19, the Pico EMG (left) is the standard wearable node with the wet electrodes connectors below the case; the Mini Wave Infinity (center) is identical to the previous module with the exception to provide the cables for the electrode in order to adapt the inter-electrode distance; the Mini Wave Waterproof (right) represents the latest evolution to perform also under water acquisition. With the exception of marginal differences among the models, the units features 2 kHz sampling frequency, wireless transmission or limited on-board storage location, accelerometer sensor (Pico EMG), a variable functioning time from 8 h to 12 h and a lightweight package.

(a) Pico EMG. (b) Mini Wave Infinite. (c) Mini Wave Waterproof

Fig. 1.19 sEMG acquisition units developed by the Cometa srl company [17].

Trigno Avanti Sensor

The Trigno Avanti Sensor (Fig. 1.20) is another wearable, compact and durable sensor for movement analysis, which features an on-board signal processing, cable-free design and sectable EMG bandwidths [19]. It includes both an sEMG module, with a sampling frequency up to 4.37 kHz, and a 6-axes IMU unit. Comparable to the other described devices, also this sensor presents a small size of $27\times37\times13$ mm, with the limited weight of 14 g, and a battery life ranging from 4 h to 8 h depending on the sensor data request.

Table 1.2 summarizes the technical and functional characteristics of the presented commercial sEMG devices. As stated in the motivation of this thesis, although these sensors provide very compact and functional solutions, their application is still

Fig. 1.20 Trigno Avanti sensors produced by Delsys Incorporated [19].

limited to a short-term usage, often confined to clinical supervised application. Indeed, from one side, with a maximum operating time of 8 h (without a direct declaration of related functionalities), these devices can not perform long-term muscle monitoring of one or more days. On the other side, despite the possibility to use the probes outside dedicated environment (e.g., at sport facilities), their application usually requires a custom data receiver, therefore loosing the versatility to connect the system to the preferred device (e.g., a smartphone) and to effectively provide a system to be used everywhere.

Table 1.2 Technical features of commercial sEMG acquisition devices.

Device	**Wireless**	**Size**	**Weight**	**Battery life**
FREEEMG	IEEE 802.15.4	41.5×24.8×14 mm master + ⌀16×12 mm satellite	13 g	6 h
DataLITE	WiFi	42×24×14 mm	17 g	8 h
Pico EMG	n.a.	n.a.	7 g	8 h
Mini Wave Infinity	n.a.	<5 cm^3	n.a.	8 h
Mini Wave Waterproof	n.a.	n.a.	10 g	8 h
Trigno Avanti Sensors	Propetary RF protocol BLE 4.2	27×37×13 mm	14 g	8 h

1.5 The Average Threshold Crossing (ATC) Approach

[1] The need for efficient solutions, able to overcome the current challenges in the design of bio-signal acquisition systems, led the investigations towards the definition of the event-driven Average Threshold Crossing (ATC) approach. Three design paradigms have been taken into consideration for the conception of this technique [32], combining them in order to complement the functionalities of each other in a unique solution:

- Bio-inspired: looking at the biological neuro-muscular system, the idea is to mimic the neural spikes communication by coding electronic signals in the form of digital pulses (i.e., the quantitative information is mapped onto the time domain as spikes series).
- Event-based: the *event* is identified as the informative phenomena related to a specific task. Taking into consideration the sEMG signal, the interested *events* could be associated to an increasing of the myocytes firing rate during muscle contractions, which is electrically represented by a rising of the signal energy in the sEMG spectrum. As a consequence, the coding of the muscle activity into finite *events* allows the design of a event-based system whose functionalities are strictly related to the events detection. In this way, the amount of resources needed to acquire and process the muscle signal could be reduced to some spot actions limiting as much as possible the total power consumption.
- Information synthesis: the overall amount of acquired data could be drastically reduced by achieving a feature extraction process directly on the sensor node (i.e., edge-computing), thus lowering the transmission payload while providing high-level user information.

[1] Disclaimer: This Section contains some parts and arguments taken or (partially) rephrased of the following published work:

- **F. Rossi**, A. Mongardi, P. Motto Ros, M. Ruo Roch, M. Martina and D. Demarchi, "Tutorial: A Versatile Bio-Inspired System for Processing and Transmission of Muscular Information," in *IEEE Sensors Journal*, vol. 21, no. 20, pp. 22285-22303, 15 Oct.15, 2021, doi: 10.1109/JSEN.2021.3103608.

Fig. 1.21 clearly depicts the definition, implementation, and advantages of the ATC technique, pointing out where the above paradigms take action. The main idea is to compare the sEMG signal, once it has been amplified and filtered, with a threshold; the *informative event* has been identified with the signals Threshold Crossings (TC) (i.e., event-based). From the distribution of the events (i.e., bio-inspired), the TC information has been compressed (i.e., information synthesis) by counting how many events have been generated in an observation window (later also referred as ATC window), consequently defining the ATC parameter as in Eq. 1.5, where $\#TC_{events}$ states for the number of TC events and T_{window} normalizes the parameter to the duration of the observation window.

$$ATC = \frac{\#TC_{events}}{T_{window}} \tag{1.5}$$

As also reported in [61, 62], ATC and other similar techniques, e.g., Zero-Crossing (ZC), Wilson Amplitude (WAMP), fit particularly well to the sEMG signal because of their amplitude proportionality and incremental variability in presence of muscle activity (i.e., bio-inspired). Thus, the ATC parameter could be identified as a

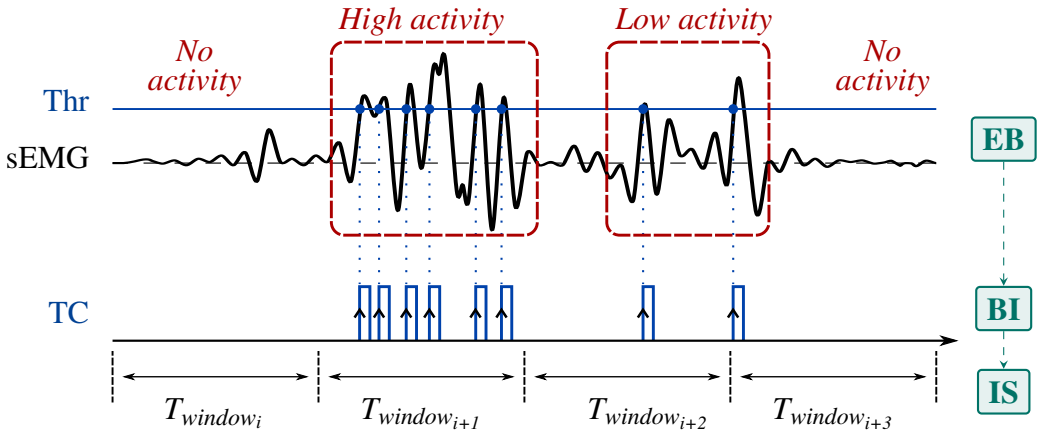

Fig. 1.21 Average Threshold Crossing (ATC) technique: following the Event-Based (EB) paradigm, the threshold crossing (TC) points are identified as the *events* carrying the information of muscle activation, and they can be represented with a time-distribution of electrical spikes, as it happens in the biological communication among neuron cells, i.e., a Bio-Inspired (BI) process. Information Synthesis (IS) is achieved by applying a time-window (T_{window}) approach on the TC distribution in order to compute the ATC parameter, which summarized the state of muscle contraction (e.g., high, low or no activity) [60].

novel indicator for monitoring the muscle behavior, with the design and processing advantages of the above paradigms w.r.t. the common literature evaluators.

In the first work [63], the feasibility of using the ATC parameter in monitoring the force exerted by muscles was investigated: both the ATC parameter and the Absolute Rectified Value (ARV), identified as gold standard sEMG estimator for force evaluation, were examined. Experiments were conducted on eight subjects pushing a dynamometer up to 70 % of their Maximum Voluntary Contraction (MVC); ARV and ATC trends have been extracted (observation window of 500 ms) from sEMG signals acquired by forearm muscles; the overall average correlation has been computed for both the ATC-force and the ARV-force pairs obtaining values of 0.95±0.02 and 0.97±0.02 for respective comparisons. Continuing in the same direction, the following work [64] demonstrated how the measured correlation maintains an acceptable value above 0.9, despite the 70 % of the TC events are lost. Therefore, although the ATC-force correlation decreases for low MVC values (< 23 %), the ATC-force and ARV-force comparisons do not show significant differences, also presenting a solid robustness to event losses, so opening the road to the use of ATC as a reliable force estimator.

In two consecutive works [65, 66], the study of the ATC-force relation has been continued trying to discriminate different force levels by performing standardized isometric contractions with a set of weights. Results on ATC extraction (ATC window of 130 ms) confirmed the possibility to discern among three coarse levels: natural load (0 kg), low activation state (2 kg, 4 kg and 6 kg), and high activation state (8 kg and 10 kg). From these tests, the optimization of the threshold per subject (six in total) results to have an effect on lowering the overlap among the ATC values related to different weights, therefore enabling an enhanced distinction between the muscle loads.

As it seems clear, the choice of the right threshold value is relevant on the extraction of TC events. Indeed, a proper threshold has to detect as many sEMG events as possible so to get all the useful information content while maintaining strong robustness to the environmental noise and bio-signal related artifacts. As it will be demonstrated in Section 2.3.1, after different investigations [67, 68], the best choice for calibrating the threshold is to set its value just above the sEMG signal baseline, during the muscle rest condition, in order to detect the muscle activation events even at very low muscular contractions.

The possibility to determine different force levels based on the ATC parameter led the research activities to evolve toward the study and development of human-machine interfaces based on ATC. In [69] and [70] the performance of some machine learning algorithms for the recognition of hand gestures have been investigated: a specific configuration of the acquisition electrodes allowed the classification of six active gestures by employing only three ATC channels, proving the effectiveness of the event-based approach in supporting, as a feature extraction stage, AI-based applications. In the same studies, the advantages of an embedded implementation of such algorithms, in order to move the entire ATC feature extraction and gesture classification directly on a wearable system, have been demonstrated.

After assessing the usability of ATC, next step was to focus on the design of an sEMG-ATC acquisition system. In [66, 71] a first definition of the device architecture has been introduced, also reviewing the standard functional blocks of an acquisition unit, i.e., conditioning circuitry, digital interface, and wireless connectivity, by introducing and implementing the ATC approach.

Starting from the feature extraction process, this task is directly performed on the acquisition channel, since the generation of the TC signal can be achieved simply using a voltage comparator on the amplified sEMG signal. Moreover, due to the *quasi-*

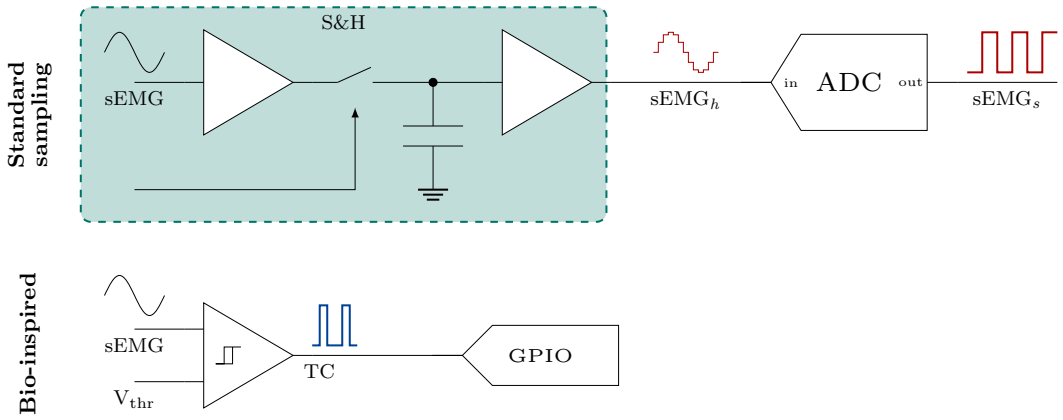

Fig. 1.22 Differences between the standard sampling approach and the combination of the event-based and bio-inspired methodologies: in the first case, the Sample and Hold (S&H) block is generally required to hold the muscle signal (sEMG$_h$) previous its Analog-to-Digital Converter (ADC) digitization (sEMG$_s$); in contrast, the proposed circuit compares the analog sEMG signal with a voltage threshold to generate the TC signal, which is subsequently driven at the GPIO input for the ATC computation [60].

digital properties of the TC signal (i.e., digital signal shape, time-analog information, see Fig. 1.21), the events count (i.e., ATC) could be computed by directly connecting the TC signal to standard input/output (I/O) interfaces of a microcontroller, thus not requiring any Sample and Hold (S&H) and Analog-to-Digital Converter (ADC) additional interfacing circuitry. Therefore, as depicted in Fig. 1.22, by applying the event-based and bio-inspired paradigms, the feature extraction process can be moved from the firmware (FW) or software (SW) domain, as usually done, to the HW one: this modification distances the ATC technique from the similar ZC and WAMP parameters, which usually require to sample sEMG data and to process them only after digitization [62]. In this way, minimizing the HW and SW/FW resources required to extract the sEMG feature, the related power consumption and the computational effort are drastically reduced. These modifications have been implemented both realizing an Application Specific Integrated Circuit (ASIC) [65] and developing a Printed Circuit Board (PCB) with Commercial Off-The-Shelf (COTS) components [66] in order to demonstrate the HW versatility of this approach.

Focusing now on the wireless domain, in [69] is demonstrated how, employing the widespread Bluetooth Low Energy (BLE) short-range communication protocol (standard 4.0 [72]), it is possible to save up to 14 % of a defined power budget (i.e., ~20 mW) transmitting the information of four ATC channels w.r.t. just one of sampled sEMG. Essentially, this behavior is strictly related to the application throughput of the above methodologies, as graphically represented in Fig. 1.23: as required by the Nyquist-Shannon theorem, the sEMG signal has been sampled at 1 kHz (considering its frequency spectrum [24]) with 12 b ADC resolution, thus obtaining a data transfer rate of $2\,\mathrm{kB\,s^{-1}}$; in contrast, the ATC approach, taking advantages of its intrinsic information synthesis, brings to a significant reduction of the recording data, which, considering an ATC window of 130 ms, results in a throughput of only $28\,\mathrm{B\,s^{-1}}$. However, although the benefits of an event-driven approach are clearly visible in terms of transmitted data (about two order of magnitude less), it was discovered that, even optimally setting the BLE connection parameters for individual cases (sEMG and ATC), the BLE wireless standard could limit the real applicability of the selected design paradigms (i.e., event-based, bio-inspired, information synthesis). Indeed, the possibility of directly transmitting the TC events in real-time, only in the presence of muscle activity (i.e., event-based transmission), can not be consistently achieved considering the connection timing management implemented by the BLE stack, which sets 7.5 ms as the minimum distance among connection events [73].

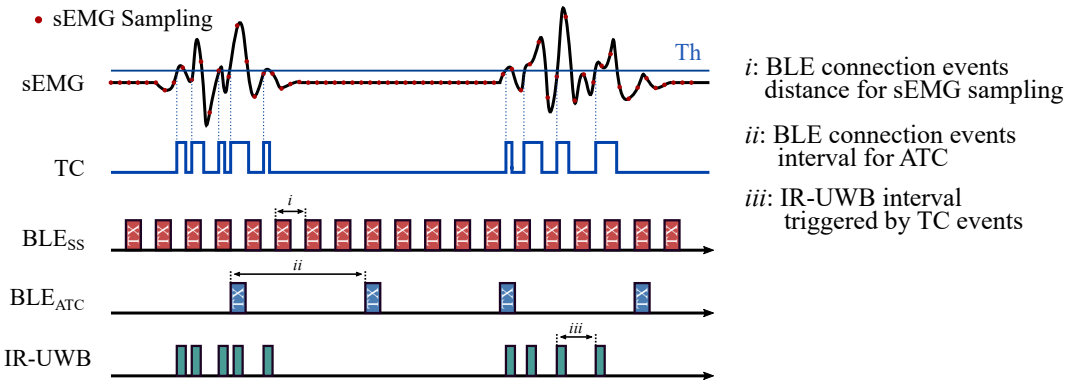

Fig. 1.23 Wireless transmission for sEMG and ATC: considering the BLE protocol, the common sampling (BLE$_{SS}$) approach needs a dense distribution of connection events in order to successfully transmit (TX) sEMG data; on the other hand, the window approach of the ATC technique (BLE$_{ATC}$) relaxes the timing of the transmission. Moving away from standard protocols, IR-UWB perfectly fits an event-driven transmission since each TX occurrence is directly triggered by threshold crossings [60].

On the other side, although the overhead structure of a BLE packet (i.e., 21 B [74, 75]) mismatches with the minimal data rate supported by the ATC technique, the transmission of the ATC parameter is not affected by the protocol timing constraints because of the relaxed window approach, which in the worst case could cause a slight jitter of one connection event in the ATC reconstruction.

A more efficient but less commonly employed (and not standard) solution could be represented by the Impulse-Radio Ultra-Wide Band (IR-UWB) technology [63, 64, 67, 65]: as shown in the lower axes of Fig. 1.23, IR-UWB pulses can be directly triggered by TC events, allowing the TX to send data only in presence of muscle activation. In this way, the limitation of a real-time TC transmission could be overcame, but with the downside inherent to the loss in interoperability because of a full-custom transceiver and protocol. In [64] this IR-UWB configuration is extended to a multi-channel system using dedicated address event representation, which can be easily involved in lab-on-chip bio-sensing measurements [76].

To summarize, the interest in using (and studying) the ATC technique instead of other bio-signal indicators relies on its advantages in terms of information extraction complexity (e.g., event generation and detection vs. ADC sampling), extremely reduced data transfer rate, and relaxed wireless communication protocol parameters,

all impacting on the overall power consumption and, consequently, on the device functional operating time.

Chapter 2

Event-based sEMG Acquisition Node Design

[1] This chapter aims to provide the reader the design rules and the electronics circuits for the realization of an event-based acquisition and processing system suitable for sEMG. The first section analyzes the fundamental aspects for the development of such a system, starting with a discussion about the different methodologies for sEMG processing to be coupled with the selected design paradigms (Section 1.5), and ending with the definition of the complete framework. The second section describes in details, one block at a time, the analog circuits for conditioning the raw sEMG signal and for extracting the quasi-digital TC signal. Thereafter, the last section completes the design of the acquisition node by interfacing the analog chain with the digital part, clarifying the main routines of the firmware and giving the specifics for wireless connectivity.

[1] Disclaimer: This Chapter contains some parts and arguments taken or (partially) rephrased of the following published work:

- **F. Rossi**, A. Mongardi, P. Motto Ros, M. Ruo Roch, M. Martina and D. Demarchi, "Tutorial: A Versatile Bio-Inspired System for Processing and Transmission of Muscular Information," in *IEEE Sensors Journal*, vol. 21, no. 20, pp. 22285-22303, 15 Oct.15, 2021, doi: 10.1109/JSEN.2021.3103608.

2.1 System level architecture

The definition of the most suitable framework for the development and implementation of the proposed sEMG ATC-based system needs to cover four main aspects:

1. Circuits and systems for sEMG detection;
2. Feature extraction technique;
3. Digital interface;
4. Wireless connectivity.

Considering the scenario described in Section 1.5 and selecting the ATC parameter as the feature for muscle monitoring, points 1) and 2) can be co-designed into a single solution due to their strict symbiotic dependence. Since the TC signal is extracted by comparing the amplified and filtered sEMG signal with a threshold, the evaluation of the proper HW bio-signal conditioning circuits (e.g., amplifiers, filters) for the processing of the raw signal have to be considered. Besides, keeping in mind the advantages of the event-driven approach and the possibility to extract the TC signal in HW (lowering FW computational effort), also the electronics for the TC generation can be added at the end of the sEMG-conditioning chain. On the other hand, filters and amplifiers design rules and best practices (e.g., filter order, bandwidth ripple, bandwidth-gain product) can be appreciably relaxed considering the implementation of the subsequent thresholding process, thus enabling to reduce the complexity of the entire circuit. Lastly, among the methodologies for the sEMG detection, the differential (bipolar) one has been selected because of its robustness to the noise sources and consequent enhanced signal quality.

Point 3) could be investigated considering application functionalities (e.g., data acquisition, processing and transmission) and system configurable settings (I/O communication with microchips, antenna, etc.) while focusing on low-power and energy efficiency aspects of the final solution. Therefore, the use of a MicroController Unit (MCU) was considered as an adequate choice to join together all these tasks.

The above considerations bring directly to the definition of point 4) since the selected MCU has to support the suitable wireless standard. Among the expansive list of available commercial protocols (e.g., Bluetooth, Zig-Bee, Wi-Fi, IEEE 802.15.4,

Table 2.1 MCUs comparison for digital selection. All devices feature an Arm® 32-bit Cortex®-M4F CPU, Bluetooth 4.2 standard, and 1.8 V power supply. [60]

	[77]	[78]	[79]	[80]	[81]
Clock frequency (MHz)	48	64	48	64	32
Power efficiency (typ.) ($\mu A\,MHz^{-1}$)	6	52	71	53	34
Flash/ROM (kB)	1024	1024	352	1024	512
RAM (kB)	384	256	80	256	128
TX current (typ.) (mA @ 0 dBm)	3	4.8	7.3	5.2	3.5
Package (mm x mm)	4.5 x 4.5	7 x 7	7 x 7	7 x 7	6 x 6

[77]: Apollo3 Blue, [78]: nRF52840, [79]: CC2642R, [80]: STM32WB55
[81]: QN9080-001

Thread), the Bluetooth (low energy version 4.2 [73]) properly fit the design requisites because of its low power features, flexible throughput, widespread adoption, and also considering the discussed feasibility of the ATC-BLE transmission (Section 1.5) [69].

Table 2.1 reports the fundamental features of commercial MCUs, filtered out from the vast sea of available devices searching for the ones able to satisfy the above requirements. In particular, all selected MCUs have a Central Processing Unit (CPU) based on an ARM® 32-bit Cortex®-M4 with Floating Point Unit (FPU), support Bluetooth 4.2 wireless protocol or newer, feature similar peripherals (e.g., ADC, Serial Peripheral Interface (SPI), Universal Asynchronous Receiver Transmitter (UART), timer), and their power supply can be lowered to 1.8 V for low-power applications. Among the comparison features, the main clock frequency and the related power efficiency are the most significant because they represent how fast the CPU processes the operations at fixed current absorption per MHz. Wireless transmitter (TX) output level strongly affects power consumption during continuous data streaming, thus looking for the best power efficiency could improve battery life-

time. MCU physical size had been taken into consideration too, since the component package could impact on final device area.

Furthermore, non volatile (e.g., Flash) and volatile (e.g., RAM) memories need to be sufficiently large to store application data and to enable the proper firmware performance in edge-computing tasks. Indeed, since the proposed system can be employed in several different applications (as highlighted in the motivation of this thesis work, Section 1.1), although the ATC itself implies a very low computational overhead, the MCU has to be chosen powerful enough to handle relatively high amount of data with fast response time. For example, considering to use the device to perform on-board computing for gesture recognition application, the Flash or RAM memories have to be large enough to contain all the parameters needed by the classifier to predict the movements, while ensuring a fast response to allow the CPU to handle the predictions in real time.

Therefore, analyzing the above specifications all together, the AmbiqMicro Apollo3 Blue [77] has been selected as the MCU which fulfills the design and application requirements with the best trade-off among the discussed features. Looking at its characteristics, it requires low current absorption of $6\,\mu A\,MHz^{-1}$ for the CPU (running up to 48 MHz) and 3 mA TX power for transmitting at 0 dBm; it has a RAM availability of 384 kB, combined with a acceptable Flash of 1024 kB; and its physical dimension fits into a very low area of $20.25\,mm^2$.

To summarize, the selected system level architecture has been defined as follows: a custom sEMG analog conditioning circuit for the raw signal acquisition and TC feature extraction, the Apollo3 Blue as the MCU for the digital control of the system, and the Bluetooth 4.2 as the wireless standard for the data transmission.

Parallel to the this high-level organization, additional design rules have been followed for the selection of the other components (than MCU), which require a meticulous analysis of the electrical and physical properties to fit at better the development of the sensing node. In particular, the three following major constraints have been considered:

- The current absorption – Considering a small battery as power supply source, the *low power* keyword must be the central focus in selecting all the integrated

devices since their concomitant operation result in the summation of each power requirement;

- The package – Each component has to be chosen by considering its dimension carefully. During the design phase, the physical arrangement of all the pieces has to match the volume (m^3) restrictions of a wearable device;
- The accuracy – The filtering and amplification stages require the use of precise component values. Therefore, the tolerance from nominal values needs to be take into consideration. However, as explained before, by exploiting the advantages of ATC approach, this last optimization can be conveniently relaxed.

In conclusion, all the above specifications are combined with a fixed power-supply (V_{DD}) of 1.8 V, which, further limiting the power consumption, aims to extend the device operating-time as much as possible.

2.2 Hardware Front-end for sEMG Processing

As clarified in section 2.1, the realization of a custom sEMG conditioning circuit allows the developer to implement the event-based processing technique(s) directly (in hardware) on the acquisition device, totally exploiting the benefits of this approach (e.g., relaxation of filters constraints, no need of ADC).

Fig. 2.1 shows the first functional version of the designed sEMG front-end, which merges and finalizes the studies and experiments described in Section 1.5. It works with the typical bipolar electrodes configuration [2] (see Section 1.3.4), hence using two sensing electrodes (V_{E1}[2] and V_{E2}) to detect the myofibers depolarization and a third one to refer the body potential w.r.t. the acquisition device (V_{ER}) [82]. All blocks have been designed using commercial off-the-shelf components to demonstrate the complete feasibility of the event-based approach (no custom IC – ASIC) and, considering the absence of digital circuitry (with the exception related to how TC threshold has been handled), the proposed acquisition channel can be defined as an Analog Front-End (AFE).

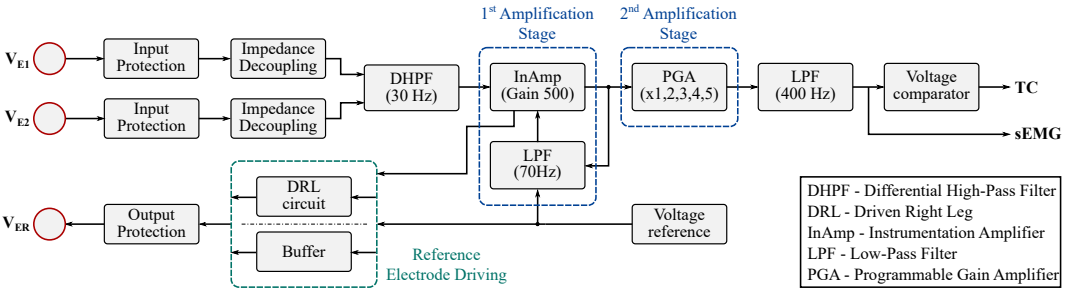

Fig. 2.1 Schematic block diagram of proposed Analog Front End (AFE) for sEMG signal acquisition and on-channel processing [60].

The next (sub-)sections focus on each AFE block, both explaining its functionality and describing which design rules have been followed during the front-end realization.

[2] All node potentials are considered with respect to the common reference of the circuit, i.e., the negative terminal of the battery.

2.2.1 Input/Output Protection

Excessive voltages, usually defined much higher than the supply voltage (V_{DD}), could damage onboard circuitry components, whose absolute maximum ratings are normally close to V_{DD}. Therefore, good practice imposes the insertion of a protection circuit able to limit the effect of undesired voltages. The protection circuitry designed for the AFE is represented in Fig. 2.2.

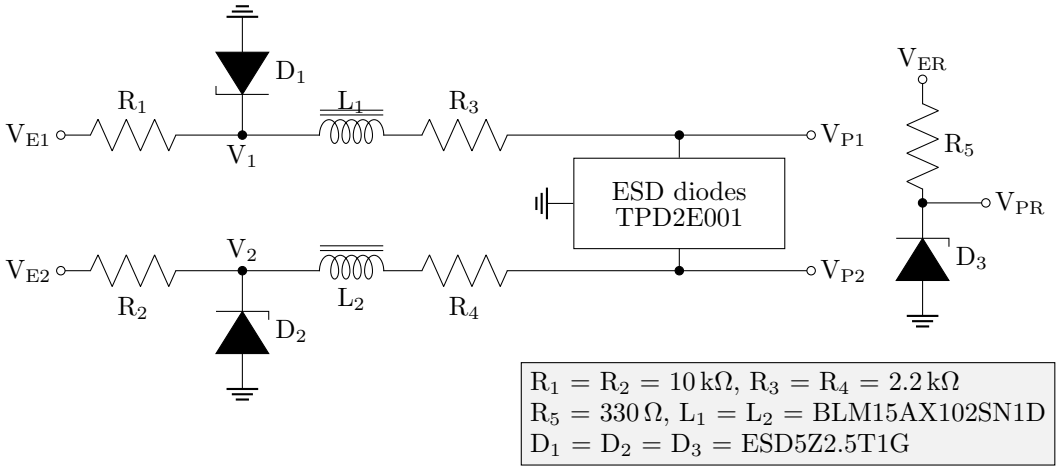

Fig. 2.2 Input/output protection: the damage of the circuitry caused by overvoltage inputs is limited using R-D networks; the high-frequency environmental noise is attenuated by using ferrite beads [60].

As the first AFE protection, an R-D network (i.e., R_1-D_1, R_2-D_2) has been designed for both inputs connected to the sensing electrodes: R_1 and R_2 account for high-voltage drops in order to have a safer V_1 and V_2 voltages, while D_1 and D_2 provide a preferential path to ground when the voltages at their ends overcome the diode breakdown voltage, thus avoiding higher voltages in the downstream circuitry.

Ferrite beads L_1 and L_2 suppress high-frequency electromagnetic and electrical interference (Section 1.3.5). R_3 and R_4 resistors limit inward currents in the Electro-Static Discharge (ESD) protection module, which completes the input stabilizer block.

From a design point of view, in order to maintain limited voltages at V_1 and V_2, the R_1 and R_2 resistors have to observe the relation in Eq. 2.1, where V_{in} is the AFE input (over)voltage, V_{br} the Zener diode breakdown voltage and I_{max} the maximal

current acceptable by ESD module.

$$R = \frac{V_{in} - V_{br}}{I_{max}} \tag{2.1}$$

In critical scenarios, V_{in} can reach tens to hundreds of V (e.g., when AFE is coupled to a FES stimulator), thus reducing V_{in} - V_{br} to V_{in}. In these situations, resistors value has to be chosen adequately w.r.t. I_{max} limitation and, considering the relative high $V_{in} \cdot I_{max}$ product in case sustained overvoltages occur, featuring $1/4$ W power dissipation.

A similar protection has been also designed for the reference electrode, here mainly focusing on current limitation (through R_5 resistor), which has been maintained below 10 mA in order to avoid physical damages or annoying perceptions to the user.

2.2.2 Decoupling Circuit

Two voltage followers, one for each sensing channel (see Fig. 2.3), have been inserted between input protections and signal conditioning. Main tasks at this stage are both to provide the proper impedance to the amplifier inputs, decoupling them from the electrode-skin impedance, and to guarantee sEMG integrity.

2.2.3 Differential High-Pass Filter

The electrode-skin interface represents a very delicate area where ionic flows are transformed into electrical currents by means of redox reactions at electrode metal surface (Section 1.3.2). As follows, any chemical or physical disturbances can drastically affect the quality of the acquired signal, also considering its extremely reduced amplitude at source location. Among them, movement artifacts, usually induced by cables motion (in standard application electrodes are wired connected to amplification stage), has been demonstrated to introduce low-frequency noise below 20 Hz-30 Hz [83, 84] (Section 1.3.5). Also improving interface stability, e.g., electrolyte gel facilitating carriers flow, glue for stable electrode attachment, does not

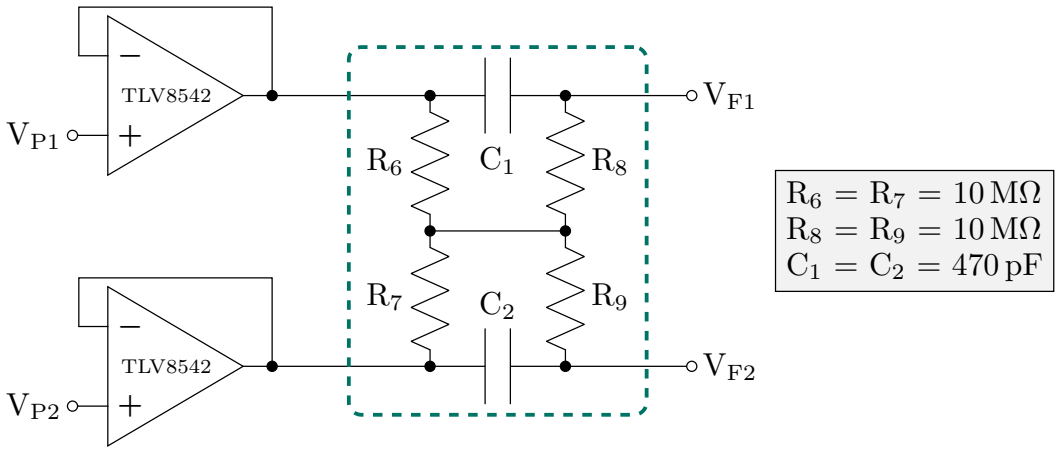

Fig. 2.3 The designed differential high-pass filter, whose inputs are decoupled by two voltage followers, limits the effect of the movement artifacts avoiding the saturation of the on-board electronic components [60].

overcome such phenomena. A possible solution concerns to attenuate these artifacts by filtering out noise frequencies at AFE inputs (Section 1.3.6).

Therefore, a first order Differential High-Pass Filter (DHPF), designed following indications reported in [85], have been inserted before the instrumentation amplifier (see Fig. 2.3), so avoiding movement artifacts amplification and the saturation of consecutive electronic components. Appropriate resistors and capacitors values have been calculated solving Eq. 2.2, where cutoff frequency f_c has been set to 30 Hz since this value is an optimal trade-off between the artifact removal and the sEMG energy-frequency integrity (Section 1.3.6).

$$f_c = \frac{1}{2\pi R_8 C_1} = \frac{1}{2\pi R_9 C_2} \tag{2.2}$$

2.2.4 Instrumentation Amplifier (1st Amplification Stage)

Bio-signal amplification is needed in order to be able to process the signal using digital electronics. For sEMG, required gains varies depending on recording muscle conditions (e.g., superficial or deep fibers, covering fat layer, fibers orientation, muscle mass and body volume) covering a 500 V/V to 6 kV/V value range [84]. Moreover, total amplification is usually divided into two or more stages (Section 1.3.6): in this way, from one side, AFE is adequately set to record electrical activity from different muscle types; from other side, gain division relaxes amplifier gain-bandwidth con-

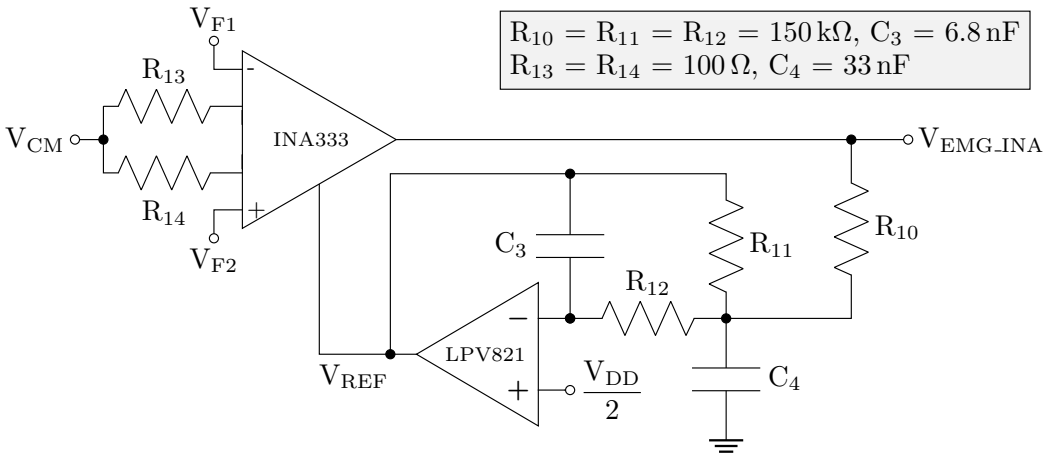

Fig. 2.4 First amplification stage: Instrumentation Amplifier (InAmp) carries out the difference between inputs, obtaining the differential signal of interest, which is further stabilized by low-pass negative feedback on the reference voltage [60].

straints, avoiding signal distortions.

In the proposed solution, the first amplification stage, reported in Fig. 2.4, has been designed using an Instrumentation Amplifier (InAmp), suitable to carry out the differential (bipolar) acquisition of sEMG signal. Basically, InAmp performs the subtraction between input channels, and amplifies this difference by the differential gain A_d, i.e., $V_{EMG\_INA} = A_d(V_{F2} - V_{F1}) + V_{REF}$, centering it to the middle of the voltage supply (V_{REF}). As general features, InAmp provides high Common Mode Rejection Ratio (CMRR) in order to reject as much as possible common noises sources (e.g., power-line interference) while detecting inter-electrode variation (i.e., sEMG signal).

Depending on the internal architecture of the InAmp, A_d gain could be easily set through an external resistor (usually named R_g). For this AFE, the INA333 [86] from Texas Instruments, featuring an adequate CRMM of 100 dB, has been selected, since it allows the external resistor (R_g) value to be physically split into the two R_{13} and R_{14} resistors, thus also enabling the driving of the sEMG common-mode (V_{CM}) to the DRL circuit. A differential gain (A_d) of 500 V/V has been set as the default amplification value since it achieves a good signal acquisition (when superficial or large muscles are considered) while maintaining constant amplification in the 0 Hz to 400 Hz range [86].

Looking at real-case scenarios, electrical and environmental noise sources (here intended as common-mode) are not completely rejected by InAmp because both real amplifier behavior has limited performances, and common-mode can be transformed into differential signal (and so amplified by A_d) by electrodes path and circuit unbalances [53]. In such circumstances, amplified sEMG could be corrupted by overlapping noise, making its interpretation difficult and misleading.

Furthermore, in order to make the output of the InAmp more stable and consistent, a negative feedback on the InAmp reference was added: it consists of a second order Butterworth multiple-feedback low pass filter with cutoff frequency f_c [87], as calculated in Eq. 2.3.

$$f_c = \frac{1}{2\pi\sqrt{R_{11}R_{12}C_3C_4}} \tag{2.3}$$

Generally, the idea is to sense the InAmp output, filter unwanted noises and, after its inversion, feed it again to the InAmp reference. In this way, the baseline of the output signal follows noise variations but, being 180 degree out-of-phase, is able to remove such interference. f_c was set to 70 Hz to take into account also the power-line interference which, depending on the environmental conditions, is not completely rejected by the InAmp itself.

2.2.5 Reference Electrode Driving

As it can be seen from the diagram in Fig. 2.1, there are two (testing) circuits to drive the body to a known reference potential through the third electrode (E_R).

The first (and low complexity) solution provides a voltage reference by means of a voltage regulator. This value is fixed to $V_{DD}/2$ in order to provide a body reference voltage (V_{ER}) matching the one driven to InAmp. The insertion of a voltage follower further stabilizes its value before the electrode interface.

The second possibility consists in the well-known Driven Right Leg (DRL) circuit [88, 53, 84], which limits the effect of the common-mode noise when it is relevant on the subject body. Among the high variety of DRL designs [89–93], the configuration proposed here focuses on low complexity, as represented in Fig. 2.5: first of all, the common-mode signal V_{CM} is sensed from InAmp gain resistors and driven to a voltage follower; then, V_{CM} feeds an inverting amplifier with unitary gain (R_{15}=R_{16}) in order to obtain a reversed common-mode voltage, referred to

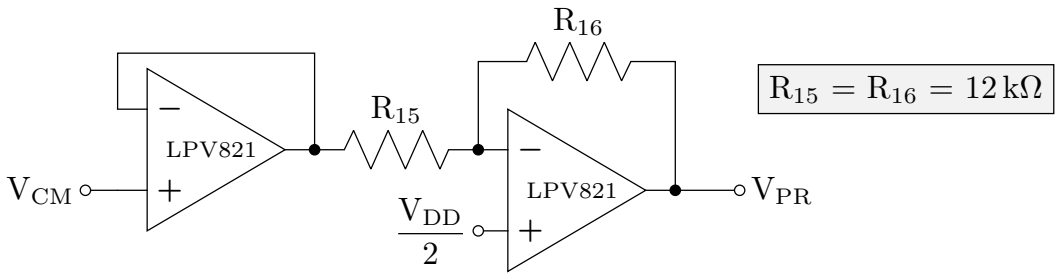

Fig. 2.5 The Driven Right Leg (DRL) circuit has been designed as a cascade of a common mode stabilization buffer and an inverting amplifier [60].

the middle of power supply, to be injected back to the subject's body through the reference electrode (E_R).

Both the solutions end with the safety circuit introduced in Section 2.2.1 (Fig. 2.2), limiting the maximal current flowing through E_R to 10 mA.

2.2.6 Programmable Gain Amplifier (2nd Amplification stage)

A second amplification stage is often required when the default gain is insufficient to adequately represent the activation of the deeper or smaller myofibers [84]. Hence, a Programmable Gain Amplifier (PGA) has been designed to provide the $\times 2$, $\times 3$, $\times 4$, and $\times 5$ additional amplification values.

With the goal to maintain the AFE at low complexity while giving the user easy control of the acquisition parameters, this stage has been realized by using an analog multiplexer, as reported in Fig. 2.6, which, depending on its digital inputs (A0, A1), provides a different electrical path (corresponding to the desired gain value) to the negative input of the operational amplifier. Each path consists of an RC circuit, acting as a high-pass filter ($f_c \simeq 30$ Hz) to avoid the amplification of the signal baseline. When no additional gain has been requested (EN disabled), this stage works as a buffer for the sEMG signal. This custom configuration has been preferred to a COTS PGAs due to their higher power consumption and to the usual complexity of their internal design (i.e., commercial PGAs usually feature a wider range of gain values w.r.t. to the ones needed by this application).

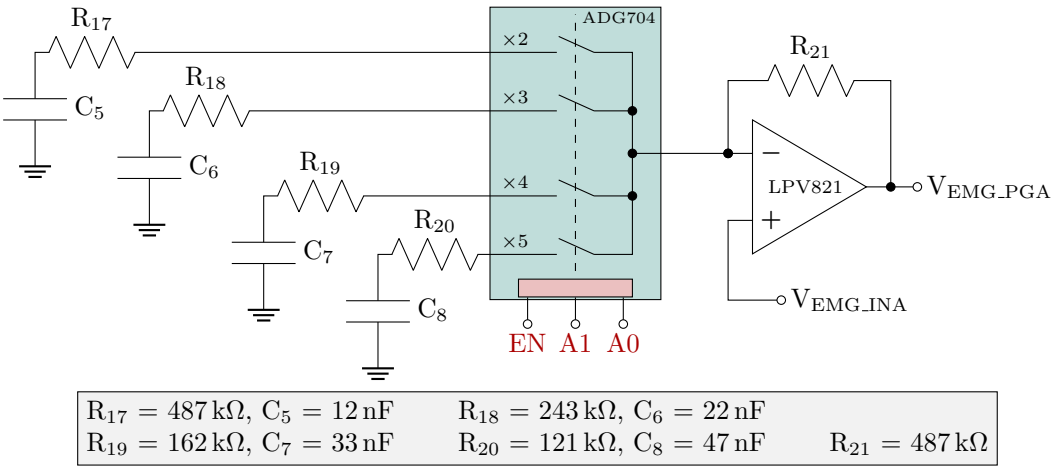

Fig. 2.6 Programmable Gain Amplifier (PGA): adaptable amplifier gains (i.e., ×2, ×3, ×4 and ×5) are obtained by controlling the analog multiplexer on the amplifier inverting branch [60].

2.2.7 Low-Pass Filter

A Sallen-Key Low-Pass Filter (LPF), represented in Fig. 2.7, is placed after amplification stages in order to limit sEMG signal bandwidth to 400 Hz, considering the most relevant energy content at 50 Hz–150 Hz [23].

The cutoff frequency f_c of this Butterworth Filter has been calculated in Eq. 2.4, according to [87].

$$f_c = \frac{1}{2\pi\sqrt{R_{22}R_{23}C_9C_{10}}} \tag{2.4}$$

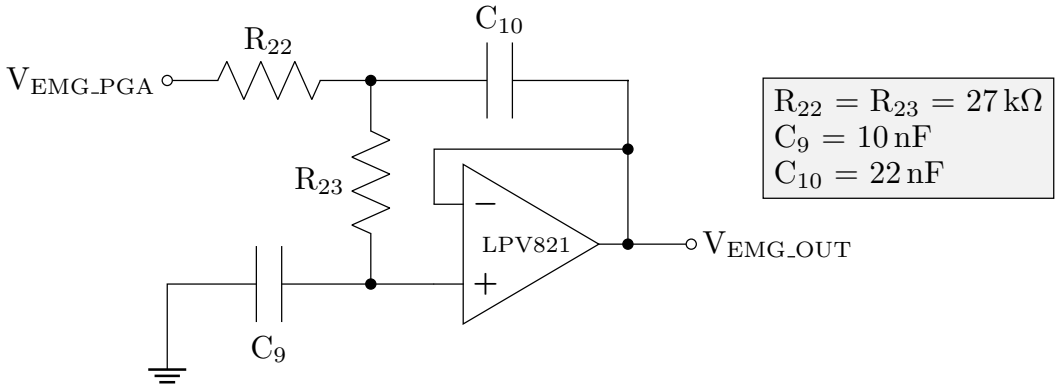

Fig. 2.7 The Sallen-Key Low-Pass Filter (LPF) configuration centered at 400 Hz limits the sEMG bandwidth, acting also as anti-aliasing filter for the (optional) signal digitization [60].

This stage prevents the TC signal to be influenced by higher frequencies w.r.t. the ones related to muscle activity, and it matches the bandwidth amplification designed for previous parts. Since the sEMG is also placed in input to an ADC at this stage, this LPF works also as an anti-aliasing filter (minimum sampling frequency of 800 Hz) [24].

2.2.8 Voltage Comparator

Finally, last stage of designed AFE consists of a voltage comparator for the extraction of TC signal, as reported in Fig. 2.8. Since a different threshold value can be required depending on muscle activity and environmental conditions, a Digital-to-Analog Converter (DAC) has been included for threshold generation. In this way, beyond the proper threshold setting, the digital control of DAC permits the user also to implement additional software routines for acquisition management.

A 30 mV hysteresis, centered around the threshold value, transforms the comparator into a more efficient Schmitt Trigger, solving the $V_{HYST} = V_{DD} \cdot R_{24}/R_{25}$ relation. The hysteresis increases the robustness of TC extraction by preventing spurious spikes when the signal is oscillating around the threshold value, thus driving in the most clean way possible the digital path to the microcontroller dedicated input.

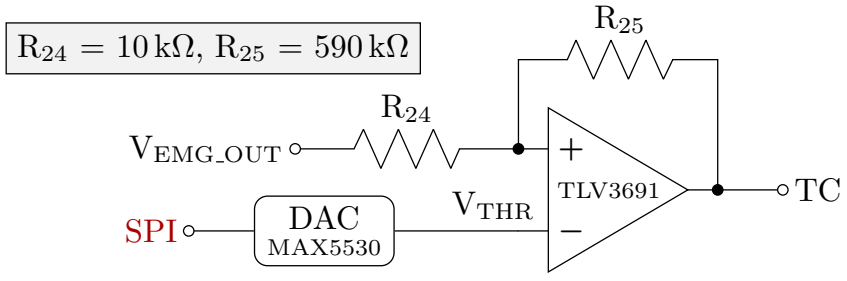

Fig. 2.8 Voltage comparator for the TC extraction with fixed hysteresis (30 mV) around V_{THR} value [60].

2.3 Digital part for signal processing

While the AFE is the key component of the analog acquisition part, the digital part is the core of the system management, comprising signal computation and user remote control access. Here, the main unit is represented by the Apollo3 Blue MCU [77], which, featuring an ARM Cortex®-M4F processor, can be involved both in wireless communication and artificial intelligence applications [94, 70], efficiently reducing the power consumption of the overall system.

In addition to the microcontroller, other components have been included in the digital section to provide a complete and functional system:

- A UART-to-USB converter, which allows the user to communicate with the microcontroller directly from a computer, enabling an easy interface for debug and firmware bootloading.
- Two I^2C connectors (input/output, slave/master), to make the board connectable in a chain bus;
- A DAC, which allows the user to perform an accurate threshold calibration, also exploiting the advantages of firmware automatic routines;
- A USB-powered battery charger circuit, to complete the wearable scenario.

A schematic diagram of the connections among the above peripherals (and of AFE) with the MCU is reported in Fig. 2.9.

Regarding the firmware, the tasks the microcontroller needs to manage could be divided into two main categories: generic peripheral handling for ATC evaluation, and user interface protocols. The first is functionally the same for each version of the system, being in charge of the configuration of peripheral parameters useful for ATC computation. The latter, instead, is more dependent on the target application and on the hardware configuration to be involved. In fact, according to required latencies and wearability, the design can vary from a serial, reliable and fast connection (e.g., UART/RS232, I^2C), to a more complete, but complex, wireless implementation (e.g., BLE, IR-UWB). Furthermore, if the application included artificial intelligence, proper routines would be integrated in the firmware to handle, e.g., recognitions and predictions.

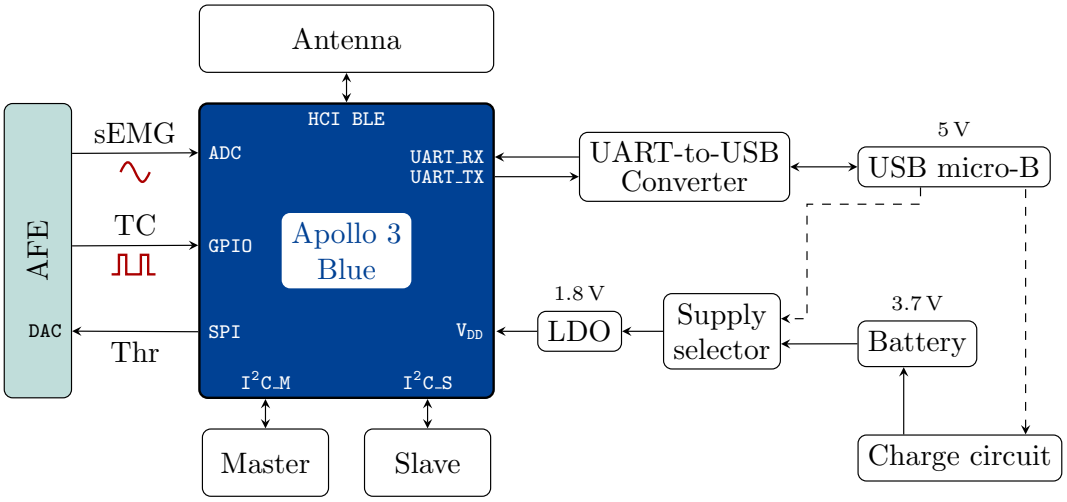

Fig. 2.9 Schematic block of the digital part: Apollo3 Blue represents the central core of the system, which processes the signals from the AFE, manages wireless communication through the BLE antenna, and provides a standard interface with both USB (micro-B) or I^2C connectors.

The present firmware solution has been implemented thanks to the FreeRTOS real time operating system [95], able to virtually manage in a concurrent way both the ATC evaluation and the Bluetooth 4.2 communication to the central user device (e.g., a computer plotting data, a smartphone/smartwatch displaying muscles activation, an actuator performing movements based on a recognized gesture [94]), but other solutions could be equally effective, depending on the hardware used.

2.3.1 Peripheral handling for ATC evaluation

The microcontroller code is first configured for low power operations, exploiting proprietary libraries capabilities. The main clock frequency is reduced from the default 48 MHz to 24 MHz to further optimize power efficiency. The application does not require high frequency clock, thus if the microcontroller could go slower, a lower setting could have been selected.

Once the initial parameters are selected, the peripherals needed for ATC management are configured, including GPIO settings and on-board wired communications. First, the pin selected to receive the TC signal is configured as input, with interrupt on rising edge enabled. Then, a proper timer configuration has to be performed, setting it to make cycles of the desired duration (e.g., a common value is 130 ms [66]); since

no excessive precision is needed to control the length of the window, a low frequency clock source can be selected, further relaxing the peripheral effort.

With the input port enabled, to complete the basic configuration, two more settings are required: the enabling of the serial ports needed by the SPI to control the DAC (Section 2.2.8), and the choice of the desired gain of the AFE, by configuring the PGA stage detailed in Section 2.2.6.

Then, threshold calibration has to be performed, in order to find the proper voltage value accordingly to environment and subject condition. In fact, in ideal conditions, the threshold would be set 16 mV above the expected signal baseline, having to take into account only the lower half of the hysteresis, thus detecting every, even minimal, activation of the muscle. Unfortunately, real cases are affected by a lot of noise sources, making the baseline of the signal not always at the desired value (i.e., middle voltage supply) and with a possible uncertainty due to unfiltered noise. According to this, the threshold calibration, performed every time the system is switched on, is able to mimic the theoretical approach to the effective signal, finding the right *delta* above the signal noise to detect actual muscle activation and neglect spurious noise spikes.

The actual firmware routine, detailed in the flowchart of Fig. 2.10, is a finite state machine, which checks the detection of TC events and modifies the threshold value accordingly, by sending proper commands to the on-board DAC. In particular, depending on the state, the behavior is the following:

1. The threshold is decreased by 150 mV every second, while no event is detected. When an event arises, the state increases, leaving the threshold unmodified.

2. A further event is expected, to confirm the previous detection. If it is captured, the threshold is set higher than last value (i.e., +200 mV) and the next state would be state 3; if not, the flow is taken back to state 1, as previous detection was generated by a temporary noise spike.

3. The fine tuning of the threshold begins, with a similar behavior w.r.t. state 1, but lowering the value by 10 mV steps.

4. Like in state 2, further events are expected, to confirm a proper identification of the signal baseline. The threshold is untouched in either case, and only the

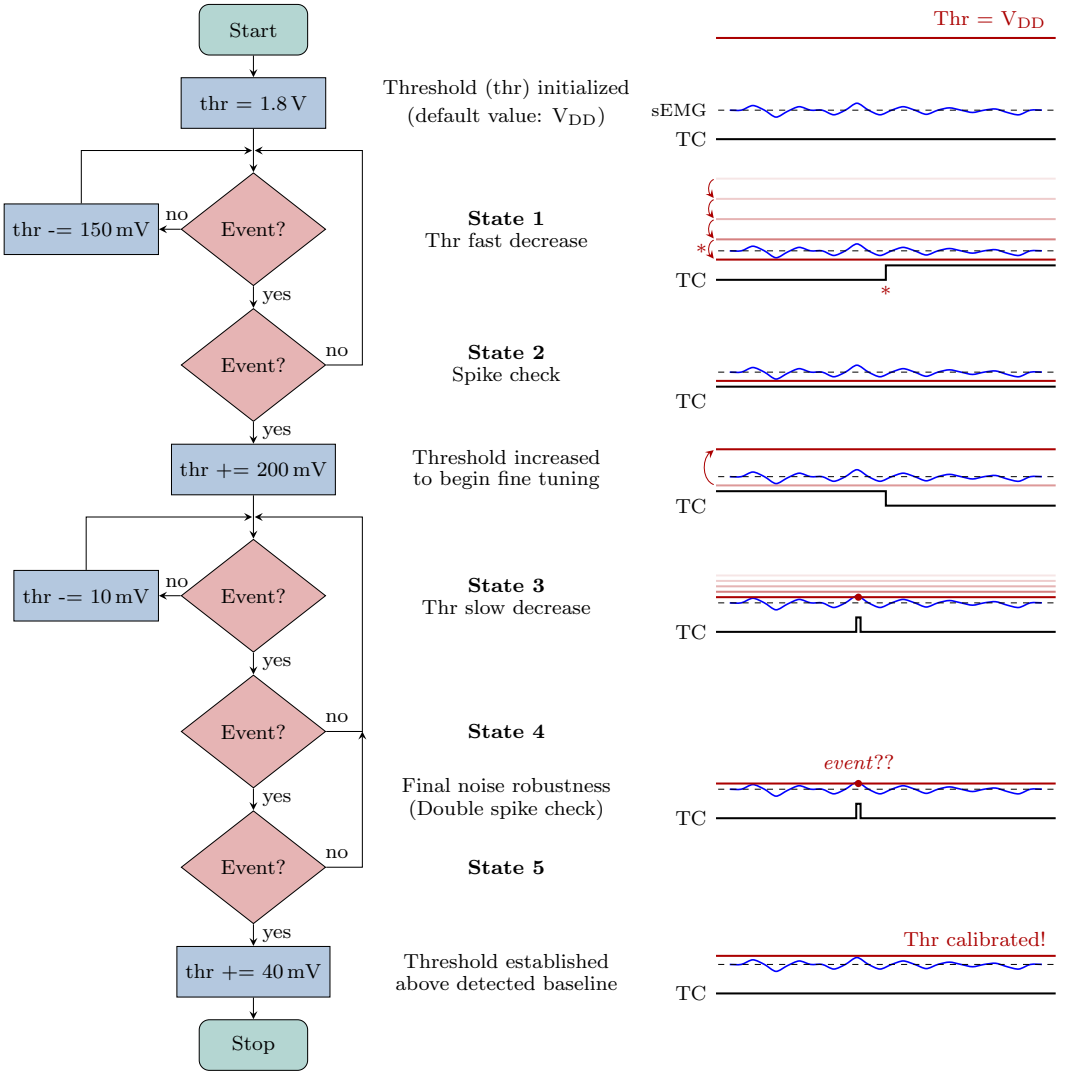

Fig. 2.10 Firmware routine for threshold auto calibration. The threshold is initialized to a value much higher than the expected signal baseline, and lowered step by step until one or more events arise. The calibration is divided in a first coarse phase, together with a check for spurious spikes, and a second fine tuning, which includes a double spike check, to ensure the final result is correct.

state changes, being set to 3 in case of a negative outcome and to 5 if it is positive.

5. Last state still checks the effective detection of the baseline. The state is brought back to 3 if no event is captured, but if the detection is confirmed the threshold is raised of 40 mV (i.e., last decreasing step plus the comparator hysteresis) and the routine is terminated.

```
while TC acquisition is requested do
    count ← 0
    while waiting for an ATC window to end do
        if an interrupt arises then
            count ← count + 1
        end if
    end while
    TC_value ← count
end while
```

Fig. 2.11 TC count evaluation. Every time an event occur, the dedicated interrupt service routine is called and the event count is incremented. When the time window reaches its configured duration, the corresponding TC value is saved and the count is reset to 0 [60].

With the threshold value set, the initial configuration can be considered concluded. The actual ATC evaluation will then be triggered by the user, starting the timer and enabling the interrupt. The TC events will be counted and saved at the end of each time window, in the simplest way possible, as detailed in Fig. 2.11, thus avoiding ADC conversion and relaxing microcontroller hardware resources.

2.3.2 User interface protocols

The remaining firmware routines are dedicated to user interface and debugging.

In a first prototyping phase, an UART connection (available through the on-board USB-to-serial converter) could be useful to send messages to a computer graphical user interface, thus displaying both data and critical information (e.g., peripherals malfunctions, BLE disconnection) and considerably speeding up device test and development. On the other hand, the final product would need a wireless communication system, in order to be quickly accessible regardless of the use case and without compromising the wearability.

The Bluetooth 4.2 stack [73] perfectly meets these requirements, providing a robust data transfer protocol, with a throughput up to 1 Mbps. According to this, a BLE server has been implemented on the Apollo3 MCU, allowing the user to fully control the device and to get data notifications of the main parameters (i.e., status, ATC and sEMG). The server structure, including handle values, relative size and permissions, is detailed in Table 2.2.

Table 2.2 BLE server for the proposed system [60]

Characteristic	**Handle**	**Size**	**Permission**[1]
Service Declaration	0x00A0	-	-
Command	0x00A2	1 B-3 B	W
Status	0x00A4	1 B	R/N
$\text{Status}_{\text{CCCD}}$	0x00A5	2 B	R/W
Gain	0x00A7	1 B	R/W
sEMG	0x00A9	20 B/200 B[2]	N
$\text{sEMG}_{\text{CCCD}}$	0x00AA	2 B	R/W
Threshold	0x00AC	2 B	R/W
ATC	0x00AE	1 B	N
ATC_{CCCD}	0x00AF	2 B	R/W

[1]R: read; W: write; N: notify. [2]LR/HR

The BLE connection with the device can be established from any remote module, and has to be performed even before initial threshold calibration. Connection parameters can be relaxed, accordingly to low data rate of the ATC technique, selecting a connection interval around the time window chosen for ATC (e.g., if 130 ms has been selected, 60 ms to 80 ms connection interval would fit the application requirements without too much delay). In the case even slower data rate are requested by the user interface, more than one notification could be grouped in a single connection event, widening the connection interval and keeping the transmitter in the idle state for even more time.

In particular, the data characteristics accessibility and behavior are:

- **Gain** contains selected amplification for PGA stage. It accepts values between 1 (default) and 5, and can be read and written: if read, the applied gain is returned; if written, the desired value is loaded in the characteristic and the PGA configuration is updated.
- **sEMG** carries the information about last ADC sampled values. It can only be notified, by writing 1 in its own Client Characteristic Configuration Descriptor (CCCD). Its dimension directly depends on the Maximum Transfer Unit

(MTU) selected. Indeed, until BLE 4.1 [72], no more than 20 bytes could be handled. According to this, two configurations have been designed: one at High Resolution (HR), which can be enabled by requesting an MTU higher than 200, and one at Low Resolution (LR) to assess back-compatibility issues of BLE 4.1 and older versions. In particular, HR mode provides 14-bit values sampled at 1 kHz, resulting in a 2 kB s^{-1} throughput, with BLE connection parameters configured to transmit a 200 B notification every 100 ms. On the other hand, LR configuration provides 8-bit resolution values, sampled at 800 Hz, which is the minimum frequency allowed by Nyquist-Shannon theorem [24] considering the cutoff frequency of 400 Hz implemented of the AFE (as detailed in Section 2.2.7). In this case, the system would send a 20 B notification every 25 ms, to handle the 0.8 kB s^{-1} application throughput.

- **Threshold** is the 12-bit binary representation of the threshold, as written to the DAC. It accepts values between 0x0000 (0 V) and 0x0FFF (1.8 V). It can be read to check the threshold value (e.g., after the calibration routine) and written to manually set a desired value. In this last case, the DAC output value is automatically updated.

- **ATC** contains last evaluated count of the TC events, as an integer value. No normalization is performed on-board, to avoid complexity increase, and it will be computed by user application only in the case a comparison among different time windows is needed. If a 1 is written in the CCCD, a notification would be sent at the end of each time window. Considering its default 130 ms duration, event-driven processing of sEMG minimizes throughput to 8 B s^{-1}, considerably reducing data amount w.r.t. standard sEMG sampling. Furthermore, this configuration is not constrained by the connection interval and, consequently, by the receiver Bluetooth stack.

The **Status** is enabled by writing a 1 in its CCCD and would send a notification every time an operation terminates or an error occurs. Its idle value is 1, while 0 is the value it holds when the notifications are not enabled.

Last, the **Command** gives the user the permission to execute task on the device. It has a variable dimension (i.e., 1 B to 3 B) attribute, thus allowing different commands to be implemented, without data padding in the array. In particular, these are the actions which can be executed:

- Debug - 1 B - Used to trigger the transmission of the debug status notification, thus checking basic connectivity.
- Gain set - 2 B - Sending this command with a value between 1 ad 5 in the second byte is equivalent to set the gain characteristic at the same value. Returns a Gain_set status in case of success.
- Automatic threshold calibration from V_{DD} - 1 B - The threshold calibration routine (see Fig. 2.10) is launched, under the Thr_searching status. If a value is found correctly, returns the Thr_found status; if errors occur, a Thr_error status is notified.
- Automatic threshold calibration from *value* - 3 B - Same operation as previous command, but beginning the search from *value*. It should be written in the lower 12 bits of the second and third byte, expressed as resulting by the formula: $value = 2^{12} \cdot Thr/V_{DD}$.
- Manual threshold set - 3 B - Updates the DAC register with the value contained in the second and third byte, like writing the Threshold characteristic. A Thr_set status should be notified.
- ATC timer set - 2 B - Changes the ATC time window accordingly with the value in the second byte, expressed in milliseconds. Recommended for advanced users only: modifying the window duration without the proper knowledge could bring to poor functionality.

As the reader can notice, while the ATC window can be adjusted by the user, no command is provided to change the raw sEMG sampling period. In fact, the ATC is an arbitrary parameter and could be adapted to different situations, but the sEMG requires a minimum sampling frequency (i.e., at least two times greater than its highest frequency content) to be reconstructed correctly. Thus, being the minimum frequency allowed already selected by default, no user command could be provided to change it.

Chapter 3

Launching the Prototype: The *Apollux*

[1] This chapter reports all the phases starting from the physical realization of the ATC board prototype to the final wearable device. The first section quickly presents the physical design of the Printed Circuit Board (PCB) to provide an overview of the arrangement of each component between the layers of the structure. Then, the second section guides the reader through the 3D project for the design and print of the wearable case for the *Apollux* device. In conclusion, last section describes the implementation of the software which, also featuring a Graphical User Interface (GUI), allows a user to efficiently interact with the system during functional operation.

[1] Disclaimer: This Chapter contains a minimal rephrased part of the following published work:

- **F. Rossi**, A. Mongardi, P. Motto Ros, M. Ruo Roch, M. Martina and D. Demarchi, "Tutorial: A Versatile Bio-Inspired System for Processing and Transmission of Muscular Information," in *IEEE Sensors Journal*, vol. 21, no. 20, pp. 22285-22303, 15 Oct.15, 2021, doi: 10.1109/JSEN.2021.3103608.

3.1 Printed Circuit Board (PCB) Realization

The PCB has been designed using Altium Designer software [96]. Four layers technology has been preferred to separate as much as possible the areas containing the analog (bottom) and digital (top) parts, while the internal layers provide for the power planes and the signal tracks routing. In particular, as shown in Figure 3.1, each layer has been organized as follows:

- Top layer: it contains all the digital components of the system (see Section 2.3), with the only exception of the UART-to-USB Converter and DAC modules;
- Mid-layer 1: it is the V_{DD} plane;
- Mid-layer 2: it represents the ground plane;
- Bottom layer: all the AFE blocks (see Section 2.2) has been arranged in this space, from the connectors for the sensing electrodes to the voltage comparator for generating the TC signal.

The Artemis Module produced by Sparkfun Electronics [97] has been selected for the integration of the Apollo3 Blue MCU because it combines into a small package (i.e.,

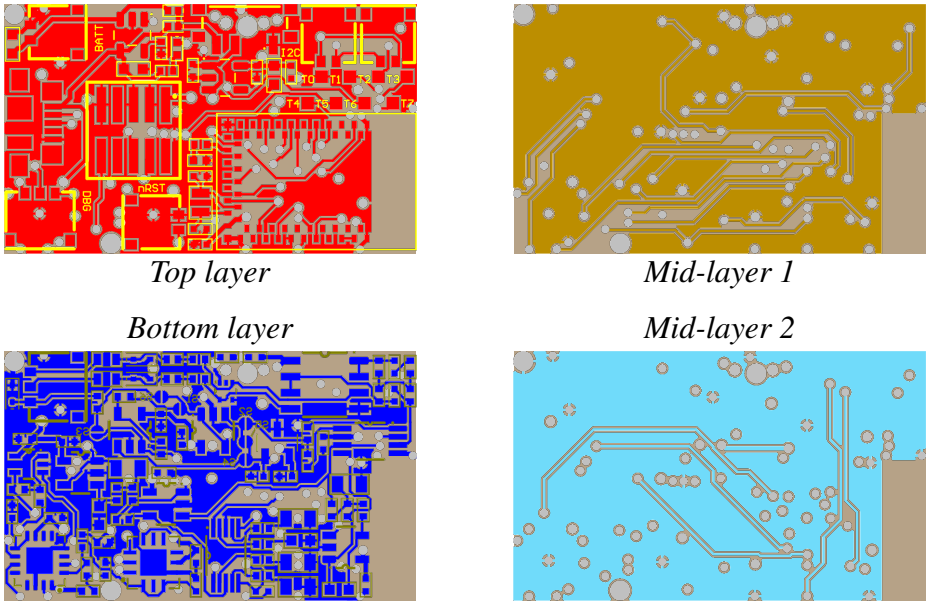

Fig. 3.1 Layers organization for the PCB prototype.

10 mm × 15 mm size) all the supporting circuitry (the MCU itself and the RF circuits) needed to access the Ambiq functionalities, also providing an easy programming interface and a standard soldering footprint. A keep-out space has been guaranteed along all layers below the antenna. The width of the routes varies depending on the type of signals they are carrying, i.e., 0.15 mm for signal, ≥ 0.25 mm for GND, and 0.3 mm (before LDO, higher current drain) or 0.25 mm (after LDO, lower current drain) for V_{DD}. In this first prototype, some test points, representing different nodes along the sEMG conditioning chain, have been inserted to ease the functional test regarding the analog circuits; surely, they will be removed in the next versions in order to save additional space. Both JTAG and USB micro-B connectors have been inserted in order to flash the firmware and provide debug operations (in future version, once the test will be completed, the prominent JTAG will be removed, leaving the MCU accessibility only through the USB micro-b). Planar connectors have been already supposed and used for battery, debug, electrodes, I^2C lines, and reset interfaces in order to save (future) device height. A manual switch enables the power supply downstream the V_{DD} selector depending on the active branch. Two leds are placed on the top layer in order to have a visual feedback from the ongoing operation: a first one, an orange led, turns on when the board is connected to an external USB for battery recharging and it is directly controlled by the 5 V detection; a second led, red color, is connected to a GPIO of the MCU, thus programming it depending on the functionalities (e.g., blinking during advertising, codifying the states of the calibration process).

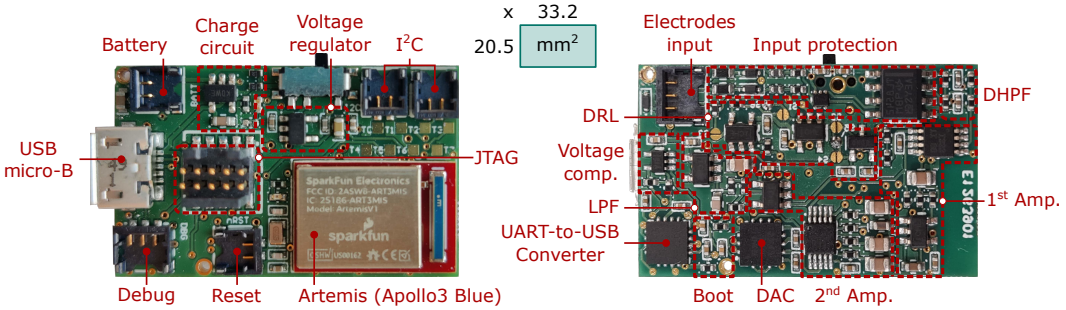

Fig. 3.2 Printed Circuit Board (PCB) of the proposed ATC-based wearable module: the electronic components has been organized in order to minimize overall PCB dimension, also taking advantage of the components distribution on both visible layers [60].

Figure 3.2 shows the manufactured and soldered prototype, which presents a final board size of 20.5 mm width $\times$ 33.2 mm length $\times$ 9.5 mm thickness (JTAG included).

3.2 3D-Printed Case Design

The complete wearable scenario has been finalized by designing the case for the board, also integrating all the additional tools including a rechargeable battery, two push buttons, and the electrode connectors.

Among the list of available rechargeable batteries with 3.7 V nominal voltage value, the ACCU-LP401230/CL [98] polymer lithium-ion battery has been selected because of its small size (4 mm $\times$ 12 mm $\times$ 30 mm), adequate nominal capacity of 110 mA h to suit the wearable application, and a sufficient number of rechargeable cycles.

The selected push buttons are the standard 6 mm $\times$ 6 mm area and 3.4 mm width typically used for breadboard applications. Their functionalities are strictly related to enable a manual control when the wireless interface does not respond as expected (e.g., triggering an hardware reset) or to implement an offline control of the device (e.g., future developments, codifying MCU routines on button press timings).

The connection with the sensor electrodes was aimed to be shorted as much as possible to reduce signal interference (e.g., power line, cable motion) at minimal. To accomplish this task, no electrode cables have been involved, thus coupling the connector of the male sensor directly with the female one, which will be placed proximal to the sEMG conditioning chain. In this way, the minimal electrode to AFE input distance follows the principles of the active probes (see Section 1.3.3), which, if properly achieved, allows the user to worn the device without too much concern about skin preparation.

Taking in mind the above aspects and design rules, the case has been designed using the SolidWorks CAD software [99] in order to draw custom geometries which can fit at better the assembling of all the components. Figures 3.3 and 3.4 show the realized sketch for the *Apollux* case and its transparent rendering highlighting the internal organization, respectively. Following a bottom-up description, the opening of the electrodes are designed on the bottom face, arranging the three electrodes in the sensing-reference-sensing line configuration, each one spaced 17.6 mm from the next one. Opportunely calibrating the external and internal diameters of the hole, the electrodes are kept in position by inserting their male tips inside the metal female

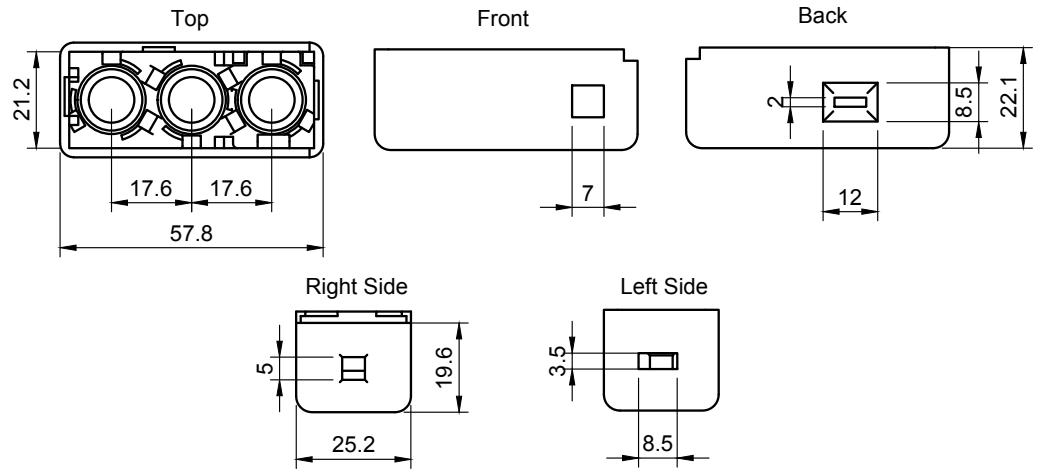

Fig. 3.3 Dimension of the designed case for *Apollux*. All the measures are expressed in mm.

connector (clip junction), placed into the box in correspondence of the punctures. The sockets are secured in position by designing three cogwheels (stopper), which are screwed in their blocking spot once the connectors are inserted. Then, the PCB can be placed on the top of the stoppers and maintained in the proper location thanks to combination of wall stops and the battery holder, which also assure the USB micro-b connector in axis with the relative opening. The minimal wires (<2 cm the longest one) connect the socket (soldering point) to the dedicated connector on the acquisition unit. Last, the push button and the battery are positioned inside the box, and the case is closed by means of a sliding cover. Thanks to the accessibility of the USB micro-b, the case does not require to be opened again during servicing

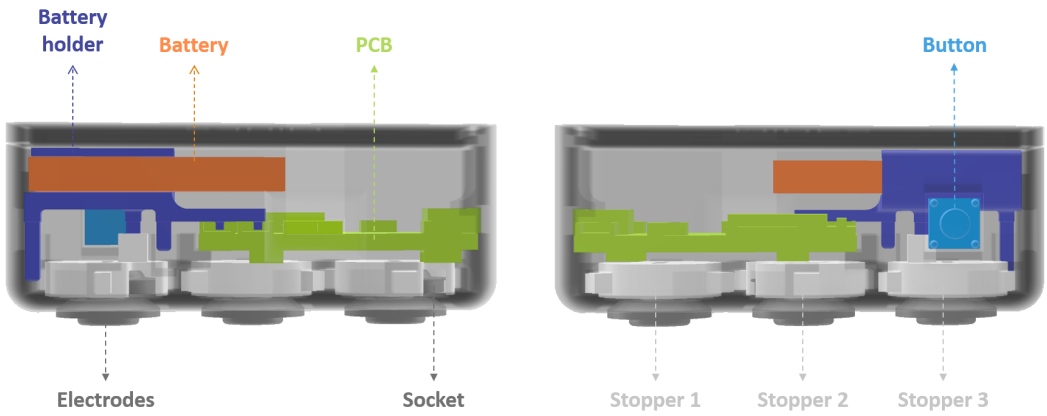

Fig. 3.4 Internal organization of the *Apollux* box.

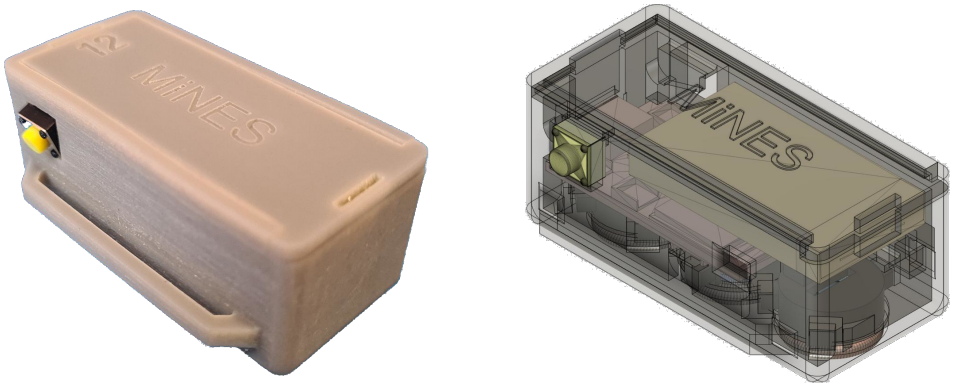

Fig. 3.5 *Apollux* case: **(left)** 3D printed and assembled prototype vs. **(right)** transparent rendering.

procedure (e.g., firmware flashing, battery recharging). Sticky electrodes permits the board to adhere to the body without any additional textile band; on the other hand, dry electrodes requires a string, secured by means of lateral wings, to correctly place the case in the proper location above the monitored muscle.

After the design, the case has been 3D printed using the ProJet MJP 2500 PLUS [100]. A photo of the final prototype (already assembled) is shown in Figure 3.5 (left), together with its 3D rendering (right) in order to visually assess their similarity. The device, i.e., *Apollux*, features an overall size of 57.8 mm length $\times$ 25.2 mm height $\times$ 22.1 mm width and a weight of 27.4 g.

3.3 *Apollux* Software

Ideally, although the sensing part of the prototype can be considered completed (the AFE and firmware are running at power-on, the device can be easily worn), the user needs to communicate with the acquisition board to start the signals recording and to set the available parameters (e.g., AFE gain, threshold for TC). A common and practical solution involves the use of a control software equipped with a Graphical User Interface (GUI) in way to display an easy communication terminal with the user (i.e., front-end) while hiding the functional algorithm's codes (i.e., back-end).

In this thesis, the control software has been developed in order to run on different machines: a laptop has been supposed as the standard device for running the interface, also considering the possibility to further process the acquired muscle data (using different software and providing sufficient computational resources); alternatively, an RPi machine can be a second-choice platform because it can be easily integrated in a portable device (e.g., tablet) which better fits outdoor or dynamic environments. Both these solutions have to provide the BLE connectivity to access the Apollux server. In the laptop case, a BLE USB-dongle external board has been preferred to the internal antenna because it allows a assisted accessibility to transceiver's settings, can be easily programmed as a peripheral device, and standardizes the wireless communication for different laptops, whose hardware and software specifications could differ. In particular, the CC2540 [101] (BLE stack 4.1 [72]) from Texas Instruments and the nRF52840 [78] (BLE stack 4.2 [73]) from Nordic Semiconductors are the two USB-dongles used as BLE receivers. On the other side, the internal transceiver can be used for the RPi since, once the RPi version (3B, 3B+, 4) has been selected, the hardware variability does not occur.

For the above reasons, the Python programming language (henceforth referred simply as Python) has been selected as multi-platform language (compatible with several Operating Systems (OSs)) which, in addition to its high versatility and third-part libraries availability, complies with the following software requirements:

- Scalability: as the number of employed acquisition units varies (e.g., from a single standalone module to a multi-channel recording setup), the software has to be able to fit different application scenarios by growing or shrinking the pieces of software to meet the changes in demands, while guaranteeing the real-time functionalities.

- Modularity: the software architecture has to be built of independent modules, each with its own tasks, able to interact with each other through properly developed Application Programming Interfaces (APIs). This is possible by following the Object-Oriented Programming (OOP) paradigm [102].
- Extensibility: the software has to be upgradable and maintainable over time to simplify future interventions for the addition of new functionalities or the updates of the current ones in case of operational variations. The proper fulfillment of this requirement closely depends on the compliance of the previous one, since the replacement of a system component (e.g., dongle BLE) would involve the modification of the respective module, adapting newest API to system architecture.
- Reliability: since the proposed system is intended for the data acquisition, the software needs to implement checks on received and transmitted data to avoid data corruption, minimizing the probability of errors and informing the user if problems arise.

In order to accomplish the OOP practice, the control software has been built on the interaction among three objects: the BLE, the Apollux and the GUI. The software intracommunication and its top-bottom architecture are depicted in Figure 3.6.

At the lowest layer there is the BLE object, which is directly interfaced with the antenna. Depending on which platform runs the software, the BLE module presents two possible implementations: it relies on the Pyserial module [103] if the BLE dongle is employed (application running on a laptop), while it uses the Bluepy library [104] (which is based on BlueZ [105], the official GNU/Linux Bluetooth stack) when the RPi antenna is utilized. Both implementations include the same attributes and methods (with some marginal differences) to achieve the BLE functionalities. Among them, the main ones include the scan for advertising devices, the establishment of the connection with them, and the exchange of data through client/server requests or notifications.

The Apollux object is a complete custom module which implements all the functionalities of its homonymous device. It represents the mid-layer among the BLE module and GUI, and acts as a bidirectional packet builder or extractor among these two levels. Since a lot of acquisition boards can be connected concurrently, an

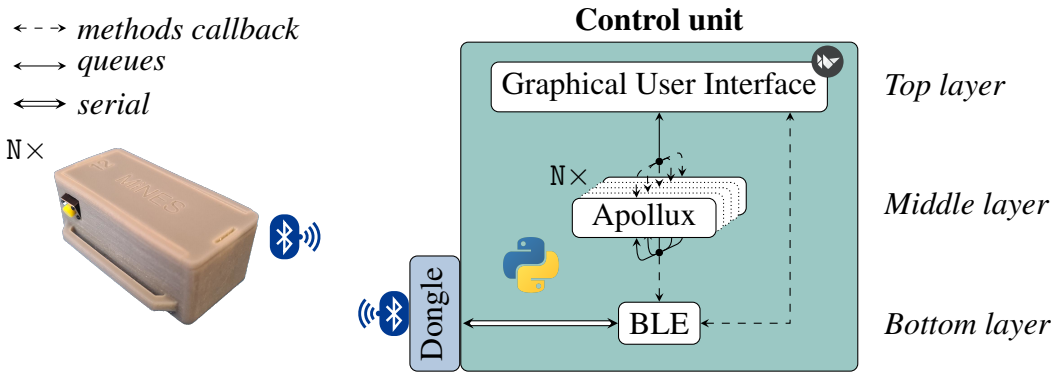

Fig. 3.6 Software layers for Apollux system following the OOP paradigm.

Apollux object is instantiated for each working device, thus obtaining a parallel-level set of objects.

Last, the GUI object has been realized using the Kivy Python-compatible framework [106] due to its light and original multi-screen feature. Since the GUI is the layer directly interfaced with the user, it has been equipped with *ad-hoc* widgets, e.g., buttons, graph, popup, spinners.

All the direct top-down functions are triggered by method callbacks, while the internal bottom-up data communication are based on queues. Indeed, each layer features one or multiple queues depending on type of data to be transmitted and on the addressee, in order to obtain a stratified and organized data flow control. In particular, the BLE module dispatches the packets received from the *Apollux* boards by putting the payload into the appropriate Apollux queue (among the ones available), and by labeling the content accordingly to the nature of the message. At the mid-layer, the Apollux object checks the queue with the BLE, gets the data and route them to internal methods for further processing (e.g., checking the board's status) or directly to the GUI (ATC or sEMG values to be displayed). At this point, since all the relevant data are ready to be used, the GUI object plots and/or stores them.

A capture of the resulting GUI is shown in Fig. 3.7. The operational flow for running the application can be summarized as follows:

1. Clicking on the *Connect* button a BLE scan is launched for the *Apollux* devices (using a white-list), which returns the information of the ones advertising.

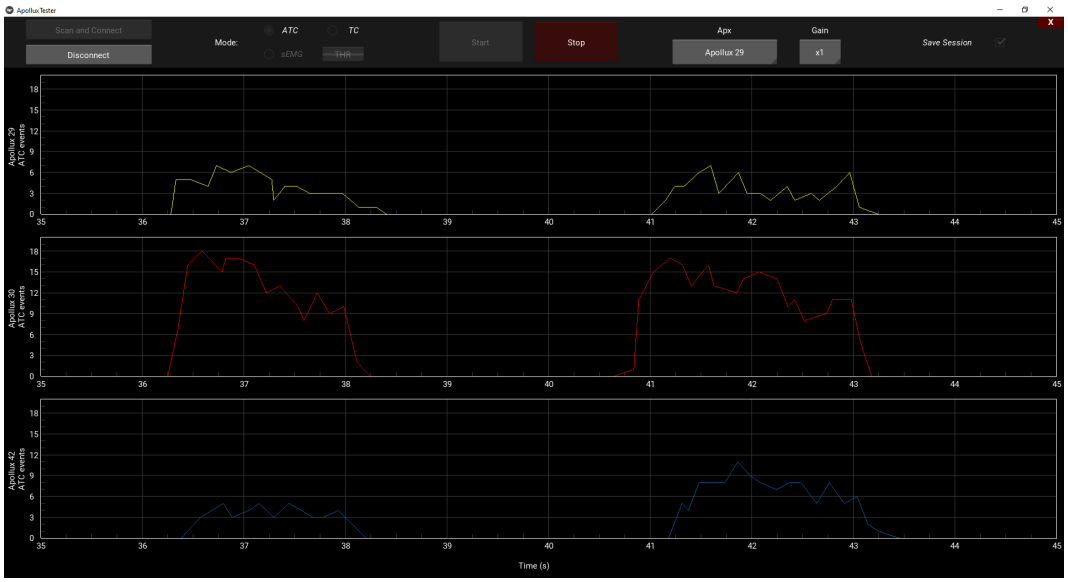

Fig. 3.7 Graphical User Interface (GUI) to control the functionalities of the *Apollux* devices.

A popup allows the user to select the devices s/he wants to connect and establishes the link with them. A graph for each working device is instantiated to plot the data run-time;

2. Selection of the operation mode: if the ATC mode is chosen, the system will acquire the ATC data from all the connected devices; on the other hand, one channel per time can be acquired in the sEMG mode (BLE limitations related to the 4.1/4.2 protocol stacks [72, 73] implemented by the receiving USB-dongle);

3. The gain of each *Apollux*'s AFE can be adjusted proportional to the amplitude of the signal by using the specific spinners;

4. The acquisition is launched and terminated by pressing the start or stop button. During it, the data are plotted on the graphs, constantly refreshing the value ticks of the axis to better represents the dynamics of the signals. In the ATC mode, the threshold calibration process is triggered and executed just before the request for ATC notifications;

5. All the acquired data can be saved on .txt files, one for each connected board, if the *Save Session* checkbox is active. The files are organized into sessions folders, within each one every document reports the timestamps and values

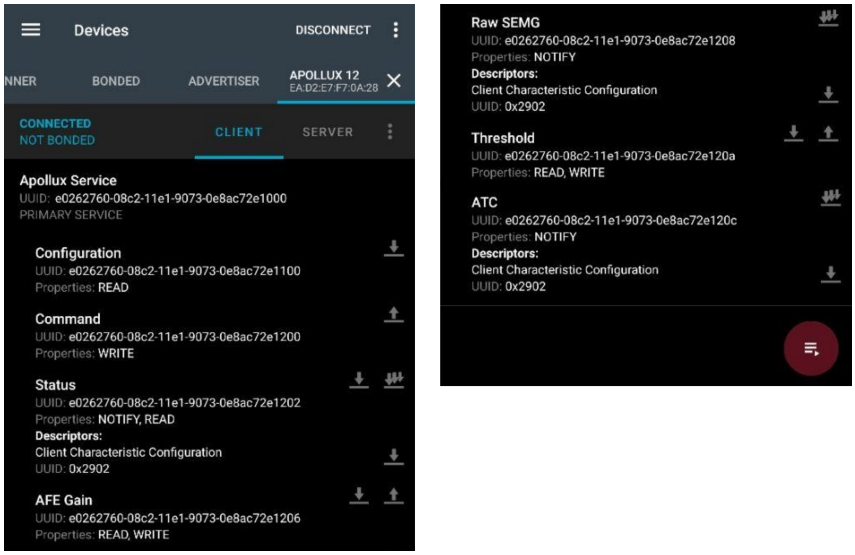

Fig. 3.8 Apollux server nRF connect smartphone application.

(with data tab-delimitation and newline at the end of each row) streamed by an *Apollux*;

6. The system is disconnected by terminating all the existing BLE links, and the GUI can be closed.

As the last point, if the laptop (or another platform running the software) is not available, still the *Apollux* board can be connected to the personal smartphone. Indeed, by using the free nRF Connect application [107], the Apollux server remains accessible (see Figure 3.8) and the configuration and acquisition commands could be handled by interacting with it. The application provides a log file for storing (user selectable) notification packets, which could be subsequently read and interpret by a custom script on the laptop. This possibility further extends the system applicability to outside and not standard scenarios (e.g., running in the park), also fulfilling the (software and firmware) possibility to achieve long-term acquisition (e.g., a walk of several hours).

3.4 Running Application

Figure 3.9a and Figure 3.9b qualitatively show how the *Apollux* system can be employed to monitor both static contractions (e.g., isometric) and dynamic movements (human gait). In order to give an example of the functionalities of the system, both an sEMG acquisition and an ATC extraction has been reported, also graphically demonstrating the multi-channel setup (Figure 3.9b). As described in the above Sections, minimal hardware and software configurations are needed to run the system: after inserting the dongle (e.g., nRF52840) in the laptop, the user can run the .exe file and, once the *Apollux* are worn (simply attaching the electrodes to their connectors, and then positioning the boards on the muscles), through few clicks the recording session begins.

(a) Static contraction.

(b) Dynamic contraction.

Fig. 3.9 (**Top**) Example of sEMG acquisition (high resolution) during an isometric contraction of the *biceps brachii*, standardized by using a 4 kg weight. (**Bottom**) Example of the *Apollux* use during a simulated human gait monitoring: the two ATC envelopes are acquired in real-time from the *gastrocnemio medialis* and *soleus* muscles and graphically represented on a user interface.

Chapter 4

Apollux - Testing Performance

[1] After the complete integration of the HW, FW and SW functionalities of the prototype, an experimental phase has been designed to examine the functional behavior of the developed device evaluating different aspects. Indeed, the tests have been conducted in order to analyze the performance of the system for the following points:

- sEMG signal quality: the correctness of the sEMG data representation is assessed by checking the frequency response of the analog channel w.r.t. the design theory, the reliability of the frequency content of the muscle signal, and the proper discrimination of the useful signal from the background noise sources;
- ATC extraction: firstly, the frequency response of the AFE channel is studied also for the TC signal; then, the correlation between sustained weights and the ATC values have been confirmed;
- Reliability analysis: a comparison study with a *gold standard* device is carried out to evaluate the consistency of the developed prototype with state of the art devices;

[1] Disclaimer: This Chapter contains some parts and arguments taken or (partially) rephrased of the following published work:

- **F. Rossi**, A. Mongardi, P. Motto Ros, M. Ruo Roch, M. Martina and D. Demarchi, "Tutorial: A Versatile Bio-Inspired System for Processing and Transmission of Muscular Information," in *IEEE Sensors Journal*, vol. 21, no. 20, pp. 22285-22303, 15 Oct.15, 2021, doi: 10.1109/JSEN.2021.3103608.

- Power consumption: this analysis has been performed to point out the maximum operating time of the designed sEMG sensing node depending on the working mode, thus giving to the user/reader an idea of the application limitation.

All the experiments reported in the following sections, concerning human subjects, have been presented to and approved by the Comitato Bioetico di Ateneo of the University of Turin [108] (experimental codes: 445136 and 445154).

After the presentation of the experimental results, the last section reports a final comparison between the *Apollux* device and the current academic and industrial (i.e., the ones already introduce in Section 1.4) solutions, highlighting the similarity and advantages of the proposed design and discussing its applicability in the sEMG scenario.

4.1 sEMG quality

Considering the ATC as the main parameter extracted from the sEMG signal, its reliability strictly depends on the integrity of detected muscle information. Therefore, different tests have been planned to evaluate if the AFE had been designed correctly.

First, the response of the filters chain to the input signals have been analyzed, thus verifying the proper band-pass behavior in the 70 Hz to 400 Hz range. By using a National Instruments data acquisition system (i.e., NI USB-6259 [109]), a LabVIEW script has been implemented to provide two sine waves with different amplitudes (i.e., 2 mV peak-to-peak difference), at varying frequency (10 Hz to 1000 Hz, 1 Hz step), as channel inputs and, consequently, to record the filtered and amplified output signals. In Figure 4.1 (blue line), the amplitude ratio (dB) between the AFE output and the one obtained by digital-mathematical processing (theoretical differential flat-band amplification) the *real* (analog) input signals is reported using a frequency semi-log plot: by imposing −3 dB as the acceptability criteria for real/theoretical difference, the sEMG conditioning circuit demonstrates to work as expected in the

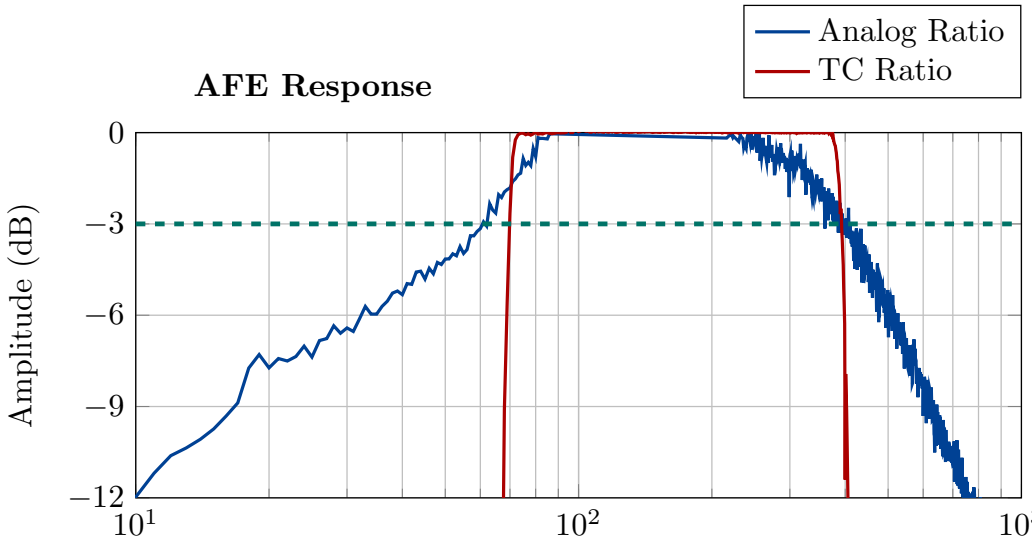

Fig. 4.1 The graph shows the results of two different characterization analyses for *Apollux* AFE in the 10 Hz to 1000 Hz frequency range. The first one (blue line) represents the dB ratio between the analog (sEMG) output of the AFE and the theoretical flat-band amplification of its inputs (Section 4.1). A similar analysis (Section 4.2) has been carried out for the analog and simulated TC signal (red line). These measurements confirmed the expected filtering behavior into the 70 Hz to 400 Hz band [60].

70 Hz to 400 Hz range, which verifies the DHPF-InAmp feedback combination and anti-aliasing LPF behaviors for low and high spectrum frequencies, respectively.

After checking the response of the AFE, the next analysis concerns if the designed circuitry properly conditions the acquired muscle signal. The sEMG signals have been acquired during the wrist extension movement, placing the sensing electrodes on the *extensor carpi ulnaris* muscle. The motion executions have been standardized

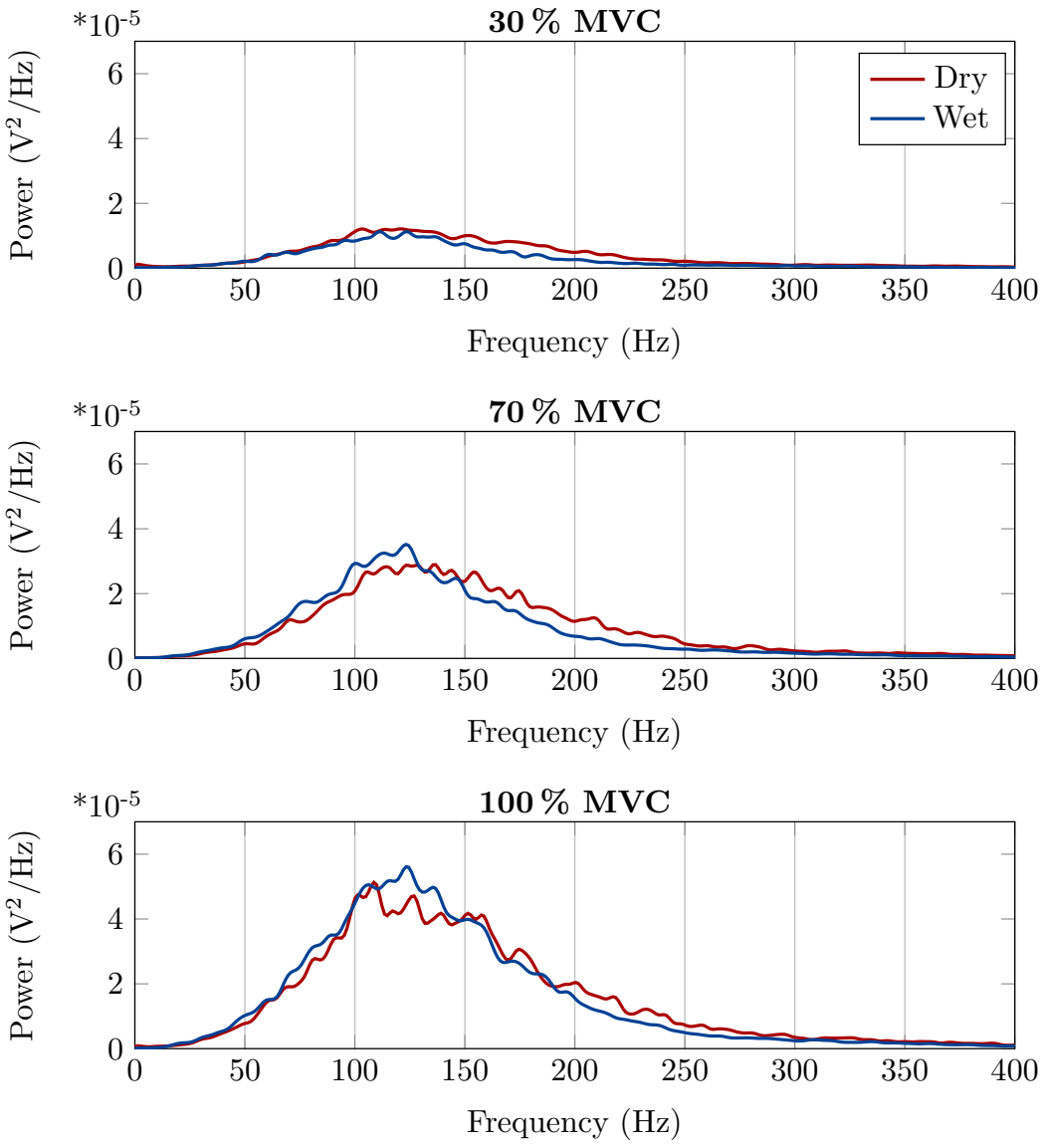

Fig. 4.2 Comparison among the Power Spectral Density (PSD) of dry and wet electrodes, standardizing the three levels of muscle activation over the Maximum Voluntary Contraction (MVC) (30 % MVC, 70 % MVC, and 100 % MVC) [60].

by measuring the Maximum Voluntary Contraction (MVC) with a dynamometer in order to observe how the sampled sEMG adequately represents muscular efforts at 30 % MVC, 70 % MVC, and 100 % MVC values. Both dry [110] and wet [111] electrodes have been compared looking at the Power Spectral Density (PSD) features (see Figure 4.2), demonstrating how they could be interchangeable in monitoring different levels of muscle contractions. As expected, the total sEMG energy increases with the raise of MVC, also satisfactory representing the typical frequencies of the sEMG spectrum [23], as it can be noticed in the 50 Hz-150 Hz interval. The calculated PSDs show no influences related to the power-line interference (neither at the 50 Hz central frequency nor at higher harmonics), proving the proper design of the physical circuit (e.g., high accuracy of components selection and PCB layout) and the effectiveness of the AFE filters. However, although dry electrodes present a major noise content above 200 Hz w.r.t wet electrodes, mainly caused by a more unstable skin-electrode interface, both acquisition setups bring to similar results, demonstrating the system versatility without the need of any adaptations to the sensors technology.

Then, a more detailed analysis has been carried out by acquiring the sEMG signals during the execution of different movements in order to evaluate how the *Apollux* performs on both upper and lower limb muscles. The elbow flexion, knee extension and flexion movements have been executed, inducing isometric contractions by employing a set of weights (0 kg, 1 kg, 2 kg, 4 kg). The acquisition protocol, whose biomedical setup is described in Table 4.1, consists of ten repetitions for each movement. A total of 10 s of sEMG signal are acquired after the stabilization of the weight, interrupted by 30 s resting time to avoid the onset of fatigue effects. Signal-to-Noise Ratio (SNR) between the squared powers of the sEMG (P_{sEMG}) and the noise (P_{noise}, here intended as the signal baseline without muscle activity) has been identified as the proper comparison parameter and calculated according to Eq. 4.1, where both powers have been estimated through the variance (σ^2) of both signal and noise.

$$SNR = 10 \cdot \log_{10}\left(\frac{P_{sEMG}}{P_{noise}}\right) = 10 \cdot \log_{10}\left(\frac{\sigma^2_{signal} - \sigma^2_{noise}}{\sigma^2_{noise}}\right) \tag{4.1}$$

Figure 4.3 reports the measurements, where all the exercise repetitions of each monitored muscle are grouped: SNR values increase together with sustained weights

Table 4.1 Monitored muscles and related executable movements [60]

Muscle	**ID**	**Movements**	**Sensors Location**[1]
Biceps brachii	BB	Elbow Flexion	On the line between the medial acromion and the fossa cubit at 1/3 from the fossa cubit
Triceps brachii	TB	Elbow Extension	At 50 % on the line between the posterior crista of the acromion and the olecranon at 2 finger widths medial to the line
Extensor carpi ulnaris	ECU	Wrist Extension	At 10 % of the line from the medial epicondyle of the humerus to the ulnar styloid process
Rectus femoris	RF	Gait, Knee Extension	At 50 % on the line from the anterior spina iliaca superior to the superior part of the patella
Vastus lateralis	VL	Gait	At 2/3 on the line from the anterior spina iliaca superior to the lateral side of the patella
Biceps femoris	BF	Gait, Knee Flexion	At 50 % on the line between the ischial tuberosity and the lateral epicondyle of the tibia
Tibialis anterior	TA	Gait	At 1/3 on the line between the tip of the fibula and the tip of the medial malleolus
Gastrocnemio medialis	GM	Gait	On the most prominent bulge of the muscle
Soleus	SL	Gait	At 2/3 of the line between the medial condylis of the femur to the medial malleolus

[1]SENIAM guidelines [51] have been followed for electrode placement

resulting in similar outcomes for both wet and dry electrodes, while differences of 5 % to 20 % are clearly visible considering activity of the DRL circuit, hence demonstrating its advantages if configured. An SNR of 15 dB (dashed green line in the box plots) has been identified as a proper threshold to obtain an sEMG signal of a quality more than acceptable [112]: all the performed measurements here reported (if described using the median statistical value) largely meet this requirement.

Lastly, the *Apollux* device has been tested during the monitoring of dynamic movements, acquiring the sEMG signals from distal and proximal leg muscles (as reported in Table 4.1) during straight human walk. Although this experimental condition could be challenging w.r.t. the static muscle analysis, both in terms of signal artifacts and muscular activity, very satisfactory SNR results have been obtained (Figure 4.4). The box plots, which group together about 20 steps, demonstrate how

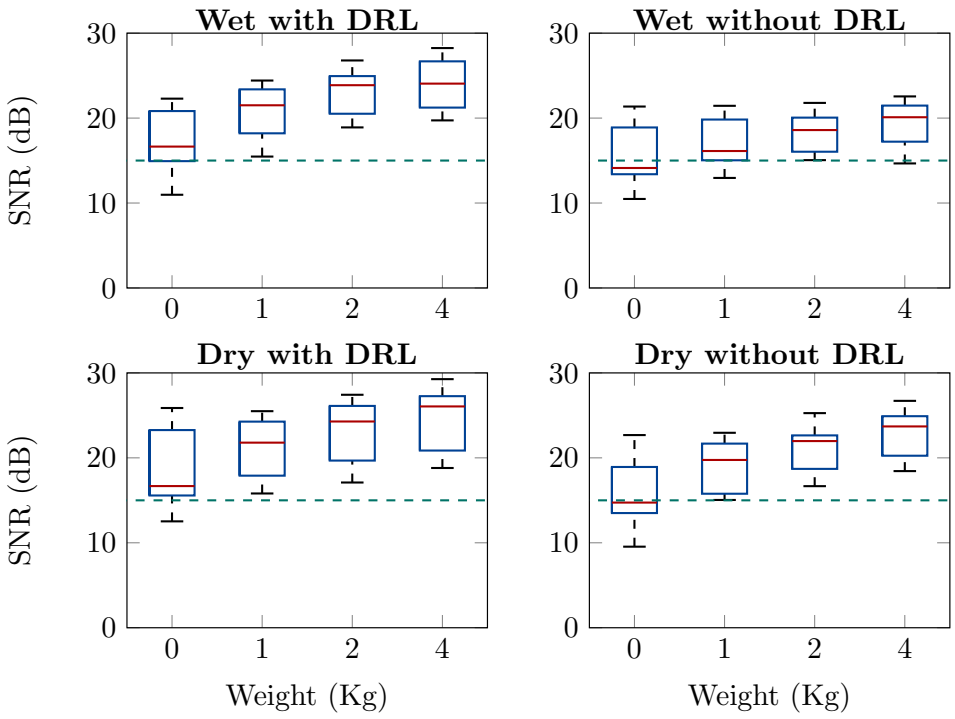

Fig. 4.3 SNR comparison between wet and dry electrodes, also evaluating the influence of the DRL circuit to drive the reference potential [60].

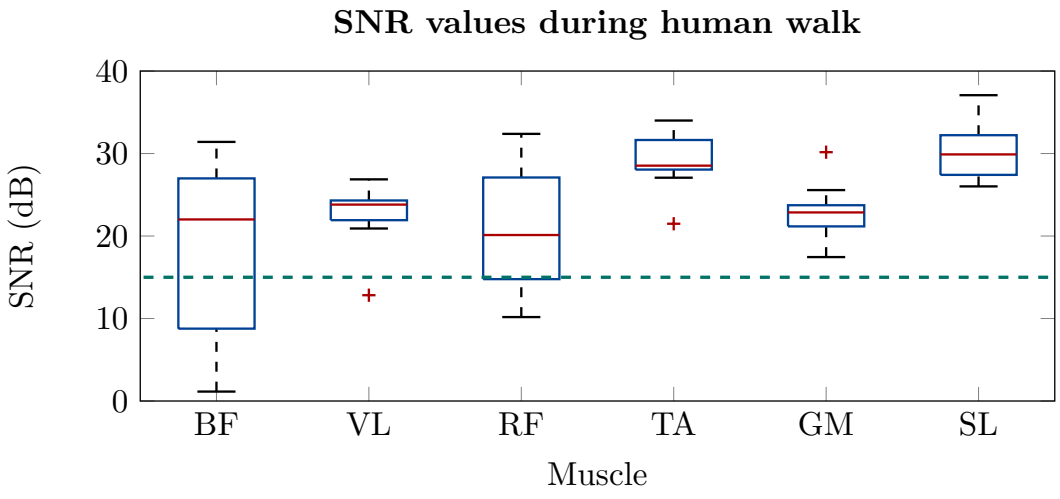

Fig. 4.4 SNR distribution of the detected sEMG signals in dynamic contractions during human walk. The following multi-muscle acquisition setup has been observed: BF - Biceps Femoris, VL - Vastus Lateralis, RF - Rectus Femoris, TA - Tibialis Anterior, GM - Gastrocnemio Medialis, SL - Soleus [60].

the system performs well in real application scenario, fulfilling again the 15 dB acceptability threshold. Boxplots width could vary depending on considered muscle because of its time-varying and multi-function activity in balancing body during straight walk. However, these outcomes verify the appropriate detection of sEMG signals, without compromising the quality of the acquired data, also with minimal muscle activity.

To summarize, these simulative and practical tests confirmed the proper acquisition of the sEMG signal (both in static and dynamic conditions), proving the AFE versatility w.r.t. the electrodes typology and the voltage reference configuration depending on the application requirements.

4.2 ATC Extraction

In order to prove the correctness of the hardware TC extraction, two different tests, both involving the NI USB-6259 acquisition system as the digital interface, have been performed.

First, the TC output signal has been analyzed using a setup similar to the one of the first sEMG response test. In fact, a LabVIEW environment has been configured to generate the two input sine waves, performing the frequency sweep from 10 Hz to 1000 Hz, and to collect the TC signal from the board. Then, TC events are counted over a 130 ms time window and compared with the theoretical ones, simulated without filtering. The obtained ratio (in dB), represented with the red line of Fig. 4.1, confirms the proper design of the 70 Hz to 400 Hz band-pass filter.

After this simulated analysis, in order to prove the correct behavior of the threshold comparator, both the sEMG and TC signals have been sampled simultaneously, monitoring the static response of *biceps brachii* at the already standardized set of weights (i.e., 0 kg, 1 kg, 2 kg and 4 kg). The sEMG data are then processed in order to compute the threshold crossings, simulating the experimental method and threshold value (also taking into account the hysteresis behavior). Figure 4.5 shows both the normalized cross-correlation coefficient (ρ) between HW and simulated TC signals (left) and the proportional growth of the HW generated TC events when the sustained load increases (right). The growth of TC events validates the direct load proportion-

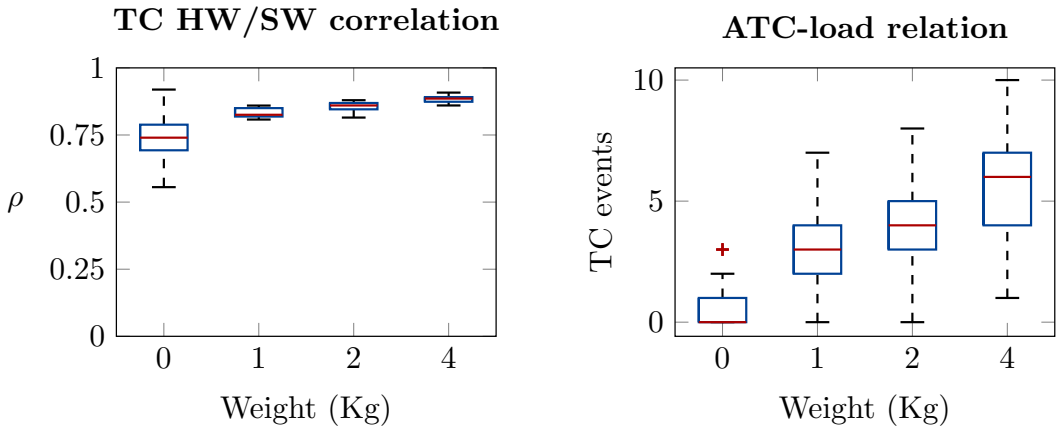

Fig. 4.5 TC hardware analysis: (left) cross-correlation with software simulation; (right) validation of direct proportionality with sustained load [60].

ality established in [65] and the good correlation w.r.t. the software simulated signal demonstrates the optimal design of the hardware threshold comparator.

4.3 Reliability Analysis

System reliability has been assessed by comparing the Root Mean Square (RMS) of the sEMG obtained with the *Apollux* device to the one acquired with the Cometa Mini Wave [17] wearable system, which can be identified as a SoA gold standard in the sEMG field. In particular, among different indexes present in literature, the Intraclass Correlation Coefficient (ICC) [113] has been selected as the appropriate indicator to evaluate the robustness of the measures, because it is not influenced by the order of the analyzed samples.

The experimental setup involved a dynamometer to measure stable MVC values, similarly to what has been done in Section 4.1, when comparing wet and dry electrodes. However, in this test, a set of four movements (elbow flexion, elbow extension, knee flexion, and knee extension) was selected to cover different typologies of muscular activity, which are acquired following the guidelines of Table 4.1. For each movement, three subjects exerted their MVC in an isotonic position; then, they performed 10 isotonic repetitions at 70 % MVC and 10 at 30 % MVC, with each repetition consisting in 10 s of activation and 30 s of rest. The same experimental protocol was executed both using the *Apollux* device and with the Cometa Mini Wave, in different sessions.

Muscular data were then processed offline to obtain the RMS indicator for each single repetition, in order to proceed with the reliability analysis itself. Considering that the Cometa device and the *Apollux* system have a different acquisition interface (i.e., the Mini Wave has only two electrodes), making a comparison between their respective values would not have been significant, but an intra-rater analysis has been performed to compare how both of them behaved along time. Since the different movements, or contraction levels, are not correlated, the model 1 of the ICC, as suggested in [114], which analyzes the variability of values obtained from different repetitions of the same class (i.e., one combination of person, force and movement), has been selected. The formula is reported in Eq. 4.2, where MS_R represents the mean square for the row, intended as the ten repetitions, k is the number of repetitions (i.e., 10), and MS_W is the mean square for residual sources of variance.

$$ICC(1,k) = \frac{MS_R - MS_W}{MS_R + (k-1)MS_W} \tag{4.2}$$

While the Cometa Mini Wave scored an ICC of 0.881, the *Apollux* device had a more robust behavior over the different trials reaching a score of 0.934, demonstrating that its reliability is consistent w.r.t. state of the art.

4.4 Power Consumption

Operational device lifetime is a crucial feature for wearable system which needs to continuously record data providing a stable streaming. Among various HW and SW optimizations (e.g., ultra-low power components for the AFE design, MCU hardware and firmware performance), the current absorption during ATC and sEMG data transmission has been minimized as much as possible by handling the BLE adjustable parameters (also considering the relevant transmission power levels), while guaranteeing real-time data accessibility. Keeping in mind the protocol constraints, and considering what reported in Section 2.3.2, variable connection intervals of 12.5 ms to 50 ms and 60 ms to 80 ms have been set in order to successfully achieve sEMG and ATC notifications transmission, respectively.

Table 4.2 reports the power measurements, representing the mean current absorption (acquired using the DMM7510 digital multimeter [115], with a sampling frequency of 1 Msample/s) for the three available services (i.e., sEMG at Low Resolution (LR), sEMG at High Resolution (HR), and ATC) and the five configurable TX powers (i.e., −20 dBm, −10 dBm, −5 dBm, 0 dBm, 4 dBm). While HR mode is configured for last Bluetooth versions (4.2, 5.0), which, thanks to MTU extension,

Table 4.2 Energy-efficiency comparison between sEMG and ATC modes [60]

	Mode		**TX Power (dBm)**				
			-20	**-10**	**-5**	**0**	**4**
Current Absorption (mA)	sEMG	HR	1.29	1.31	1.30	1.35	1.40
		LR	2.32	2.32	2.35	2.32	2.42
	ATC[1]		0.46	0.46	0.45	0.46	0.48
Operating Time[2] (hours)	sEMG	HR	85	84	85	82	79
		LR	47	48	47	48	46
	ATC[1]		237	238	246	240	231
Energy saved (%)		HR	64.1	64.5	65.5	66.0	66.0
		LR	80.0	80.0	81.1	80.2	80.3

[1] ATC window: 130 ms

[2] 110 mAh LiPo battery

allows a relaxation of the connection interval (i.e., set to 50 ms), the LR service is designed for back-compatibility with older versions (4.0, 4.1) and requires more strict parameters to keep up with real time application constraints (i.e., connection interval is set to 12.5 ms and sampling frequency is lowered to 800 Hz). Thus, even if the application throughput of LR mode is slightly lower, its shorter connection interval considerably decreases idle periods, increasing the overall current absorption.

On the other hand, ATC data reduction (i.e., ~90 %, considering Bluetooth overhead [74]) and further relaxation of the connectivity timing (i.e., 60 ms to 80 ms connection interval) allow to save up to 80 % of required sEMG energy budget, thus leading to about 230 h of constant active transmission (considering the selected LP401230 Cellevia LiPo battery with 110 mAh capacity [98]), perfectly suitable for long-time monitoring applications.

4.5 Comparison with SoA works

This final section aims to compare the proposed device looking at similar ones, trying to consider both academic and industrial solutions. A comprehensive comparison could be outlined by watching over the application scenario: if from one side commercial devices [58, 17–19] are optimized aspiring to provide a satisfying user-experience, but often concealing some technical details from public information, on the other side research activities [20–22, 28, 29] provide well-documented analyses, discussing in details the tuning of the leading system parameters, but leaving the door open to further investigations (no final market-oriented optimization). However, keeping in mind the above disparity, some considerations could be discussed (see Table 4.3) for recent (2018–2021) State-of-Art (SoA) devices.

Since the effectiveness of the *Apollux* solution in sensing the sEMG signals and in extracting the TC (or ATC) information has already been demonstrated, here the comparison points directly to the triplet of size, weight, and operating time features of the device. Their combination perfectly describes the applicability of each system, representing which specifications have been selected in the design phase (e.g., extracted feature, number of sensing channels) and how they have been technically satisfied (e.g., wireless requirements, power consumption).

Therefore, proceeding from the design of the system towards its realization, the prerequisites for the *Apollux* could be summarized into a stand-alone (single-channel) module for the sEMG/ATC transmission, whose identified and optimized application throughput allowed the ideal employment of the BLE 4.2 wireless technology [73]. Some of the listed SoA works [58, 17, 22, 28, 29] show similar application throughput values (per acquisition channel), demonstrating the validity of this design concept, some of them using the BLE 4.2 [19] protocol as in this solution, and other ones implementing (although not always necessary) more power-consuming solutions such as BlueTooth (BT) 2.0 [20] or WiFi [28, 29].

Combining the sEMG acquisition setting (e.g., sampling rate, ADC resolution), and the feature extraction process (i.e., ATC), with the wireless configuration (e.g., protocol, transmission parameters), some differences in terms of power consumption can be highlighted: by completely exploiting the advantages of the ATC approach in reducing the transmission data rate (i.e., 64 bps), and lowering the power supply of the overall on-board circuitry to 1.8 V, an average current absorption under 1 mA

Table 4.3 State of the art comparison among wearable sEMG acquisition systems [60]

Device	year	f	ch.	a.t. (kbps)	wireless	p.s. (V)	c.a. (mA)	battery (mA h)	size (cm^3)	weight (g)	o.t. (h)
[58]	2021	sEMG	1	32	IEEE 802.15.4	n.a.	n.a.	n.a.	17.4	13	6
[17]	2021	sEMG	1	32	n.a.	n.a.	n.a.	n.a.	5	7	12
[18]	2021	sEMG	1	n.a.	WiFi	n.a.	n.a.	n.a.	14.1	17	8
[19]	2021	sEMG	1	n.a.	Custom RF BLE 4.2	n.a.	n.a.	n.a.	13.0	14	8
[20]	2021	sEMG	4	n.a.	BT 2.0	n.a.	46	700	78.2	140	15
[21]	2019	sEMG	32	1040	WiFi	3.3	119	600	15.3	16.7	5
[22]	2021	sEMG	8	384	BLE 5.0	5	105	600	22.0	41.7	5
[28]	2018	sEMG	8	192	WiFi	3	n.a.	700	n.a.	n.a.	n.a.
[29]	2020	sEMG	1	32	WiFi	n.a.	n.a.	300	n.a.	n.a.	n.a.
This Thesis	2021	sEMG ATC	1	16 0.064	BLE 4.2	1.8	1.40 0.48	110	32.2	27.4	80 231

f - control feature, ch. - number of channel, a.t. - application throughput, p.s. - power supply
c.a. - current absorption, o.t. - operating time

was measured during continuous data transmission, making this designed solution quite appealing with respect to other devices [20–22].

The above considerations led to the definition of the *Apollux* prototype properties: with a minimal battery capacity of 110 mAh, the complete case for the device has been realized by containing the whole volume to 32.2 cm^3 (including bio-potential electrodes, mounted at the bottom side, as represented in Fig. 3.5) and a total weight of 27.4 g. Both fall within the average of those found in the various works reported in Table 4.3, identifying this solution compatible with current SoA wearable sEMG devices.

Lastly, since the proposed solution has been developed aiming to overcome the functional timing limitations, a final comparison about the working operating time needs to be discussed: all selected SoA works show a total duration of at least 15 h, even practically lowered to 5 h or 8 h, which adequately fits the time-requirements of clinical procedures but does not allow to achieve a constant monitoring for daily-life activities (e.g., up to 24 h to 48 h). In contrast, the different optimizations disclosed in this thesis enabled a steady sEMG transmission of 80 h, or, additionally benefiting from the ATC approach, to cover an event-driven acquisition of a week.

In conclusion, looking at Table 4.3 in its entirety, it can be observed how the proposed device fits harmoniously into this application scenario, adequately withstanding current academic or industrial solutions [17–19, 21] while providing satisfactory improvements in terms of total operating time.

After the design, prototyping, and validation of the *Apollux* board, next chapters will focus on its use in biomedical applications. In particular, Chapter 5 describes how to achieve the active control of the Functional Electrical Stimulation starting from the ATC information, while Chapter 6 reports the development of an Human-Machine Interface (HMI) based on hand gesture recognition.

Chapter 5

Application - Control of Functional Electrical Stimulation

[1] Muscle paralysis is a condition able to gravely compromise the quality of life. This illness induces several limitations to the self-sufficiency, social integration, and might cause psychological discomfort [116, 117]. The leading causes of paralysis are stroke, spinal cord injury, and multiple sclerosis [118]. These neurological deficits afflict the nervous system by inhibiting the ability of the brain to generate motor commands [119] or by compromising the neural pathway to the muscles [120, 121].

[1] Disclaimer: This Chapter contains some parts and arguments taken or (partially) rephrased of the following published works:

- **F. Rossi**, P. Motto Ros, S. Cecchini, A. Crema, S. Micera and D. Demarchi, "An Event-Driven Closed-Loop System for Real-Time FES Control," *2019 26th IEEE International Conference on Electronics, Circuits and Systems (ICECS)*, 2019, pp. 867-870, doi: 10.1109/ICECS46596.2019.8965153.
- **F. Rossi**, P. Motto Ros, R. M. Rosales, and D. Demarchi, "Embedded Bio-Mimetic System for Functional Electrical Stimulation Controlled by Event-Driven sEMG" *Sensors* , 20, no. 5: 1535, 2020, doi: 10.3390/s20051535.
- A. Prestia, **F. Rossi**, A. Mongardi, P. Motto Ros, M. Ruo Roch, M. Martina and D. Demarchi, "Motion Analysis for Experimental Evaluation of an Event-Driven FES System," in *IEEE Transactions on Biomedical Circuits and Systems*, vol. 16, no. 1, pp. 3-14, Feb. 2022, doi: 10.1109/TBCAS.2021.3137027..
- A. Prestia, **F. Rossi**, A. Mongardi, D. Demarchi and P. Motto Ros "Raspberry Pi based Modular System for Multichannel Event-Driven Functional Electrical Stimulation Control," *2022 44th Annual International Conference of the IEEE Engineering in Medicine and Biology Society (EMBC)*, 2022, pp. 2592-2597, doi: 10.1109/EMBC48229.2022.9871852.

If the neurons innervating the skeletal muscles, together with the articular joints, are still functional, the contraction of the myofibers can be induced through Functional Electrical Stimulation (FES) [122]. FES consists in applying low energy pulses to the axons of motor neurons for generation of the action potentials [122]. The primary aim of the FES therapy is to restore the movements functionalities, but also to improve blood circulation and prevent muscle atrophy due to disuse [123].

Different strategies can be employed to control FES, either by triggering the stimulation, or by modulating the energy of the stimulation pulses [124, 125]. If the control aims to be at a central level, the ElectroEncephaloGraphy (EEG) can be used by integrating FES into a Brain-Computer Interface (BCI) and exploiting approaches such as Motor Imagery (MI) [126] or Action Observation Treatment (AOT) [127]. Alternatively, focusing on the control at the peripheral level, surface ElectroMyoGraphy (sEMG) could be employed to build a Human-Machine Interface (HMI) [11] thanks to its widespread adoption in monitoring the activity of the skeletal muscle inherent to both the diagnostics and prosthetic fields [128, 129].

Among the mentioned techniques, this thesis points to an sEMG-FES system because of the advantages related to the source-actuation signal dependency and the application practicability of the solution. Indeed, in an sEMG-controlled-FES system the muscle fibers are directly activated by the processing of the information obtained by muscular activation itself, thus avoiding more complex feature extraction process (e.g., time-frequency analysis or wavelet decomposition from EEG [130]). Moreover, similar to FES, sEMG works with surface electrodes easily placed on the muscle belly, allowing the overall system to be completely non-invasive and fast to set up.

From the application point of view, typical scenario consists in the reproduction of functional movements between two subjects in the therapist-patient rehabilitation context. The muscular activity monitored from an healthy subject (therapist), e.g., doctor, physiotherapist, during the execution of a movement, is processed in order to define the FES pattern to be applied to a second subject (patient) in order to induce the replication of the same movement [131]. Alternatively, the muscles from which the sEMG signals are acquired can be contralateral of the stimulated ones (controller and the controllee are the same subject), achieving a self-stimulation configuration, known as Contralaterally Controlled FES (CCFES) [124], which is constantly

growing its interest for the therapeutic management of hemiplegia and hemiparesis. Moreover, the efficacy of the therapist-controlled FES approach could be further improved by allowing the patient to see the therapist during the movement execution. Indeed, as in AOT rehabilitation protocols, the involvement of mirror neurons, which fire during the observation of an action, promotes the neural plasticity [132, 133].

Looking at the recent state-of-the-art, sEMG parameters such as the signal envelope [134–136] or its entropy [137] are typically used to define the stimulation pattern. Further approaches involve extracting multiple time-domain features (e.g., mean absolute value, zero-crossing, number of slope sign changes) to feed a machine learning algorithm for FES parameters modulation [138, 139]. However, the features processing usually requires the full recording of the sEMG signal, followed by software or firmware extraction techniques, requesting together both computational capabilities and processing times which does not always fulfill the real-time FES control requirements [140].

Finding a way to relax these computations, this thesis proposes to employ the developed *Apollux* boards as the sensing units, which, exploiting the demonstrated benefits of the event-based approach, aims to use the ATC parameter (an sEMG feature already extracted on-board) to define the most suitable FES pattern.

Next sections will firstly describe the architecture of the proposed ATC-controlled FES system, then moving to the analyses of the control platform performances (e.g., real-time behavior, safety of the stimulation) and of the experimental FES session, concluding with an overall comparison to other similar systems.

5.1 ATC-FES System: Application Overview

A description of the proposed system can be conceptually schematized into inputs, control and output logical macro areas, as represented in Fig. 5.1, according to the actions flow from signal acquisition to stimulation application.

The input devices corresponds to the proposed *Apollux* modules which, as already deeply discussed in Chapters 2, 3, and 4, transmit the ATC values corresponding to muscle contractions through wireless connectivity (i.e., Bluetooth Low Energy). The receiving unit, the control platform, behind the general supervision of the acquisition routines, processes the ATC data and defines the appropriate stimulation profile, which is subsequently loaded into the FES device. Indeed, the electrical stimulator (i.e., RehaMove 2 [141]) closes the loop by generating the defined bio-mimetic pattern.

As previously introduced, besides the possibility to employ the system in different rehabilitation scenarios (i.e., *therapist-patient* configuration as common phys-

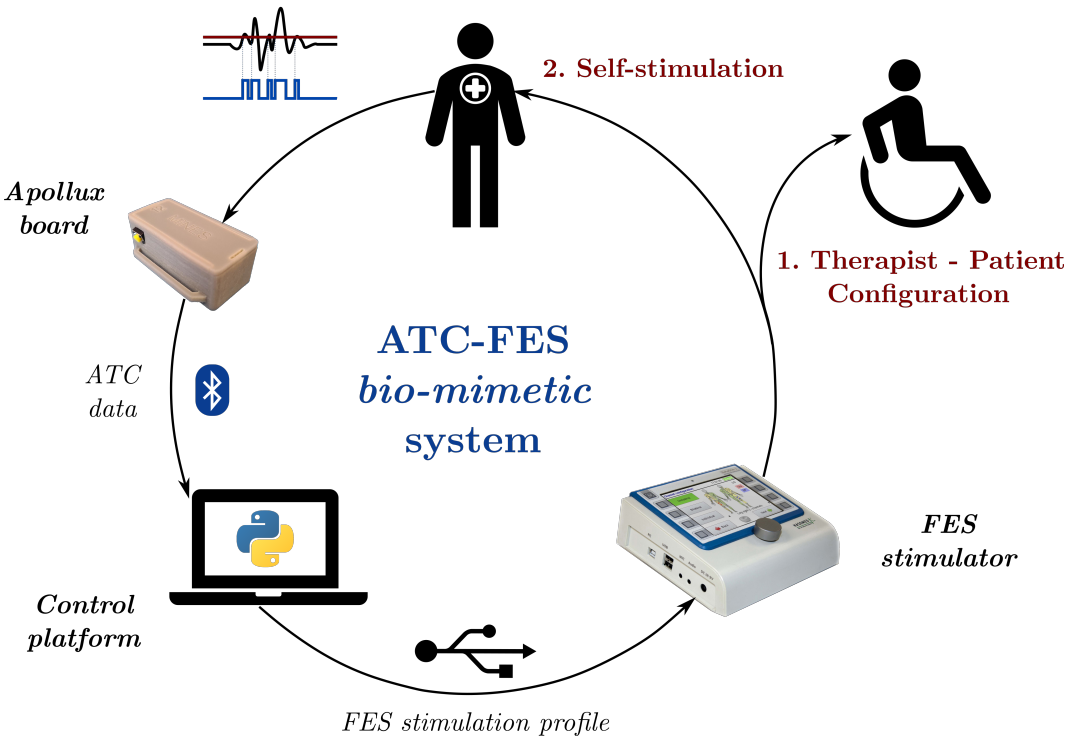

Fig. 5.1 Main application examples of the proposed ATC-FES system: *therapist-patient* and *self-stimulation* configuration.

iotherapy procedure, *self-stimulation* for hemiplegic or hemiparesic subjects), two additional and interchangeable use-cases can be defined by considering the final application:

a) *User-controlled interface*: the system is managed by means of a Graphical User Interface (GUI), which allows the user to actively supervise the stimulation session and provides a visual feedback on muscular activation and FES pulses generation.

b) *Stand-alone system*: user interaction is limited to remote control, and the main ATC-FES operations run independently from a direct user supervision.

The first application a) is intended for clinical-oriented usage, giving the operator the proper feedback to control the correctness of the FES procedure while applying it. Indeed, application a) could be imagined to take action in medical facilities (e.g., physiotherapy gym, rehabilitation center) or in an organized and supported private space (e.g., home health care), with the patient going through a rehabilitation process, consisting of multiple and standardized FES sessions, which aims to restore the impaired motion functionalities.

On the other hand, use-case b) consists of a lighter and more user-friendly setup for the FES application, which does not involve support instruments (e.g., display to plot useful signals) and allows the user to benefit from the stimulation procedure while performing standard activities of daily living.

Therefore, following these considerations and combining the two applications into a single rehabilitation process, a) can be supposed to operate during the initial phase of the physical therapy, when the patient needs adequate assistance to use the system while reinforcing her/his muscles; b) can replace a) when the patient's illness condition is guaranteed sufficiently stable to permit the patient to use the system without supervision.

Coming back to an engineering point-of-view, these two applications require different hardware and software configurations to properly work in the supposed scenario. Next sections will analyze in detail how these functionalities can be achieved by selecting and testing different control platforms.

5.2 System Architecture

This section describes in detail all the blocks (hardware and software) to properly understand how each piece interacts with the others, up to the construction of the overall system.

5.2.1 FES Stimulator

Among the commercial and certified FES stimulators, the RehaMove 2 [141] (Fig. 5.2), provided by the HASOMED GmbH company, has been selected due to its enhanced controllability, which allows the user to define complex and time-varying stimulation profiles, along with the possibility to drive up to eight channels concurrently. Indeed, the RehaMove 2 is equipped with two independent current generators, which are multiplexed to four channels each, and its serial communication is built on the ScienceMode2 protocol, which interface the stimulator with an external USB-compatible device providing an user API [123, 142]. Each stimulator channel consists of two connectors for gelled electrodes (i.e., anode and cathode), through which FES pulses are injected into the muscle tissue. A safety check, based on the skin impedance value, is carried out before any output pulse in order to guarantee muscle elicitation only if the electrode properly adhere to the skin. Moreover, the

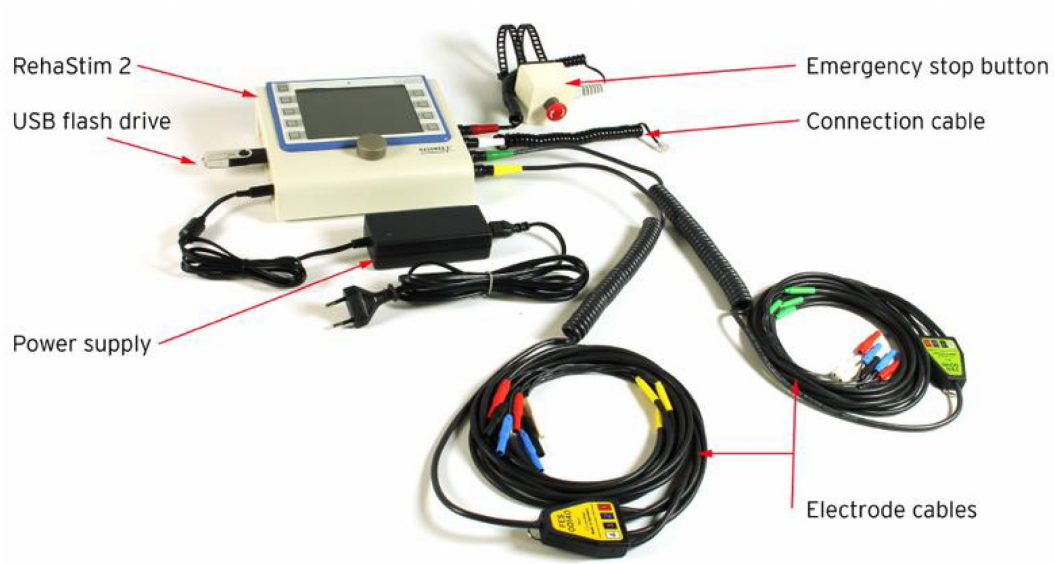

Fig. 5.2 RehaMove 2 electrical stimulator and accessories [123].

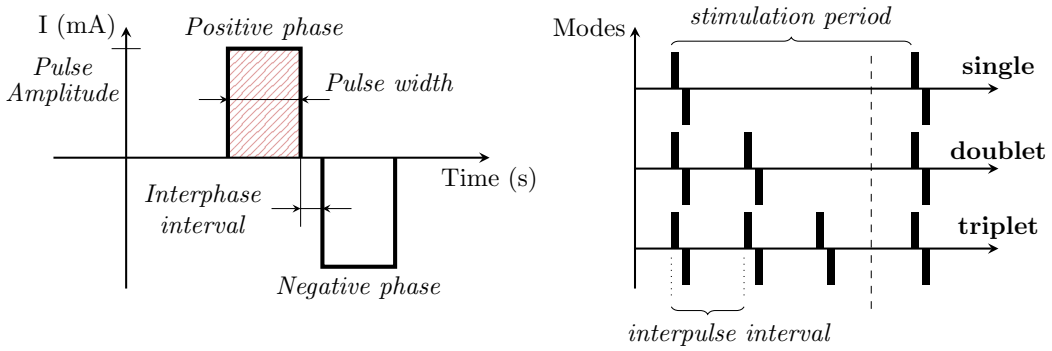

Fig. 5.3 Biphasic rectangular pulses generated by the RehaMove 2 stimulator.

device can be power supplied both using its AC/DC adapter or through the internal battery, which keeps the user isolated from power-line interference, hence resulting compatible with the acquisition of bio-signals parallel to the stimulation process. An emergency switch button, useful to manually interrupt the sequence of pulses, completes the accessories list of the RehaMove 2.

The RehaMove 2 generates bi-phasic rectangular current pulses, as the one represented on the left of Fig. 5.3, whose balanced shape avoids any charge accumulation at the skin-electrode interfaces. Its configurable parameters are the pulse amplitude (mA), the pulse width (μs), and the stimulation period (Hz), while the positive to negative interphase interval is fixed to 100 μs to promote the proper myofibers contraction [143]. Although the ScienceMode2 API provides the run-time variation, per channel, of amplitude and width of the pulses during the stimulation application (therefore modifying the energy content of each pulse), the stimulation frequency has to be defined at the beginning setting phase of the stimulator. The only permitted adjustments to the FES frequency are related to the stimulator operating mode (Fig. 5.3, right): *single* stands for the basic functionality, which generates a biphasic pulse every pre-defined stimulation interval; *doublet* and *triplet* increase the number of pulses in the stimulation interval (spaced by the interpulse interval value) of $\times 2$ and $\times 3$ factors, respectively.

Table 5.1 summarizes the FES modulation parameters (and their application range) for the RehaMove 2 device.

Considering the frequency dependent nature of both the TC signal and the ATC value, the most reasonable FES parameter to be modulate would be the stimulation frequency. However, due to the limitation of the RehaMove 2 device for the

Table 5.1 RehaMove 2 configurable parameters to modulate FES pulses.

Parameter	Description
Pulse amplitude	0 mA to 130 mA in 65 steps
Pulse width	20 µs to 500 µs in steps of 10 µs
Stimulation frequency	10 Hz to 50 Hz in steps of 5 Hz
Mode	Single, doublet, triplet

frequency modulation, the pulse amplitude and the pulse width remained the two available candidates to reach our scope, being themselves related to the ATC variation. Therefore, the developed software (see next Section 5.2.4) implements the definition of these two parameters on the basis of the ATC value, while the not modulated ones are set according to physiotherapy manuals.

5.2.2 Control Platform

As introduced, the goal of this project consists of designing an ATC-FES system adaptable to two different use-cases. Application a), i.e., user-controlled system, is intended for supervised stimulation sessions in which a medical operator controls the system functionalities by interacting with a high-level GUI. On the other side, application b), i.e., stand-alone system, does not involve constant interaction with the user, and it runs autonomously once its execution is requested. As a consequence of this diversity, a different control platform can be selected for each proposed application because its specifications vary depending on the functionalities to be achieved.

Starting from application a), a standard personal computer is identified as a suitable choice, as also confirmed by literature studies involving FES systems [136, 144]. Indeed, from one side, it provides enough computational resources to efficiently run the software and manage all the peripherals (e.g., screen, keyboard, USB ports) for user interaction and devices communication, while, from the other side, it consists of a user-friendly solution to actively operate in the supposed clinical environment.

Instead, application b) does not need a high performance machine to properly operate since the GUI, and related user inputs, should not be provided. For this simpler scenario, embedded devices play their role because they feature limited power

consumption, dimensions, cost, and complexity [145]. Among these architectures, state-of-the-art embedded systems for FES control often include the use of Raspberry Pi (RPi) machines [146] as wearable controllers to support post-stroke gait [147], or cycling for spinal cord injury victims [148], also aiming to sport competitions [149]. Main reasons for using an RPi machine as the control platform lie in its versatility, modularity, size, and cost [150] compared to a common personal computer, without loosing (if necessary) input/output units and wireless connectivity (e.g., telerehabilitation system).

In particular, among the accessible architectures (considering technical specifications still available in the next years), the following machines have been selected to study the system performance in the two use-cases (Table 5.2 highlights the resources difference):

- Lenovo ThinkPad X1 Extreme Gen 3 Personal Computer (PC), equipped with an Intel Core i9-10885H running up to 2.4 GHz clock frequency, and featuring 32 GB RAM and Microsoft® Windows® 10 Pro operating system;
- Raspeberry Pi model 4B, featuring a Cortex-A72 with a clock frequency of 1.5 GHz, a RAM of 4 GB, and Raspeberry Pi OS version 10 (buster);
- Raspeberry Pi model 3B+, featuring a Cortex-A53 with a clock frequency of 1.4 GHz, a RAM of 1 GB, and Raspeberry Pi OS version 10 (buster);
- Raspeberry Pi model 0W, featuring a ARM11 with a clock frequency of 1 GHz, a RAM of 0.5 GB, and Raspeberry Pi OS version 10 (buster);

Table 5.2 HW and SW features for the selected machines for control platform

Model	**#core**	**Architecture**	**f_{CLK} (GHz)**	**RAM (GB)**	**BLE**
Lenovo ThinkPad X1 Extreme Gen 3	8	Intel Core i9-10885H (64-bit)	2.4	32	4.2 (Dongle)
RPi-4B	4	Cortex-A72 (64-bit)	1.5	4	5.0
RPi-3B+	4	Cortex-A53 (64-bit)	1.4	1	4.2
RPi-0W	1	ARM11 (32-bit)	1	0.5	4.1

Table 5.3 Compatibility among use-cases (i.e., a) user-controlled interface, b) stand-alone system) and selected control platform

Application	**Control Platform**			
	PC	RPi 4	RPi-3B+	RPi-0W
user-controlled interface	✓	✓	✓	
stand-alone system				✓

In conclusion, Table 5.3 reports the association between each device and the related use-case: although the PC is the main machine for running application a) and the RPi-0W represents the most fitting device for implementing application b), a deeper and intermediate analysis on a) has been conducted also using the RPis model 3B+ and 4 in order to verify if the software operates unaltered while scaling down the control platform performance.

5.2.3 Software Layers and Functionalities

The control software represents the central and logistic core of the system, which makes possible to link the input and output devices effectively through a list of functionalities. Among them, the most relevant to this project is the definition of the FES pattern on the basis of the ATC parameter, which relies on the proper implementation and operation of the peripheral units (i.e., *Apollux* and RehaMove 2) and their communication protocols. Furthermore, as already introduced for the *Apollux* software in Section 3.3, the control unit has to fulfill multiple technical requirements to be compliant with a biomedical application [102, 151]: it must be scalable to efficiently perform with a variable number of interfaced devices (one or more *Apollux* sensors or RehaMove stimulators); it should be modular (e.g., object-oriented programming) to ease the development and integration of each (new) module; and it has to be sufficiently reliable to minimize failure probability and to ensure user's safety. Moreover, the real-time control of FES represents an additional and essential application requirement [152].

Therefore, also for this solution, and considering the proposed use cases a) and b), Python language has been selected because of its versatility and rapidity of development in addition to its multi-platform compatibility, which allows the application to run independently by the hardware architecture, e.g., from common

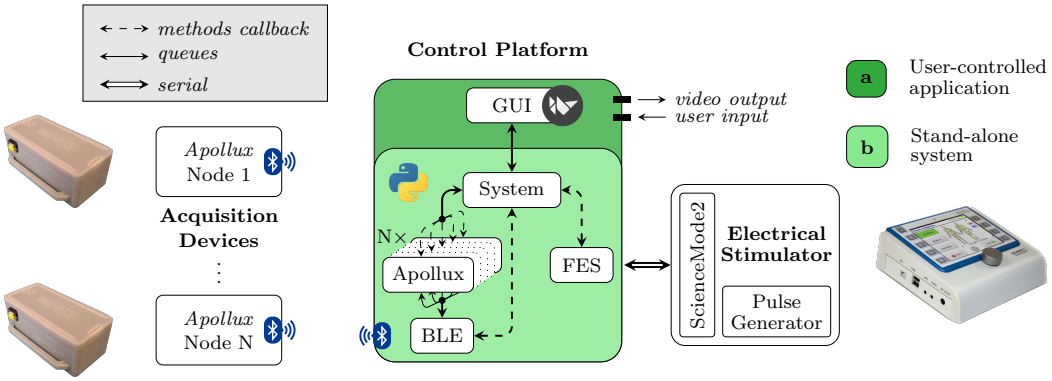

Fig. 5.4 Representation of ATC-FES system blocks and internal software layers.

PCs to embedded systems.

The internal structure of the software follows the one of the *Apollux* standalone application (see Section 3.3) with the integration of the FES object and the System interlayer.

The BLE object is built on the Pyserial [103] or Blatann [153] module (depending on the CC2540 [101] or nRF52840 [78] dongles, respectively) if the control platform requires the use of an external antenna device, while it relies on the Bluepy library [104] if an RPi machine is employed. Its functionalities regard the scan for the *Apollux* devices, the connection to their servers and the bidirectional data flow between the user commands and the received BLE packets.

The Apollux object, as already described, once it is instantiated (after a successful connection) works as a translator for its own functionalities: it redirects the high-level user commands to the related *Apollux* server characteristics by driving the BLE transceiver, and it decodes the payload of the BLE packets accordingly to their classification.

At the other side, the RehaMove 2 is controlled through the serial ScienceMode2 communication protocol [142], which needed to develop a custom library relying on the Pyserial [103] one. The object is in charge of maintaining the connection with the stimulator (through a watchdog approach), updating the stimulation parameter every time a new FES profile is extracted, and handling possible errors from the device.

Above these layers, the System module manages the input/output communications with the peripheral devices and the interaction among them. In particular, it computes the suitable FES pattern every time a valid ATC data is received by an Apollux object, as described in the next Section 5.2.4. This additional layer (w.r.t. the *Apollux* standalone software) has been introduced to split the functionalities of the GUI and below layers and to implement both the use-cases a) and b).

At the top layer, a multi-screen GUI has been implemented for application a), which, using the Kivy Python-compatible framework [106], features multiple buttons and graphs to provide the end-user the complete control of the system.

The different tasks of the above modules have been assigned to multiple threads in order to concurrently execute operations and achieve an overall real-time performance. In particular, one thread per module has been created working as a message handler, which continuously waits for the reception of a message (e.g., BLE from the serial port with the antenna, System from the queue with each Apollux object) in order to redirect it towards its final user (e.g., GUI for data plotting). According to these methodology, the number of active threads results in a minimum of four when the application works in the use-case b) with only one acquisition device connected (System + FES + BLE + 1 Acq. Dev.) and a maximum of twelve operative threads when using the implementation a) with eight operating devices (System + FES + BLE + GUI + 8 Acq. Dev.).

Following the same approach of the *Apollux* standalone application, the data flow control is configured using method callbacks for the internal top-down user requests while thread-safe queues [154] stream upward the peripheral messages, also promoting the system scalability by easing the management of concurrent multiple channels. Furthermore, this implementation allows the system to operate in synchronous or asynchronous mode. In the first case, the ATC-FES definition is performed only after the proper reception of all the ATC values from corresponding queues of all the connected boards. Vice versa, in the asynchronous case, the thread does not wait for the availability of all the data, thus updating the FES parameters only for the channels whose ATC value is received at the same time.

5.2.4 ATC-FES parameters conversion

The definition of the pulses features by the processing of the ATC parameter represents the algorithm for the FES control mechanism, which links the acquisition data with the stimulation one. Since the real-time processing is a key requirement for rehabilitative systems and the algorithm has to be versatile depending on the control platform (e.g., embedded devices have extremely low-computational power), the FES definition process has been implemented trying to keep the complexity lower as much as possible. Taking advantage of the on-board ATC feature extraction process, which directly provides an index of the muscle activity without the need of additional operations, the idea was to mimic the simple values association of a Look-Up Table (LUT) structure, whose parameters (input: ATC, output: pulse amplitude, pulse width) are defined by a linear regression algorithm normalized on the maximum output values obtained after an initial system calibration.

Fig. 5.5 reports, as example, how the algorithm works when the stimulator is driven in pulse amplitude, generally considering n active stimulation channels (and *Apollux ones*): every time a new ATC packet arrives, containing the ATC data of one or more acquisition channels (depending on the a-/synchronous setting), the inside data are appended to an $n \times 3$ matrix (ATC input matrix), which also includes the two past ATC-window data. Then, the row-median operation is computed in order to obtain a robust ATC value, which does not vary impulsively to avoid a painful FES-induced contraction (Ch 3), maintains stable during isotonic activity (Ch 1), and filters any spurious noise corruption (Ch 2). Since the ATC input matrix is continuously updated (every ATC window), this operation basically represents a *moving* median. In this way, an $n \times 1$ array is obtained, whose values are interpreted as *indexes* pointing to the FES current values stored into the LUT structure. Once the new stimulation data are defined through this algorithm, a FES data packet is built up and the command is transmitted to the stimulator.

However, since different subjects could produce different ATC values or be stimulated by a diverse amount of current, a calibration process for the optimization of the acquisition and stimulation parameters is fundamental, permitting the development of an adaptable system, able to fit different users, while maintaining the benefits of a proper and safe per-subject stimulation. Hence, the following four steps calibration process is executed to build the LUT:

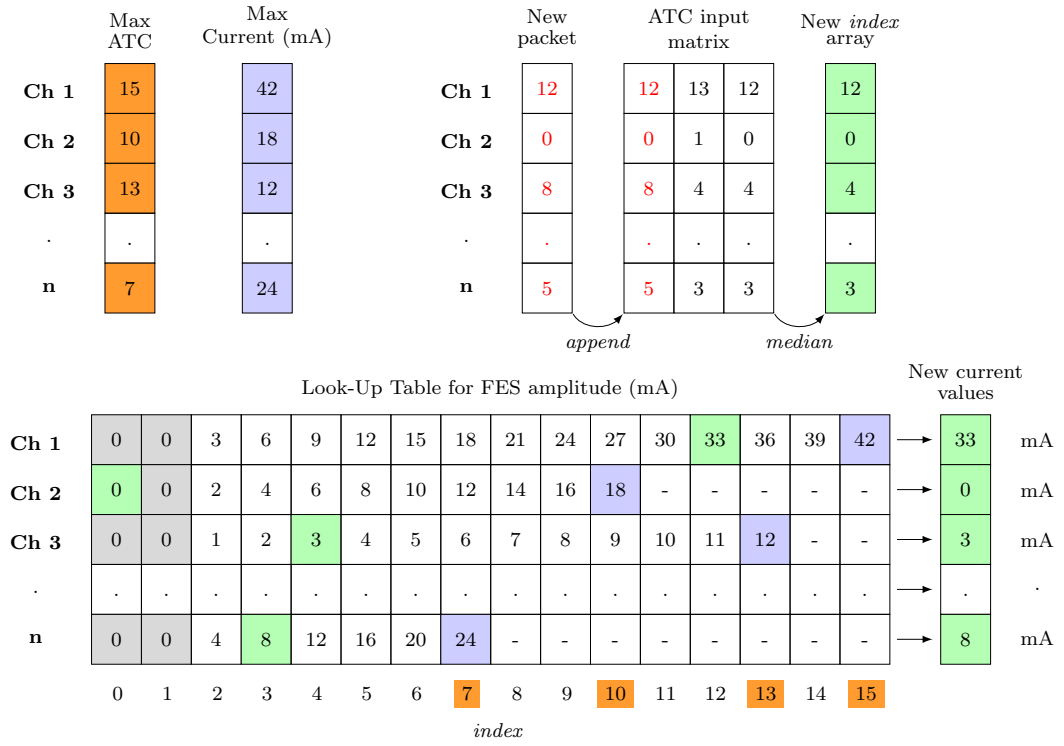

Fig. 5.5 Look-Up Table (LUT) construction and ATC-FES pattern definition: *green* cells represent the links between ATC inputs data and pulses current outputs; *orange* labels identify the *indexes* of the FES LUT defined by the *Max ATC* calibration step; *blue* values correspond to the maximal FES amplitude values calibrated with the *Max Current* process [155].

1. *Threshold setting*: as already explained in Section 2.3.1, this step consists in the optimization of the threshold for the generation of the TC signal. During this calibration, the subject has to maintain her/his muscles relaxed in order to adjust the threshold just above the sEMG signal baseline in way to detect TC events even with minimal muscle effort.

2. *Maximal ATC*: once the threshold is calibrated, the subject has to repeat the movement to be performed at least three times. The maximal ATC value produced during the exercise is calculated as the median value among the maximum of each repetition. This value will limit the *index* dimension of the row, related to the calibrated channel, inside the LUT, highlighted in orange in Figure 5.5.

3. *AROM evaluation (optional)*: the maximal Absolute Range of Motion (AROM) of the involved articulation has been assessed. This measure standardizes the

FES application and provides a comparison feedback between the voluntary movement and the stimulated one. This step is defined as optional because it does not have consequences on the calibration process.

4. *Current limitation*: the maximal current value, useful to properly reproduce the movement in the stimulated subject, is defined as the 110% of the current able to produce the quasi totality of the movement (which could be also determined by monitoring the 70 % of the AROM variation, if step 3 is completed). The obtained values, represented in blue color in the LUT of Figure 5.5, related to the *indexes* defined by the *Max ATC* array, define the proper stimulation values inter-step.

Following this approach, the LUT structure defines a perfect matching between the muscular activation of the therapist and the pulses amplitude to adequately stimulate the patient limb. Looking at the example represented in Figure 5.5, the LUT has different column-dimensions per channel, each one defined by the maximal ATC values. In this way, by setting also the maximum current values, steps and ranges of pulse amplitude are defined. Concluding, simply controlling the lower values of the stimulation matrix (i.e., LUT[(:, 1:2)], grey cells), combined with the moving median gate operation, a very low complex but efficient noise-gateway control has been implemented.

5.2.5 Graphical User Interface

The Graphical User Interface (GUI) for the control of FES application a) has been developed trying to produce a high-level interface for clinical environment. Indeed, the GUI hides the background algorithms discussed in Sections 5.2.3 and 5.2.4, and provides graphical tools to help the user to interact with the system. In particular, it is divided in the following three screens:

- *Login* screen (Fig. 5.6): it simply asks to the user tho insert her/his authentication credentials to access the software;
- *Medical* screen, which allows the user to insert all the personal information of the subject and the selected therapy. It is also divided into three main tabs:
  - *First Visit* (Fig. 5.7): it corresponds to the patient's anamnesis;

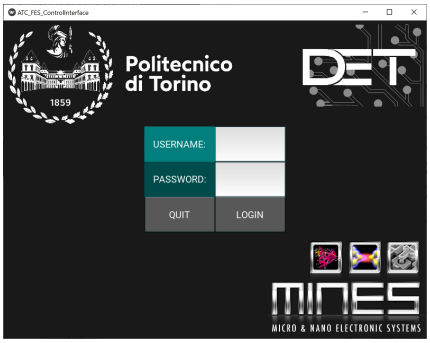

Fig. 5.6 Login screen: user credentials enables the access to the other screens.

  - *FES Session* (Fig. 5.8): it summarizes the FES exercises and provides an help guide to the user to setup the system (e.g., where to locate the acquisition and stimulation electrodes);
  - *Check-up*: with a similar organization of Fig. 5.8, it provides all the information to use the *Apollux* device for performing an evaluation of the muscular activity of the subject.

- *Main stimulation* screen: it is the central graphical core of the application where all the main steps are executed, from the devices connection and association, through system calibration, to online training. Bluetooth module (i.e., dongle or internal transceiver depending on control platform), RehaMove 2 stimulator, and *Apollux* boards are connected as first action (a.). Then, ac-

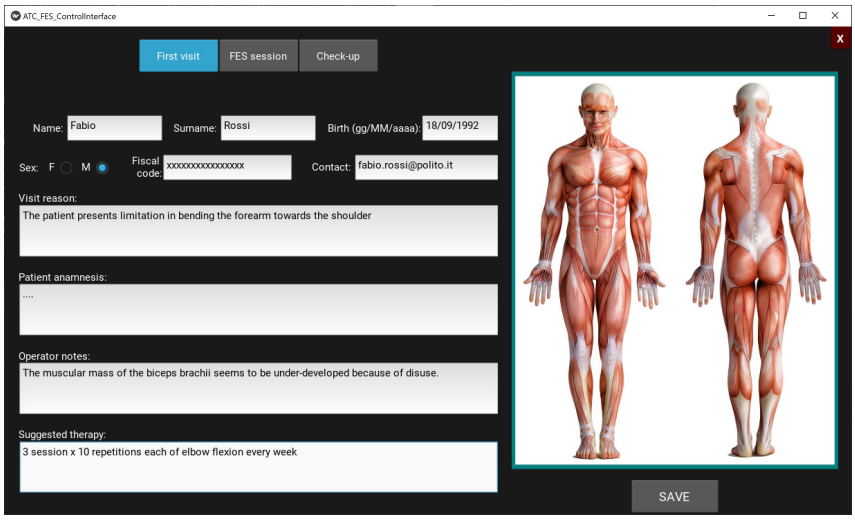

Fig. 5.7 Anamnesis of the patient and proposed FES therapy can be inserted here.

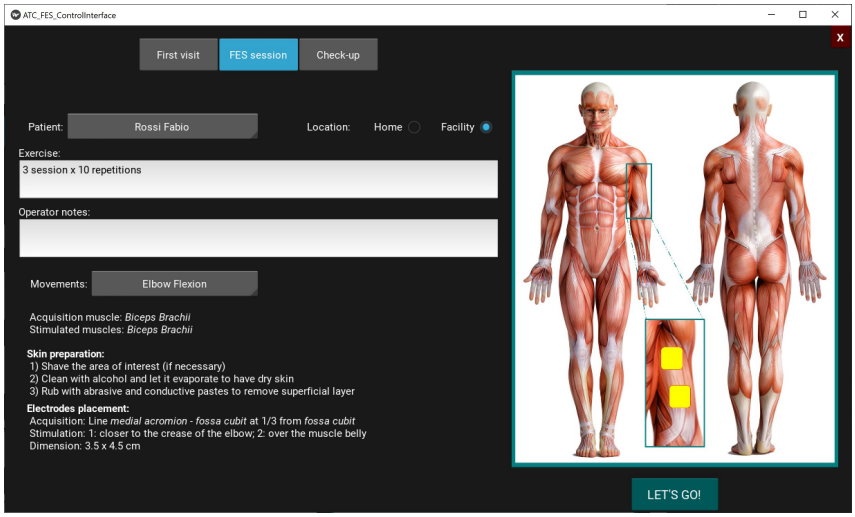

Fig. 5.8 FES session tab, also reporting the guidelines for electrodes positioning.

quisition and stimulation devices are linked in order to setup the one-to-one association (b. and c.). Non-modulated FES parameters (i.e., pulse width, frequency, and mode) can be adjusted using the related sliders and buttons (d.). After the passive setup, both therapist and patient calibration need to be run in order to build the LUT (e.). At this point, the *Start Training* button (f.) starts the online stimulation, which can be constantly monitored by looking at the ATC (g.) and pulse amplitude (h.) graphs.

All the session data, from subjects' information (e.g., anamnesis) and acquisition/FES setup (e.g., electrode positioning, stimulator parameters) to the online

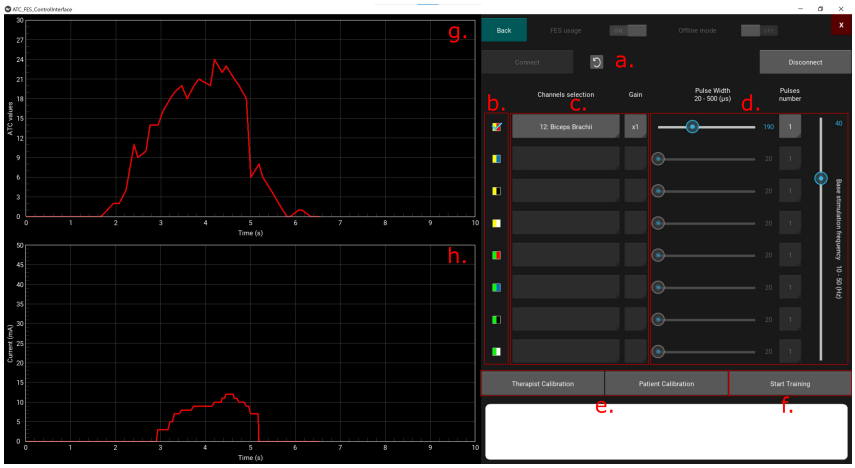

Fig. 5.9 Main user screen during stimulation.

training profiles (ATC and FES-defined values), are saved in organized files structure, which can be used as reference for future sessions, in order to speed up the setup, or processed to analyze the history and evolution of the therapy.

5.3 Control Platform Performance

Before evaluating the ATC-FES system in a real application scenario, some tests have been carried out to verify if the performance of the control platform corresponds to the requested design rules. In particular, as pointed out in Section 5.2.3, the implemented software has to fulfill different technical requirements: if its modularity, scalability, and reliability (in terms of error checks) have been assessed by using the paradigms of the object-oriented programming along with safety routines for error managing, the real-time behavior of the system needs to be confirmed yet. The selected hypothesis to prove the effectiveness of the proposed solution consists of measuring the processing time which occurs between the reception of new ATC data and the related FES pattern updated (acknowledged by the stimulator), which needs to be lower than the interval between two new input data (i.e., ATC window).

5.3.1 Test setup

Fig. 5.10 shows the processing data flow representing the entire procedure from the ATC data reception to the acknowledgment of FES parameters update command. The first step is to retrieve the ATC data from the queue of each active acquisition device. Then, as discussed in Section 5.2.4, the new data are appended to the matrix containing the two most recently acquired ATC values for each channel, and a median operation is performed. The result is used as the index for the LUT to set the modulated stimulation parameter (e.g., pulse amplitude, pulse width) needed by the associated stimulation channel. In order to create the packet containing the pulse parameters, both the results obtained from the LUT and the pre-defined

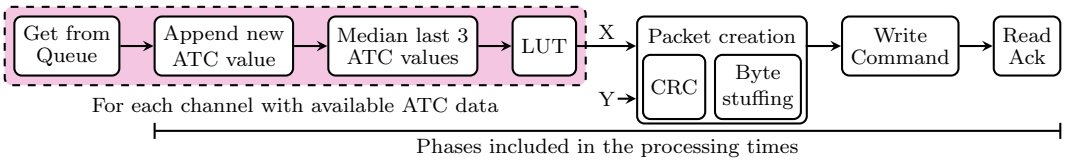

Fig. 5.10 Following the first phase of retrieving ATC data from the queue of each acquisition device, the modulated stimulation parameter X (pulse amplitude/width) is computed through three processing steps and provided as input to the (ScienceMode2) packet creation block together with the not modulated parameters Y (pulse width/amplitude, frequency). The measured processing times start after the get from the acquisition queues, and end at the acknowledgment reception from the stimulation device.

not modulated stimulation parameters are provided as input. The ScienceMode2 communication protocol [142] requires using a 1-byte checksum through Cyclic Redundancy Check (CRC) and the use of byte stuffing to avoid the presence of bytes equal to the start or stop sequence of the packet. Finally, the last steps are the serial transmission (to the electrical stimulator) of the created packet and the corresponding reception of the acknowledgment sent back.

Processing times were measured from the end of the phase of getting data from the acquisition queues to the acknowledgment reception from the stimulation device. The combinations of tested configurations consist of the use of multiple acquisition devices, synchronous/asynchronous processing of received data, and the optional use of the GUI.

The number of connected *Apollux* devices ranges from 1 to 8 (maximum number of channels managed by the electrical stimulator) with a one-to-one control. In particular, considering the performance of the selected laptop, the configurations involving the PC have been directly tested in the worst case setup comprising 1 (reference) and 8 connected boards. Instead, a more detailed analysis has been carried out for the configuration with an RPi acting as the control platform in order to effectively see how the proposed embedded system performs at increasing its workload. In these configurations, for the sake of synthesis and without loss of generality, the tested configurations involved 1, 3, 5, or 8 active channels.

Processing synchronization was evaluated to satisfy possible application requirements, which may need to apply FES only when data are received from all connected acquisition devices. As it can be guessed, synchronization implies just one processing cycle per ATC window period, since the ATC data from all the available channels are processed together, while in the non synchronized scenario the number of (sequential) processing cycles is equal to the number of connected *Apollux* devices. As follows, between the two modes, the asynchronous is the one with the greater impact on computation effort. Again, in order to synthesize the results, PC configuration has been only tested using the asynchronous processing modality.

Last, considering the platform marketed as embedded, although RPi-3B+ and RPi-4B involve the use of the GUI, their configurations with 8 channels have also been tested without it for the sake of completeness and to understand its effect on the system. In particular, the tests without GUI were carried out by communicating

with the system via the command line, and so having one less thread since ATC and FES profiles were not plotted.

Each test included 3 minutes of continuous operation, with CPU and RAM usage constantly monitored.

5.3.2 Test Results and Discussion

This section presents the characterization of the system across the multiple tested configurations, whose results are reported in Fig. 5.11: the table on the left summarizes the analyzed configuration and provides the numerical results concerning the resources request (i.e., CPU, RAM) and reliability indicators (i.e., discarded packets, exceeding processing), while the graph on the right shows the distribution of the processing latencies.

For both system implementations (i.e., the user-controlled and the stand-alone system), the increase of acquisition devices results in longer processing times. This is mainly due to two factors: each input device is managed by a thread, so the number of active threads increases; the size of the (stimulator) command packet is proportional to the number of initialized stimulation channels, thus requiring more time to build the packet.

Enabling the synchronization among input channels relaxes the processing phase, as the control platform needs to build the command packet fewer times. However, since waiting for data from all queues may take longer, the probability of queued data piling during subsequent processing steps increases: in these cases, only the most recent data are processed (for each input device), while older data are discarded. The percentage of data lost, w.r.t. those streamed by the acquisition devices, is reported in the *Losses* column in the table on Fig. 5.11. As expected, this percentage gets higher when the number of input devices increases. <

Vice versa, the asynchronous data processing rarely encounters the issue of data piling, guaranteeing about 0 % of discarded packets, but it can suffer from excessive delays (longer than the ATC window constrain of 130 ms), specially going through resource limitation of the platform. In the *Delays* column of Fig. 5.11, the percentage of data that took longer than one ATC window to be processed is reported.

ID	M[1]	N[2]	Sync	Win (ms)	GUI	CPU (%)	RAM (MB)	Losses (%)	Delays (%)
C1	PC	1	no	130	yes	0.38	204.33	0	0
C2		8	no	130	yes	1.71	218.19	0	0
C3	4B	1	no	130	yes	9.55	85.01	0	0
C4		3	no	130	yes	12.35	86.32	0	0
C5			yes	130	yes	10.57	86.31	0.03	0
C6		5	no	130	yes	15.57	87.44	0	0
C7			yes	130	yes	11.93	87.3	0.1	0
C8		8	no	130	yes	17.9	88.97	0	0
C9			no	130	no	5.6	23.2	0	0
C10			yes	130	yes	15	88.8	0.1	0
C11			yes	130	no	3.38	22.89	0.14	0
C12	3B+	1	no	130	yes	74.72	138.48	0	0
C13		3	no	130	yes	71.17	139.85	0	0.07
C14			yes	130	yes	71.83	139.42	1.53	0
C15		5	no	130	yes	67.62	139.98	0.14	0.11
C16			yes	130	yes	69.03	139.41	3.04	0.07
C17		8	no	130	yes	63.3	140.71	0.93	3.11
C18			no	130	no	10.55	23.09	0	0
C19			yes	130	yes	65.82	140.39	3.63	0.72
C20			yes	130	no	5.7	22.92	0.18	0
C21	0W	1	no	130	no	37.6	22.99	0	0
C22		3	no	130	no	64.3	22.58	0	0
C23			yes	130	no	37.7	22.85	0	0
C24		5	no	130	no	77.9	22.98	0.02	0
C25			yes	130	no	56.2	23.21	0.02	0
C26		8	no	130	no	92.8	23.19	0.03	0
C27			yes	130	no	81.4	23.55	0.08	0

[1]M: Machine for control platform [2]N: number of active channels

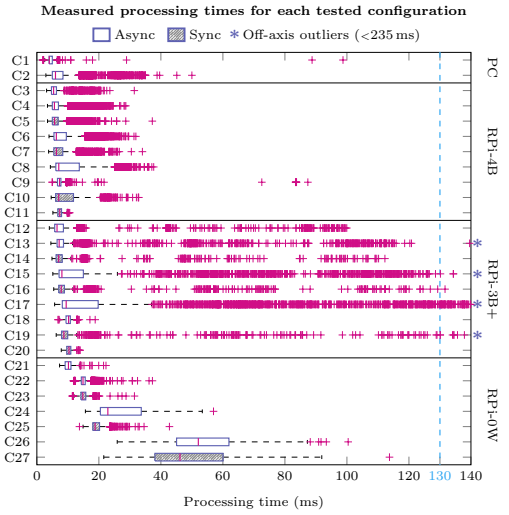

Fig. 5.11 Obtained results for each tested configuration. The table on the left reports the CPU and RAM usage, the percentages of lost packets, and those for which the processing times exceeded our constraint (i.e., ATC window). The boxplots on the right show the measured processing latencies as described in Section 5.3.1.

Starting from the PC as the standard machine running the user-controlled application (configuration C1 and C2), its performance confirm the proper real-time processing of the data, with a median latency value of 4.01 ms and 6.00 ms for the cases involving 1 and 8 channels, respectively. Moreover, also the reliability of the results is assured by the complete absence of lost packets or delayed processing, along with the very contained maximum CPU usage of 1.71 %. For the same application, the RPi-4B features negligible losses (e.g., 0.14 % when controlling 8 stimulation channels) and zero delays, combined with a maximum CPU utilization of 17.9 % when data are processed asynchronously. These results confirm also the RPi-4B as an ideal platform for the user-controlled interface implementation. On the other hand, the use of the RPi-3B+ involves more losses and delays (as evidenced by the high presence of outliers in Fig. 5.11), which reflect in an increase of RAM utilization w.r.t. the RPi-4B. A reasonable explanation for this behavior is related to the less performant GPU available on the RPi-3B+, which does not fully support the graphical requirements of the application. Although its performance decrease, considering that the interquartile range of the processing times is always within the ATC window, the use of the RPi-3B+ is still a feasible solution for the user-controlled interface use-case.

The stand-alone system implementation, i.e., based on the RPi-0W, exhibits good performance for all tested configurations, confirming (also in this case) the lightness of the proposed ATC-FES control mechanism based on the LUT concept. Clearly, considering the lower computational capability of the Rpi-0W w.r.t. the other platforms (see Table 5.2), the processing latencies result higher than the above setup, e.g., reaching a median value of 52.07 ms in the most critical configuration (8 channels, no synchronization). In addition, by comparing these outcomes with what was obtained using the RPi-3B+ (when the GUI was not used), the amount of RAM utilization is the same (about 23 MB), while the percentage of CPU usage is much higher (92.8 % versus 10.55 % in the configuration with 8 channels, asynchronous processing, and 130 ms window). Concluding, despite the higher CPU usage, all data are processed on time, thus allowing this implementation to be efficiently used even with 8 channels.

5.4 Real-case scenario evaluation

The effectiveness of the proposed ATC-FES motor control was investigated simulating clinical rehabilitative sessions. In particular, during the experimental campaign, the therapist-patient configuration, instead of the self-stimulation approach (i.e., CCFES), has been selected as test scenario to promote the muscular relaxation of the stimulated subject, which could not be entirely achieved if the same subject is already executing another movement. Each test involved two subjects: the therapist performs the movement voluntarily and the patient replicates the movements as a consequence of FES application. In this situation, ATC values expressed by the therapist were used in the definition of FES intensity. From these tests, the trajectory of the voluntary and stimulated movements were extracted and compared to analyze their similarity. To this scope, subjects' body movements were captured using the Vicon system, configured with a total of 12 cameras recording the motion volume, as it is the commercial gold standard tool for motion capture [156]. Investigating clinical procedures and state-of-the-art works [157, 139, 158–160], a total of six movements, concerning both upper and lower limbs, are defined as follows with their reference positions [161–163]:

- Elbow Flexion (EF): subjects starts seated with the forearm in supine position and the elbow leaning on the table, then the elbow is bend moving the forearm parallel to the sagittal plane. Considering an healthy subject, its Range of Motion (ROM) typically goes from 0° to 60°, although the maximum flexion can vary depending on the anatomical features of the arm.
- Wrist Extension (WE): subjects are seated with the forearm in neutral position and the elbow leaning on the table. The exercise evolves moving the back of the hand towards the distal part of the forearm, generally reaching a ROM of about 70°.
- Wrist Flexion (WF): starting from the same reference position of WE, the the palm of the hand bends on the inner arm. A normal articular condition expects a ROM of 70°.
- Knee Extension (KE): subjects are seated on a chair high enough to avoid any impairment between the foot and the floor during movement execution. It

consists of extending the leg until the tibia is parallel to the femur, typically arriving to 90° of extension considering the reference position. Among analyzed movements, this is the one loading the greatest weight, since the lower leg has to be risen totally.

- Ankle Extension (AE): the subject is placed in the same reference position of KE; then, s/he moves the tip of the finger down, until a ROM of about 20° is achieved. This movement is the one with the lowest ROM among the ones listed.
- Ankle Flexion (AF): starting from the reference position of KE/AE, the foot is bent towards the tibia, covering a ROM of approximately 45°.

The test campaign involved a total of 17 healthy volunteers, 12 males and 5 females, aged between 24 and 30 years old. In compliance with regulations regarding COVID-19 [164], the proper distance between the subjects was guaranteed and each of them was required to wear a protective mask. The sanitizer gel was used during the preparation phase of the subjects and it was made available for further use. These experimental tests were approved by the Comitato Bioetico di Ateneo of the University of Turin [108] (experimental code: 445154).

5.4.1 Test setup and execution

The following paragraphs describe how the experimental phase has been conducted, starting from the explanation of the tests to the subjects, through the environment setup, to the exercises execution.

Procedures explanation

The goal of the test and how it would be performed were explained to the volunteers, also detailing technical information about the instrumentation. The informed consent signature was required from participants to proceed with the testing phase, and the information sheet has been given to them.

Vicon system setup

After placing all the necessary equipment in the 3D motion capture environment, Vicon infrared cameras were masked to limit instrumentation reflection, which could lead to data corruption [165]. Then, the sampling volume was calibrated and the origin of the axes was set. Reflective markers were applied to subjects' bodies following the positioning guideline reported in [166]. In particular, considering that the proposed tests only concern the upper and lower limbs, the total number of applied markers is reduced to the standard setup involving the entire body, hence excluding head, torso, and pelvis not relevant areas.

Electrodes application

Kendall™ H124SG (Ag/AgCl, 24 mm ⌀) pre-gelled electrodes [111] were used for sEMG detection. The SENIAM project recommendations [51] were followed to adequately prepare the skin before electrodes attachments, preventing the sEMG signal to be corrupted by noise sources (e.g., motion artifacts) or electrodes imbalance. Sensors locations, as reported in Table 5.4, were identified both considering SENIAM project indications [51] and through manual palpation, thus assuring the correct and standardized placement w.r.t. the muscles condition of involved subjects.

As regards the stimulation electrodes, the HASOMED® RehaTrode [123] (5 cm × 9 cm) and the FIAB PG470W [170] (3.5 cm × 4.5 cm) products have been em-

Table 5.4 Summary of the monitored muscles and the anatomical reference position to place the *Apollux* sensing devices [167]

ID	Acq. muscles	Acquisition sites[1,2]
EF	*Biceps Brachii*	*on the line between the medial acromion and the fossa cubit at 1/3 from the fossa cubit*
WF	*Extensor Carpi Ulnaris*	*At* 10 % *of the line from the medial epicondyle of the humerus to the ulnar styloid process*
WF	*Flexor Carpi Radialis*	*At* 10 % *of the line from the medial epicondyle of the humerus to the radial styloid process*
KE	*Rectus Femoris*	*at* 50 % *on the line from the anterior spina iliaca superior to the superior part of the patella*
AE	*Gastrocnemius*	*on the most prominent bulge of the muscle.*
AF	*Tibialis Anterior*	*at 1/3 on the line between the tip of the fibula and the tip of the medial malleolus*

[1]Compliant with [51]; [2]Adjustable to account for variability across subjects.

Table 5.5 For each tested movement, the stimulation electrodes location, together with the involved muscles and the FES parameters are reported [167]

ID	Stimulation muscles	Stimulation sites[1,2]	f_s[1,2]	PW[1,2]
EF	*Biceps Brachii*	E1: closer to the crease of the elbow, E2: over the muscle belly	40 Hz	250 µs - 350 µs
WE	*Extensor Carpi Ulnaris, Extensor Digitorum*	E1: over the tendinous area of the forearm, E2: just distal to lateral condyle	40 Hz	200 µs - 300 µs
WF	*Flexor Carpi Radialis, Palmaris Longus*	E1: over the flexor surface of tendons, E2: high towards the medial condyle	40 Hz	200 µs - 300 µs
KE	*Quadriceps Femoris*	E1: proximal and towards the lateral side, E2: distal and slightly to the medial side	40 Hz	350 µs - 500 µs
AE	*Gastrocnemius, Soleus*	E1: over the origins of both the medial and the lateral gastrocnemius, E2: over the soleus	40 Hz	300 µs - 400 µs
AF	*Tibialis Anterior, Peroneus*	E1: close to the tibia, further down the shank, E2: over the muscle belly, very midline	40 Hz	250 µs - 300 µs

[1]Compliant with [168, 169]; [2]Adjustable to account for variability across subjects.

ployed to provide the appropriate stimulation intensity considering (among the exercises) the diverse typology and orientation of muscle fibers [168]. As for sEMG, skin preparation and standardization of electrode placement were provided following the indications reported in [168] and [169], also taking care to apply a conductive gel on electrode surface to enhance the current flow and to minimize the discomfort perception. A summary of the FES setup is described in Table 5.5. These indications are not strictly binding, since depending on the subjects' anatomy and their comfort with stimulation, the positioning can be modified.

ATC-FES system calibration

As described in Section 5.2.4, the creation of the ATC-FES relationship by means of the LUT structure allows the system to completely exploit its versatility, making possible the adaptation of the physiological muscle conditions (e.g., muscular tone, exerted force) among therapists and patients. At the end of this two-step process, the therapist ATC values drive a stimulation intensity (i.e., pulse amplitude) able to reproduce a similar action in the patient body, although their different muscle status.

To recap, the first step includes the calibration of the ATC threshold during the muscular rest condition and the subsequent repetition (at least three times) of the desired movement in order to identify the maximal variation of the ATC value. Then, in the second step, the maximal value of the stimulation intensity, able to

induce the target action in the patient, is determined. To accomplish this task, the stimulation intensity is gradually increased until the proper setting is identified. If the subject feels discomfort (e.g., cramp, burning or pain), non-modulated stimulation parameters (i.e., frequency, pulse width) or the electrodes position could be changed trying to better adapt to subject condition.

Test execution

Every trial consists of three sessions, during which each target movement is repeated ten times, preserving 10 s inter-repetition and 5 min inter-session pause times to prevent muscle fatigue effects.

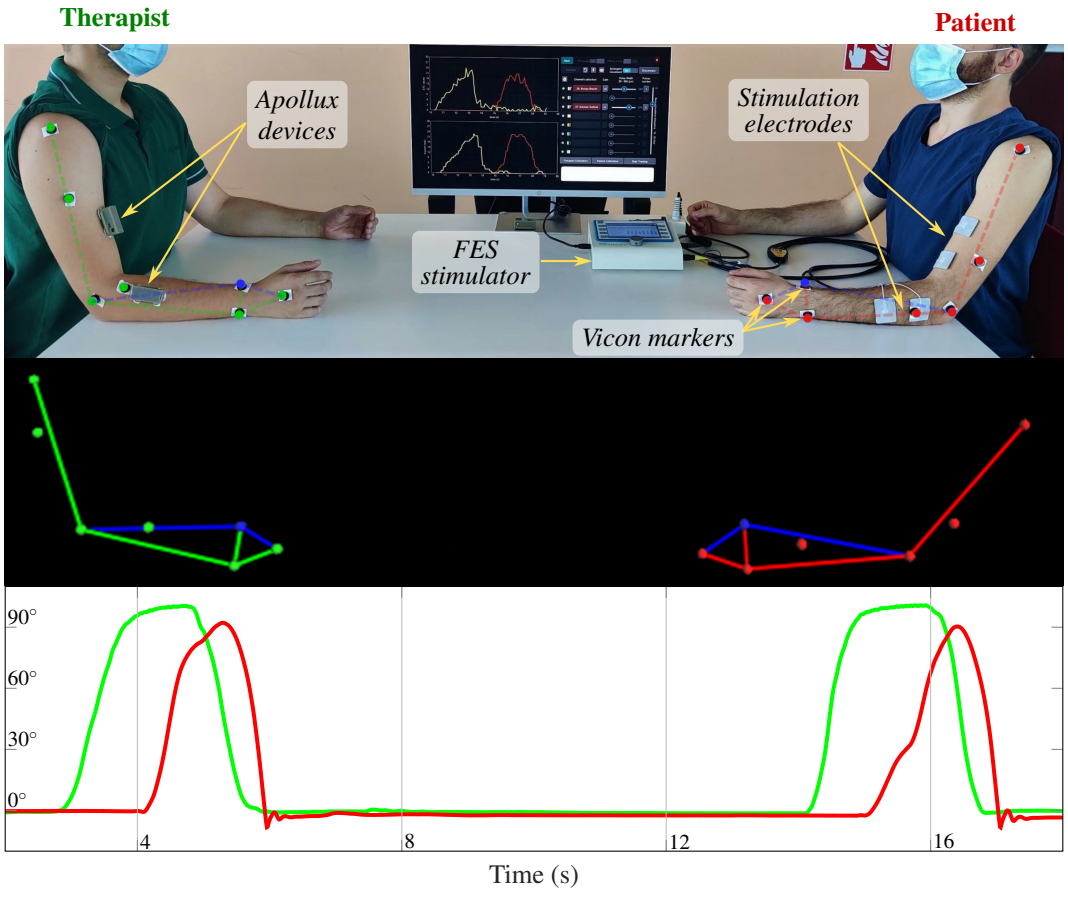

Fig. 5.12 (**top**) Experimental setup: the therapist, on the left, wears the *Apollux* modules; on the right, the patient maintains the same posture and is connected to the electrical stimulator, respectively; Vicon markers are applied on both subjects; (**middle**) Upper limbs reconstruction using Vicon system; (**bottom**) Exported elbow flexion trajectories [167].

Since each type of movement was performed by 8 volunteers at least, with the exception of WF with 9 volunteers (because not all the subjects had the time availability to participate in testing all the six movements), a minimum number of 240 repetition has been obtained for each movement.

The selected stimulation frequency (f_s) and pulse width (PW) for each movement, employed during the calibration and execution phases, are reported in the right columns of Table 5.5.

Fig. 5.12 (top) shows the experimental setup for upper limbs movements, where the two subjects are positioned frontally with the electrodes and markers applied. The reference position features the subjects sitting upright with the limbs aligned. In Fig. 5.12 (middle) an example of the reconstruction of body segments for upper limbs, thanks to the identification of Vicon markers, is reported. The angular trajectories of both subjects are accordingly extracted, as represented in Fig. 5.12 (bottom).

5.4.2 Data Processing

The sampling frequency of Vicon cameras was set to 100 Hz, a suitable value to accurately reconstruct human joint flexions and extensions [171]. Starting from markers identification and human body segments reconstruction, limb trajectories were extracted using the Nexus software [172]. Since the Vicon cameras may not recognize some markers during the execution of the test, data interpolation was often needed to reconstruct the totality of the rigid body. At this point, movements trajectories were obtained by running the Kinfit tool of the Nexus software, which, by processing markers coordinates, results in the extraction of 3D volume trajectories.

Vicon data were further processed on MATLAB®. Pre-processing steps include the discard of segments that do not belong to the test execution, and the signal sign adjustment in order to match the system reference for the two acquired trajectories (e.g., therapist and patient are sited in position facing each other). Then, a segmentation process was performed to identify four temporal coordinates for each movement repetition (see Fig. 5.13): the start (s_1) and the end (s_2) of the rise, which corresponds to the limb segment reaching its voluntary or stimulated ROM; the start (s_3) and the end (s_4) of the fall, identifying the return of the limb segment at the initial (reference) position.

Basically, the implemented segmentation algorithm works by scanning for variations in the derivative of the signal. It is provided with the following parameters: Diff_{min} is the minimum signal variation for the definition of the rising (s_1, s_2) and falling (s_3, s_4) points; N_{s_1,s_4} and N_{s_2,s_3} are the number of analyzed consecutive points to identify s_1 and s_4, or s_2 and s_3, respectively. For the identification of s_1 and s_4, N_{agree} and N_{disagree} are also used, both percentages relative to N_{s_1,s_4}: N_{agree} defines the minimum number of points that must be consistent with the identification (e.g., in the case of s_1 the subsequent points must be rising ones); N_{disagree} defines the maximum number of allowed contrary points (e.g., the maximum number of falling points in the rising phase).

The steps of the segmentation algorithm are summarized in the following list:

1. Application of a moving median operator, with window length equal to 41 samples, to suppress the noise resulting from the possible flickering of the markers (which can be present despite Nexus interpolation) and to allow the algorithm to neglect the non-relevant signal fluctuations, such as those resulting from the return of the limb to its reference position (see Fig. 5.13 (a), at 2.8 s);

2. Down-sampling of the signal by $\times 2$ factor to simplify and speed up the segmentation process, since it depends on the number of points in the trajectory and the difference of their values (this step is not strictly necessary, but a high sampling rate is not required for segmentation and a lower rate makes the choice of tuning parameters less critical);

3. Identification of the rising and falling points of the trajectory by applying a threshold (i.e., Diff_{min}) to the derivative of the signal, as reported in Equation 5.1:

$$p_i \in \begin{cases} \textit{Rising}, & \text{if } p_i - p_{i-1} \geq \text{Diff}_{\text{min}} \\ \textit{Falling}, & \text{if } p_i - p_{i-1} \leq -\text{Diff}_{\text{min}} \end{cases} \tag{5.1}$$

   where p_i is the i-th point of the trajectory.

4. Moving forward on the signal one point at a time; if the current point is a rising one, and at least the N_{agree} percent of the next N_{s_1,s_4} points are rising point, and less than the N_{disagree} percent of them are falling points, then the current point is identified as s_1;

5. Moving backward on the signal one point at a time (starting five seconds after s_1, considering the movement completed), if the current point is a falling one, and at least the N_{agree} percent of the next N_{s_1,s_4} points are falling point, and less than the $N_{disagree}$ percent of them are rising points, then the current point is identified as s_4;

6. Identification of the maximum value between s_1 and s_4;

7. Starting from the 70% of the maximum value (left side), moving forward one point at a time, if the current point is a rising point, and there is at least one rising point among the next N_{s_2,s_3} points, then the current point is identified as s_2. If s_2 is not identified within the maximum point, s_2 is located at the point before the maximum point;

8. Starting from the 70% of the maximum value (right side), moving backward one point at a time, if the current point is a falling point, and there is at least one falling point among the next N_{s_2,s_3} points, then the current point is identified as s_3. If s_3 is not identified within the maximum point, s_3 is located at the point after the maximum point.

Due to the variability among acquired trajectories, the parameters of the algorithm can vary slightly between different movements. Table 5.6 reports the typically used values, which, although not constraining, can be used as reference. Still, it is up to the user to determine the most appropriate ones.

Table 5.6 Typical parameters tuning for the trajectories segmentation algorithm [167].

ID	**$Diff_{min}$ (°)**	**N_{s_1,s_4}**	**N_{s_2,s_3}**	**N_{agree} (%)**	**$N_{disagree}$ (%)**
EF	0.8	10	7	70	20
WE	0.6	10	7	70	20
WF	0.4	12	9	70	20
KE	0.6	10	7	70	15
AE	0.2	10	7	50	20
AF	0.4	12	7	50	20

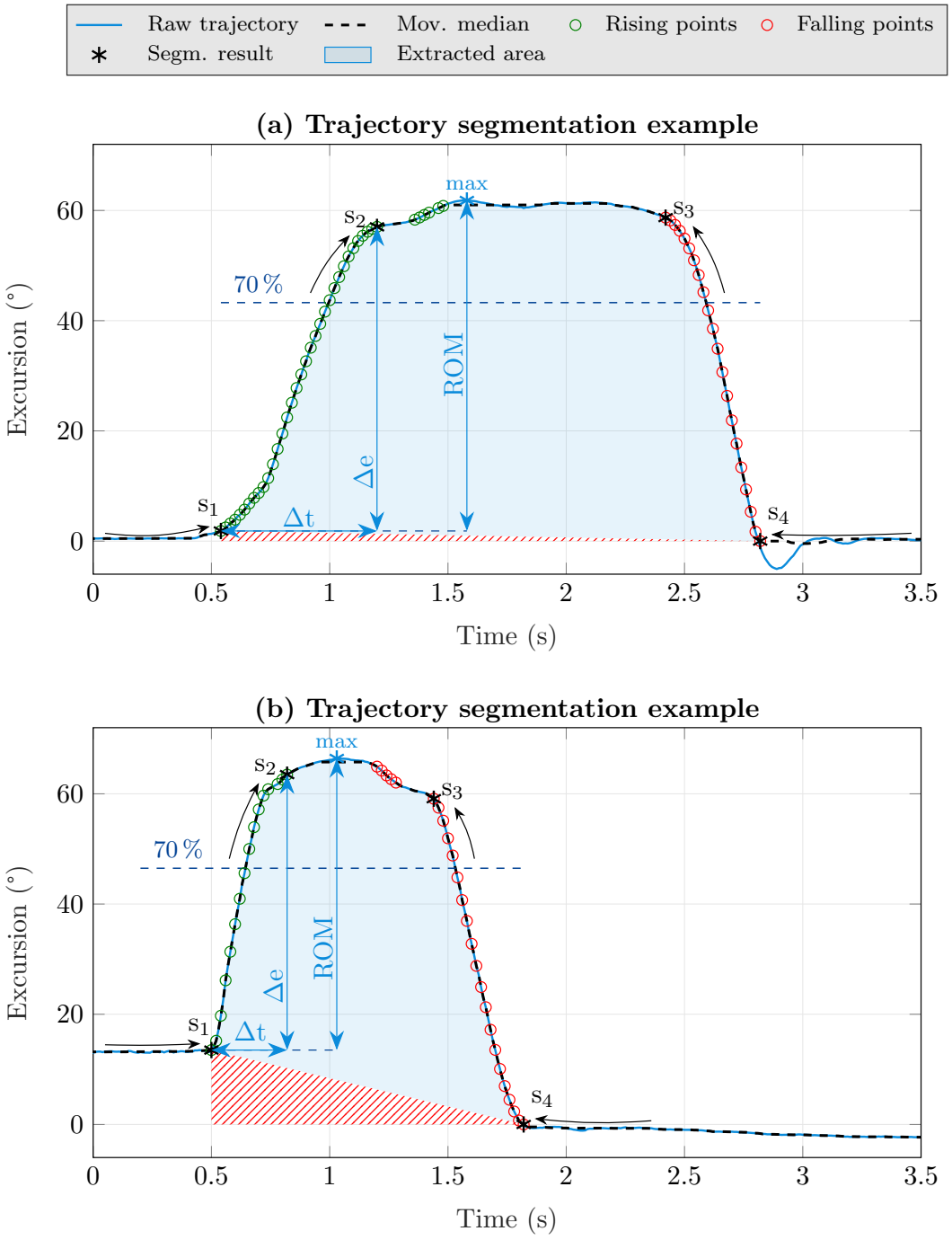

Fig. 5.13 The example (a), top graph, reports a trajectory with no significant baseline changes between the beginning and end of the movement, in contrast to the trajectory shown on the bottom (b). Starting from the rising (green) and falling (red) points of the curve, the markers s_1, s_2, s_3, and s_4 have been obtained from the segmentation. Using them, the evaluation parameters of interest (ρ_{max}, D, ROM, v, and A) have been extracted for each movement repetition [167].

The alterations made to the signal during the processing stage (e.g., down-sampling) regard only the segmentation algorithm, while the extraction of the evaluation features (described below) is carried out on the original signal, to which just a moving median operation with window length equal to 11 samples is applied for noise suppression.

In the below formulas, for the calculation of the evaluation features, $e_{k,x}$ and $t_{k,x}$ are the excursion and time components of the k-th sample of the therapist ($x =$ *'th'*) or patient ($x =$ *'pt'*) trajectory.

In order to test the performances of the system, the normalized cross-correlation coefficient (ρ) and the delay (D) between therapist and patient movements were computed to evaluate the effectiveness of the FES control, as also reported in [138, 173]. While ρ perfectly represents the similarity among movements, D carries the overall information about FES application timings, including both computational and physiological latencies. Moreover, ρ was also calculated between the subjects' trajectories and their respective ATC and FES profiles to better understand the most critical step during the transfer of information[2]. Equations 5.2 and 5.3 show the formulas for $\rho_{\max}$ and D:

$$\rho_{\max} = \max\left(\rho(m)\right) = \max\left(\frac{\hat{R}_{a,b}(m)}{\sqrt{\hat{R}_{a,a}(0)\hat{R}_{b,b}(0)}}\right) \tag{5.2}$$

$$D = t_{s_1,pt} - t_{s_1,th} \tag{5.3}$$

where $\hat{R}_{a,b}$ is the estimated correlation between a and b (i.e., therapist or patient trajectory, ATC or FES profile) and m is the lag between the signals.

Also a complementary analysis has been performed by evaluating Range Of Motion (*ROM*), rise velocity (v) (i.e., the velocity of the concentric phase of the movement), and area under the curve (A) quantities, calculated as follows:

$$ROM_x = e_{\max,x} - e_{s_1,x} \tag{5.4}$$

[2]Here intended as the information flow from the therapist to the patient: therapist movement - ATC values; ATC values - FES parameters; FES parameters - patient movement

$$v_x = \frac{\Delta e}{\Delta t} = \frac{e_{s_2,x} - e_{s_1,x}}{t_{s_2,x} - t_{s_1,x}} \tag{5.5}$$

$$A_x = \sum_{i=s_1}^{s_4} \left(e_{i,x} - \min\left(e_{s_1,x}, e_{s_4,x}\right) \right) \cdot t_s \; - \; \frac{\left|e_{s_4,x} - e_{s_1,x}\right| \cdot \left(t_{s_4,x} - t_{s_1,x}\right)}{2} \tag{5.6}$$

where t_s is the Vicon sampling period (i.e., 10 ms).

The use of these three additional features extracted from the trajectory effectively complete the qualitative analysis about the executed movements. Fall velocity (i.e., the velocity of the eccentric phase of the movement), on the other hand, was not taken into account since the focus of the tests is addressed to the active phase of the movement.

Fig. 5.13 reports an example of the results of the proposed segmentation algorithm, also providing the figurative concept of all the extracted parameters.

In Equation 5.6, the subtraction of $\min\left(e_{s_1}, e_{s_4}\right)$ takes into account the possibility of negative excursion values caused by baseline oscillation. Indeed, after some movement repetitions, the baseline usually differs from zero because the subject does not always return to the starting reference position (see Fig. 5.13(b)). The second term of Equation 5.6 takes into consideration the effect of the baseline changes in terms of computed areas by removing over-estimation, as depicted by red dashed area in Fig. 5.13.

In conclusion, in order to evaluate relative, rather than absolute, quantities, parameters *ROM*, v, and A extracted from each patient movement are normalized to those obtained from the corresponding therapist one as reported in Equation 5.7:

$$X_{pt/th} = \frac{X_{pt}}{X_{th}} \cdot \frac{\max(ROM_{th})}{\max(ROM_{pt})} \tag{5.7}$$

where X can be *ROM*, v, or A.

Therefore, each parameter is referenced to the maximum *ROM* value obtained from each subject to consider her/his maximum excursion capabilities.

5.4.3 Results and Discussion

This section reports the results, and their discussion, to properly evaluate the functional behavior of the proposed system. The experimental analysis about the volun-

Table 5.7 Extracted parameters for motion assessment [167].

Param.	**Description**
$\rho_{\max}$	Maximum normalized cross-correlation coefficient
D	Delay between therapist and patient movement
ROM	Movement excursion
v	Limb velocity during concentric phase
A	Area under angular trajectory
SR	Successful rate of movement replications

tary and stimulated movements replication is here reported, discussing the appropriateness of ATC-FES approach w.r.t. the descriptive parameters extracted from the limbs trajectories. Table 5.7 summarizes the evaluation parameters used for the following discussion.

Fig. 5.14 and 5.15 show the results of the comparison analysis, between the therapist and patient angular data, for all the extracted parameters, which are organized into box plots to adequately represent the information variability of each movement along the total number of repetitions. Furthermore, the median value has been used to synthesize the test outcomes because it adequately describes a population of measurements while being more robust (to the outliers) than the mean value.

Since the real-time control of the stimulation still remains one the major aspect for this application, giving the possibility to the therapist to correct her/his movement according to the one executed by the patient, the delays in movement reproduction have been extracted. Delay values (see Fig. 5.14 (a)) are generally up to about 100 times higher than the computational latencies of the control software, which, considering the PC as the platform to run this experimentation, is typically within 6 ms (as demonstrated in Section 5.3). Indeed, the computational delay has to be summed to the 130 ms of implicit delay due to the use of the ATC window. In addition, the measured delay also includes the lag between the onset of the therapist movement and the first TC events indicating muscle activity. Finally, an additional delay component is the physiological response time between the start of the stimulation and the beginning of the movement, usually known as ElectroMechanical Delay (EMD) [174], which can be over 300 ms [175]. The highest median value of replication delay, equal to 1.08 s, has been obtained during knee extension repetitions while the lowest results have been found for ankle flexion, calculating a median value

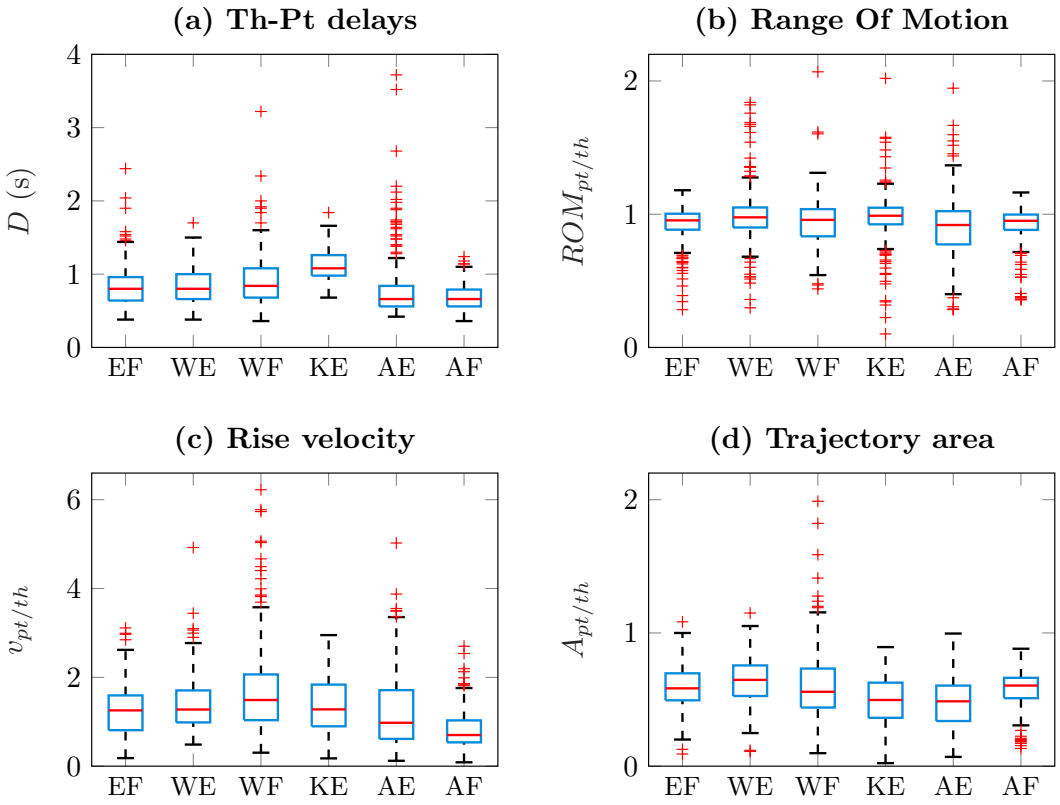

Fig. 5.14 Comparison of the features extracted by therapist and patient trajectories among all the repetitions. Movements acronyms are defined as follows: Elbow Flexion (EF), Wrist Extension (WE), Wrist Flexion (WF), Knee Extension (KE), Ankle Extension (AE), Ankle Flexion (AF). Please refer to Equation 5.7 to see the normalization performed for the features presenting the subscript pt/th [167].

equal to 660 ms. The significant difference between these two movements, which both act against gravity, is that the *tibialis anterior* muscle reaches its maximum activation values after few degrees of excursion, while the *quadriceps femoris* muscles are mainly activated during the last stages of excursion, when the load has the greatest weight. Following the above discussion, these delay values, with an overall median of 800 ms, are sufficiently low to permit the therapist to adjust and modulate her/his movement in response to the patient's activity. This possibility surely increases the application versatility of the proposed system since it gives the user the opportunity to control the stimulation during the session, e.g., updating the FES intensity to help the patient reach the target exercise according to the subject's physical abilities.

Looking at Fig. 5.14 (b), the median of the obtained $ROM_{pt/th}$ values is about 1 (0.92 to 0.99) for all movements. This can be discussed considering that, in general, the experimental protocol avoids the onset of muscle fatigue, which would affect the patient's movement more than the therapist one, because the excursions were proportional between the two subjects. However, a discrete presence of outliers, indicating a limited excursion by the patient, concerns both the knee and wrist extension movements. For the knee extension, these outliers are related to the lack of ATC values sufficiently high to generate a stimulation intensity suitable to complete the execution of the movement, also considering both the weight of the leg and how gravity acts w.r.t. initial reference position. This issue could be solved by adapting the calibration strategy to update the reference ATC values since, with the progress of the exercise, the therapist may express lower values than those obtained during the calibration phase. Instead, for wrist extension the outliers are related to the fact that, during the tests, each repetition of wrist extension did not alternate with a repetition of wrist flexion. Hence, sometimes the patient's wrist did not return to the same starting position (see Fig. 5.13 (b)), thus reducing the resulting *ROM*. In particular, in order to understand the periodicity of this behavior, it was calculated how many times the voluntary return of the wrist at its reference position features a baseline drop greater than 20 % of the total excursion performed, resulting in the limited amount of 4 % of the total wrist extension repetitions.

With the exception of ankle movements, the rise velocity comparison (Fig. 5.14 (c)) presents $v_{pt/th}$ with medians greater than 1: the movement of the patient, in fact, is typically faster than the one of the therapist due to stimulation effect. While for ankle extension the median $v_{pt/th}$ is equal to 0.98, for ankle flexion it is 0.70. A plausible explanation for having lower values for these movements is that the ankle joint is also the one with the lowest *ROM* among those analyzed: hence, both the subjects soon reach the maximum joint excursion.

The area comparison box plot (Fig. 5.14 (d)) shows median $A_{pt/th}$ values between 0.49 and 0.65 among the tested movements. Considering that the areas are normalized over the maximum *ROM* obtained from the respective subject, this comparison parameter is strictly dependent on the movement replication delays. Indeed, the delay mainly affects the beginning of the movement, whereas the end of the activity of the two subjects is almost simultaneous (the calculation of the median delay in ending the movements is of about 20 ms). Moreover, the area also includes an overall information related to the shape of the trajectory, thus being dependent on

the rise velocity. In fact, ankle flexion and extension involve similar replication delays (their median value is equal to 660 ms) but this behavior is not reflected by the corresponding $A_{pt/th}$ (median values of 0.48 for AE and 0.60 for AF). This aspect can be justified by looking at rise velocity box plot (Fig. 5.14 (c)), where the $v_{pt/th}$ value results in ankle extension movements (0.97) faster than ankle flexion (0.70), thus reducing the area under the curve.

The correlation for each step of the information transfer (i.e., movement to ATC, ATC to FES, FES to movement) is reported in Fig. 5.15.

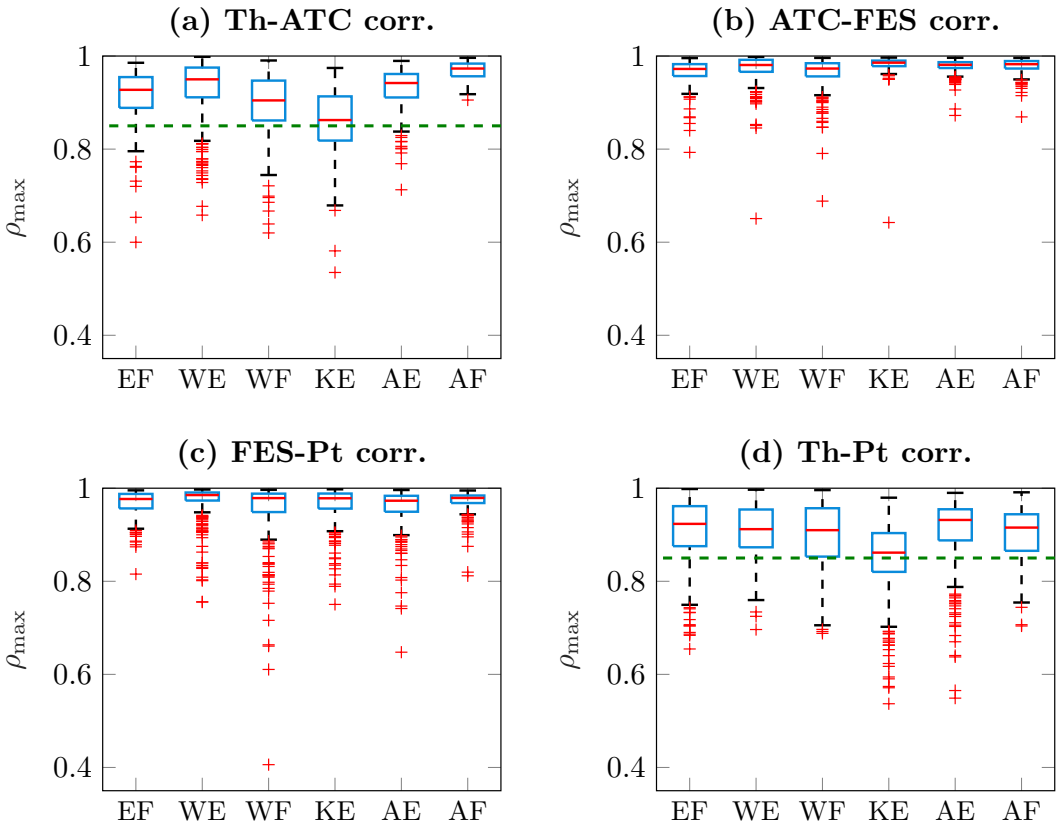

Fig. 5.15 Maximum of the cross-correlation coefficient ($\rho_{\max}$) for each step of the information flow, divided among movement types: Elbow Flexion (EF), Wrist Extension (WE), Wrist Flexion (WF), Knee Extension (KE), Ankle Extension (AE), Ankle Flexion (AF). The green dashed line at $\rho_{\max} = 0.850$ in (a) defines the threshold used for the classification of *ATC poor*, whereas in (d) indicates the selected acceptability threshold for the overall correlation (i.e., therapist and patient trajectories similarity) [167].

As regards $\rho_{\max}$ between therapist trajectory and ATC profile (Fig. 5.15 (a)), the highest results have been obtained for wrist extension, ankle extension and ankle flexion, with the median of $\rho_{\max}$ equal to 0.950, 0.942, and 0.973, respectively. A considerable contribution to these outcomes is that, for these three cases, the muscle activity is easily detectable during the whole execution of the movement, thus increasing the overlap between the therapist trajectory and the corresponding ATC profile. While for elbow flexion and wrist flexion the median of $\rho_{\max}$ is still quite high (0.927 and 0.905, respectively), for knee extension its value decreases to 0.862. In fact, as discussed above, the main activity occurs during the isometric phase of the KE movement, rather than during the concentric or eccentric one, resulting in a perceived discrepancy between the trajectory and ATC profiles.

The median values of $\rho_{\max}$ among ATC and FES profiles (Fig. 5.15 (b)) are always higher than 0.970, since the only non-linearity during the ATC processing is the moving median operation (Section 5.2.4).

Also for the correlations between the FES profiles and the patients trajectories (Fig. 5.15 (c)) the computed values are sufficiently high, although the presence of a greater number of outliers related to the cases which presented a stimulation profile not adequate completely execute the movement.

Last, for $\rho_{\max}$ among therapist and patient limb trajectories (Fig. 5.15 (d)), an acceptability threshold equal to 0.850, consistent with what is found in the literature [138, 176, 137], has been chosen to properly classified the success or failure of the movement reproduction. The obtained median value among all the executed exercises is equal to 0.910, largely satisfying the chosen constraint. Going into details, the lowest result has been obtained for knee extension, with a median value of $\rho_{\max}$ equal to 0.861, as a consequence of what has been discussed before. The highest outcomes, instead, have been obtained during ankle extension and elbow flexion repetitions, with median values equal to 0.931 and 0.923, respectively. For ankle extension, such a high $\rho_{\max}$ is not surprising, since among the six proposed movements this is the simplest one, with the lowest excursion.

In order to account also for movements not replicated by the patient, a labeling operation has been achieved to classify the reason of the failures, as reported in Table 5.8. If the $\rho_{\max}$ between the therapist trajectory and the ATC profile is lower than 0.850, the movement is classified as failed for *ATC poor*. Otherwise, if the

Table 5.8 The total number of repetitions for each type of movement (e.g., EF, WE) has been analyzed to classify the replication outcome: a *valid* label means that the therapist and patient trajectories are almost similar; otherwise, an unsatisfactory replication of movements is marked as *ATC poor*, *FES poor*, or *FES ineffective* depending on the cause of failure. The Successful Rate (*SR*) is calculated as the percentage ratio between the valid and total movement repetitions [167].

ID	Total	Valid	ATC poor	FES poor	FES ineff.	SR %
EF	273	263	7	2	1	96.34
WE	260	254	2	3	1	97.69
WF	290	282	1	5	2	97.24
KE	256	249	5	1	1	97.27
AE	264	255	3	1	5	96.59
AF	250	248	0	1	1	99.20

failed movement is consecutive to a stimulation pattern with a maximum intensity 60 % lower than the stimulation value established during calibration, the *FES poor* label is associated. Lastly, if the failure of the movement is not ascribable to either of these two cases, the movement is classified as *FES ineffective*. From these labels, the Successful Rate (*SR*) parameter has been defined as the number of valid repetitions over the total ones, to summarize the replication success for each tested movement. Even if the SR values are satisfactory for all the tests, it is interesting to note that elbow flexion and ankle extension are the movements with the lowest reproduction rate (below 97 %), although their (median) cross-correlation coefficient is the highest among all the movements.

This final outcome, in addition to the above discussion, points out how a multi-parameters approach is needed to characterize an FES system effectively: the motor control and the movement reproduction could not be described simply by analyzing the cross-correlation coefficient among the therapist and patient trajectories, but additional parameters (e.g., area, velocity) and the evaluation of the FES definition process (i.e., Fig. 5.15) are essential to better understand the effectiveness of an induced movement.

In conclusion, a last analysis takes into account how the variable execution of an exercise could have consequences on movements reproduction. Indeed, although the execution of a movement has been standardized as much as possible (e.g., by defining a reference posture), a variability among therapists actions needs to be considered. Rise velocity and movement duration have been selected as the parameters able to discriminate the difference in therapist movements, as it can be seen by the boxplots (e.g., looking at whiskers) in Fig. 5.16 (a) and (b). For the sake of the synthesis, here the discussion of these results is focused on the cross-correlation coefficient: $\rho_{\max}$ between the therapist and patient trajectories was computed for all cases in which these two parameters are greater than the third quartile (Q3) (Fig. 5.16 (c) and (d)) or less than the first quartile (Q1) (Fig. 5.16 (e) and (f)). Comparing all the permutations of movement velocity and duration, each combination still ensured a median $\rho_{\max}$ above the defined acceptability criteria ($\rho_{\max} \geq 0.850$), although slower movements (lower rise velocity and longer duration) featured lower $\rho_{\max}$ values.

The last aspect to be taken into consideration regards the variability of the human response to FES, related to the calibration process. Indeed, while the effect of the modulated parameter (i.e., pulse amplitude) has been discussed by analyzing the information transfer process, also the initial setting of the non-modulated features (i.e., pulse width and stimulation frequency) could impact the outcomes of the tests. Although a reference manual [168] has been used to determine their standard values (for each experimental exercise), sometimes both pulse width and frequency have been varied from the normal values to better achieved the functional movement execution or to meet the patient needs (e.g., reduce the perceived discomfort). Their adjustment could have effects on the performance indicators: for example, an increase of both pulse width and frequency generally brings to the injection of higher energy through the muscular tissue corresponding with a greater probability of developing muscle fatigue, which could affect the quality of the replicated movements over time (e.g., decreasing of *ROM*, *Area*, and $\rho_{\max}$); differently, a decrease of these quantities could easily prevent muscle fatigue, but could also reduce the possibility to effectively complete the tested movement caused by the lack of proper FES intensity.

A similar discussion involves the positioning of FES electrodes w.r.t. the muscle fibers to elicit. Despite proper guidelines [141, 169] have been followed, the body anatomy of each subject has been taken in consideration too, leading to an electrode

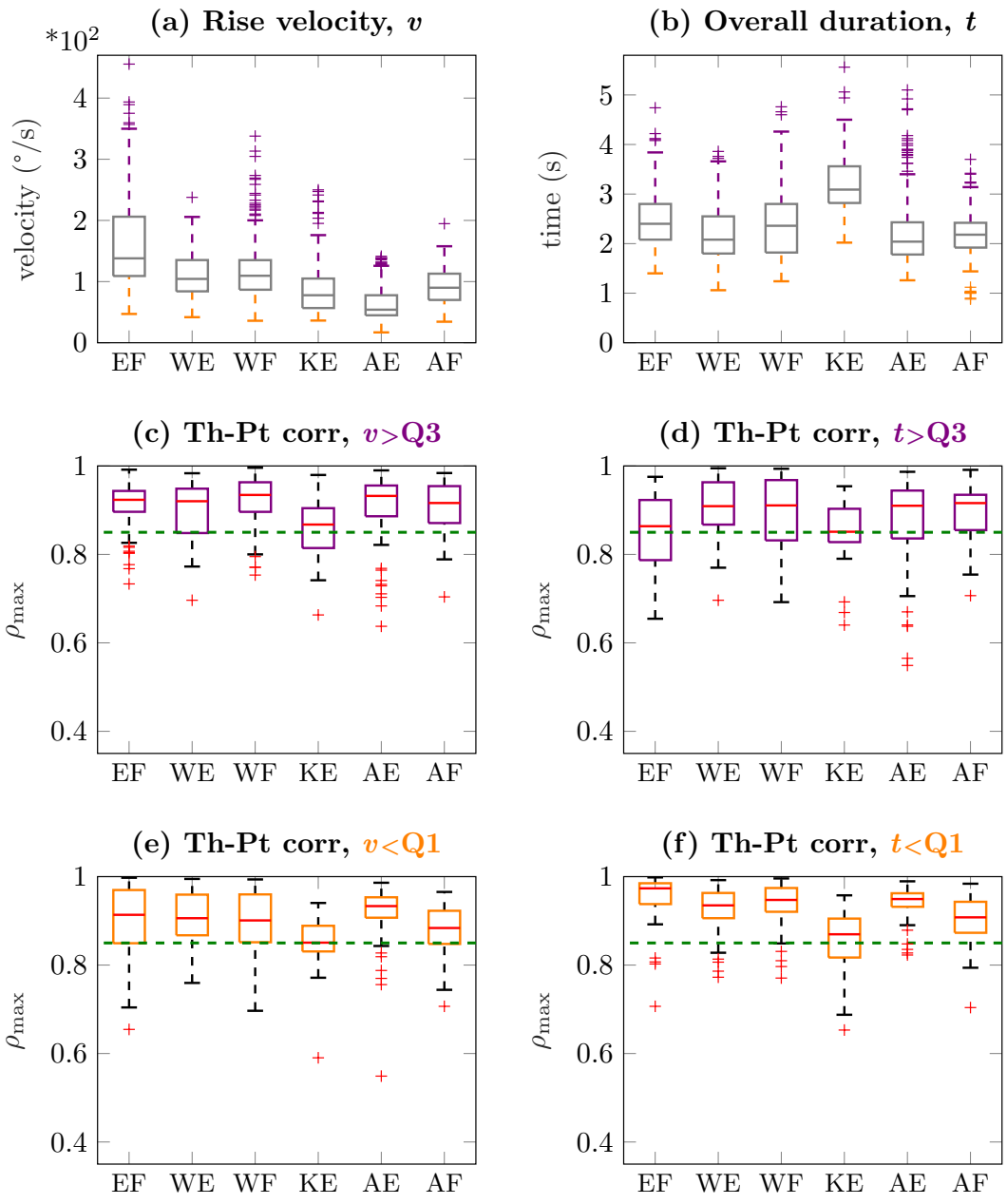

Fig. 5.16 Movements execution variability among different therapists in concentric phase velocity (a) and overall movement duration (b). Sub-figures (c) and (d) report therapist-patient cross-correlations obtained when velocity and duration are above Q3, respectively. On the other hand, (e) and (f) report what was obtained below Q1 [167].

placement that could differ from the manual standards. Also in this case, (marginal) differences in the electrode positioning could implicate diversities in the test out-

comes, because, e.g., the body stimulation volume could consist of different muscle segments (or fibers), and could excite them along different directions.

However, although the effects of these contributions could be attributed to specific (per-subject) tests, their generalization to the whole population of subjects is still an open issue, which will be analyzed more carefully in future works.

5.5 Comparison with SoA works

Despite the differences among the state-of-the-art systems for the active control of the FES, which space from bio-signals recording to bio-mechanical angular analysis, a brief (almost inclusive) comparison with other similar works is reported in Table 5.9.

Looking at the *Control* column, representing which methodologies and sensors have been studied by different researchers, it is possible to see that the innovative aspect of the proposed system mainly regards the modulation of the stimulation intensity based on the ATC event-driven technique, which provides the information (already processed) about the muscle activity without even sampling the sEMG signal. Other works [176, 137–139, 136], instead, usually employs time-domains features extracted by the digital analysis of the sEMG signal, which, depending on the machine computing these parameters (e.g., computer, microcontroller), could have a heavier or lighter impact on the computational effort and FES responsiveness. Moreover, the above sEMG strategy can be also combined with angular data extracted using IMU sensors [177] or wearable electrogoniometers [144], which, although they collect a wider information spectrum, increase the complexity of the system, also impacting on its portability and setup simplicity.

Focusing on the FES modulation (*Mod* column), among the settable pulse features, some groups [139, 136] implement the pulse amplitude (PA) approach, as in this work, while others prefer to achieve the control of pulse width (PW) or frequency (f), probably because they better fits their experimentation or depending on the features of the used stimulator.

Passing to the experimental setup, this work analyzes different flexion-extension joints movements (see *Mov* column), which are at the basis of rehabilitative protocols, mimicking therapist-patient sessions. The literature studies reported in the table also selected the same movements, someone following the similar physioterapic procedure with two people, others studying the closed-loop self-stimulation. Generally, the works in Table 5.9, this one comprised, conducts the experimentation on an healthy population (with the exception of [138] and [144]) in order to prove the feasibility and correctness of the developed system before to proceed towards an experimentation with pathological subjects.

Moving now to the analysis of the figures of merit, looking at the performance of the proposed ATC-FES system with the ones of the research group who pub-

Table 5.9 Comparison among recent state-of-the-art works for FES control [167].

Work	Control	Mod[1]	Mov[2]	Population	Th-Pt[3]	Evaluation Parameters
[157]	Hybrid FES exoskeleton	PW	EF	7 healthy	No	94 % tracking error reduction and less 74 % control effort w.r.t. exoskeleton alone
[176]	Time-domain sEMG features	PW, f	W	6 healthy	Yes	*Delay* $<$ 300 ms; $\rho_{\max} > 0.840$; *mean(SR)* = 92.5 %
[137]	Time-domain sEMG features	PW, f	AE, AF	6 healthy	Yes	*Delay* $<$ 300 ms; $\rho_{\max} > 0.820$; *mean(SR)* = 92.5 %
[138]	Time-domain sEMG features	PW f	W	6 hemiplegic, 1 healthy	Yes	*Classification accuracy* $>$ 90 %; *mean(Delay)* = 270 ms; *mean*($\rho_{\max}$) = 0.840
[139]	Time-domain sEMG features	PA	W	2 healthy	No	*Classification accuracy* = 100 %; *mean(Delay)* = 600 ms (CCFES scenario)
[136]	sEMG envelope	PA	HG, OH	1 healthy	No	*mean(Classification accuracy)* = 81.72 %; *Delay* $>$ 2 s (CCFES scenario)
[144]	Angular velocity, EMG modeling	PW	AF	10 healthy 6 drop foot	No	*mean*($\rho_{\max}$) = 0.902 between FES-evoked EMG and natural EMG during gait
[177]	Angular velocity flexion angle	PW	AF	10 healthy	No	*Goodness of fit* = 77.87 % between real and reference ankle trajectories
This	ATC	PA	AE, AF, EF, KE, WE, WF	17 healthy	Yes	*median(Delay)* = 660 ms to 1080 ms; *median*($\rho_{\max}$) = 0.861 to 0.931; *SR* = 96.34 % to 99.20 %

[1]FES modulation: PA - Pulse Amplitude, PW - Pulse Width, f - frequency
[2]Movement: AE - Ankle Extension, AF - Ankle Flexion, EF - Elbow Flexion, HG - Hand Grasp
KE - Knee Extension, OH - Open Hand, W - Wrist movements, WE - Wrist Extension
WF - Wrist Flexion
[3]Therapist-Patient approach

lished [176, 137, 138], a potential margin for improvements can be identified w.r.t. the delay of movement replication. Indeed, although the computed delays are comparable with [139] and lower than [136], the further decrement in system latency for obtaining a functional movement achieved by [176, 137, 138] could improve the benefits of the mirror control in a rehabilitation scenario (e.g., promoting neural plasticity).

Looking at the system applicability, the main difference between [138] and this system consists in the the use of a custom stimulator, while both the works developed an architecture for controlling the FES in an autonomous way. However, in [138] there is not a control platform and the FES parameters are directly defined on the acquisition node. As already introduced, from one side, a completely embedded

system (with no GUI) could be appealing in implementing an autonomous and wearable system to be employed by the patient at home without supervision. Still, if a clinical trial needs to be performed, the user looses the possibility to actively monitor the ongoing of the stimulation in this configuration. On the other side, dedicated FES solutions [138] (e.g., stimulator algorithms and structure) optimize the effectiveness of the stimulation for a set of movements but reducing the application versatility of the system at different body parts.

Nevertheless, considering the analyzed case study, the proposed ATC-FES system shows good performance in controlling an induced motor activity (e.g., assessed by cross-correlation and successful rate parameters), featuring some of the highest values if compared with the figures of merit proposed in the other works.

Chapter 6

Application - Hand Gesture Recognition

[1] During the last decade, hand gesture recognition has been increasingly investigated by both academia and industry, following the versatility and easiness of its implementation. Indeed, thanks to technology progresses in the electronics fields, the recognition of hand movements can be now performed directly with body sensors [178], without the needing of a complex equipment, making it one of the best candidates for data processing in Human-Machine Interface (HMI) systems. A common approach is to acquire the sEMG signals from the forearm (by easily applying electrodes on the skin surface), which provide the information about the activation of the musculoskeletal system, directly reflecting the execution of a particular movement.

The main market response to this phenomenon is surely the realization of the Myo armband by Thalmic Labs, which is composed by 8 channels for the acquisition

[1] Disclaimer: This Chapter contains some parts and arguments taken or (partially) rephrased of the following published works:

- A. Mongardi, P. Motto Ros, **F. Rossi**, M. Ruo Roch, M. Martina and D. Demarchi, "A Low-Power Embedded System for Real-Time sEMG based Event-Driven Gesture Recognition," *2019 26th IEEE International Conference on Electronics, Circuits and Systems (ICECS)*, 2019, pp. 65-68, doi: 10.1109/ICECS46596.2019.8964944.
- A. Mongardi, **F. Rossi**, A. Prestia, P. Motto Ros, M. Ruo Roch, M. Martina and D. Demarchi, "Hand Gestures Recognition for Human-Machine Interfaces: a Low-Power Bio-Inspired Armband," in *IEEE Transactions on Biomedical Circuits and Systems*, 2022, doi: 10.1109/TBCAS.2022.3211424.

of surface ElectroMyoGraphic (sEMG) signals. Thanks to its capability to adapt to many different scenarios [179], this armband received a huge positive feedback from the community. Indeed, even if its production was halted some years ago, the literature is still packed with contributions which involve the Myo armband as the main acquisition device [180–183], exploiting its small, compact design which fits into many different practical applications. On the other hand, there are still many studies where the circumstances demand the design of a custom armband, e.g., to address specific constraints like low power consumption [184] or low noise contribution on the signal [185], or to obtain solutions with augmented functionalities and an increased number of recognized gestures [186–190].

Therefore, the large availability of commercial devices and the knowledge acquired by multiple research groups around the world, made hand gesture recognition be involved in many HMI use-cases, starting from the most common computer interaction [191] or outdoor music handling [192], through biomedical applications like prostheses [193–195] and robotic arm control [183, 196, 197], to sign language communication [198, 199], which requires a lot of sensitivity in recognizing each single finger movements. Furthermore, by exploiting the other actor of the HMI (i.e., the machine), hand gesture recognition can be involved also in the emerging (tele-)rehabilitation field, both with passive and active approaches. Indeed, standard rehabilitative sessions can motivate the patients making them interact with the so-called serious games [200–202] or by giving them more simple feedback during movements execution [203–205]. On the other hand, for people which are not able to autonomously perform the rehabilitation routine, the therapist can, for example, apply the functional electrical stimulation on the injured muscle(s), both involving data compression [206] and maintaining the association of the gestures one by one.

Regarding the features involved in the recognition, many studies take the raw sEMG signal as input, sampling wide time windows (e.g., longer than 250 ms) on the available channels and, in most cases, feeding a deep learning algorithm like the Convolutional Neural Network (CNN), which can be configured with multiple internal structures [193, 207, 208] emulating the functions of the human brain. Furthermore, few studies tried to exploit the real brain behavior as the classifier for hand gesture recognition, both designing liquid spiking network structures [209] and trying to directly classify the brain electrical signals [204]. However, considering the strong spreading of Internet of Things (IoT) applications and the increasing use of embedded devices, some studies [205, 210–212] focus on the implementation

and on the optimization of less complex Machine Learning (ML) algorithms (e.g., Artificial Neural Networks (ANN), Support Vector Machines (SVM) and Decision Trees (DT)) to fulfill the requirements of most common microcontrollers, which typically have less than 1 MB of memory space and cannot perform computations at high speed.

Considering the above scenario, this chapter of the thesis reports the studies about gesture recognition carried out during the Ph.D. activities, with the final aim to design a multi-channel custom armband. As for the FES application, also in this case the armband prototype is developed by using the custom acquisition device, i.e., the *Apollux*. Therefore, as better described in the related sections, slightly re-adapting the geometry of the case, and re-configuring the firmware, a set of *Apollux* units are arranged together to build an armband for HMI applications.

Next sections are organized as follows: Section 6.1 introduces the background studies investigating the ATC as input features for hand gesture classification; Sections 6.2 and Section 6.3 report two minimal setups (based on the *Apollux* units) to achieved ATC-HMI interfaces with three or more degrees of freedom; then, Section 6.4 (the longest one) describes in details all the designing and prototyping phases for the realization of the armband, also focusing on its experimental validation and discussing its pros and cons w.r.t. similar state-of-the-art works.

6.1 Introduction to ATC-based classifiers

The first work of our research group about the use of the ATC parameter as input feature for machine learning algorithms has been reported in the master thesis's work [213]. The study started by collecting a dataset of muscular signals acquired from the forearm muscles during the execution of five hand gestures [214, 215] (i.e., Figure 6.1), one passive (rest condition) and four active (refereed to the passive one):

- Idle state: the hand is maintained in steady position with the same axis of the forearm, trying to relax forearm muscle and without contrasting gravity;
- Wrist extension: the back of the hand moves towards the distal part of the forearm;
- Wrist flexion: the palm of the hand bends on the inner arm;
- Radial deviation: the hands moves up following the direction of the extended thumb;
- Grasp: all the fingers close towards the hand palm.

The *flexor digitorium superficialis*, *flexor carpi ulnaris* and *extensor carpi ulnaris* have been selected as the muscles primarily active during the gestures [216], whose activity has been monitored by placing exploring electrodes on muscle belly and the reference one at wrist location. A total of ten subjects have been enrolled for the dataset collection, each one performing the gestures with minimal force intensity.

At the time, the acquisition board [217] featured slight differences (e.g., gain, bandwidth) from the proposed one (i.e., *Apollux*); therefore, it required the use of the National Instruments NI-6251 device to sample both the sEMG and TC signals. As

Fig. 6.1 Selected hand gestures.

partially introduced in Section 1.5, a preliminary analysis on this dataset determined the use of an ATC window of 130 ms as an adequate trade-off among the amount of TC events suitable to discriminate different force levels (for several movements at 30 % and 70 % of MVC), the classification accuracy, and the overall latency of the system (which has to fulfill the upper limit of 300 ms for soft real-time applicability). In addition to the ATC data, common sEMG features (e.g., MAV, RMS, WA) have been also extracted to carry out a comparison between the standard approach and the event-based one.

The SVM classifier has been trained and tested on the MATLAB software obtaining an overall accuracy of 92.87 % for ATC and 98.21 % for sEMG [69]. Although the ATC classification performance appeared slightly lower (i.e., −5.34 %) than the sEMG one, the ATC technique showed promising results in terms of system processing stages latency: indeed, the ATC computing required only 5 ms versus the 74 ms needed by the extraction of the sEMG features, totally demonstrating the the low computational load of the event-based processing; moreover, the advantages of this approach are also reflected on the prediction latency (i.e., 55 ms ATC vs. 63 ms sEMG) which, although the both values present the same order of magnitude, highlight the fastness ($\simeq$ 14.5 % time saved) of the ATC prediction. In light of these findings, also considering the benefits of transmitting the TC events w.r.t. sEMG values (see Section 1.5), the intention towards further investigations on an ATC-based classifiers has been reinforced.

In [218, 94, 70], the previous work has been continued by moving the classifier from the software level to the microcontroller firmware, thus addressing and studying the performance of the ATC classification on an embedded system. Therefore, this new scenario evolves from the architecture of the previous one because it predicts the hand gestures directly on the sensing node, with the final purpose to stream only the class result. The Ambiq Apollo2 MCU [219] has been selected as the processing core since its ultra low power performance, combined with an ARM Cortex-M4F processor, made it a good choice for implementing embedded machine learning algorithms.

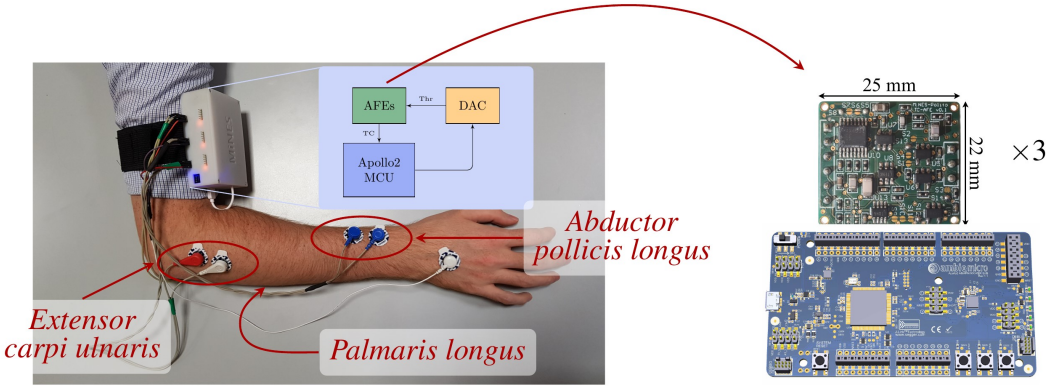

Fig. 6.3 Wearable setup for ATC-based gesture classification application with three electrodes configuration. [70]

Moreover, the ulnar deviation gesture, which, opposite to the radial deviation, consists in moving the hand down along the little finger direction (Figure 6.2), has been added to the gesture collection.

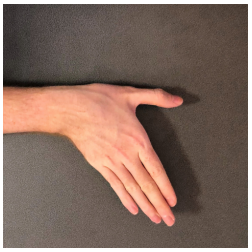

Fig. 6.2 Hand ulnar deviation.

Figure 6.3 shows the wearable setup for the creation of a new ATC-gesture dataset, the offline training of classifiers and their validation during the online test phase. The system, contained inside the white resin box, is composed by three AFEs (a previous version of the *Apollux* one discussed in Section 2.2, but functionally equivalent), the evaluation board of Apollo2 MCU and a 9 V alkaline battery as supply source. Although the physical dimensions of the prototype are still far from a typical embedded device, the use of the evaluation module made this feasibility analysis simpler and faster. The monitored muscles slightly differed from previous work: the *extensor carpi ulnaris* has been selected to detect hand related extension movements, the *palmaris longus* has been chose as superficial forearm flexor, and the *abductor pollics longus* exhibits the activity of the thumb [216].

The functionalities of the system comprise an automatic calibration phase to set up the proper threshold for each channel, the streaming of the ATC data, or the prediction of the hand movements.

The acquisition campaign for the algorithms training phase involved 20 subjects, each one performing the entire list of six movements for three sessions. Each movement has been maintained for 13 s to obtain a total of 100 ATC values (considering

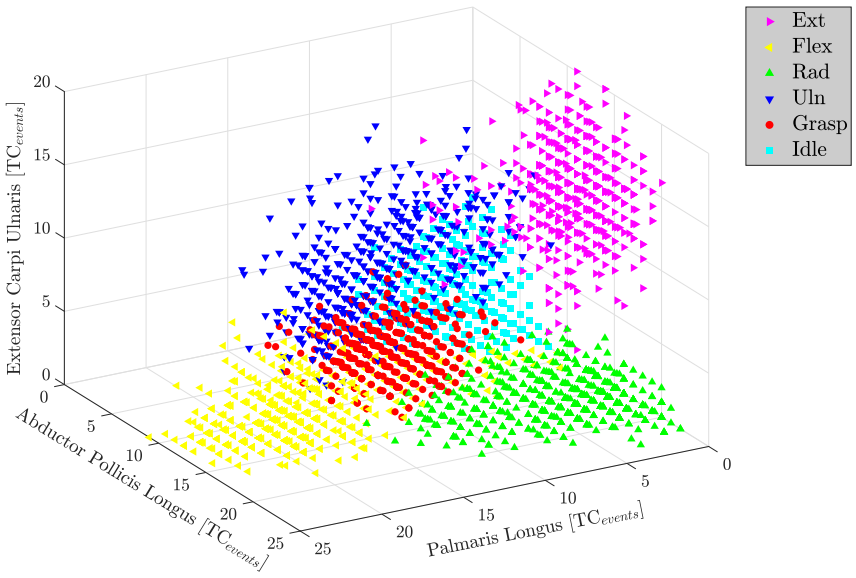

Fig. 6.4 Labeled dataset for hand gesture movements [70]. The clusters, related to each movement typology, are quite distinguishable in the 3D space.

the ATC window of 130 ms) per repetition. A rest period of 10 s has been assured among the repetitions, and it is increased to 1 min between the sessions in order to prevent the muscle fatigue of arm and forearm muscles which have to contrast the gravity during the acquisition. A partial 3D-visualization of the acquired dataset after the labeling operation is shown in Figure 6.4.

Since the purpose of the project was to maintain low-power consumption and (consequently) low-complexity computations to better fit a wearable device, and considering the small dimension of the TC input matrix (3 inputs $\times$ 1 ATC window), the Neural Network (NN) algorithm has been selected. The training has been carried out in MATLAB environment using a fully-connected NN operating with a simple back-propagation algorithm [220]. The training and hyperparameters tuning algorithms provided as output an NN architecture made of 2 hidden layers of 26 neurons each, which demonstrated to be the best one fulfilling the trade-off between run-time performance and accuracy. The network has been then implemented on the Apollo2 MCU using the CMSIS-DSP ARM library [221], which provides basic math functions suitable to perform the direct matrices multiplication of the back-propagation algorithm matching the low-power capability of the ARM Cortex-M4F.

The testing phase involved five new volunteers, each one performing all six gestures in a random order to prove system robustness. No feedback has been provided

Table 6.1 Comparison among ML algorithms tested on the dataset acquired in [218].

Algorithm	**Accuracy (%)**	**Computational time (s)**	**Power consumption (mW)**
NN	96.34	8.5	0.80
SVM	94.45	54.8	0.93
RF	94.23	185.5	0.51
K-Means	92.15	61.9	0.51
NB	93.83	140.5	0.37

to the participants in way to avoid bias and the possibility to adjust limb posture during movement execution. The classifier demonstrated an overall accuracy of 96.34 % while predicting the class in 8.5 ms. The power consumption has been measured during both the idle (0.70 mW) and active (2.05 mW) phases obtaining an average value of 0.80 mW considering the duty cycle of 6.5 % (i.e., 8.5 ms over 130 ms).

A more extensively analysis on this novel dataset has been conducted in the [222, 223] master thesis works. Here, in addition to NN, also the SVM, Random Forest (RF), K-Means, and Naive Bayes (NB) algorithms has been trained and tested online. Their results in terms of accuracy, computational time, and power consumption have been reported in Table 6.1: all the classifiers proved a satisfactory accuracy and a suitable power consumption but RF and NB require a prediction time too large w.r.t the ATC window used.

Although above analyses confirm the feasibility of embedded ATC-based classifiers for the recognition of hand movements with performance appropriate for a wearable device, three issues still needed to be addressed:

1. A three electrodes configuration limits the amount of gestures to be recognized. Moving to a model based on additional features would enrich the application, giving enhanced user control.

2. Surface electrodes have to be placed following anatomical muscles fascicles, thus requiring physiology competency by the user. A misplacement could carry to a degradation of the accuracy up to 30 %.

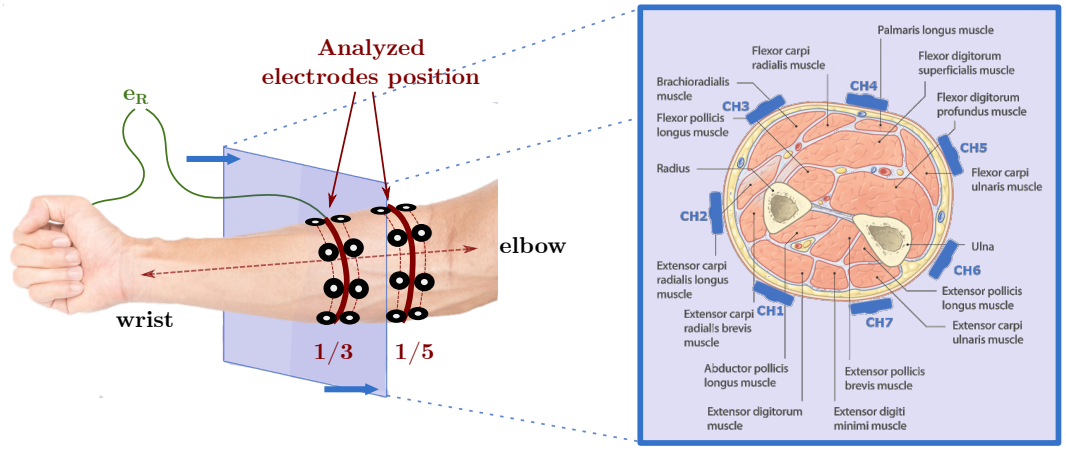

Fig. 6.5 Analysis on the electrodes position and their arrangement around the forearm [223].

3. The system wearability is compromised by encumbrance of the cable which connect distal and proximal electrodes to the central unit. A more versatile solution (e.g., different sEMG sources, anatomical comfort of the device) would permit any user to wear the system without limiting her/his freedom of motion.

The above points started to be addressed in the master thesis' work [223]. The main focus was to change the system structure by arranging it in a more compact and comfortable solution, also acquiring the muscular information from more channels than the previous application. Searching the literature [224–226], an armband arrangement has been identified as the proper configuration to record multiple sEMG signals from an entire section of the forearm.

Figure 6.5 shows the preliminary studies towards the realization of the armband. The first step consisted of discerning at which forearm section the sEMG signals can be recorded at sufficient energy. A total of seven couples of electrodes (trade-off among the number of features, electrode size, and forearm circumference) have been placed around the forearm at $1/3$ and $1/5$ of the distance between the elbow and the wrist, since muscle bellies result more accessible at these locations. Standardization of the placement of the electrodes has been followed by placing the first couple above the *extensor digitorum* and then equally spacing the others continuing along the medial section [227]. The sEMG signals have been acquired using the g.HIamp-Research amplifier [228] during the execution of some gestures, and they have been processed to assess which of the two

Table 6.2 Summary of the ATC-based investigations for hand gesture recognition.

Work	#Channel	#Gesture	Algorithm	Embedded	Accuracy (%)
[69]	3	5	SVM	yes	92.8
[70]	3	6	NN	yes	96.3
[222]	3	6	SVM	yes	89.5
	3	6	K-Means	yes	83.3
[223]	3	6	RF	yes	82.7
	3	6	NB	yes	83.0
	7	8	NN	no	80.3
	7	8	SVM	no	78.1
	7	8	K-Means	no	35.7
	7	8	RF	no	78.9
	7	8	GMM NB[1]	no	70.9

[1]Gaussian Mixture Model Naive Bayes

locations exhibited a major muscle activation in terms of SNR. The study demonstrated that the 1/3 elbow-wrist configuration minimized the noise making the muscle signal more distinguishable. In parallel, also the position of the reference electrode has been taken into account: no significant difference has been found by placing it on the back of the hand or in the middle crown between the sensing electrodes, thus preferring the latter solution because of its more compact design.

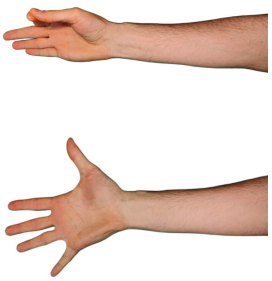

Fig. 6.6 Pinch grip and open hand gestures.

With respect to previous gesture, here other two gestures has been added:

- Pinch grip: the palmar surface of the index and the thumb close to each other generating a grip;
- Open hand: all the finger extend by opening the palm.

in order to have a total of 8 recognizable gestures, 7 related to an action and one representing the idle state.

A novel dataset has been created acquiring (with the g.HIamp-research amplifier) the sEMG signals from 14 subjects, and extracting offline the ATC parameter to

train the ML algorithms. The study stopped to a first evaluation of the classifiers performance without completing an online test phase. As can it be seen from Table 6.2 (which also summarizes the ATC studies in this filed), although the results needed further validation, the ATC technique works also in the armband configuration proving its feasible use in developing an armband for the recognition of hand multiple gestures.

6.2 2-D Human-Computer Interface

A very basic but functional example of an Human-Machine Interface (HMI) system based on the ATC processing of muscular data has been developed and presented in [229].

The HMI setup, here presented as a gamin tool, is reported in Figure 6.7. Two acquisition devices (i.e., *Apollux* board) are placed on the forearm above the *extensor carpi ulnaris* and *palmaris longus* muscles and their ATC values are constantly streamed to a laptop. There, a Python script runs a classifier in order to recognize four hand gestures, i.e., idle, wrist extension, wrist flexion, and grasp. Depending on the predicted class, a keyboard emulation tool has been configured to link the hand gestures to the button functions in way to give user the possibility to interact with the laptop directly using her/his hand movements. For example, considering *Space Invaders* game in Figure 6.7, the space shuttle moves following wrist extension (to the right) and flexion (to the left), fires when the grasp is performed, or stays still

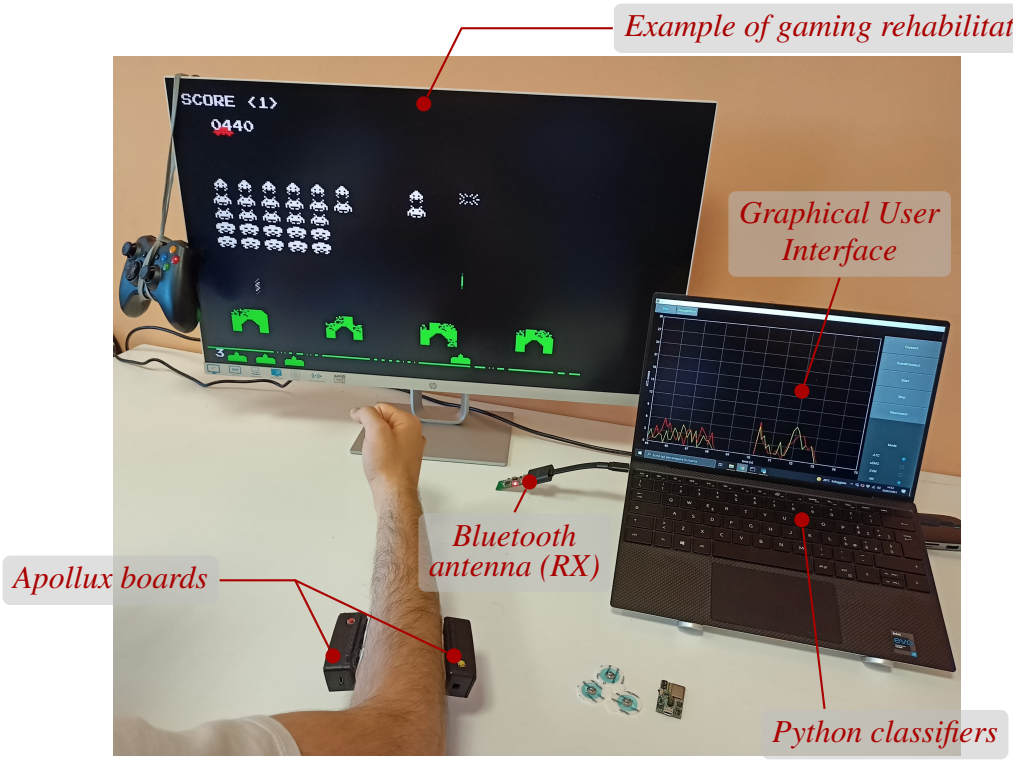

Fig. 6.7 HMI system for game-based rehabilitation [229].

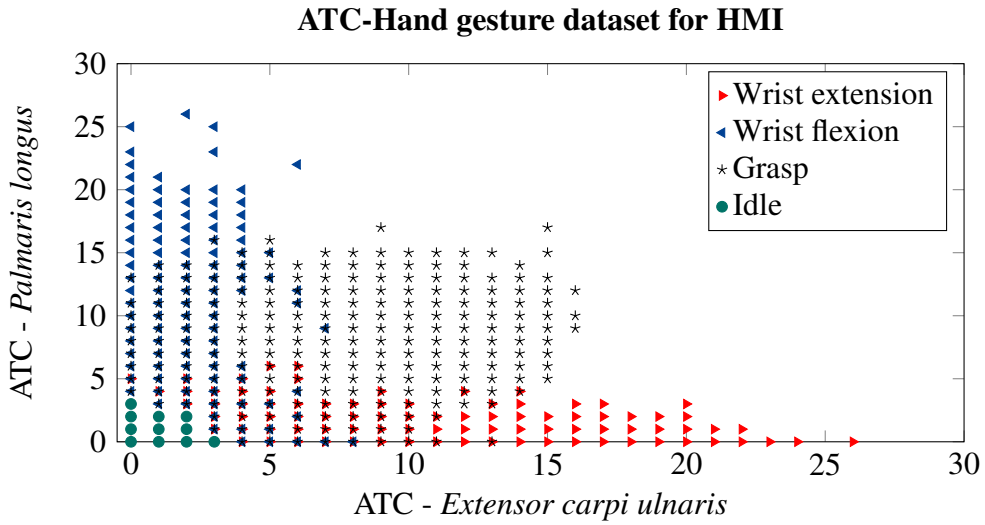

Fig. 6.8 Acquired dataset for NN training. All the four classes are visible in the 2-D plane, also making distinguishable the idling process (light green bullets).

when the hand is stationary. Anyway, the keyboard setup up to four keys (gestures) can be freely configured in order to better fit the user needs. Moreover, a Graphical User Interface (GUI) has been developed to ease the boards placement and check the muscular response before starting the application. During the run-time, it can also be employed to have visual feedback on the ATC streamed values.

As regard the classifier, the 2-D features dimension of the ATC inputs perfectly fits the light structure of a fully connected NN, which has been defined of 2 hidden layers of 19 neurons each after hypertuning parameters selection. The training data has been reinforced by implementing a noise robustness procedure (e.g., idle identification check) on the squared norm of the ATC values, as graphically represented in Figure 6.8. The mathematical formulation of the norm is reported in Eq. 6.1, where ATC_{ECU} and ATC_{PL} stands for the ATC data recorded from the *extensor carpi ulnaris* and *palmaris longus* muscles, respectively.

$$\|ATC_{ECU}, ATC_{PL}\| \leq 3 \tag{6.1}$$

The classifier has been tested, demonstrating a 97.89 % accuracy value and an application latency totally due to the ATC timing (i.e., 130 ms). Since it is a software classifier, this system operating time strictly depends on the power consumption of

the acquisition devices, which, requiring only 0.48 mA, enable the application to run up to 230 h (considering the 110 mA h battery), as reported in Section 4.4.

Although the limits of this simple HMI, its implementation and related performance (accuracy and timing response) prove the proper role of the ATC parameter in achieving the functional control of a machine.

6.3 3-D Planar Device Control

Adding another degree of freedom, a system for the control of a planar device (e.g., experience belonging to rehabilitative serious game [8, 201]) has been achieved, as presented in [94]. The prototype, shown in Figure 6.9 during operation (the acquisition hardware is equivalent at the one of Figure 6.3, here with the components taken apart), consists of driving a planar tank, i.e., Zumo robot [230], in a plane.

Considering what has been obtained in [70] and already explained in Section 6.1, the six gestures are mapped into the following driving commands acting on the crawlers:

- *Wrist extension*: turn right;
- *Wrist flexion*: turn left;
- *Radial deviation*: move forward;
- *Ulnar deviation*: move backward;
- *Hand Grasp*: not used, but functionally available;
- *Idle*: idle state of the motors.

In order to achieve a wireless and dynamic control of the tank, both the acquisition and actuation units have been equipped with a BlueTooth (BT) 3.0 module. In particular, Zumo has been shielded with the compatible Arduino UNO [231] board, which interface the wireless sensor. In this way, every time a new hand gesture has been predicted on the acquisition (and processing) node, a BT packet is sent to Zumo, which translates the class of the gesture in the correct sequence of moving commands.

For this HMI application, an additional delay slot has been implement on the predicted class for robustness reason, which means that the action BT packet is transmitted only when the recognized gestures is maintained stable for at least two consecutive predictions. Following this approach, the drive of the tank has been perceived effectively more comfortable and controllable than updating the driving command at each classification. The unique (but limited) drawback consists of an enlarged maximal application latency of 268.5 ms, resulting from the two waiting

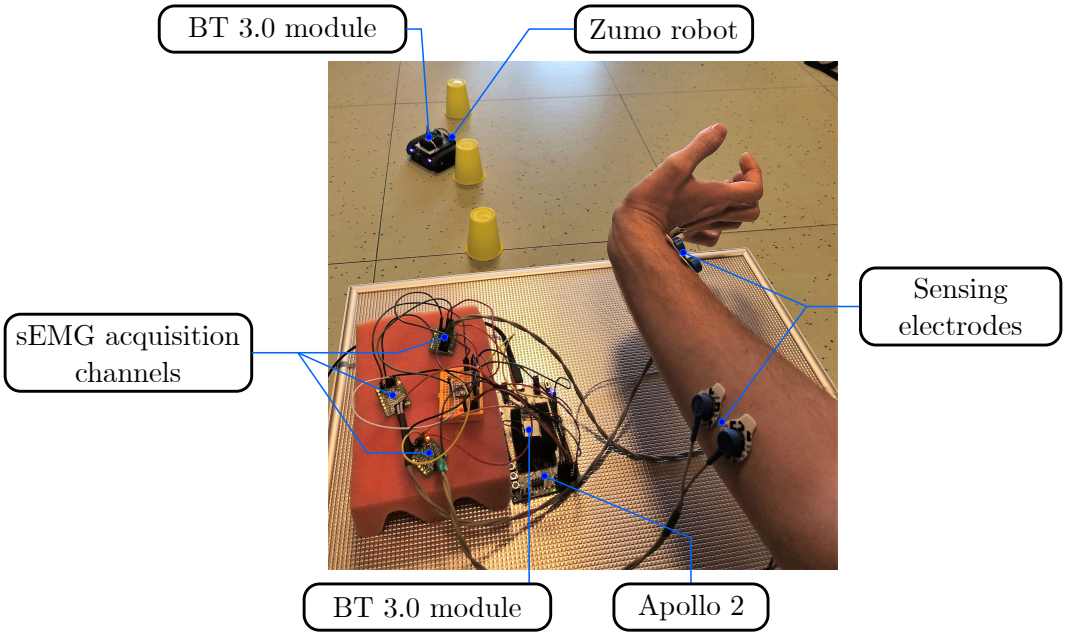

Fig. 6.9 Representative setup for the online planar device control.

ATC windows (2 $\times$ 130 ms) plus the prediction time (8.5 ms), which however fulfills the typical real-time constrain of 300 ms for biomedical applications [140].

6.4 The Armband

6.4.1 Hardware setup

The armband has been designed as a circular ring, to fit around the forearm, composed by seven units: one working as the master board, which provides the wireless interface with the user and controls all the operations, and the remaining six acting as its slaves, which respond to the commands sent by the master. Data communication among the armband boards is achieved by arranging the units in an I^2C closed-loop daisy-chain configuration, whose Application Programming Interface (API) implements a custom protocol.

As already anticipated, all the modules are based on the *Apollux* ATC/sEMG acquisition channel (deeply detailed in Chapters 2 and 3), which totally represents a wearable edge-computing node, providing an adaptable AFE for the TC signal, a low-power MCU for embedded ATC computations, and a BLE antenna for wireless connectivity. In particular, a second version of *Apollux* prototype has been employed to build the armband, because it is equipped with the enhanced features (e.g., more selectable AFE gains to cover a wider amplification range, i.e., 250 V/V^{-1} to 4000 V/V^{-1}) w.r.t. its predecessor.

If in the previous applications (i.e., 2-D and 3-D) each *Apollux* board works as a standalone module, streaming the ATC data independently, here the devices have been reconfigured to operate their functional role in the armband setup. In particular, since the master board has to provide an accessible Bluetooth Low Energy (BLE) server while controlling the slave devices and performing its computations, its firmware runs the FreeRTOS operating system [95] to manage different parallel tasks, similarly to what has been implemented on the *Apollux*. Differently, since the wireless user interface is ensured by the master and the inter-board connections are wired, the firmware requirements for the slave modules can be relaxed to some sporadic I^2C-triggered actions (i.e., initial configuration commands and TC events counting), which are quickly executed leaving and re-entering the (low power) sleeping state.

Regarding gesture recognition, considering both the computational effort during the classification task and the memory requirements needed to store the Artificial Neural Network (ANN) parameters, a separate board from the master has been

preferred to achieved all the ML computations, thus avoiding to overstress the central unit. Therefore, an additional board (sub-)role of the predictor has been introduced, which, being a slave module itself, follows the same firmware structure of the other slaves but is equipped with the proper resources to perform the gesture prediction when requested.

As a consequence of the above discussion, merging the above roles, the structure of the armband has been functionally organized as follows (see Fig. 6.10):

- Channel 1: *master* board – it represents the operative center of the device, which translates the user actions into executable tasks; as the first channel, it is employed to arrange the armband in the right location of the forearm;
- Channels 2 to 6: *slave* board – it silently waits a command from the master to perform the related function;
- Channel 7: *predictor* board – as a slave, it responds only to a master interaction; additionally, it is in charge of gesture recognition.

A single rechargeable battery has been supposed to power up all the boards. Therefore, a total of seven bridging connectors, each one composed by four wires

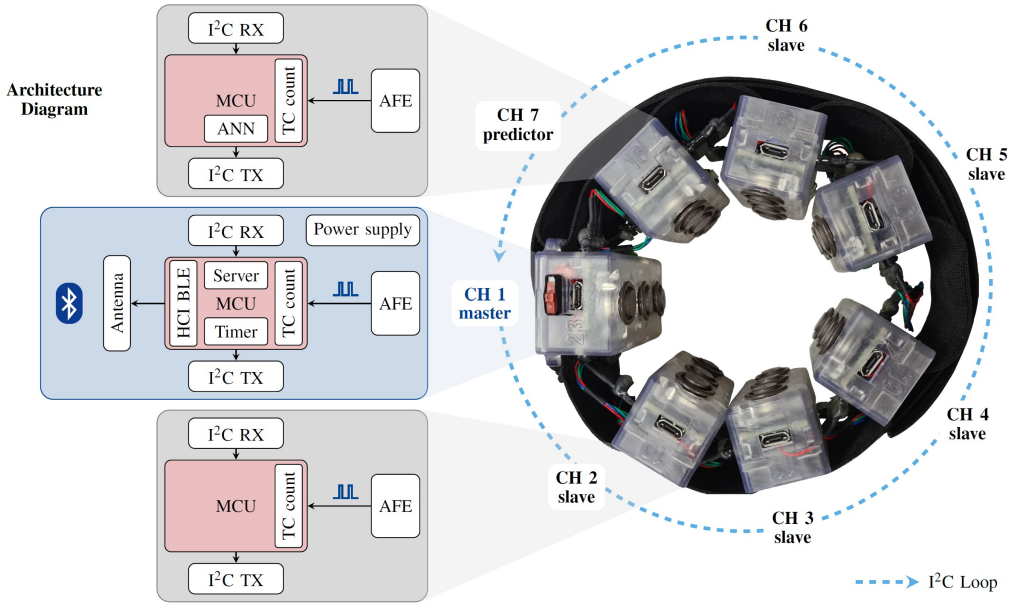

Fig. 6.10 Prototype of the armband. Power and I^2C communication wires electrically connect the boards, while the elastic band physically keeps the modules in the proper position.

(i.e., power (V_{DD}), GND, I^2C data, and I^2C clock), have been provided for the interconnection between the boards.

As the last design concept, an elastic band has been considered as the proper closure mechanism to secure the armband on the forearm because, in addition to adequately tightening the acquisition channels in contact with the skin (above the muscles), it allows the device to fit limbs of different anatomical dimensions.

6.4.2 BLE Server

As previously briefly introduced, data exchange and user controls are based on the BLE server built on the master board, which acts as the peripheral node in a client/server communication with a central device (e.g., a laptop, tablet, or smartphone). Starting from the private service of the *Apollux* device (see Section 2.3.2), its structure has been adapted and redefined to suit the seven channels configuration (see Table 6.3) as follows:

- *Service Declaration*: it lists the descriptors and values of all the available characteristics in the service;
- *Command*: when written, it triggers the execution of a specific task (e.g., ATC threshold calibration);
- *Status*: it represents the current operating state of the armband; its value can be read or directly notified to the user at changing;
- *ID*: when read, it returns the identifiers of the *Apollux* boards composing the armband;
- *Gain*: a write operation results in the gain setting for each AFE (through the correspondence between values indexes and board channel numbers); when read, the characteristic provides the gain multiplier of each module;
- *ATC*: the values contained in this characteristic represents the latest computed ATC data, which are updated every ATC window (i.e., 130 ms) when the related notifications are enabled;
- *Gesture*: when its notifications are active, its value (coded onto 1 B) corresponds the latest predicted class (i.e., hand gesture).

Table 6.3 BLE server for the armband application

Characteristic	**Handle**	**Size**	**Permission**[1]
Service Declaration	0x00A0	-	-
Command	0x00A2	1 B-3 B	W
Status	0x00A4	1 B	R/N
$\text{Status}_{\text{CCCD}}$	0x00A5	2 B	R/W
ID	0x00A7	7 B	R
Gain	0x00A9	7 B	R/W
ATC	0x00AB	7 B-8 B	N
ATC_{CCCD}	0x00AC	2 B	R/W
Gesture	0x00AE	1 B-2 B	N
$\text{Gesture}_{\text{CCCD}}$	0x00AF	2 B	R/W

[1]R: read; W: write; N: notify.

As it can be seen from Table 6.3, both *ATC* and *Gesture* characteristics present a variable size: when their notifications are enabled singularly, the dimension of the characteristics match the data representation of the values they are carrying (i.e., 7 B for 7 channels ATC values, and 1 B to store the gesture class); alternatively, if the ATC and ML notifications stream concurrently, the above dimensions are slightly increased by one more byte, standing as the packet number, in order to correctly pair the two BLE packets in the receiving software routine.

6.4.3 Armband Communication Protocol

Fulfilling its role of master node of the armband, the main board also handles the I^2C loop protocol. I^2C commands have been implemented to actively and remotely control the functionalities of the armband. As introduced, the hardware setup involves seven *Apollux* devices (the master and six slaves, one operating as the predictor board) in a closed-loop daisy-chain configuration, where each board acts as an Input-Output Master (IOM) module for the following one, which functions as an Input-Output Slave (IOS) module. Basically, as depicted in Fig. 6.11, the master board interfaces with the BLE Host-Controller Interface (HCI) layer and loops the relative commands through the ring while waiting for the slave responses. Any device in the chain presents the same structure for the command management, which could be functionally divided into four modules:

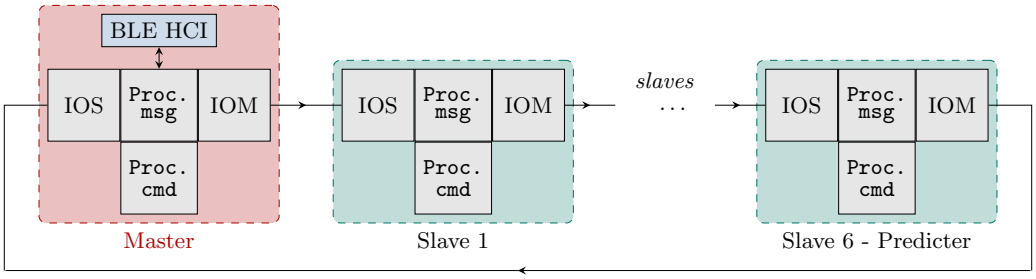

Fig. 6.11 I^{2}C armband closed-loop configuration.

- IOM module: sends the I^{2}C commands to the next board;
- IOS module: receives the I^{2}C commands from the previous board;
- Processing messages (`Proc. msg`): checks the package stored by the IOS and executes the command if the board is the message target or dispatches the package to the next board;
- Processing commands (`Proc. cmd`): only if the `Proc. msg` module detects that the message is reserved to the current board its payload is sent to the `Proc. cmd` module, which unpacks the command and perform the related action.

The unique format of the I^{2}C packets has been defined as reported in Fig. 6.12, which implements the following fields:

- `I2C ADDR`: it represents the address of the receiving board; here it has been generally fixed to the `0x41` ('A') value because of the simple peer-to-peer communication among each couple of boards;
- `#Byte`: it identifies the total number of bytes included into the I^{2}C packet payload;
- `Target board`: this value points the message to the right receiver; it could be an *Apollux* ID (if the command has to be performed only by one board) or `0xFF`, acting as broadcast indicator (if the operation has to be executed by each board in the armband);
- `Command`: it gives the information on which action needs to be executed;

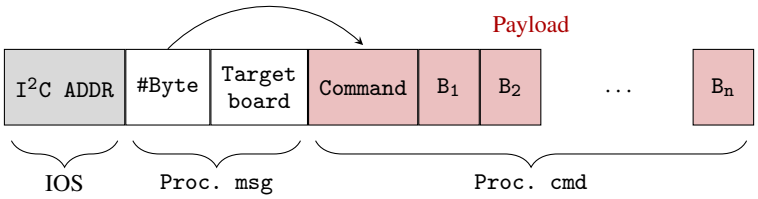

Fig. 6.12 I^{2}C IOM-IOS communication packet.

- B_1 - B_n: they compose the variable length data payload of the I^{2}C packet.

On the master side, after the reception of a BLE command, it executes the required action if it is the target; alternatively, it builds the I^{2}C packets and sends it to the armband loop.

On the slave side, any time an I^{2}C packet is correctly received by the IOS module (which checks the `I²C ADDR` field and the entirety of the data exchange), the packet has been sent to the `Proc. msg` module. At this level, only the `#Byte` and the `Target board` blocks are processed: if the message's target is verified, the entire payload is passed to the `Proc. cmd`; otherwise, the message is directly sent again through the loop. The `Proc. cmd` module unpacks the payload by extracting the command byte (and the additional ones) in order to start the related function. Once the operation is completed, a boolean result is appended at the end of the payload and the entire message is transmitted to the next board (to another slave or to the master). The loop ends when the master receives back its message on its IOS module. After the proper check of the boolean result indicator(s), the master notifies the BLE central of the success or failure of the requested operation.

A simple but effective graphical representation of the above process, concerning a reduced HW setup (only four boards), is shown in Fig. 6.13, where three functional examples have been reported. In the first case (violet color), the user requests the master board (`ID:0x01`) to set the AFE gain (`cmd:0x90` BLE, `cmd:0x03` I^{2}C) with $\times 4$ multiplier (`value:0x04`); since the operation is limited to the master device, none I^{2}C message is sent through the loop, so directly triggering the BLE notification reporting the status of the performed task. In the second case (red color), the same action is requested but pointing to a single slave board (`ID:0x02`); after the commands reception, the master passes the message in the loop, the target board (i.e., slave, ID: `0x02`) identifies itself as receiver, sets the gain, and appends the *success* result (`0x01`) to the return message to the master; consequently, the master notifies

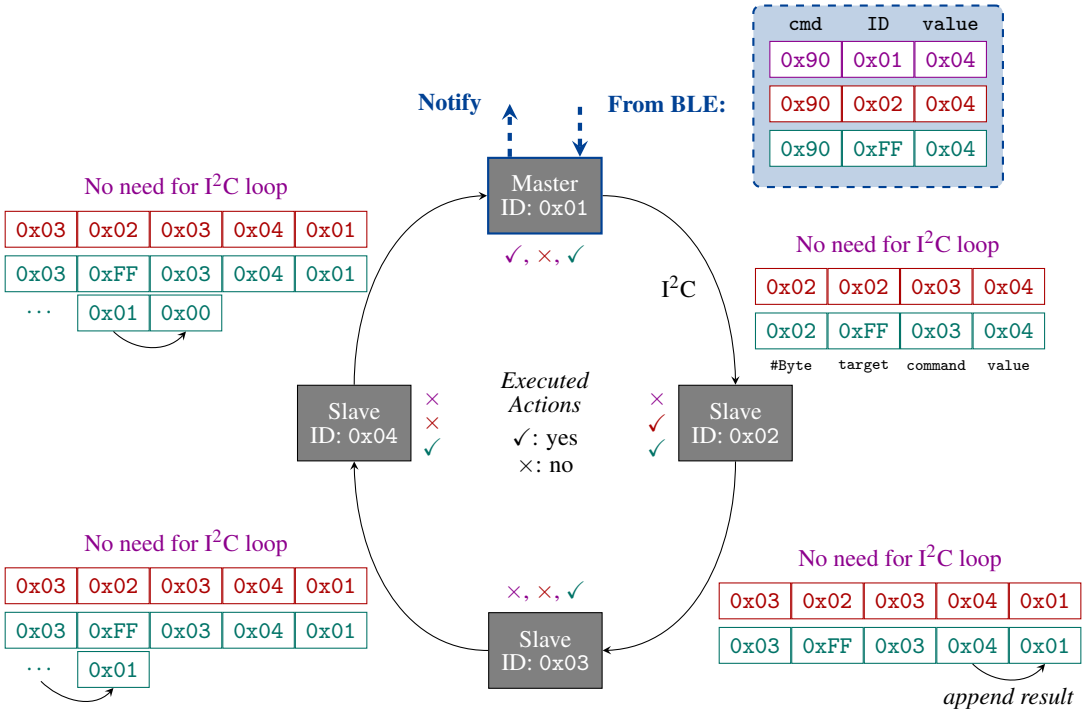

Fig. 6.13 I²C protocol communication example.

the user. Finally, last case (green color) shows the action when the command is requested for all the boards: each slave in the sequence sets the gain and appends the task result, which will be checked by the master at the completion of the loop (in the example all the board execute successfully the operation with the exception of the slave board ID: 0x04, whose task status 0x00 will be notified as failure on the BLE server).

Since the I²C loop strictly depends on the proper functioning of each board, a variable timeout (depending on the processing time related to each task) has been implemented on the master side as a control mechanism. If no I²C message loops back to the master in the defined timeout, a *hardware* error is notified to the BLE central.

Additional operation failures are supervised by checking the content of the payload: it can be achieved by assessing the task result (e.g., *auto_thr*) or by verifying the appropriate data range of values (e.g., *req_gain*). Consequently, errors are handled by updating the server *Status* characteristic and sending the notification to the user.

Table 6.4 I^2C API for armband loop functionalities.

Action	Timeout	I^2C packet			
		`#Byte`	`Target`	`Command`	B_1-B_n
null	5 s	0x01	ID/0xFF	0x00	[ ]
req_IDs	5 s	0x01-0x07	ID/0xFF	0x01	[*Apollux* IDs]
req_gain	5 s	0x01-0x07	ID/0xFF	0x02	[AFE gains]
set_gain	5 s	0x02-0x08	ID/0xFF	0x03	[value, result(s)[1]]
auto_thr	30 s	0x01-0x07	ID/0xFF	0x04	[result(s)[1]]
start_ATC	5 s	0x01	ID/0xFF	0x05	[ ]
ATC_win	5 s	0x01-0x08	ID/0xFF	0x06	[ATC value(s)]
stop_ATC	5 s	0x01	ID/0xFF	0x07	[ ]
predict	-	0x02	ID/0xFF	0x08	[pred. class]

[1]boolean value

An all inclusive description of the I^2C commands combination is reported in Table 6.4, while main features are listed below:

- *null*: no action is triggered; it can be used to check the correct HW setup.
- *req_IDs*: it requests the *Apollux* IDs of all the boards.
- *req_gain*: it logs the current AFE gains for each board.
- *set_gain*: it sets the AFE gain to the multiplier value (i.e., $\times$1,...,$\times$16) written on B_1.
- *auto_thr*: it launches the automatic threshold searching (from V_{DD}).
- *start_ATC*: it starts the timer counting for the ATC window on master device and enables the GPIO interrupt on the TC signal for the slaves boards.
- *ATC_win*: it records the ATC values when the ATC window expires.
- *stop_ATC*: it stops the ATC timer on master device and disables the GPIO interrupts on slave boards.
- *predict*: it is the only command which is always sent from the predictor board to the master after the completion of the prediction operation, and its packet contains the corresponding gesture class.

6.4.4 Functional operations

Apart from the configuration commands, two main armband functionalities are defined, i.e., ATC mode and ML mode, designed for data acquisition and class prediction, respectively. Their implementation was performed by interfacing the properties of the BLE server, the defined I^2C commands, and the firmware routines corresponding to the different board roles. Particular attention needs to be given to explaining how I^2C commands trigger ATC computation and gesture prediction considering the protocol logic, graphically schematized in Fig. 6.14.

In ATC mode, after enabling the ATC notifications, the master board starts the ATC timer and sends the *start_ATC* command to activate the TC signal edge-detection for all the slave boards. Then, every time the capture and compare unit of the timer raises an interrupt for the end of an ATC window, the master loops the *ATC_win* command to collect the TC count from all the other boards and, after appending its value last, it updates the server characteristic and sends the notification. The *ATC_win* cycle continues until the notifications are disabled, stopping the timer and commanding the *stop_ATC*, which consequently inactivates the TC interrupts on all the boards. Considering the above configuration, only the master board runs the timer for the ATC window while all the slaves wait for the *ATC_win* command to end their observation window and to attach their TC count.

Differently, during the ML mode (gesture notifications enabled), the master slightly changes the above behavior during the ATC collection: when the ATC timer expires, it attaches its ATC value as first payload byte while looping the *ATC_win* command; in this way, the I^2C packet arrives to the predictor board with the payload containing the ATC values of all the other modules which, integrated with its one, represent the entire input to perform the gesture prediction. Once the ML operations are completed, the predictor puts the result into the prediction packet and sends it to the master.

Therefore, the predictor board passively understands which operation it needs to perform by checking the length of the I^2C packet payload (when the command is *ATC_win*), i.e, 5 B in ATC mode and 6 B in ML mode.

Moreover, both modalities can work together, with the predictor also returning the ATC packet to the master (before the prediction) as unique protocol difference.

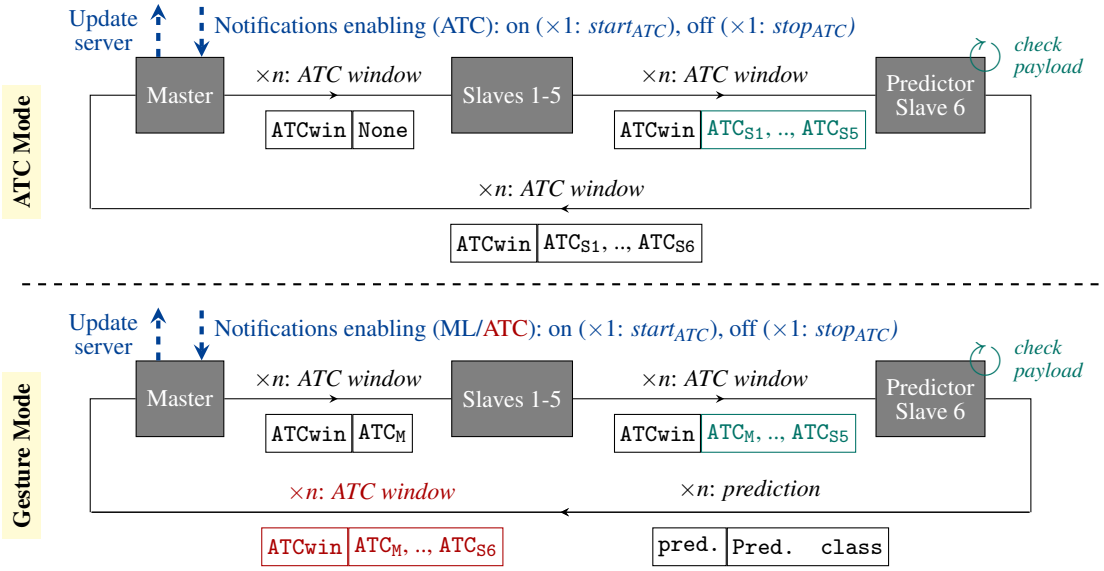

Fig. 6.14 ATC and ML working modes along the armband loop.

6.4.5 3D Modeling

Besides the electronic aspects discussed until here, the physical realization of the armband still needs to be presented in order to complete the wearable prototype. As reported in Figures 6.15 and 6.16, two distinct cases have been designed for the master and slave boards using the commercial Form 3+ 3D printer [232], which employs a photopolymeric, bio-compatible and lightweight resin to extrude the model.

Identically to the *Apollux* box, both the printed cases feature the openings to dispose the dry electrodes, arranged in lines following the sensing-reference-sensing configuration, on their bottom surface, just barely below the acquisition unit to minimize electrodes-to-circuit interference. The electrodes are kept in a secure position thanks to internal metal clips, which grab the tips of the electrodes, and by some blocker cogwheels, that limit the vertical displacements. At the right and left sides, two rectangular slots have been opened to insert the four pins connectors from which attach the bridging (among the boards) cables carrying the I^2C and power supply lines. The micro-USB connector remains accessible from the front wall, thus giving to the user the possibility to easily debug and flash the modules. As last common trait, both cases provide a push-button to manually achieve the MCU reset when needed.

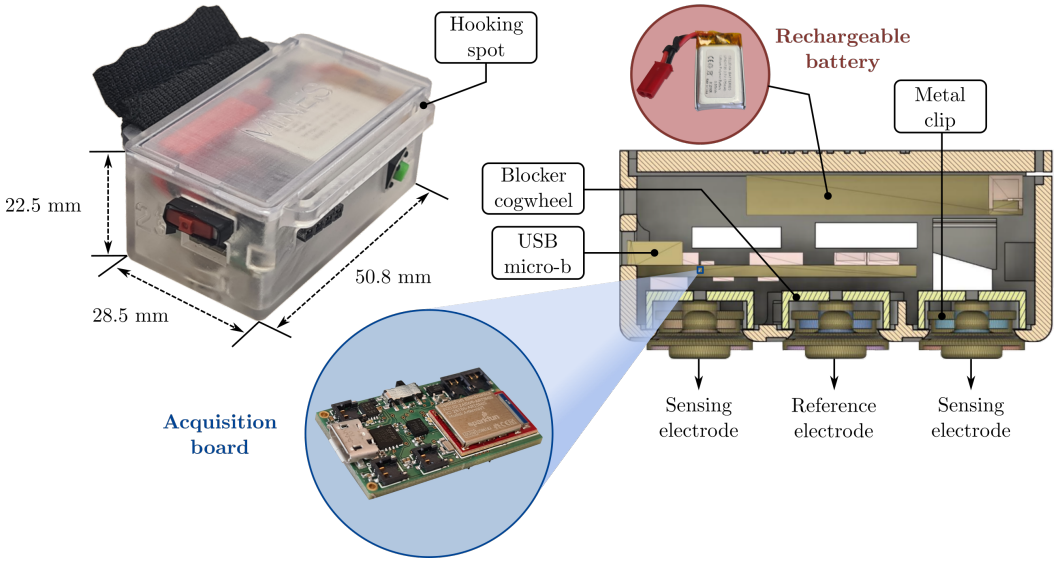

Fig. 6.15 Detailed views of the 3D-printed master case and its internal organization.

Additionally, the internal space of the master package was arranged to contain also a small rechargeable battery (i.e., a 175 mA h LiPo battery [233]), which powers all the seven boards, and two switches, one directly placed on the positive pole of the battery, to completely turn off the armband, and a second one inserted on the V_{DD} branch which powers the slave boards, to allow a faster recharge time when needed.

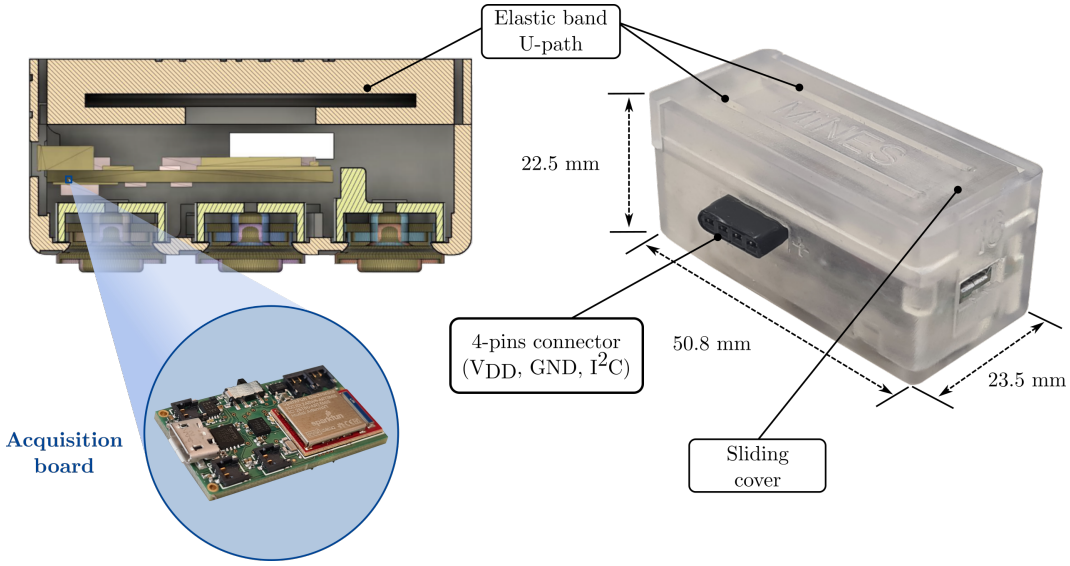

Fig. 6.16 3D-printed case for slave boards. Internally, the same space of the battery (in the master) here is used to secure the elastic band inside the U-path.

At last, the boxes are closed by means of sliding covers, which also provide the hooking spots for the elastic band to shrink the armband around the forearm. Indeed, the strip is sewed to one of the two wings of the master cover, while, at the other extremity, it is pulled until the armband is properly positioned. Differently, the slave case features an eyelet U-path inside its cover, which, thanks to the internal squared corners, avoids the band to slip away once the armband is worn.

In conclusion, the resulting armband prototype, shown in Fig. 6.10, consists of seven modules with a dimension of 50.8 mm length, 22.5 mm height, and 28.5 mm or 23.5 mm width depending on the master or slave case, respectively.

6.4.6 PC interface

Once the physical structure of the armband and its communication protocols were defined, next step was the implementation of the software for controlling the armband from an external device, e.g., a laptop. Similar to the *Apollux*, the code has been developed using the Python programming language and it is divided into three layers with a bottom-up structure: the lowest layer corresponds to the BLE module, which establishes the connection with the armband and handles the data communication with it, accessing the server functionalities and dispatching the input/output packets; at the mid-layer, the armband module translates all the user commands into executable actions, driving the correspondent BLE antenna operations, and processes the received packet's content to extract the meaningful data for further usage; at the top layer, the application layer, there is the Graphical User Interface (GUI), which features multiple widgets (e.g., button, spinner), to ease the interface with the user, and plots the requested acquisition data, i.e., ATC values and the recognized gesture.

Also for this application, the intra-software data flow control is achieved by combining the objects methods callback, to accomplish top-down functionalities, with multiple queues, which organize and stratify the bottom-up communications.

Regarding the wireless connectivity and considering a laptop as the standard machine running the software (although the Python multi-platform nature extends its compatibility to multiple devices), the BLE server implemented on the armband is accessed by using an external USB-dongle (i.e., CC2540 [101] or nRF52840 [78], which feature the 4.1 and 4.2 BLE stack, respectively) to guarantee the performance of the application by standardizing the wireless protocol.

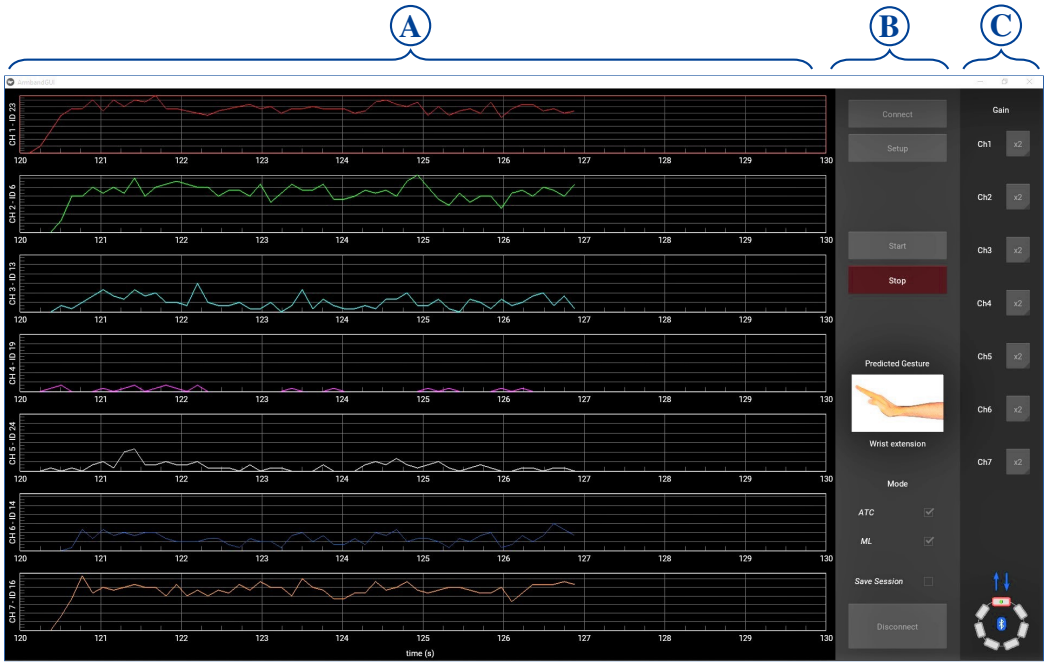

Fig. 6.17 Screenshot of the proposed GUI composed of a graph for each armband channel (A), a control panel (B), and the gain selectors (C).

A screenshot of the proposed GUI is reported in Fig. 6.17, where A, B, and C labels show the panels division for graphical representation and user controls. Following the operational flow for the *Apollux* module, the main steps for the armband application, once the device is worn and turned on, can be summarized as follows:

1. Connection: the USB-dongle is initialized as the central device, and the scan operation (with a *white-list* to filter undesired devices) is launched to search for the armband's advertising packet. If found, the connection is established, the armband's status notifications are enabled, and the IDs request (i.e., *req_ID*) is performed to check the correct hardware connectivity and to log the boards information. Lastly, seven ATC graphs are instantiated, one for each board belonging to the armband.

2. Setup: it consists of the ATC thresholds calibration process, which performs this task one board at a time along the armband loop (15 s ca. total); the user needs to maintain the forearm relaxed during this step.

3. Operation mode selection: if the ATC mode is chosen, the armband will stream the ATC values; vice versa, the ML mode only requests for the predicted gesture class. As previously introduced, the two modes can work concurrently.

4. Gain selection: the multiplier factor of each board's AFE can be adjusted proportionally to the captured signals amplitude; default value is $\times 2$ (i.e., $500\,\mathrm{V\,V^{-1}}$).

5. Data acquisition: the data stream is started by enabling the notifications for the proper server characteristic (i.e., ATC and/or ML depending on the selected working mode(s)). Every time a packet arrives, if it contains ATC values, they are plotted on the graphs; otherwise, a picture showing the recognized gesture is displayed.

6. Data saving: the acquired data can be saved on files if the *Save Session* checkbox is active. The files are organized into sessions folders; within each one every document reports the ATC values and/or the recognized class along with their timestamps.

7. Disconnection: the existing BLE link is terminated and the GUI can be closed.

6.4.7 Acquisition Protocol and Dataset Creation

Once the hardware and software components described in previous sections were finalized and fully tested, a data acquisition campaign was launched. In particular, 20 healthy people, 7 females and 13 males, aged between 23 and 29 years old, were involved. The experimental campaign accurately followed the ethical procedures specified in the Application n. 445136 approved by the Comitato Bioetico di Ateneo of the University of Turin [108]. Each participant was informed about the physical safety of the armband itself and about how their data would be anonymized and encrypted for the purposes allowed by the experimentation.

For each attending person, the armband is positioned on the right forearm, at one third of the line between the elbow and the wrist, with CH 1 (i.e., the master board) above the *Extensor Digitorum*. This position was previously determined, both according to the previous study [223], literature reference positions [234, 51], and by consulting with some fellow physicians about how deep and superficial muscles

interact in this area. In particular, the final standardized position, starting from CH 1, involves the following muscles:

1. *Extensor digitorum*
2. *Extensor carpi ulnaris*
3. *Flexor digitorum profundus*
4. *Flexor carpi ulnaris*
5. *Flexor carpi radialis*
6. *Brachioradialis*
7. *Extensor carpi radialis*

After the armband is tighten up with the elastic band, the GUI is run in ATC mode to check if the acquisition channels are behaving correctly and if the obtained TC values are consistent with each channel position around the limb. In case one or more channels do not react as expected, the armband can be rotated slightly to fix an incorrect positioning. Furthermore, the gain of the misbehaving channels can be modified in order to enhance the sensitivity of the acquired information, most of the time going to balance particularly under- or over-developed forearms. This procedure is repeated until the acquired TC signals are sufficiently responsive to gestures change.

Once the initial calibration is completed, the subject is asked to not lean the forearm on any surface and to keep it in the neutral position (i.e., with the fingers vertically overlapping). Then, each volunteer is instructed with the gestures s/he has to perform during the session, as depicted in Fig. 6.18, in this particular order:

1. **Wrist extension (WE)**: the hand has to be moved right, with its back going toward the distal section of the forearm;
2. **Wrist flexion (WF)**: the hand moves left, with the fingers moderately closing toward the inner part of the forearm;
3. **Radial deviation (RD)**: the hand is moved up, keeping the fingers adjacent to each other and the thumb as much relaxed as possible;

Fig. 6.18 Hand gestures analyzed in this study, ordered (from left to right and from top to bottom) as performed in the acquisition campaign.

4. **Ulnar deviation (UD)**: the fingers point down toward the floor, maintaining themselves straight and aligned with the forearm;
5. **Hand grasp (HG)**: the fingers are bent towards the hand palm, resulting in a fist;
6. **Pinch 1-2 (P2)**: the thumb (i.e., finger 1) is internally rotated and the index finger (i.e., finger 2) is flexed to make their distal phalanges touch;
7. **Pinch 1-3 (P3)**: same intent of gesture 6, but involving the middle finger (i.e., finger 3) instead of the index finger;
8. **Open hand (OH)**: the fingers are stretched and opened out, trying to make the hand as tense as possible.

This sequence of gestures has to be performed respecting a specific timing in order to keep each gesture clearly distinct from the previous and following ones, making the post-processing phase more efficient. The subject is helped in following the time schedule by a custom application, which simply displays on the laptop monitor a countdown and a graphical indication of the gesture to be performed. In

particular, after the supervisor starts the ATC mode to begin the signals acquisition, the following routine commence:

1. 15 s of rest are observed, in order to avoid glitches in the first part of the acquisition;
2. the gesture displayed by the application is performed and maintained for 10 s;
3. the hand is relaxed for 10 s to avoid muscular fatigue;
4. the previously executed gesture is repeated, again maintaining it for 10 s;
5. a 15 s rest period is observed, also being instructed about the following gesture;
6. step 2 to 5 are repeated until the last gesture is performed and the graphical help displays the end signal;
7. a 60 s rest period allows the subject to fully relax and stretch her/his hand;
8. step 2 to 7 are repeated for three times, in order to acquire a consistent amount of data.

In Fig. 6.19, the signals acquired during a typical acquisition session are plotted. Each subplot represents the ATC values obtained from one of the acquisition boards, ordered as in the physical position they occupy in the armband. Each gesture has a particular combination of the seven force indicators, with antagonist movements galvanizing the electrodes of opposite boards, as expected. As an example, WE presents muscular activation on CHs 1, 2, and 7, which are placed on the lateral section of the forearm, while WF activity is mainly sensed by CHs 3, 4, 5, and 6, which are positioned on the forearm's medial section.

At the end of the 20 trials, performed in different days and with non-controlled ambient conditions, the anonymized data were processed to obtain a labeled dataset suitable for machine learning training. In particular, the signals from each subject have been segmented according to the timings detailed above, obtaining many 40 s slices, each one consisting of the two consequent repetitions of a single gesture, the rest period between them, and 5 s of rest for both the begin and end of each slice. Then, before labeling each slice, a threshold was established on the norm of each set

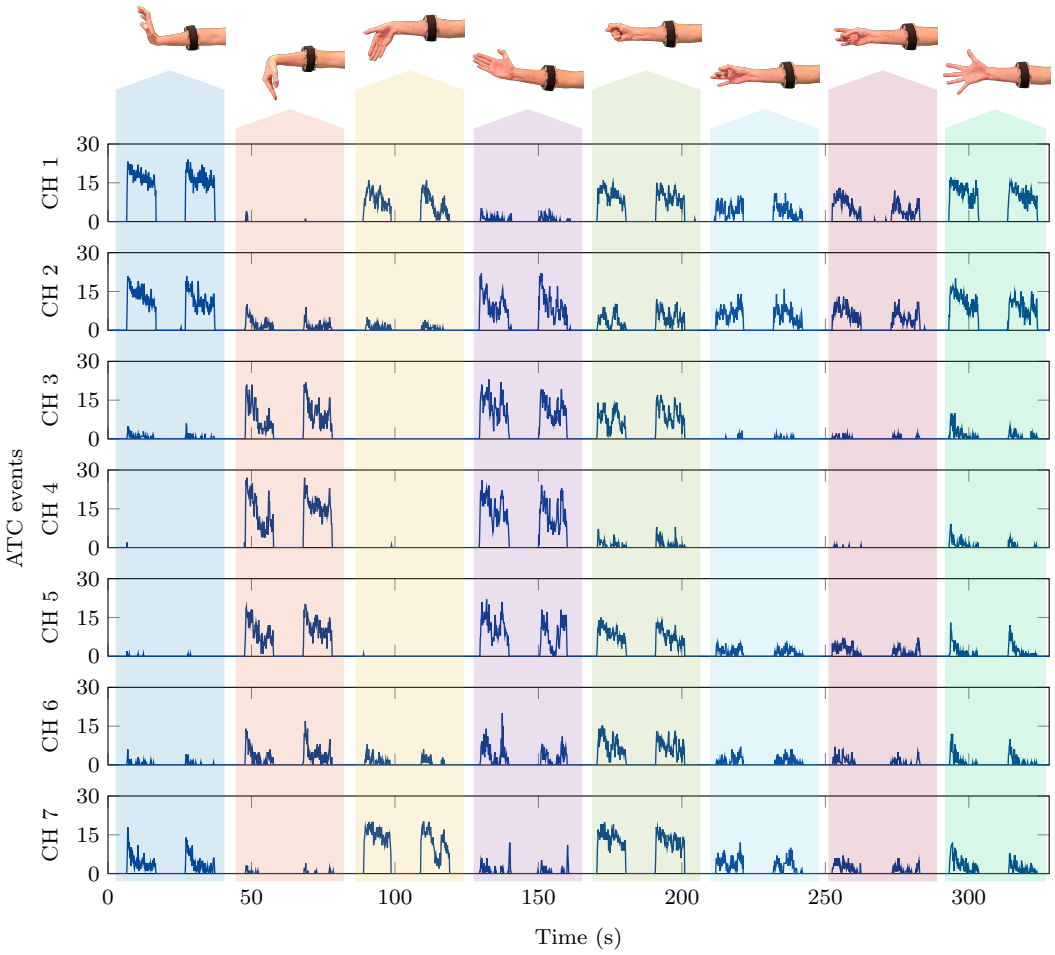

Fig. 6.19 ATC profiles during dataset acquisition.

of ATC values, as reported in Eq. 6.2, where f_x is the TC value of the x^{th} channel.

$$N = \sqrt{f_1^2 + f_2^2 + f_3^2 + f_4^2 + f_5^2 + f_6^2 + f_7^2} \tag{6.2}$$

The values whose norm was greater than or equal to the threshold were labeled according to the class performed at that particular timing, while the values whose norm was lower were identified as **Idle state (IS)** (i.e., the ninth class), as summarized in Eq. 6.3, where Th is the chosen threshold value.

$$Class = \begin{cases} \text{Actual class}, & N \geq Th \\ \text{Idle}, & N < Th \end{cases} \tag{6.3}$$

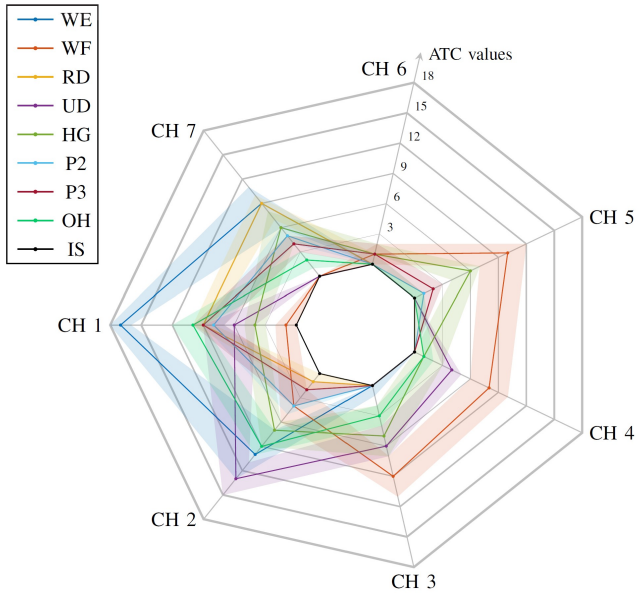

Fig. 6.20 Acquired dataset with idle norm set at 5. Each color represents a different gesture and the light colored areas take into account from the 40th to 60th percentile.

After this process a completely labeled dataset, which includes also the information on the rest periods of the acquisition sessions, was obtained. In order to perform an exhaustive analysis on the effects of the chosen threshold on the final implementation of the ANN for the testing phase, a labeled dataset (from the ATC raw data) for each value of N included in the range $[1,30]$ has been extracted. Thus, after a proper selection of the idle threshold, the classifier for the final application would have the possibility to discern among a voluntary movement and little contractions due to body posture or to interactions with external objects. In Fig. 6.20, a representation of the dataset, obtained by setting the norm value to 5, is displayed by exploiting the parallel coordinates paradigm [235], wrapped in a heptagonal shape, thus recalling the spatial distribution of the activation of the forearm muscles..

6.4.8 Offline Training

The machine learning training phase, based on the multiple obtained datasets, was performed on the MATLAB® environment. The ANN was primarily selected for its simple internal structure and the small size of its final MCU implementation w.r.t. other supervised algorithms (e.g., SVM, K-Nearest Neighbors (KNN) or Naive Bayes). Indeed, the complexity of an ANN is not dependent on the dimension of the

dataset, but only on the information the algorithm needs to extract from the input data to obtain the output classes.

The ANN optimization routine was structured by taking advantage of the Deep Learning Toolbox™, which allows the user to precisely customize the overall network structure and the training parameters. In particular, a 5-fold cross-validation process, based on the Adam method gradient optimizer [236], has been chosen to strengthen the training procedure. The learning rate is set to start from 0.03, and it automatically decreases every 10 epochs in order to improve training accuracy. Furthermore, a learning patience of 5 was selected to stop the procedure when the validation error does not decrease over 5 consecutive samples, thus increasing the timing efficiency of the whole routine.

Once the main parameters of the learner were defined, an extensive analysis has been carried out to find the best available implementation at varying the physical structure of the ANN and involving all the 30 processed dataset. In particular, the optimizer tries all the possible permutations, going from 2 to 4 hidden layers and from 10 nodes for each layer up to 200, with steps of 10 nodes. Moreover, each one of the 60 different configurations was given as input to all the 30 datasets with increasing idle norms, thus resulting in an overall analysis covering 1800 possibilities.

This hyper-parameter training phase aimed to identify the best solutions to maximize the prediction accuracy while maintaining an acceptable user comfort at operating armband. In fact, the increasing of the idle norm could bring to a final implementation which would require much more effort from the subjects to activate the desired gesture, or could even implicate the disappearance of one of the less powerful gestures from the dataset, thus making it impossible to be predicted during the online phase.

The above hyper-parameters tuning brought to very homogeneous results across all the possible combinations of idle norm and hidden layers structures. In Fig. 6.21 all the 1800 obtained accuracies are plotted as function of the idle norm, making possible to observe how the results of the different configurations overlap on the same trend, starting from about 77 % with an idle norm of 1 up to more than 99 % with a norm value of 30. The few exceptions to this trend are the configurations with 10 and 20 nodes, which are the ones slightly below the main curve, having the lowest accuracy of 74 %.

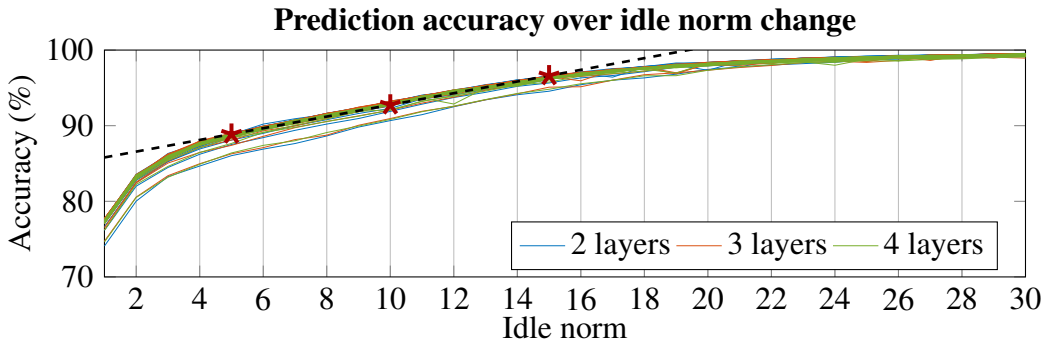

Fig. 6.21 ANN accuracy of the 1800 configurations trained. Each line represents a single network structure, which is trained with input dataset ranging from idle norm 1 up to 30.

Going into details of this uniform behavior, it is also possible to observe how the derivatives of the curves vary with the increasing of the norm. In particular:

- in the region between 1 and 5, the growing is almost logarithmic, with a fast increase from 1 to 2 and then an asymptotic slowdown;
- from 5 to 15, the accuracies follow an almost perfect linear trend (i.e., with an RMSE of 0.0056), as highlighted by the black line interpolation in Fig. 6.21, with an angular coefficient of 0.0077;
- from 15 to the end of our analysis, the derivatives of the accuracies begin a further decline, with their values exiting the linear trend and going asymptotically to 100 %.

All the above considered, the configurations involving as inputs the datasets with idle norm of 5, 10, and 15 have been taken into consideration for the final ANN implementation. First, these three values are all in the linear region, having passed the first fast growing phase and being before the final slackening; and then, they are selected as the more suitable options to analyze how the differences in the norm affect the users effort, during the online testing.

Then, the physical internal structure of the ANN was still to be selected. In Fig. 6.22, the accuracies of all the trained networks, with in input the dataset built on an idle norm of 5, are shown. The results obtained increasing the number of hidden layers are practically the same. In fact, all the three solutions present a high increase

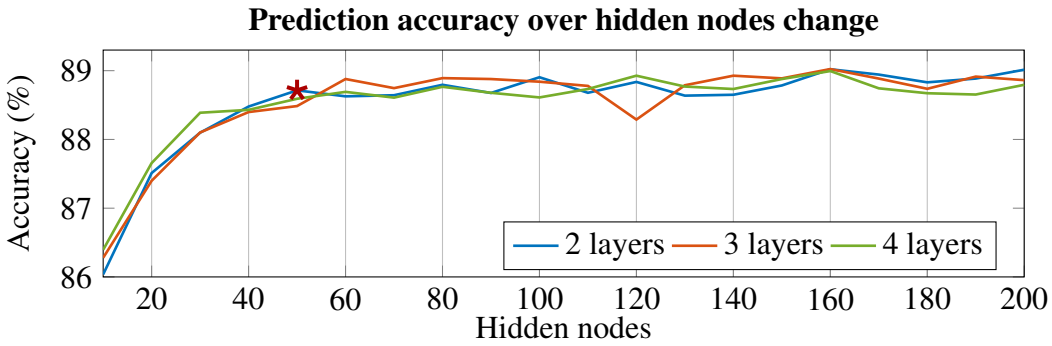

Fig. 6.22 ANN accuracy for a defined idle norm (i.e., 5). The performance behavior is highlighted at varying the network configuration.

in accuracy through the first 5 configurations (i.e., moving from 10 to 50 hidden nodes) and than continue flat till the end of the analysis sweep.

Therefore, the configuration composed by 2 hidden layers with 50 nodes each has been chosen, being the best trade-off among complexity and performance, with an accuracy of 88.71 %. The weights obtained from the training in this configuration were saved and successively used for the online testing phase on the MCU.

6.4.9 Online testing protocol

The testing campaign involved 6 healthy volunteers (none of whom were included in the training phase), 1 female and 5 males aged between 24 and 28 years old, who were informed about the purpose and conduct of our research.

Armband positioning was performed as reported in Section 6.4.7, supervising the quality of acquired muscle activity and adjusting the armband placement accordingly. Since the armband performances are dependent on the ability of the user to perform the desired movement correctly, each subject was instructed prior to the testing phase in the proper movements execution.

The fulfillment of the testing phase required the subject to comply with the indications provided by an application displaying the movements to be performed on a monitor. Its routine was the same as in Section 6.4.7, except for step 8, where the number of repetitions was decreased to two instead of three. The entire process was repeated three times, updating the firmware of the *predictor* board with the ANN parameters obtained from the training procedures with an idle norm equal

to 5, 10, and 15, respectively (see Section 6.4.8). During the testing phase, the predicted output class was not provided to the subject in order to avoid any conscious adjustments of the hand movements.

The data collected from the testing campaign are reported in Fig. 6.23, divided according to the three different tested idle norms. In particular, confusion matrices (Fig. 6.23, left), accuracy, precision, recall, and f1-score metrics [237] (Fig. 6.23, right) are disclosed. To this end, the classes *predicted* by the armband were compared with the *true* classes obtained by segmenting the acquired signals. The segmentation of the movements and the subsequent *true* labeling are based on what was indicated by the support application during the testing phase. The *true* IS class was labeled as described in Section 6.4.7, by setting the same idle norm applied to the training dataset of the tested ANN. The reported confusion matrices were computed by summing those obtained from the six involved volunteers.

To balance the testing dataset, only 40 s of IS were considered in order to match the total timing of the other gestures (during the testing phase). Clearly, the dataset does not contain the same number of total elements for all the classes because of the physiological reaction times of the subjects, who do not respond instantaneously to the changes of the displayed gestures. Moreover, since the labeling process comes after the idle norm operation, the total number of labeled movements could differ for low and high idle norm (e.g., the two pinches) because the associated muscles activities could be too weak to be labeled differently from idle.

Looking at Fig. 6.23, and considering the evaluation metrics overall, the movement with the best outcomes is WF. It resulted in accuracies of 97.26 %, 97.84 %, and 98.83 % for the three idle norms analyzed, respectively. On the other hand, P2 and P3 show the worst results. Although the accuracies of the two pinches are higher than that of OH, the obtained values of precision, recall, and consequently f1-score are lower, especially in the case of idle norm equal to 15. Considering the similarity of the two gestures, which often leads to interchange the predicted class between them (as evidenced by the confusion matrices), an additional analysis, whose result are reported in Table 6.5, evaluated how the metrics change by merging these two gestures into the same class. Despite a worsening of accuracy for the merged pinches class (the number of true negatives decreased more than the increase of true positives), which, however, is still above 80 %, precision and recall improved

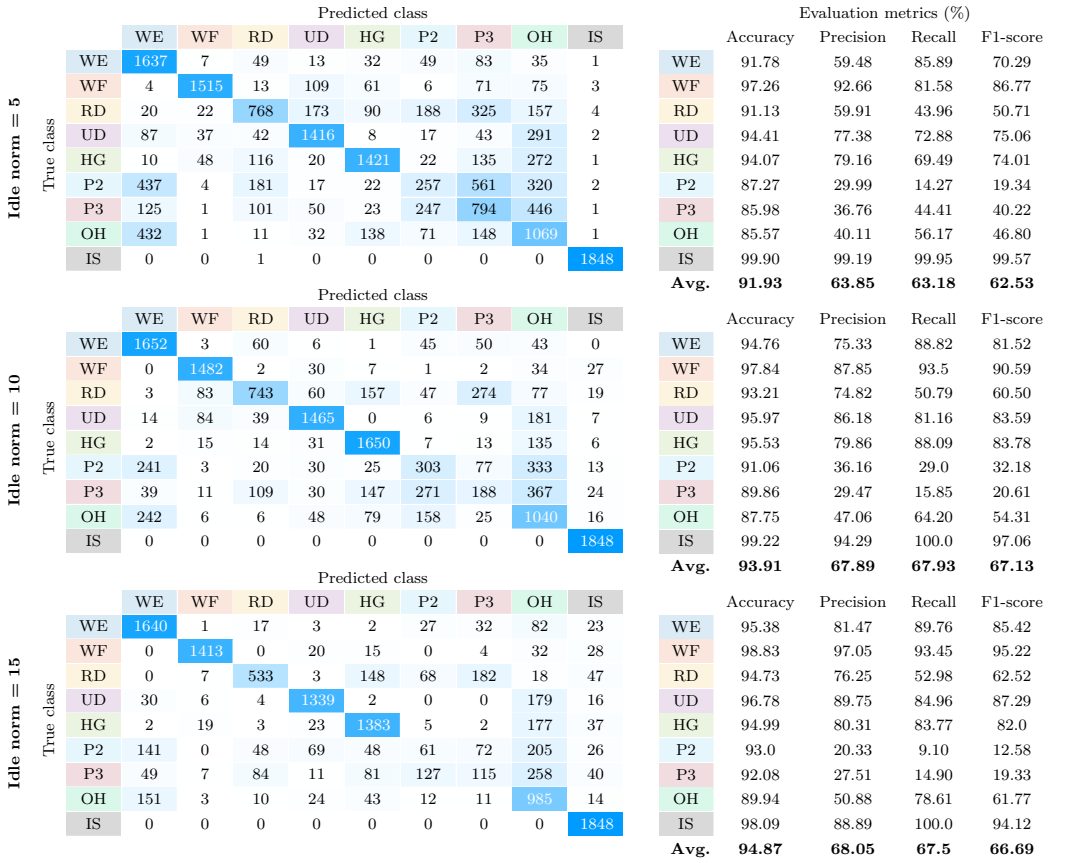

Fig. 6.23 Confusion matrices and evaluation metrics concerning the entire testing dataset. Obtained results are divided according the three idle norms used, i.e., 5, 10, and 15.

considerably. Indeed, in correspondence of idle norm equal to 15, a recall value of 26.01 % was obtained, which overcomes the lower 9.1 % resulted by the prediction of P2 as a distinct gesture.

As mentioned before, OH is among the gestures that, together with the two pinches, provides not totally satisfactory outcomes. However, while for the two pinches the difficulty lies in their poor amount of predictions, the reasons for the low performance of OH are caused by its misclassifications with other gestures (as can be seen from the confusion matrices). As an explanation for this behavior, it was observed that the volunteers who took part in the testing phase tended to extend their fingers during the execution of other gestures, obtaining values of muscular activation similar to the one related with OH.

Table 6.5 Evaluation metrics for merged pinches class

Idle norm	Evaluation metrics (%)			
	Accuracy	Precision	Recall	F1-score
5	82.85	61.62	51.80	56.28
10	85.80	56.84	37.61	45.27
15	88.36	52.23	26.01	34.72

Although using the idle norm equal to 5 results in the lowest values among the reported evaluation metrics, the overall outcomes of this test scenarios (including volunteers' feedback and considering the data distribution) makes it the most efficient in an application context (e.g., to control an HMI). Indeed, using higher idle norms has the consequence of losing many movements samples, such as reported for the case of the two pinches. Moreover, using a lower value of the idle norm allows the armband user to achieve the classification of the gesture being performed with minimal muscular effort. Furthermore, considering the IS row of the confusion matrix with an idle norm equal to 5, the number of misclassified idles as active movements is already practically equal to zero. Therefore, there is no stringent need to use high idle norms, even to cope with the noise of acquired muscle activity.

6.4.10 Prediction Latency

The prediction latency was evaluated directly on the MCU of the predictor board, by involving one of the timer peripherals. In particular, during the setup phase of the armband, the `TIMER2` of the predictor is configured, taking in input a 6 MHz clock, in order to obtain the most precision possible. Then, during active operations, if the selected mode is ML, the timer is started just before the execution of the prediction and its value is read immediately after the predicted class is returned. The obtained timer value is converted in ms and transmitted via UART communication to a computer, which saves the delays and performs the average at the end of the test. In order to obtain a statistically significant database, this time analysis was performed continuously for about 5 min, thus acquiring more than 2000 samples.

The timing latencies measured using the timer on the predictor board, involving the idle norm equal to 5, are analyzed in details. The obtained values are practically

constant, having an average value of 1.492 ms. In particular, the distribution presents a minimum value of 1.490 ms and a very sporadic maximum value at 1.548 ms. While the lower component of the distribution has to be attributed to a statistical deviation of the measured timer value, the higher value can derive from the concomitant TC counting of the predictor board itself. Indeed, even if the timer counting and the prediction are performed in the main code routine of the board, the arrival of one TC event during this operation would force the CPU to stop its execution, handle the TC count increment, and then resume to what it was evaluating before. This interruption, which does not introduce statistical relevance due to its low probability (i.e., the frequency of the TC events is bounded to 400 Hz by the *Apollux* AFE conditioning circuit, although usually it is far lower), can indeed cause the observed small increment in latency.

The application latency of a possible HMI which would involve this armband as human control sensor would be of 131.5 ms, considering that the ATC window contribution would be added to the predictor latency alone in this case. Even considering this overall delay, the proposed armband will still react a lot faster than the 300 ms threshold, commonly considered for the real-time control of robots and prostheses [25].

6.4.11 Power Consumption

The last analysis concerned the measure of the current absorbed by the developed armband. In order to maintain the size of the device as small as possible, a current sense resistor has not be placed on the PCB during the design phase, so an external setup was to be prepared for the measurement. It consists of the INA240 current sense amplifier by Texas Instruments [238], which, thanks to its enhanced switching noise rejection, better reacts to MCU state change w.r.t. a current probe or a multimeter, which is even worse due to the RMS characteristic of its measurements. A 10 Ω sense resistor was placed at the amplifiers inputs and the INA240A1 version (i.e., 20 V V^{-1} gain) was selected. Last, the output of the amplifier was captured with a standard probe of the Rigol MSO5104 digital signal oscilloscope [239], which allowed to digitally save the current measurements for further processing.

In particular, 2 s of data has been acquired for each one of the more significant armband active states, which are listed here below:

- Advertising: few seconds after being switched on, the master board starts advertising its presence to potential listening devices. The slave nodes are at this time inactive, with the MCU already in its deep sleep state;
- Connected: once a BLE client initialize a link with the armband, the master board enters the stable connection status. Both client and server nodes wait for the other to send some data and periodically check if the other peer is still active. The armband slave boards are still in deep sleep;
- ATC mode: when the BLE client requests for ATC notifications, the master module has to inform the slave boards of the requested task and all the seven boards start counting the TC values. Every 130 ms the master board sends a notification command to the lower levels of the BLE stack, which will effectively send the packet over the air at the next available connection interval;
- ML mode: as for the ATC mode, all the boards are active and counting. Furthermore, the predictor performs the ANN forward propagation every times it receives a valid ATC payload in the I^2C packet;
- ATC and ML mode combined: the boards effort is the same of the two previous modes, with the master sending both notifications, almost concurrently, to the BLE client.

The recorded current absorption values, shown in Table 6.6, have a quite low variance, with the lowest value during advertising (i.e., 2.712 mA) and the highest during the active mode involving both notifications sending (i.e., 3.029 mA), as supposed. Furthermore, the reported values are coherent w.r.t. the ones obtained in Section 4.4, when measured on a single *Apollux* board. However, the current drained in this application is lower to the expected value of 3.36 mA (i.e., 7×0.48 mA), thanks to the differentiation among the firmware of the master and slave boards, which allows the latters to enter the deep sleep state and save power.

In order to confirm the correct behavior of the setup and of the armband itself, a detailed analysis of the digitized waveforms has been carried out. In Fig. 6.24, a representative window of 300 ms, captured during ML mode, is reported. As it is possible to observe, the variations of the current requested by the armband are coherent with the specifications of the BLE protocol and with the expected behavior of the armband itself. In particular, few regular events alter the baseline:

Table 6.6 Current absorption in different operating conditions

	Advertising	Connected	Active mode		
			ATC	ML	Both
C.A.[1] **(mA)**	2.712	2.750	2.986	2.920	3.029
O.T.[2,3] **(h)**	64.5	63.6	58.6	59.9	57.8

[1]Current Absorption, [2]Operating Time

[3]Considering our 175 mA h Lithium Polymer Battery

- The double bump waveforms starting at about 1.51 s, 1.64 s and 1.77 s are to be attributed to the master board handling the end of each ATC window (i.e., every 130 ms) and to the consequent I^2C activity. Indeed, during that period of time, the six slave boards have to wake up and communicate with the following one, and the predictor has also to perform the ML computations. The width of the waveform during this type of activity is related to the low speed of the MCU clock (i.e., 24 MHz) and of the I^2C module, which exchanges data at 400 kHz. However, the amplitude is limited to 2 mA, thus having a modest impact on the average consumption;

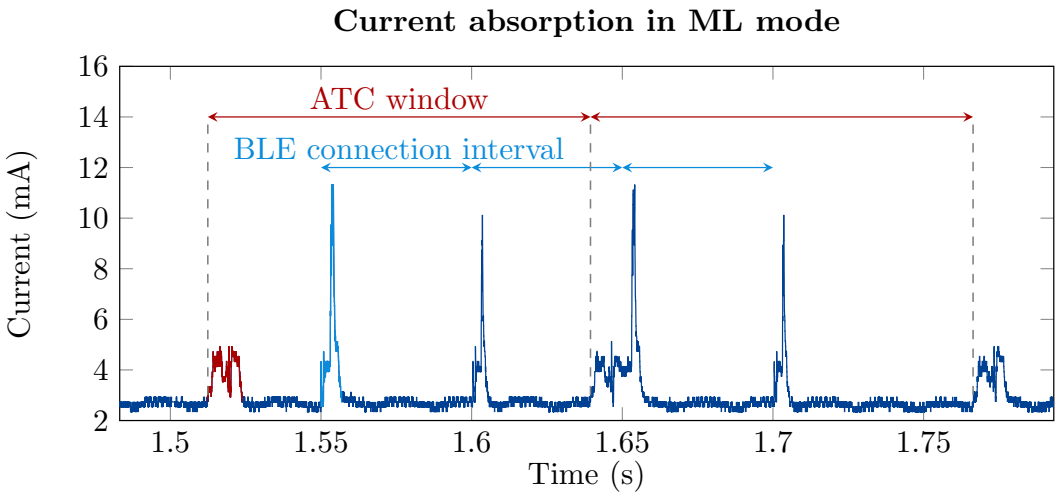

Fig. 6.24 Profile of the current absorbed by the armband, whose average measured value is 2.92 mA. Both the consumption concerning ATC data management (red) and the peaks related to the BLE communication (light blue) are distinguishable.

- The highest peaks, which reach 11 mA, are related to the sending of the BLE notifications, which requires the RF module to be powered on, even if for a very small amount of time. These peaks are always at steps of 50 ms due to the selected connection interval, and, thanks to a slave latency of 4, it appears only after a master action occurs within the previous connection interval (e.g., no transmission is visible at 1.75 ms);
- Peaks similar to the previous ones but slightly lower in amplitude, reaching almost 10 mA, are to be attributed to a BLE check for further packets, acknowledging to have received the previous notification packet. Most probably they have the same amplitude of the notifications ones, but their very short duration makes them too fast to be entirely captured by the DSO sampling. Also these peaks follow the timing of the BLE connection, being aligned to the 50 ms ticks too.

All the above considered, the calculated mean current absorption of 2.92 mA is practically represented by the baseline of the graph, since the three main activities of the armband have a current request either small in amplitude or short in duration, thus not affecting the average value very much. In conclusion, the armband can continuously operate in ML mode for about 60 h, without needing a battery recharge, thus allowing its inclusion in outdoor activities, even if spread on more than one day.

6.4.12 Comparison with SoA works

Having analyzed in details the performance and the overall behavior of the armband prototype, this final section concludes the discussion by inserting it into the perspective of other literature studies. Since the state of the art regarding sEMG-based hand gesture recognition is very broad, as introduced at the beginning of the chapter, here the most relevant works (for the sake of the comparison) have been selected. Tables 6.7 and 6.8 report two of the predecessors [70, 229] of this study and seven works of other research groups, all published in the last four years. The variety of applications and, sometimes, the ambiguous phrasing of some results make the performances indicators (i.e., column 2–7 of Table 6.8) not properly populated, but this analysis tried to examine the different situations in details (not always traceable).

All the reported works have developed their wearable device, but only [184, 70, 206, 193] managed to fit their learner into the embedded prototype. The armband de-

Table 6.7 Comparison with state of the art sEMG-based hand gesture classifiers (Part I)

Work	Year	f	#Ch.	#Mov.	Armband	MCU	Classifier Type
[184]	2018	DWT[1]	4	5		✓	SVM
[186]	2019	raw sEMG	10	11	✓		ConvNet
[70]	2020	ATC	3	6		✓	ANN
[206]	2020	multiple	8	4	✓	✓	LDA[2]
[180]	2020	multiple	8	6	✓		ANN
[200]	2020	raw sEMG	8	7	✓		Conv-GRU[3]
[193]	2020	custom	32	8		✓	CNN
[208]	2021	raw sEMG	128	30			CNN
[229]	2021	ATC	2	3			ANN
This	2022	ATC	7	9	✓	✓	ANN

[1]Discrete Wavelet Transform, [2]Linear Discriminant Analysis, [3]Gated Recurrent Unit

veloped in [186], for example, is reported to be designed to support the development of embedded ML algorithms, but all the predictions are still evaluated on a computer. Similarly, [200, 180] use the Myo armband as acquisition device, sending data via wireless communication to an elaboration unit, and [208] still involves electrodes matrices wired to a data collection unit, which sends the processed information to a computer for the further prediction. Also in the ATC-related introductory work [229] the ML computations were not performed on-board, since the *Apollux* were still employed as standalone modules.

Regarding the implemented algorithms, the totality of the computer-based works involve the NN structure in their predictions. Many research groups exploit the capability of the CNN paradigm, even with some enhanced features added, while only [180] maintains the simpler ANN structure. On the other hand, all the embedded solutions fell back on more compact classifiers, like smaller ANNs [70], SVM [184] or even the Linear Discriminant Analysis (LDA) [206]. The only work that was able to perform a CNN computation on a microcomputer inside a prosthesis is [193], which, applying 32 High-Density (HD) sEMG electrodes on the skin covered by the prosthesis body, was able to recognize 8 gestures with 98.2 % accuracy. Apart from this study, the numbers of channels used to predict the gestures are pretty stable across the literature, maintaining a 1 vs 1 ratio with a value around 8 (probably due to the big influence the Myo armband has on the field at this moment). The

Table 6.8 Comparison with state of the art sEMG-based hand gesture classifiers (Part II)

Work	Classifier Type	Acc. (%)	Δt (ms)	V_{DD} (V)	C.A.[1] (mA)	B.C.[2] (mA h)	O.T.[3] (h)
[184]	SVM	94.0	256	n.a.	n.a.	200	129
[186]	ConvNet	89.5	n.a.	n.a.	n.a.	100	6
[70]	ANN	96.3	8.5	n.a.	n.a.	n.a.	n.a.
[206]	LDA[4]	>90	360	3.7	n.a.	380	n.a.
[180]	ANN	94.7	338	n.a.	n.a.	n.a.	n.a.
[200]	Conv-GRU[5]	82.2	39	n.a.	n.a.	n.a.	n.a.
[193]	CNN	98.2	5	3.3	15	n.a.	n.a.
[208]	CNN	92.4	n.a.	n.a.	n.a.	n.a.	n.a.
[229]	ANN	97.9	n.a.	3.7	0.96	220	230
This	ANN	91.9[6]	1.49	3.7	2.92	175	60

[1]Current Absorption, [2]Battery Capacity, [3]Operating Time
[4]Linear Discriminant Analysis, [5]Gated Recurrent Unit
[6]Considering the most comfortable use-case with idle norm equal to 5

other few exceptions found are represented by [186], in which a 10-channel custom armband is developed, recognizing 11 different hand movements with an overall accuracy of 89.5 %, and [208], whose HD electrodes matrices allows the researchers to predict (on a computer) 30 movements with an average accuracy of 92.4 %. The accuracies of the remaining studies are all around the 90 %, with variations due to more channels involved or to less complexity of the output space.

On the other hand, the prediction latency presents wider variations, with a few values missing, going from the lowest delay of this work (i.e., 1.49 ms) and increasing up to 360 ms for [206]. Nevertheless, these values have to be interpreted according to the indication of when they are sampled, in order to obtain a meaningful relation. Indeed, even if not explicitly reported, most probably the values obtained from [200, 193] take into account only the real prediction time, while [184, 206, 180] probably consider broader acquisition windows needed as input of their algorithms. In this thesis, both considering the pure prediction latency and adding the ATC window needed for the TC computation (i.e., a total of 131.5 ms), the proposed architecture is still well competitive w.r.t. the other works, with a delay of less than the half of the others'.

Last, regarding power consumption and consequent operating time, the poor data availability from the other works made difficult to perform an all-around significant

analysis. Apart from the other ATC previous works, the data under discussion have been found only for three studies: the CNN implementations of [186, 193] brought their prototype battery life down to 6 h or even less, while [184] has the longer operating time (among embedded solutions), with a battery life of about 129 h. However, since the duration of their acquisition window is twice as long as the ATC one, the reported hours of operation are comparable with the battery duration of this proposed device.

All the above considered, the developed armband fits pretty well into present state of the art literature, not with only top scores, but with a good balance of all the considered metrics. So, to the best of my knowledge, this prototype can fulfill its purpose in the field of wearable armbands for HMI applications, giving the users a wider choice when selecting the device needed for rehabilitation as well as robotic control.

Chapter 7

Conclusions

During this Ph.D project a multi-channel system for the long-term monitoring and processing of the skeletal muscle information, assessed through the surface ElectroMyoGraphy (sEMG) technique, has been designed. After the identification of the limitations of the current commercial sEMG acquisition devices (e.g., limited operating time, high computational effort for sEMG processing), which confine their application to clinical environments, three design paradigms (i.e., bio-inspired, event-based, information synthesis) have been selected for the development of the custom sensing nodes. Combining the paradigms into the event-driven Average Threshold Crossing (ATC) approach, which basically extracts the informative events from the sEMG signal by counting how many times it crosses a threshold during an observation window (i.e., ATC window of 130 ms), it was possible to obtain a first functional prototype featuring, in an all-inclusive Printed Circuit Board (PCB), the following characteristics:

- Analog Front End (AFE) for the bipolar conditioning of sEMG signal, which comprises a band-pass filter in the 30 Hz to 400 Hz frequency band to discriminate only the muscular contributions, a variable amplification covering the 500-2500 gain range in order to detect both superficial or deeper muscles with a sufficient resolution, the voltage comparator to extract the Threshold Crossing (TC) signal. All the filter and amplification designed rules and best practices have been considerably relaxed because of the final analog TC extraction stage, which, by comparing the signal with a threshold, does not requires the maximal fidelity of the conditioned sEMG signal.

- Digital interface, implemented through the Apollo 3 Blue MicroController Unit (MCU), which handles the acquisition and calibration routines, error management, and data transmission (often) concurrently thanks to the FreeRTOS embedded operating system. Although the sEMG sampling has been maintained at user's request for debug and comparison, the main focus is related to the ATC computing, which finalizes the feature extraction process without involving the typical MCU peripherals for signal sampling (e.g., ADC, DMA), thus allowing the MCU to stay in its sleeping states longer saving energy.

- Bluetooth Low Energy (BLE) 4.2 wireless communication, which, implementing its own server, provides to the user an accessible service containing all the functional characteristics (e.g., command, sEMG, ATC). Besides the main settings (threshold value, AFE gain), the BLE parameters of the sEMG and ATC working modes have been optimized for each case, thus totally exploiting the benefits of the event-driven approach in term of application payload (i.e., $8\,\mathrm{B\,s^{-1}}$ ATC vs. $1\,\mathrm{kB\,s^{-1}}$ sEMG), to reach the real-time data transmission.

- A final PCB dimension of 20.5 mm x 33.2 mm x 9.5 mm including, beside the above components, the charger circuit for the battery, the debug and flashing interfaces, the connectors for battery, electrodes, and I^2C lines, which complete the wearable scenario.

The acquisition setup, shown in Figure 7.1, has been completed by designing the case for the board, boxing together PCB, battery, and electrode connectors (with a final dimension of 57.8 mm x 25.2 mm x 22.1 mm), and developing the software for the user interface.

Once the prototyping phase has been completed, the validation analyses have been performed. Firstly, the correct behavior of the AFE has been assessed by checking the frequency response for both the TC and sEMG signals; then, static and dynamic contraction tests have been carried out to evaluate if the muscular signals have been correctly conditioned. In particular, the outcomes confirmed a detection of the sEMG signal over the defined constraint (i.e., $\mathrm{SNR} \geq 15\,\mathrm{dB}$) for all the considered cases, and an ATC correlation with the exerted force close to 1. Moreover, also a reliability analysis, conducted by comparing the proposed device with the Cometa Mini Wave (gold standard) using the ICC index, demonstrated the

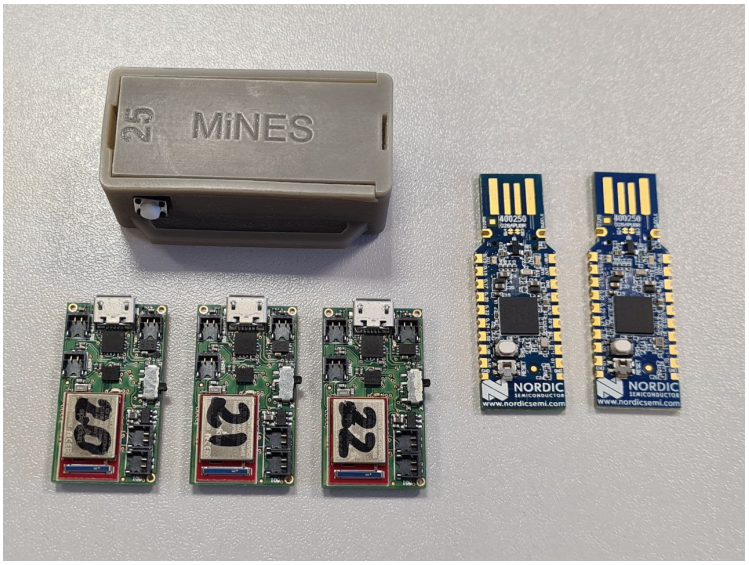

Fig. 7.1 Acquisition setup: here the complete device (no. 25), three PCBs and two BLE dongles (for standardizing connectivity of the laptop) are represented.

robust behavior of the sEMG measurements, consistent w.r.t. state of the art devices. Last, the evaluation of power consumption concluded the test phase proving the designed device to be suitable for long-term monitoring, since it achieved a steady sEMG transmission of 80 h, or, additionally benefiting from the ATC approach, to cover an event-driven acquisition of a week.

After the validation of the acquisition and processing system, it has been employed as sensing unit to build up two biomedical systems.

The first one concerns the active control of the Functional Electrical Stimulation (FES), which aims to define the FES profiles (e.g., a sequence of pulses) on the basis of the muscular activation every time a new ATC value is available. An ATC-FES system, comprising the developed acquisition units, a platform running the custom software, and the RehaMove 2 stimulator, has been developed aiming to work in two main configurations: a therapist-patient one, in which the movement performed by a first subject is replicated by a second one, and the self-stimulation, which allows the user to acquire the muscle signals by her/his limbs and to stimulate the controlateral ones. Among the informatics test, which involve different platforms in order to prove the performance of the approach w.r.t. the machine specifications (i.e., starting

from a standard laptop and then scaling down to an RPi-0W), it was possible to achieve an ATC-FES processing time always lower than the constraint of 130 ms (i.e., the ATC window), also going down below the 10 ms if a laptop is used for the computation. On the other side, with an experimental campaign involving 17 healthy subjects, the system has been functionally evaluated considering the effectiveness of the stimulated movement w.r.t. the voluntary one. A multi-parameter approach (e.g., cross-correlation, execution delay, area under the curve) has been setup and analyzed in order to confirm the proper behavior of the FES control, also carrying out a comparison with similar state of the art works.

The second application regards the realization of a custom armband for the hand gesture recognition. The device, which comprises seven channels, has been build using the proposed sensor unit as the basic block. Here, the three roles of master, slave and predictor board has been defined: the first one is in charge of controlling the armband functionalities while providing the BLE connectivity to communicate with it; the second one corresponds to the node which only senses the muscle activation; the last one, the predictor, is also in charge to classify on-board the hand gesture. After the design and prototyping of the armband, it was employed to create an ATC-based dataset of muscle activation from 21 subjects. An Artificial Neural-Network (ANN) classifier architecture has been trained on these data, and its parameters have been loaded on the predictor board for the online testing phase. Five subjects took part at this stage, each of them performing a set of hand movements. An overall accuracy of 91.9 %, with a prediction time of 1.49 ms, have been obtained as the best results. Moreover, by combining the ATC approach with the firmware optimization, the power consumption of the armband has been reduced to 2.92 mA, allowing the device to operate up to 60 h.

Now, after the above recap of the main outcomes achieved during this Ph.D. project, a personal and critical discussion about how the developed technology fits in the target analyzed biomedical applications could finally be addressed.

As deeply discussed in this thesis, the main peculiarity of the developed system is the (hardware and firmware) implementation of the ATC technique, which, thanks to the combination of three design paradigms (i.e., bio-inspired, event-based, information synthesis), allows the monitoring of the muscle activity to be easily

assessed by means of a single, hardware-extracted, low computational parameter. This technique takes the distance from standard acquisition methodologies, which generally sample and process the sEMG signal at the firmware or software domains aiming to extract the relevant parameters, because it does not even require a digital signal conversion (i.e., using an ADC) to obtain an indicator of the muscular activation. Indeed, only by using the proposed analog circuitry is it possible to detect the informative events contained in the sEMG signal, thus not requiring the digitization, storing, and transmission of the whole (raw) muscle signal. Therefore, looking at the differences between the standard approach and the event-driven one, the following question could be asked: does the partial discard of the sEMG signal information (e.g., waveform, energy, and frequency content) be an issue for the correct evaluation of the muscle activity?

From my experience, the correct answer is related to the target application. Indeed, as reported in the introduction to this thesis, nowadays the use of sEMG spreads from its clinical adoption as a diagnostic tool (e.g., gait analysis, muscle recovery) to its employment for monitoring sport performance (e.g., wearable multi-sensors unit) or for building HMI system (e.g., control of a prosthetic hand).

Starting from the clinical scenario, the medical assessment of a neuro-muscular pathology still needs an in-depth evaluation of the sEMG signal, concerning, e.g., the analysis of waveform associated with the myofibers contraction, the conduction velocity of the muscular and nerve fibers. In this context, the synthesis of the information resulting from the ATC approach, and its intrinsic lower time resolution, is limited for performing a robust diagnosis based on the ATC parameter alone. On the other hand, the implementation of the ATC demonstrated several benefits (e.g., device miniaturization, real-time responsiveness, long operating time) for developing sEMG systems able to operate also outside of dedicated facilities, an achievement not yet reached by standard sEMG devices. For these reasons, I believe that the combination of both the methodologies could be the way to provide an efficient solution to obtain a correct diagnosis, which is also supported by the long monitoring of the muscle condition during the daily-life activities. In other words, an ATC-based device can work as an holder to achieve constant monitoring of the muscle activity while the user (or patient) is conducting her/his life as usual, and, when a *failure* index arises (e.g., the muscle does not respond as expect), a more detailed analysis could be carried out by using the standard (and more complete) electromyography.

Vice versa, the discussion is reversed considering HMI and similar applications. Indeed, all these applications generally require an index of the muscle activity to perform a related action, e.g., controlling the motion of a device, enabling/disabling the application of rehabilitative therapies, interacting with an informatics system. In these circumstances, the detailed analysis of the entire sEMG signals is unnecessary because the final goal is to provide an intensity indicator. In order to accomplish this task, depending on the application requirements, the feature extraction process could be achieved offline, e.g., on a laptop, or online, directly on the sensing node. In the last situation, in particular, the sampling and processing of the sEMG signals represent the bottleneck to achieving fast, low-power, and long-lasting HMI systems. Precisely for these reasons, here the ATC technique finds its best applicability: since it performs the feature extraction process in hardware (with a marginal involvement of the MCU unit), it not only provides a muscle parameter directly suitable for the interfacing commands but also enables a cascade of benefits in terms of energy savings. Furthermore, considering the extensive involvement of machine learning methods for HMI applications, the ATC approach has been demonstrated to drastically reduce the complexity of these algorithms, easing their implementation for the limited-resources devices without impacting the classifiers performance.

In conclusion, looking at the above discussion in its entirety, from the design of the ATC processing node to its use in biomedical applications, and keeping in mind the advantages and the limitations of the ATC approach, I can confirm that the proposed device performs pretty well wherever it is employed, from its standalone usage to the control of the FES, also satisfying the requisites when it works for gesture recognition.

References

[1] J. Cram, "The history of surface electromyography," *Applied psychophysiology and biofeedback*, vol. 28, pp. 81–91, 07 2003.

[2] R. Merletti, A. Botter, and U. Barone, *Detection and Conditioning of Surface EMG Signals*, ch. 3, pp. 1–37. John Wiley & Sons, Ltd, 2016.

[3] C. Steele, *Applications of EMG in Clinical and Sports Medicine*. IntechOpen, 2012.

[4] I. Campanini, C. Disselhorst-Klug, W. Z. Rymer, and R. Merletti, "Surface EMG in clinical assessment and neurorehabilitation: Barriers limiting its use," *Frontiers in Neurology*, vol. 11, p. 934, 2020.

[5] R. Pilkar, K. Momeni, A. Ramanujam, M. Ravi, E. Garbarini, and G. F. Forrest, "Use of surface EMG in clinical rehabilitation of individuals with SCI: Barriers and future considerations," *Frontiers in Neurology*, vol. 11, p. 1680, 2020.

[6] P. Leelaarporn, P. Wachiraphan, T. Kaewlee, T. Udsa, R. Chaisaen, T. Choksatchawathi, R. Laosirirat, P. Lakhan, P. Natnithikarat, K. Thanontip, W. Chen, S. C. Mukhopadhyay, and T. Wilaiprasitporn, "Sensor-driven achieving of smart living: A review," *IEEE Sensors Journal*, vol. 21, no. 9, pp. 10369–10391, 2021.

[7] G. Biagetti, P. Crippa, L. Falaschetti, and S. Orcioni, "Human activity monitoring system based on wearable sEMG and accelerometer wireless sensor nodes," *BioMedical Engineering OnLine*, vol. 17, 11 2018.

[8] C. Prahm, I. Vujaklija, F. Kayali, P. Purgathofer, and O. C. Aszmann, "Game-based rehabilitation for myoelectric prosthesis control," *JMIR Serious Games*, vol. 5, p. e3, 02 2017.

[9] A. B. Soares, E. A. L. Junior, A. de Oliveira Andrade, and A. Cardoso, *Virtual and Augmented Reality: A New Approach to Aid Users of Myoelectric Prostheses*, ch. 17. Rijeka: IntechOpen, 2012.

[10] M. Simão, N. Mendes, O. Gibaru, and P. Neto, "A review on electromyography decoding and pattern recognition for human-machine interaction," *IEEE Access*, vol. 7, pp. 39564–39582, 2019.

[11] L. Bi, A. G. Feleke, and C. Guan, "A review on EMG-based motor intention prediction of continuous human upper limb motion for human-robot collaboration," *Biomedical Signal Processing and Control*, vol. 51, pp. 113–127, 2019.

[12] G. Meltzner, J. Heaton, Y. Deng, G. Luca, S. Roy, and J. Kline, "Development of sEMG sensors and algorithms for silent speech recognition," *Journal of Neural Engineering*, vol. 15, 06 2018.

[13] A. Calado, F. Soares, and D. Matos, "A review on commercially available anthropomorphic myoelectric prosthetic hands, pattern-recognition-based microcontrollers and sEMG sensors used for prosthetic control," in *2019 IEEE International Conference on Autonomous Robot Systems and Competitions (ICARSC)*, pp. 1–6, 2019.

[14] K. Li, J. Zhang, L. Wang, M. Zhang, J. Li, and S. Bao, "A review of the key technologies for sEMG-based human-robot interaction systems," *Biomedical Signal Processing and Control*, vol. 62, p. 102074, 2020.

[15] Digital Science & Research Solutions, Inc., ""surface electromyography" in Publications - Dimension." Accessed: Monday 10th October, 2022.

[16] National Library of Medicine, ""surface electromyography" - Search Results - PubMed." Accessed: Monday 10th October, 2022.

[17] Cometa srl, "Cometa systems." Accessed: Monday 10th October, 2022.

[18] Biometrics Ltd, "Surface EMG sensor." Accessed: Monday 10th October, 2022.

[19] Delsys Incorporated, "Delsys family of products." Accessed: Monday 10th October, 2022.

[20] PLUX Wireless Biosignals S.A., "BITalino (r)evolution MuscleBIT BT." Accessed: Monday 10th October, 2022.

[21] G. L. Cerone, A. Botter, and M. Gazzoni, "A modular, smart, and wearable system for high density sEMG detection," *IEEE Transactions on Biomedical Engineering*, vol. 66, no. 12, pp. 3371–3380, 2019.

[22] L. Zhu, G. Mao, H. Su, Z. Zhou, W. Li, X. Lü, and Z. Wang, "A wearable, high-resolution, and wireless system for multichannel surface electromyography detection," *IEEE Sensors Journal*, vol. 21, no. 8, pp. 9937–9948, 2021.

[23] C. J. D. Luca, *Surface Electromyography: Detection and Recording*.

[24] G. De Luca, *Fundamental Concepts in EMG Signal Acquisition*. DelSys Incorporated, 2001.

[25] B. Gao, C. Wei, H. Ma, S. Yang, X. Ma, and S. Zhang, "Real-time evaluation of the signal processing of sEMG used in limb exoskeleton rehabilitation system," *Applied Bionics and Biomechanics*, vol. 2018, pp. 1–6, 10 2018.

[26] K.-M. Chang, S.-H. Liu, and X.-H. Wu, "A wireless sEMG recording system and its application to muscle fatigue detection," *Sensors*, vol. 12, no. 1, pp. 489–499, 2012.

[27] D. Brunelli, E. Farella, D. Giovanelli, B. Milosevic, and I. Minakov, "Design considerations for wireless acquisition of multichannel sEMG signals in prosthetic hand control," *IEEE Sensors Journal*, vol. 16, no. 23, pp. 8338–8347, 2016.

[28] M. Ergeneci, K. Gokcesu, E. Ertan, and P. Kosmas, "An embedded, eight channel, noise canceling, wireless, wearable sEMG data acquisition system with adaptive muscle contraction detection," *IEEE Transactions on Biomedical Circuits and Systems*, vol. 12, no. 1, pp. 68–79, 2018.

[29] Y.-H. Yang, S.-J. Ruan, P.-C. Chen, Y.-T. Liu, and Y.-H. Hsueh, "A low-cost wireless multichannel surface EMG acquisition system," *IEEE Consumer Electronics Magazine*, vol. 9, no. 5, pp. 14–19, 2020.

[30] A. Prakash, B. Kumari, and S. Sharma, "A low-cost, wearable sEMG sensor for upper limb prosthetic application," *Journal of Medical Engineering & Technology*, vol. 43, no. 4, pp. 235–247, 2019. PMID: 31414614.

[31] SparkFun Electronics®, "MyoWare muscle sensor kit." Accessed: Monday 10th October, 2022.

[32] P. Motto Ros, A. Sanginario, M. Crepaldi, and D. Demarchi, "Quality-energy trade-off and bio-inspired electronic systems," in *2018 IEEE International Conference on the Science of Electrical Engineering in Israel (ICSEE)*, pp. 1–5, 2018.

[33] E. M. Mcnally, K. A. Lapidos, and M. T. Wheeler, *Skeletal Muscle Structure and Function*, pp. 674–681. Totowa, NJ: Humana Press, 2006.

[34] W. Frontera and J. Ochala, "Skeletal muscle: A brief review of structure and function," *Calcified tissue international*, vol. 96, 10 2015.

[35] Nephron.

[36] H. Gray and H. V. Charter, *Gray's Anatomy: Descriptive and Surgical*. New York: Barnes & Noble, 1995.

[37] M. Hutchinson, J. Mallatt, E. Marieb, R. Hutchings, P. Wilhelm, and N. Zanetti, *A Brief Atlas of the Human Body*. Anatomy & physiology, Pearson Benjamin Cummings, 2007.

[38] B. staff, "Medical gallery of blausen medical 2014." WikiJournal of Medicine 1 (2).

[39] C. L. Stanfield, *Principles of Human Physiology*. Pearson Education Limited, 6th ed., 2017.

[40] R. M. Enoka and J. Duchateau, *Physiology of Muscle Activation and Force Generation*, ch. 1, pp. 1–29. John Wiley & Sons, Ltd, 2016.

[41] G. J. Tortora and B. Derrickson, *Principles of anatomy & physiology*. John Wiley & Sons, Inc., 14th ed., 2014.

[42] K. Mukund and S. Subramaniam, "Skeletal muscle: A review of molecular structure and function, in health and disease," *Wiley Interdisciplinary Reviews: Systems Biology and Medicine*, vol. 12, 08 2019.

[43] G. Kamen, *Electromyographic Kinesiology*, ch. 8. Champaign, IL : Human Kinetics, 2014.

[44] M. Neuman, *Biopotential electrodes*, pp. 4–1. 01 2014.

[45] D. Farina, D. F. Stegeman, and R. Merletti, *Biophysics of the Generation of EMG Signals*, ch. 2, pp. 1–24. John Wiley & Sons, Ltd, 2016.

[46] G. V. Dimitrov and N. A. Dimitrova, "Precise and fast calculation of the motor unit potentials detected by a point and rectangular plate electrode.," *Medical engineering & physics*, vol. 20 5, pp. 374–81, 1998.

[47] C. J. D. Luca and W. J. Forrest, "Some properties of motor unit action potential trains recorded during constant force isometric contractions in man," *Kybernetik*, vol. 12, pp. 160–168, 1973.

[48] C. J. De Luca, "Physiology and mathematics of myoelectric signals," *IEEE Transactions on Biomedical Engineering*, vol. BME-26, no. 6, pp. 313–325, 1979.

[49] Y. M. Chi, T. Jung, and G. Cauwenberghs, "Dry-contact and noncontact biopotential electrodes: Methodological review," *IEEE Reviews in Biomedical Engineering*, vol. 3, pp. 106–119, 2010.

[50] C. J. D. Luca, "The use of surface electromyography in biomechanics," *Journal of Applied Biomechanics*, vol. 13, no. 2, pp. 135 – 163, 1997.

[51] H. Hermens, B. Freriks, R. Merletti, G. Rau, C. Disselhorst-Klug, D. Stegeman, and G. Hägg, "SENIAM project." Accessed: Monday 10th October, 2022.

[52] M. Z. Jamal, "Signal acquisition using surface emg and circuit design considerations for robotic prosthesis," in *Computational Intelligence in Electromyography Analysis* (G. R. Naik, ed.), ch. 18, Rijeka: IntechOpen, 2012.

[53] E. Spinelli and F. Guerrero, *Chapter 12-THE BIOLOGICAL AMPLIFIER*, ch. 12. World Scientific, 07 2019.

[54] C. Levkov, G. Mihov, R. Ivanov, I. Daskalov, I. Christov, and I. Dotsinsky, "Removal of power-line interference from the ecg: A review of the subtraction procedure," *Biomedical engineering online*, vol. 4, p. 50, 09 2005.

[55] A. Goen and D. Tiwari, "Review of surface electromyogram signals: Its analysis and applications," *International Journal of Electrical, Computer, Energetic, Electronic and Communication Engineering*, vol. 7, pp. 1429–1437, 01 2013.

[56] R. H. Chowdhury, M. B. I. Reaz, M. A. B. M. Ali, A. A. A. Bakar, K. Chellappan, and T. G. Chang, "Surface electromyography signal processing and classification techniques," *Sensors*, vol. 13, no. 9, pp. 12431–12466, 2013.

[57] C. Spiewak, M. R. Islam, M. Assad-Uz-Zaman, and M. Rahman, "A comprehensive study on emg feature extraction and classifiers," *Open Access Journal of Biomedical Engineering and its Applications*, vol. 1, 02 2018.

[58] BTS Bioengineering Corp., "Freeemg." Accessed: Monday 10th October, 2022.

[59] BTS Bioengineering Corp., "Freeemg 1000 h_20." Accessed: Monday 10th October, 2022.

[60] F. Rossi, A. Mongardi, P. M. Ros, M. R. Roch, M. Martina, and D. Demarchi, "Tutorial: A versatile bio-inspired system for processing and transmission of muscular information," *IEEE Sensors Journal*, vol. 21, no. 20, pp. 22285–22303, 2021.

[61] R. Barioul, S. Fakhfakh, H. Derbel, and O. Kanoun, "Evaluation of EMG signal time domain features for hand gesture distinction," in *2019 16th International Multi-Conference on Systems, Signals Devices (SSD)*, pp. 489–493, 2019.

[62] D. C. Toledo-Pérez, J. Rodríguez-Reséndiz, and R. A. Gómez-Loenzo, "A study of computing zero crossing methods and an improved proposal for EMG signals," *IEEE Access*, vol. 8, pp. 8783–8790, 2020.

[63] M. Crepaldi, M. Paleari, A. Bonanno, A. Sanginario, P. Ariano, D. H. Tran, and D. Demarchi, "A quasi-digital radio system for muscle force transmission based on event-driven ir-uwb," in *2012 IEEE Biomedical Circuits and Systems Conference (BioCAS)*, pp. 116–119, 2012.

[64] P. Motto Ros, M. Paleari, N. Celadon, A. Sanginario, A. Bonanno, M. Crepaldi, P. Ariano, and D. Demarchi, "A wireless address-event representation system for ATC-based multi-channel force wireless transmission," *5th IEEE International Workshop on Advances in Sensors and Interfaces IWASI*, pp. 51–56, 2013.

[65] S. Sapienza, M. Crepaldi, P. Motto Ros, A. Bonanno, and D. Demarchi, "On integration and validation of a very low complexity ATC UWB system for muscle force transmission," *IEEE Transactions on Biomedical Circuits and Systems*, vol. 10, no. 2, pp. 497–506, 2016.

[66] D. A. F. Guzman, S. Sapienza, B. Sereni, and P. Motto Ros, "Very low power event-based surface emg acquisition system with off-the-shelf components," in *2017 IEEE Biomedical Circuits and Systems Conference (BioCAS)*, pp. 1–4, 2017.

[67] A. Shahshahani, M. Shahshahani, P. Motto Ros, A. Bonanno, M. Crepaldi, M. Martina, D. Demarchi, and G. Masera, "An all-digital spike-based ultra-low-power IR-UWB dynamic average threshold crossing scheme for muscle force wireless transmission," in *2015 Design, Automation Test in Europe Conference Exhibition (DATE)*, pp. 1479–1484, 2015.

[68] F. Rossi, P. Motto Ros, S. Cecchini, A. Crema, S. Micera, and D. Demarchi, "An event-driven closed-loop system for real-time FES control," in *2019 26th IEEE International Conference on Electronics, Circuits and Systems (ICECS)*, pp. 867–870, 2019.

[69] S. Sapienza, P. M. Ros, D. A. F. Guzman, F. Rossi, R. Terracciano, E. Cordedda, and D. Demarchi, "On-line event-driven hand gesture recognition based on surface electromyographic signals," in *2018 IEEE International Symposium on Circuits and Systems (ISCAS)*, pp. 1–5, 2018.

[70] A. Mongardi, P. Motto Ros, F. Rossi, M. Ruo Roch, M. Martina, and D. Demarchi, "A low-power embedded system for real-time sEMG based event-driven gesture recognition," in *2019 26th IEEE International Conference on Electronics, Circuits and Systems (ICECS)*, pp. 65–68, 2019.

[71] F. Rossi, P. Motto Ros, S. Sapienza, P. Bonato, E. Bizzi, and D. Demarchi, "Wireless low energy system architecture for event-driven surface electromyography," in *Applications in Electronics Pervading Industry, Environment and Society* (S. Saponara and A. De Gloria, eds.), (Cham), pp. 179–185, Springer International Publishing, 2019.

[72] Bluetooth SIG Inc., "Bluetooth specification version 4.1." Accessed: Monday 10th October, 2022.

[73] Bluetooth SIG Inc., "Bluetooth specification version 4.2." Accessed: Monday 10th October, 2022.

[74] J. Tosi, F. Taffoni, M. Santacatterina, R. Sannino, and D. Formica, "Performance evaluation of bluetooth low energy: A systematic review," *Sensors*, vol. 17, no. 12, 2017.

[75] Microchip Technology, Inc., "Bluetooth® low energy packet types." Accessed: 26/01/2022.

[76] P. Motto Ros, B. Miccoli, A. Sanginario, and D. Demarchi, "Low-power architecture for integrated CMOS bio-sensing," in *2017 IEEE Biomedical Circuits and Systems Conference (BioCAS)*, pp. 1–4, 2017.

[77] Ambiq Micro, Inc., "Apollo3 MCU Datasheet." PDF document, 5 2021. Revision 0.15.0, URL: https://ambiq.com/apollo3-blue/, last accessed on Monday 10th October, 2022.

[78] Nordic Semicondutor, "nRF52840 Dongle." Accessed: Monday 10th October, 2022.

[79] Texas Instruments, "CC2642R." Accessed: Monday 10th October, 2022.

[80] ST Microelectronics, "STM32WB55VG." Accessed: Monday 10th October, 2022.

[81] NXP, "QN908x: Ultra-Low-Power Bluetooth Low Energy System on Chip Solution." Accessed: Monday 10th October, 2022.

[82] R. Merletti and S. Muceli, "Tutorial. surface EMG detection in space and time: Best practices," *Journal of Electromyography and Kinesiology*, vol. 49, p. 102363, 2019.

[83] C. J. De Luca, L. Donald Gilmore, M. Kuznetsov, and S. H. Roy, "Filtering the surface EMG signal: Movement artifact and baseline noise contamination," *Journal of Biomechanics*, vol. 43, no. 8, pp. 1573–1579, 2010.

[84] R. Merletti and G. Cerone, "Tutorial. surface EMG detection, conditioning and pre-processing: Best practices," *Journal of Electromyography and Kinesiology*, vol. 54, p. 102440, 2020.

[85] E. M. Spinelli, R. Pallas-Areny, and M. A. Mayosky, "AC-coupled front-end for biopotential measurements," *IEEE Transactions on Biomedical Engineering*, vol. 50, no. 3, pp. 391–395, 2003.

[86] Texas Instruments, "INA333 micro-power (50 μa), zerø-drift, rail-to-rail out instrumentation amplifier," 7 2008. Revised December 2015, accessed: 26/01/2022.

[87] S. Franco, *Design with operational amplifiers and analog integrated circuits*. McGraw-Hill's, 2002.

[88] B. B. Winter and J. G. Webster, "Driven-right-leg circuit design," *IEEE Transactions on Biomedical Engineering*, vol. BME-30, no. 1, pp. 62–66, 1983.

[89] E. Spinelli, N. Martinez, and M. Mayosky, "A transconductance driven-right-leg circuit," *IEEE Transactions on Biomedical Engineering*, vol. 46, no. 12, pp. 1466–1470, 1999.

[90] M. Haberman and E. Spinelli, "A digital driven right leg circuit," in *2010 Annual International Conference of the IEEE Engineering in Medicine and Biology*, pp. 6559–6562, 2010.

[91] Y. G. Lim, G. S. Chung, and K. S. Park, "Capacitive driven-right-leg grounding in indirect-contact ecg measurement," in *2010 Annual International Conference of the IEEE Engineering in Medicine and Biology*, pp. 1250–1253, 2010.

[92] R. Mahajan and B. I. Morshed, "Performance analysis of a DRL-less AFE for battery-powered wearable EEG," *Measurement*, vol. 90, pp. 583–591, 2016.

[93] X.-B. Chen, Y.-X. Zhou, H.-P. Wang, X.-Y. Lü, and Z.-G. Wang, "Design of sEMG-detecting circuit for EMG-bridge," in *2017 39th Annual International Conference of the IEEE Engineering in Medicine and Biology Society (EMBC)*, pp. 382–385, 2017.

[94] A. Mongardi, F. Rossi, P. Motto Ros, A. Sanginario, M. Ruo Roch, M. Martina, and D. Demarchi, "Live demonstration: Low power embedded system for event-driven hand gesture recognition," in *2019 IEEE Biomedical Circuits and Systems Conference (BioCAS)*, pp. 1–1, 2019.

[95] Amazon Web Services, Inc., "FreeRTOS: Real-time operating system for microcontrollers." Accessed: Monday 10th October, 2022.

[96] Altium, "Altium Designer." Accessed: 27/01/2022.

[97] SparkFun Electronics®, "ARTEMIS FEATURES." Accessed: Monday 10th October, 2022.

[98] Cellevia Batteries, "Specification approval datasheet - name: Polymer lithium-ion battery - model: Cellevia batteries lp401230," 3 2016. Release 1.

[99] D. S. S. Corporation, "Solidworks." Accessed: 26/04/2022.

[100] I. 3D Systems, "ProJet MJP 2500/2500 Plus." Accessed: 26/04/2022.

[101] Texas Instruments, "CC2540EMK-USB Bluetooth Low Energy and proprietary wireless MCU." Accessed: Monday 10th October, 2022.

[102] R. K. EGE, ed., *Programming in an Object-Oriented Environment*. Academic Press, 1992.

[103] C. Liechti, "Pyserial." Accessed: Monday 10th October, 2022.

[104] I. Harvey, "Bluepy." Accessed: Monday 10th October, 2022.

[105] B. Project, "BlueZ." Accessed: Monday 10th October, 2022.

[106] K. Project, "Kivy." Accessed: Monday 10th October, 2022.

[107] N. Semiconductor, "nRF Connect for Mobile." Accessed: 26/04/2022.

[108] Università degli Studi di Torino, "Comitato di bioetica dell'ateneo." Accessed: Monday 10th October, 2022.

[109] National Instruments Corp., "USB-6259 - multifunction I/O device." Accessed: Monday 10th October, 2022.

[110] BITalino, "Non-gelled Reusable Ag/AgCl." Accessed: Monday 10th October, 2022.

[111] Cardinal Health, "Kendall H124SG Electrodes." Accessed: Monday 10th October, 2022.

[112] Delsys Incorporated, "How to improve EMG signal quality: The Signal to Noise Ratio (SNR)." Accessed: Monday 10th October, 2022.

[113] D. Liljequist, B. Elfving, and K. Skavberg Roaldsen, "Intraclass correlation – a discussion and demonstration of basic features," *PLOS ONE*, vol. 14, pp. 1–35, 07 2019.

[114] T. K. Koo and M. Y. Li, "A guideline of selecting and reporting intraclass correlation coefficients for reliability research," *Journal of chiropractic medicine*, vol. 15, no. 2, pp. 155–163, 2016.

[115] Tektronix, "DMM7510." Accessed: Monday 10th October, 2022.

[116] M. Johnston, M. Diab, S.-S. Kim, and S. Kirshblum, "Health literacy, morbidity, and quality of life among individuals with spinal cord injury," *The journal of spinal cord medicine*, vol. 28, pp. 230–40, 02 2005.

[117] R. Lo, O. Y. Cheng, M. Wong, W. Tang, K. Wong, J. Woo, and T. Kwok, "Handicap and its determinants of change in stroke survivors one-year follow-up study," *Stroke; a journal of cerebral circulation*, vol. 39, pp. 148–53, 02 2008.

[118] B. Armour, E. Courtney-Long, M. Fox, H. Fredine, and A. Cahill, "Prevalence and causes of paralysis-united states, 2013," *American journal of public health*, vol. 106, pp. e1–e3, 08 2016.

[119] S. Hatem, G. Saussez, M. Faille, V. Prist, X. Zhang, D. Dispa, and Y. Bleyenheuft, "Rehabilitation of motor function after stroke: A multiple systematic review focused on techniques to stimulate upper extremity recovery," *Frontiers in Human Neuroscience*, vol. 10, 09 2016.

[120] "World Health Organization (WHO), Spinal cord injury." Accessed: Monday 10th October, 2022.

[121] "MS International Federation (MSIF), What is MS?." Accessed: Monday 10th October, 2022.

[122] K. Masani and M. Popovic, *Functional Electrical Stimulation in Rehabilitation and Neurorehabilitation*, pp. 877–896. Springer, Berlin, Heidelberg, 01 2011.

[123] HASOMED GmbH, *Operation Manual RehaStim 2, RehaMove 2*, 09 2012.

[124] Y. Hara, "Rehabilitation with functional electrical stimulation in stroke patients," *International Journal of Physical Medicine and Rehabilitation*, vol. 01, 01 2013.

[125] C. Marquez Chin and M. Popovic, "Functional electrical stimulation therapy for restoration of motor function after spinal cord injury and stroke: a review," *BioMedical Engineering OnLine*, vol. 19, 05 2020.

[126] Z. Wang, L. Chen, W. Yi, B. Gu, S. Liu, X. An, M. Xu, H. Qi, F. He, B. Wan, and D. Ming, "Enhancement of cortical activation for motor imagery during BCI-FES training," in *2018 40th Annual International Conference of the IEEE Engineering in Medicine and Biology Society (EMBC)*, pp. 2527–2530, 2018.

[127] G. Buccino and L. Riggio, "The role of the mirror neuron system in motor learning," *Kinesiology 38(2006) 1:1-13*, 12 2013.

[128] A. Benazzouz, R. Guilal, F. Amirouche, and Z. Slimane, "EMG Feature Selection for Diagnosis of Neuromuscular Disorders," pp. 1–5, 06 2019.

[129] N. Parajulli, N. Sreenivasan, P. Bifulco, M. Cesarelli, S. Savino, V. Niola, D. Esposito, T. Hamilton, G. Naik, U. Gunawardana, and G. Gargiulo, "Real-Time EMG Based Pattern Recognition Control for Hand Prostheses: A Review on Existing Methods, Challenges and Future Implementation," *Sensors*, vol. 19, p. 4596, 10 2019.

[130] M. A. Garcés and L. L. Orosco, "Chapter 5 - eeg signal processing in brain–computer interface," in *Smart Wheelchairs and Brain-Computer Interfaces* (P. Diez, ed.), pp. 95–110, Academic Press, 2008.

[131] K. Shima and K. Shimatani, "A new approach to direct rehabilitation based on functional electrical stimulation and emg classification," in *2016 International Symposium on Micro-NanoMechatronics and Human Science (MHS)*, pp. 1–6, 2016.

[132] S.-H. Lee, S. S. Kim, and B.-H. Lee, "Action observation training and brain-computer interface controlled functional electrical stimulation enhance upper extremity performance and cortical activation in patients with stroke: a randomized controlled trial," *Physiotherapy Theory and Practice*, pp. 1–9, 2020.

[133] H. Mao, Y. Li, L. Tang, Y. Chen, J. Ni, L. Liu, and C. Shan, "Effects of mirror neuron system-based training on rehabilitation of stroke patients," *Brain and Behavior*, vol. 10, no. 8, p. e01729, 2020.

[134] L. Fonseca, W. Tigra, B. Navarro, D. Guiraud, C. Fattal, A. Bó, E. Fachin-Martins, V. Leynaert, A. Gélis, and C. Azevedo-Coste, "Assisted grasping in individuals with tetraplegia: Improving control through residual muscle contraction and movement," *Sensors*, vol. 19, no. 20, 2019.

[135] A. Jasuja, V. Gupta, N. S. Sreenivasalu, M. Liu, J. Monz, J. S. Nir, and S. Bhasin, "Development of an extensible, wireless framework for personalized muscle rehabilitation," in *2019 IEEE Healthcare Innovations and Point of Care Technologies, (HI-POCT)*, pp. 17–20, 2019.

[136] E. M. Camilo, J. A. M. Gutiérrez, O. P. Ramírez, J. G. Martínez, A. V. Hernández, and L. L. Salas, "A Functional Electrical Stimulation Controller for Contralateral Hand Movements Based on EMG Signals," in *2020 17th International Conference on Electrical Engineering, Computing Science and Automatic Control (CCE)*, pp. 1–6, 2020.

[137] Z. Bi, X. Bao, H. Wang, X. Lv, and Z. Wang, "Prototype System Design and Experimental Validation of Gait-Oriented EMG Bridge for Volitional Motion Function Rebuilding of Paralyzed Leg," in *2019 IEEE 7th International Conference on Bioinformatics and Computational Biology (ICBCB)*, pp. 79–82, 2019.

[138] Z. Bi, Y. Wang, H. Wang, Y. Zhou, C. Xie, L. Zhu, H. Wang, B. Wang, J. Huang, X. Lü, and Z. Wang, "Wearable emg bridge—a multiple-gesture reconstruction system using electrical stimulation controlled by the volitional surface electromyogram of a healthy forearm," *IEEE Access*, vol. 8, pp. 137330–137341, 2020.

[139] Y. Chen, C. Dai, and W. Chen, "A real-time emg-controlled functional electrical stimulation system for mirror therapy," in *2019 IEEE Biomedical Circuits and Systems Conference (BioCAS)*, pp. 1–4, 2019.

[140] Z. Li, D. Guiraud, D. Andreu, M. Benoussaad, C. Fattal, and M. Hayashibe, "Real-time estimation of fes-induced joint torque with evoked emg : Application to spinal cord injured patients," *Journal of NeuroEngineering and Rehabilitation*, vol. 13, 12 2016.

[141] HASOMED GmbH, "Rehamove – motion training with functional electrical stimulation (fes)." Accessed: Monday 10th October, 2022.

[142] B. Kuberski, *ScienceMode2, RehaStim2 Stimulation Device, Description and Protocol*, 12 2012.

[143] M. R. Popovic, K. Masani, and S. Micera, *Functional Electrical Stimulation Therapy: Recovery of Function Following Spinal Cord Injury and Stroke*, pp. 513–532. Cham: Reinkensmeyer, David J. and Dietz, Volker, 2016.

[144] Y. Li, X. Yang, Y. Zhou, J. Chen, M. Du, and Y. Yang, "Adaptive stimulation profiles modulation for foot drop correction using functional electrical stimulation: a proof of concept study," *IEEE journal of biomedical and health informatics*, vol. 25, no. 1, pp. 59–68, 2020.

[145] M. Peter, *Embedded System Design: Embedded Systems Foundations of Cyber-Physical Systems, and the Internet of Things*. Springer Nature, 2021.

[146] S. J. Johnston and S. J. Cox, "The Raspberry Pi: A technology disrupter, and the enabler of dreams," *Electronics*, vol. 6, no. 3, 2017.

[147] B. Sijobert, C. Azevedo, J. Pontier, S. Graf, and C. Fattal, "A sensor-based multichannel FES system to control knee joint and reduce stance phase asymmetry in post-stroke gait," *Sensors*, vol. 21, no. 6, 2021.

[148] B. Sijobert, R. Le Guillou, C. Fattal, and C. Azevedo Coste, "FES-induced cycling in complete SCI: A simpler control method based on inertial sensors," *Sensors*, vol. 19, no. 19, 2019.

[149] A. Bo, L. da Fonseca, J. Guimaraes, E. Fachin-Martins, M. Paredes, G. Brindeiro, A. de Sousa, M. Dorado, and F. Ramos, "Cycling with spinal cord injury: A novel system for cycling using electrical stimulation for individuals with paraplegia, and preparation for cybathlon 2016," *IEEE Robotics Automation Magazine*, vol. 24, no. 4, pp. 58–65, 2017.

[150] N. S. Dhillon, A. Sutandi, M. Vishwanath, M. M. Lim, H. Cao, and D. Si, "A Raspberry Pi-based traumatic brain injury detection system for single-channel electroencephalogram," *Sensors*, vol. 21, no. 8, 2021.

[151] R. Oshana and M. Kraeling, *Software engineering for embedded systems: Methods, practical techniques, and applications*. Newnes, 2019.

[152] Z. Li, D. Guiraud, D. Andreu, M. Benoussaad, C. Fattal, and M. Hayashibe, "Real-time estimation of FES-induced joint torque with evoked EMG," *Journal of neuroengineering and rehabilitation*, vol. 13, no. 1, pp. 1–11, 2016.

[153] T. Gerstenberg, "Blatann." Accessed: Monday 10th October, 2022.

[154] P. S. Foundation, "Queue — A synchronized queue class." Accessed: Monday 10th October, 2022.

[155] F. Rossi, P. Motto Ros, R. M. Rosales, and D. Demarchi, "Embedded biomimetic system for functional electrical stimulation controlled by event-driven sEMG," *Sensors*, vol. 20, no. 5, 2020.

[156] V. M. S. Ltd, "Vicon." Accessed: Monday 10th October, 2022.

[157] D. Wolf, N. Dunkelberger, C. McDonald, K. Rudy, C. Beck, M. O'Malley, and E. Schearer, "Combining functional electrical stimulation and a powered exoskeleton to control elbow flexion," pp. 1–2, 11 2017.

[158] C. Lynch, D. Sayenko, and M. Popovic, "Co-contraction of antagonist muscles during knee extension against gravity: Insights for functional electrical stimulation control design," *Conference proceedings : ... Annual International Conference of the IEEE Engineering in Medicine and Biology Society.*

IEEE Engineering in Medicine and Biology Society. Conference, vol. 2012, pp. 1843–6, 08 2012.

[159] W. Huo, V. Arnez-Paniagua, M. Ghedira, Y. Amirat, J.-M. Gracies, and S. Mohammed, "Adaptive fes assistance using a novel gait phase detection approach," in *2018 IEEE/RSJ International Conference on Intelligent Robots and Systems (IROS)*, pp. 1–9, 2018.

[160] S.-Y. Ha, J.-H. Han, Y. Ko, and Y.-H. Sung, "Ankle exercise with functional electrical stimulation affects spasticity and balance in stroke patients," *Journal of Exercise Rehabilitation*, vol. 16, pp. 496–502, 12 2020.

[161] J. Soucie, C. Wang, A. Forsyth, S. Funk, M. Denny, K. Roach, and D. Boone, "Range of motion measurements: Reference values and a database for comparison studies," *Haemophilia : the official journal of the World Federation of Hemophilia*, vol. 17, pp. 500–7, 11 2010.

[162] J. Ryu, W. P. Cooney, L. J. Askew, K.-N. An, and E. Y. Chao, "Functional ranges of motion of the wrist joint," *The Journal of Hand Surgery*, vol. 16, no. 3, pp. 409–419, 1991.

[163] C. C. Norkin and D. J. White, *Measurement of Joint Motion: A Guide to Goniometry, 4e*. New York, NY: F A Davis Co, 2009.

[164] W. H. O. (WHO, "Advice for the public: Coronavirus disease (covid-19)." Accessed: Monday 10th October, 2022.

[165] Vicon Motion Systems Ltd, "Vicon Nexus User Guide." Accessed: Monday 10th October, 2022.

[166] Vicon Motion Systems Ltd, "Plug-in Gait Reference Guide." Accessed: Monday 10th October, 2022.

[167] A. Prestia, F. Rossi, A. Mongardi, P. M. Ros, M. R. Roch, M. Martina, and D. Demarchi, "Motion analysis for experimental evaluation of an event-driven fes system," *IEEE Transactions on Biomedical Circuits and Systems*, vol. 16, no. 1, pp. 3–14, 2022.

[168] HASOMED GmbH, *RehaMove, Functional electrical stimulation - FES applications*, June 2015.

[169] "Electrode placement and functional movement." Accessed: Monday 10th October, 2022.

[170] "FIAB products." Accessed: Monday 10th October, 2022.

[171] D. Jessop and M. Pain, "Maximum velocities in flexion and extension actions for sport," *Journal of Human Kinetics*, vol. 50, 03 2016.

[172] V. M. S. Ltd, "Nexus." Accessed: Monday 10th October, 2022.

[173] A. Do, P. Wang, C. King, A. Abiri, and Z. Nenadic, "Brain-computer interface controlled functional electrical stimulation system for ankle movement," *Journal of neuroengineering and rehabilitation*, vol. 8, p. 49, 08 2011.

[174] A. Vette, K. Masani, and M. Popovic, "Time Delay from Muscle Activation to Torque Generation during Quiet Stance: Implications for Closed-Loop Control via FES," *Biomed Tech*, vol. 53, 01 2008.

[175] R. J. Downey, M. Merad, E. J. Gonzalez, and W. E. Dixon, "The time-varying nature of electromechanical delay and muscle control effectiveness in response to stimulation-induced fatigue," *IEEE Transactions on Neural Systems and Rehabilitation Engineering*, vol. 25, no. 9, pp. 1397–1408, 2017.

[176] Y.-X. Zhou, H.-P. Wang, X.-P. Cao, Z.-Y. Bi, Y.-J. Gao, X.-B. Chen, X.-Y. Lü, and Z.-G. Wang, "Electromyographic bridge—a multi-movement volitional control method for functional electrical stimulation: prototype system design and experimental validation," in *2017 39th Annual International Conference of the IEEE Engineering in Medicine and Biology Society (EMBC)*, pp. 205–208, 2017.

[177] S. Carvalho, A. Correia, J. Figueiredo, J. M. Martins, and C. P. Santos, "Functional electrical stimulation system for drop foot correction using a dynamic narx neural network," *Machines*, vol. 9, no. 11, p. 253, 2021.

[178] S. Jiang, P. Kang, X. Song, B. P. Lo, and P. B. Shull, "Emerging wearable interfaces and algorithms for hand gesture recognition: A survey," *IEEE Reviews in Biomedical Engineering*, vol. 15, pp. 85–102, 2022.

[179] P. Visconti, F. Gaetani, G. Zappatore, and P. Primiceri, "Technical features and functionalities of Myo armband: An overview on related literature and advanced applications of myoelectric armbands mainly focused on arm prostheses," *International Journal on Smart Sensing and Intelligent Systems*, vol. 11, no. 1178-5608, pp. 1–25, 2018.

[180] Z. Xu, L. Shen, J. Qian, and Z. Zhang, "Advanced hand gesture prediction robust to electrode shift with an arbitrary angle," *Sensors*, vol. 20, no. 4, 2020.

[181] B. Kundu and D. Subarram Naidu, "Classification and feature extraction of different hand movements from EMG signal using machine leaning based algorithms," in *2021 International Conference on Electrical, Communication, and Computer Engineering (ICECCE)*, pp. 1–5, 2021.

[182] X. Hu, H. Zeng, A. Song, and D. Chen, "Robust continuous hand motion recognition using wearable array myoelectric sensor," *IEEE Sensors Journal*, vol. 21, no. 18, pp. 20596–20605, 2021.

[183] C. Tepe and M. Erdim, "Classification of EMG finger data acquired with Myo armband," in *2020 International Congress on Human-Computer Interaction, Optimization and Robotic Applications (HORA)*, pp. 1–4, 2020.

[184] V. Kartsch, S. Benatti, M. Mancini, M. Magno, and L. Benini, "Smart wearable wristband for EMG based gesture recognition powered by solar energy harvester," in *2018 IEEE International Symposium on Circuits and Systems (ISCAS)*, pp. 1–5, IEEE, 2018.

[185] M. Ergeneci, K. Gokcesu, E. Ertan, and P. Kosmas, "An embedded, eight channel, noise canceling, wireless, wearable sEMG data acquisition system with adaptive muscle contraction detection," *IEEE Transactions on Biomedical Circuits and Systems*, vol. 12, no. 1, pp. 68–79, 2018.

[186] U. Côté-Allard, G. Gagnon-Turcotte, F. Laviolette, and B. Gosselin, "A low-cost, wireless, 3-D-printed custom armband for sEMG hand gesture recognition," *Sensors*, vol. 19, no. 12, 2019.

[187] A. Toro Ossaba, J. Jose Jaramillo Tigreros, and J. Camilo Tejada Orjuela, "Open source multichannel EMG armband design," in *2020 IX International Congress of Mechatronics Engineering and Automation (CIIMA)*, pp. 1–6, 2020.

[188] S. Jiang, Q. Gao, H. Liu, and P. B. Shull, "A novel, co-located EMG-FMG-sensing wearable armband for hand gesture recognition," *Sensors and Actuators A: Physical*, vol. 301, p. 111738, 2020.

[189] O. Ozturk, A. Golparvar, and M. K. Yapici, "Smart armband with graphene textile electrodes for EMG-based muscle fatigue monitoring," in *2021 IEEE Sensors*, pp. 1–4, 2021.

[190] Z. Lu, X. Chen, Q. Li, X. Zhang, and P. Zhou, "A hand gesture recognition framework and wearable gesture-based interaction prototype for mobile devices," *IEEE Transactions on Human-Machine Systems*, vol. 44, no. 2, pp. 293–299, 2014.

[191] T. Phienthrakul, "Armband gesture recognition on electromyography signal for virtual control," in *2018 10th International Conference on Knowledge and Smart Technology (KST)*, pp. 149–153, 2018.

[192] M. Woźniak, P. Pomykalski, D. Sielski, K. Grudzień, N. Paluch, and Z. Chaniecki, "Exploring EMG gesture recognition-interactive armband for audio playback control," in *2018 Federated Conference on Computer Science and Information Systems (FedCSIS)*, pp. 919–923, 2018.

[193] S. Tam, M. Boukadoum, A. Campeau-Lecours, and B. Gosselin, "A fully embedded adaptive real-time hand gesture classifier leveraging HD-sEMG and deep learning," *IEEE Transactions on Biomedical Circuits and Systems*, vol. 14, no. 2, pp. 232–243, 2020.

[194] M. Arozi, M. Ariyanto, A. Kristianto, Munadi, and J. D. Setiawan, "EMG signal processing of Myo armband sensor for prosthetic hand input using RMS and ANFIS," in *2020 7th International Conference on Information Technology, Computer, and Electrical Engineering (ICITACEE)*, pp. 36–40, 2020.

[195] O. W. Samuel, M. G. Asogbon, Y. Geng, A. H. Al-Timemy, S. Pirbhulal, N. Ji, S. Chen, P. Fang, and G. Li, "Intelligent EMG pattern recognition control method for upper-limb multifunctional prostheses: Advances, current challenges, and future prospects," *IEEE Access*, vol. 7, pp. 10150–10165, 2019.

[196] S. Kim, J. Kim, B. Koo, T. Kim, H. Jung, S. Park, S. Kim, and Y. Kim, "Development of an armband EMG module and a pattern recognition algorithm for the 5-finger myoelectric hand prosthesis," *International Journal of Precision Engineering and Manufacturing*, vol. 20, pp. 1997–2006, 2019.

[197] S. Singhvi and H. Ren, "Comparative study of motion recognition with temporal modelling of electromyography for thumb and index finger movements aiming for wearable robotic finger exercises," in *2018 3rd International Conference on Advanced Robotics and Mechatronics (ICARM)*, pp. 509–514, 2018.

[198] A. B. H. Amor, O. E. Ghoul, and M. Jemni, "Sign language handshape recognition using Myo armband," 2019.

[199] S. Kim, J. Kim, S. Ahn, and Y. Kim, "Finger language recognition based on ensemble artificial neural network learning using armband EMG sensors," *Technology and health care: official journal of the European Society for Engineering and Medicine*, vol. 26, pp. 249–258, 2018.

[200] N. Nasri, S. Orts-Escolano, and M. Cazorla, "An sEMG-controlled 3D game for rehabilitation therapies: Real-time time hand gesture recognition using deep learning techniques," *Sensors*, vol. 20, no. 22, 2020.

[201] L. van Dijk, C. K. van der Sluis, H. W. van Dijk, and R. M. Bongers, "Learning an EMG controlled game: Task-specific adaptations and transfer," *PLoS ONE*, vol. 11, 2016.

[202] P. N. Müller, P. Achenbach, A. M. Kleebe, J. U. Schmitt, U. Lehmann, T. Tregel, and S. Göbel, "Flex your muscles: EMG-based serious game controls," in *Serious Games*, pp. 230–242, Springer International Publishing, 2020.

[203] S. Sadeghi Esfahlani, B. Muresan, A. Sanaei, and G. Wilson, "Validity of the Kinect and Myo armband in a serious game for assessing upper limb movement," *Entertainment Computing*, vol. 27, pp. 150–156, 2018.

[204] F. Rossi, F. Savi, A. Prestia, A. Mongardi, D. Demarchi, and G. Buccino, "Combining action observation treatment with a brain-computer interface system: Perspectives on neurorehabilitation," *Sensors*, vol. 21, no. 24, 2021.

[205] A. Baraka, H. Shaban, M. Abou El-Nasr, and O. Attallah, "Wearable accelerometer and sEMG-based upper limb BSN for tele-rehabilitation," *Applied Sciences*, vol. 9, no. 14, 2019.

[206] Z. Bi, Y. Wang, H. Wang, Y. Zhou, C. Xie, L. Zhu, H. Wang, B. Wang, J. Huang, X. Lü, and Z. Wang, "Wearable EMG bridge—a multiple-gesture reconstruction system using electrical stimulation controlled by the volitional surface electromyogram of a healthy forearm," *IEEE Access*, vol. 8, pp. 137330–137341, 2020.

[207] J. O. Pinzón-Arenas, R. Jiménez-Moreno, and J. E. Herrera-Benavides, "Convolutional neural network for hand gesture recognition using 8 different EMG signals," in *2019 XXII Symposium on Image, Signal Processing and Artificial Vision (STSIVA)*, pp. 1–5, 2019.

[208] X. Chen, Y. Li, R. Hu, X. Zhang, and X. Chen, "Hand gesture recognition based on surface electromyography using convolutional neural network with transfer learning method," *IEEE Journal of Biomedical and Health Informatics*, vol. 25, no. 4, pp. 1292–1304, 2021.

[209] E. Donati, M. Payvand, N. Risi, R. Krause, K. Burelo, G. Indiveri, T. Dalgaty, and E. Vianello, "Processing EMG signals using reservoir computing on an event-based neuromorphic system," in *2018 IEEE Biomedical Circuits and Systems Conference (BioCAS)*, pp. 1–4, 2018.

[210] M. Tavakoli, C. Benussi, P. Alhais Lopes, L. B. Osorio, and A. T. de Almeida, "Robust hand gesture recognition with a double channel surface EMG wearable armband and SVM classifier," *Biomedical Signal Processing and Control*, vol. 46, pp. 121–130, 2018.

[211] A. Phinyomark and E. Scheme, "A feature extraction issue for myoelectric control based on wearable EMG sensors," in *2018 IEEE Sensors Applications Symposium (SAS)*, pp. 1–6, 2018.

[212] Y. Hu, Y. Wong, Q. Dai, M. Kankanhalli, W. Geng, and X. Li, "sEMG-based gesture recognition with embedded virtual hand poses and adversarial learning," *IEEE Access*, vol. 7, pp. 104108–104120, 2019.

[213] E. Cordedda, "Riconoscimento real time di gesti applicato a segnali emg super ciali basato su atc," 12 2016.

[214] B. Crawford, K. Miller, P. Shenoy, and R. Rao, "Real-time classification of electromyographic signals for robotic control," in *Proceedings of the 20th National Conference on Artificial Intelligence - Volume 2*, AAAI'05, p. 523–528, AAAI Press, 2005.

[215] P. Shenoy, K. J. Miller, B. Crawford, and R. P. N. Rao, "Online electromyographic control of a robotic prosthesis," *IEEE Transactions on Biomedical Engineering*, vol. 55, no. 3, pp. 1128–1135, 2008.

[216] Mitchell, B and Whited, L, "Anatomy, Shoulder and Upper Limb, Forearm Muscles." StatPearls [Internet]. Treasure Island (FL): StatPearls Publishing, 06 2022. Updated 2022 Jun 14, Available from: https://www.ncbi.nlm.nih.gov/books/NBK536975/, last accessed on 01/09/22.

[217] I. Furfaro, "Integration and validation of average threshold crossing (atc) applied to surface electromyography (semg)," 10 2015.

[218] A. Mongardi, "A low power embedded system for real-time emg based event-driven gesture recognition," 07 2019.

[219] Ambiq Micro, Inc., "Apollo2 MCU Datasheet." PDF document, 09 2020. Revision 1.2, URL:https://ambiq.com/apollo2/, last accessed on Monday 10th October, 2022.

[220] A. Ng, "Machine Learning *by Stanford University*." Accessed: 12/01/2022.

[221] ARM, "CMSIS Library," 2019. Accessed: 14/01/2022.

[222] V. Barresi, "Machine learning approaches for embedded real-time gesture recognition," 07 2020.

[223] M. Tolomei, "Towards an electromyographic armband: an embedded machine learning algorithms comparison," 12 2020.

[224] P. Visconti, F. Gaetani, G. Zappatore, and P. Primiceri, "Technical features and functionalities of myo armband: An overview on related literature and advanced applications of myoelectric armbands mainly focused on arm prostheses," *International Journal on Smart Sensing and Intelligent Systems*, vol. 11, pp. 1–25, 06 2018.

[225] O. T. Co., "gForcePro+ EMG Armband." Accessed: 19/01/2022.

[226] U. Côté-Allard, G. Gagnon-Turcotte, F. Laviolette, and B. Gosselin, "A low-cost, wireless, 3-d-printed custom armband for semg hand gesture recognition," *Sensors*, vol. 19, no. 12, 2019.

[227] Z. Xu, L. Shen, J. Qian, and Z. Zhang, "Advanced hand gesture prediction robust to electrode shift with an arbitrary angle," *Sensors*, vol. 20, no. 4, 2020.

[228] g.tec medical engineering GmbH, "g.HIamp - 256 Biosignal Amplifier." Accessed: 21/01/2022.

[229] M. Becchio, N. Voster, A. Prestia, A. Mongardi, F. Rossi, P. M. Ros, M. R. Roch, M. Martina, and D. Demarchi, "Live demonstration: Event-driven hand gesture recognition for wearable human-machine interface," in *2021 IEEE Biomedical Circuits and Systems Conference (BioCAS)*, pp. 1–1, 2021.

[230] Pololu Corporation, "Zumo Robot for Arduino." Accessed: 28/04/2022.

[231] Arduino S.r.l., "Arduino Uno Rev3." Accessed: 28/04/2022.

[232] Formlabs, "Form 3+ - Rapid, Flawless Prints, Every Time." Accessed: 16/03/2022.

[233] Cellevia Batteries, "Polymer Lithium-Ion Battery." Accessed: Monday 10th October, 2022.

[234] J. Tomczyński, T. Mańkowski, and P. Kaczmarek, "Influence of sEMG electrode matrix configuration on hand gesture recognition performance," in *2017 Signal Processing: Algorithms, Architectures, Arrangements, and Applications (SPA)*, pp. 42–47, 2017.

[235] A. Inselberg, "The plane with parallel coordinates," *The Visual Computer*, vol. 1, pp. 69–91, 1985.

[236] D. P. Kingma and J. Ba, "Adam: A method for stochastic optimization." Accessed: Monday 10th October, 2022.

[237] D. M. W. Powers, "Evaluation: from precision, recall and F-measure to ROC, informedness, markedness and correlation," *CoRR*, 2020.

[238] Texas Instruments Inc., "INA240." Accessed: Monday 10th October, 2022.

[239] Rigol Technologies EU GMBH, "Digital Oscilloscope MSO5104." Accessed: Monday 10th October, 2022.